Fall 2013

Multiscale Simulation of Thermocline Energy Storage for Concentrating Solar Power

Scott Michael Flueckiger
Purdue University

Follow this and additional works at: https://docs.lib.purdue.edu/open_access_dissertations

 Part of the Mechanical Engineering Commons

PURDUE UNIVERSITY
GRADUATE SCHOOL
Thesis/Dissertation Acceptance

This is to certify that the thesis/dissertation prepared

By _Scott M. Flueckiger_

Entitled
Multiscale Simulation of Thermocline Energy Storage for Concentrating Solar Power.

For the degree of ____Doctor of Philosophy____

Is approved by the final examining committee:

Suresh Garimella
_____
Chair

Timothy Fisher
_____

Eckhard Groll
_____

Rakesh Agrawal
_____

To the best of my knowledge and as understood by the student in the *Research Integrity and Copyright Disclaimer (Graduate School Form 20)*, this thesis/dissertation adheres to the provisions of Purdue University's "Policy on Integrity in Research" and the use of copyrighted material.

Approved by Major Professor(s): _Suresh Garimella_____

_____

Approved by: _David Anderson_____ 10/08/2013
Head of the Graduate Program   Date

MULTISCALE SIMULATION OF THERMOCLINE ENERGY STORAGE FOR
CONCENTRATING SOLAR POWER

A Dissertation

Submitted to the Faculty

of

Purdue University

by

Scott M. Flueckiger

In Partial Fulfillment of the

Requirements for the Degree

of

Doctor of Philosophy

December 2013

Purdue University

West Lafayette, Indiana

To Tiffany and Owen

ACKNOWLEDGEMENTS

I would like to thank my advisor Prof. Suresh Garimella for his support, patience, and optimism throughout my graduate studies. The value of his guidance cannot be overstated and I am forever grateful. I must also extend gratitude to Prof. Eckhard Groll for his technical insights and to my advisory committee for their helpful advice. Additional thanks to Dr. Justin Weibel, Dr. Craig Bradshaw, Matthew Rau, Dr. Karthik Bodla, and Seth Holloway for their assistance, generosity, and friendship.

The Concentrating Solar Technologies Department of Sandia National Laboratories has been an invaluable asset to me as well as a continuing source of inspiration. Dr. Brian Iverson, Greg Kolb, and Jim Pacheco were integral to the development of this work and I am privileged to have their contributed expertise. I also owe much to Brian Ehrhart for his assistance with power tower modeling.

And a final thank you to my wife and son, who give this work its meaning.

TABLE OF CONTENTS

LIST OF TABLES

LIST OF FIGURES

Figure   Page

NOMENCLATURE

A	area, m^2
A_y	annual plant availability
Bi	Biot number
C_0	nondimensional heat-exchange region velocity
C_P	specific heat, J/kg-K
CF	capacity factor
CSP	concentrating solar power
d	thermocline tank diameter, m
d'	thermocline tank port diameter, m
d_{abs}	absorber tube diameter, m
d_{rec}	solar receiver diameter, m
d_s	effective granule diameter, m
Da	Darcy number
DCC	direct capital cost, $¢/kW_e$
DNI	direct normal irradiance, W/m^2
e	mushy region half span, K
E	Energy, J
E_M	Young's modulus, Pa
Ec	Eckert number

F	inertial coefficient
F_s	solid fraction
FCR	fixed charge rate, 1/yr
FOM	fixed operation and maintenance, ¢/kW$_e$
g	gravitational constant, m/s^2
h	thermocline tank height, m
h'	thermocline tank distributor height, m
h_{fs}	heat of fusion, J/kg
h_i	interstitial heat transfer coefficient, W/m^3-K
h_{rec}	solar receiver height, m
h_w	wall convection coefficient, W/m^2-K
H	nondimensional tank height
HTF	heat transfer fluid
i	enthalpy, J/kg
I	second moment of inertia, m^4
j	current porous bed cell
k	thermal conductivity, W/m-K
K	permeability, m^2
L	length, m
L_{fs}	latent heat, J/kg
$LCOE$	levelized cost of electricity, ¢/kWh$_e$
m	mass, kg
N	number of porous bed cells
N_v	nondimensional viscous dissipation

Nu	Nusselt number
p	pressure, Pa
P	thermal power, W
Pr	Prandtl number
PCM	phase change material
q	heat rate, W
Q	volumetric flow rate, m^3/s
Q_{rec}	solar receiver energy, J
r	radial location, m
R	nondimensional radial location
Re	Reynolds number
S	entropy, J/K
Ste	Stefan number
SM	solar multiple
t	time, s
T	temperature, °C
TCC	total capital cost, ¢/kW_e
u	velocity, m/s
U	overall heat transfer coefficient, W/m^2-K
U_{lat}	latent heat utilization
U_{sen}	sensible heat utilization
U'	port inlet velocity, m/s
v	heat-exchange region velocity, m/s
VOM	variable operation and maintenance, ¢/kWh_e

W	work output, W
x	axial location, m
X	exergy, J

Greek

α	coefficient of linear thermal expansion, 1/K
δ	thickness, m
Δh_{fs}	heat of fusion, J/kg
Δh_s	isentropic enthalpy change, J/kg
Δy	change in absorber tube height, m
ε	porosity
ε_{HX}	heat exchanger effectiveness
ε_M	mechanical strain
ε_T	thermal strain
ε_{tank}	storage effectiveness
ε_w	wall emissivity
η	efficiency
θ	angle, rad
Θ	nondimensional temperature
μ	dynamic viscosity, Pa-s
v	kinematic viscosity, m^2/s
v_P	Poisson's ratio
ρ	density, kg/m^3
σ	stress, Pa
σ_{rad}	Stefan-Boltzmann constant, W/m^2-K^4

σ_y	yield strength, Pa
τ	nondimensional time
Φ	viscous dissipation function, $1/\text{s}^2$
X	nondimensional axial location
Ψ	length ratio
ω	nondimensional stress
ω_t	turbine rotational speed, rpm

Subscript

0	reference
1	internal firebrick insulation
2	steel shell layer
3	external ceramic insulation
95	95th percentile
abs	absorber tube
b	bulk
bot	bottom
c	cold temperature limit
chg	charge mode
comp	compressor
cyc	power cycle
des	destruction
dis	discharge mode
e	electric
eff	effective

ext	external tube surface
gen	generation
h	hot temperature limit
heel	liquid heel
hel	heliostat
HX	heat exchanger
i	interstitial
in	inlet
init	intial
I	first law
II	second law
l	heat transfer fluid
lat	latent heat
liq	liquidus temperature
m	melting point
max	maximum
min	minimum
net	net output
out	outlet
p	pump
par	parasitic
rec	solar receiver
s	thermocline tank filler
sag	gravitational sag

sen	sensible heat
sol	solidus temperature
sur	internal tube surface
t	thermal
turb	turbine
top	top
tow	solar tower
w	wall
wat	water
x	axial location
∞	ambient

ABSTRACT

Flueckiger, Scott M. Ph.D., Purdue University, December 2013. Multiscale Simulation of Thermocline Energy Storage for Concentrating Solar Power. Major Professor: Suresh V. Garimella, School of Mechanical Engineering.

Concentrating solar power (CSP) is a renewable and demonstrated technology for large-scale power generation but requires multiple engineering advancements to achieve grid parity with conventional fossil fuels. Part of this advancement includes novel and inexpensive thermal energy systems to decouple daily power production from intermittent solar collection. Dual-media thermocline tanks, composed of molten salt and solid rock filler, offer low-cost storage capability but the concept has experienced limited deployment in CSP plants due to unresolved concerns about long-term thermal and structural stability. The main objective of the present work is to advance the understanding of thermocline storage design and operation necessary for future commercial implementations. A multiscale numerical approach is conducted to investigate tank behavior at both a device level for comprehensive short-term analysis and at a system-level for reduced-order long-term analysis.

A computational fluid dynamics (CFD) model is first developed to simulate molten-salt thermocline tanks in response to cyclic charge and discharge modes of operation. The model builds upon previous work in the literature with an expanded study of the internal solid filler size as well as added consideration for practical limits on tank height. Reducing the internal filler size improves thermal stratification inside the tank but decreases the bed permeability, resulting in a design tradeoff between storage performance and required pumping power. An effective rock diameter of 1 cm is found to be the most practical selection among the sizes considered. Also of interest is the structural stability of the thermocline tank wall in response to large temperature

fluctuations associated with repeated charging and discharging. If sufficient hoop stress is generated from storage cycles, the tank becomes susceptible to failure via thermal ratcheting. The thermocline tank model is therefore extended to predict wall stress associated with operation and determine if ratcheting is expected to occur. Analysis is first performed with a multilayer structure to identify stable tank wall designs. Inclusion of internal thermal insulation between the porous bed and the steel wall is found to best prevent thermal ratcheting by decoupling the thermal response of the wall from the interior salt behavior. The structural modeling approach is then validated with a simulation of the 182 MWh$_t$ thermocline tank installed at the historic Solar One power tower plant. The hoop stress predictions are found to show reasonable agreement with reported strain gage data along the tank wall and verify that the tank was not susceptible to ratcheting.

The preceding use of commercial CFD software for thermocline tank simulation provides comprehensive solutions but the ease of application of this approach with respect to different operating scenarios is constrained by high computing costs. A new reduced-order model of energy transport inside a thermocline tank is therefore developed to provide thermal solutions at much lower computational cost. The storage model is first validated with past experimental data and then integrated into a system model of a 100 MW$_e$ molten-salt power tower plant, such that the thermocline tank is subjected to realistic solar collection and power production processes. Results from the system-level approach verify that a thermocline tank remains an effective and viable energy storage system over long-term operation within a CSP plant. The system-level analysis is then extended with an economic assessment of thermocline storage in a power tower plant. A parametric study of the plant solar multiple and thermocline tank size highlights suitable plant designs to minimize the levelized cost of electricity. Among the cases considered, a minimum levelized cost of 12.2 ¢/kWh$_e$ is achieved, indicating that cost reductions outside of thermal energy storage remain necessary to obtain grid parity.

As a sensible heat storage method, dual-media thermocline tanks remains subject to low energy densities and require large tank volumes. A possible design modification to reduce tank size is a substitution of the internal rock filler with an encapsulated phase-

change material (PCM), which adds a high density latent heat storage mechanism to the tank assembly. The reduced-order thermocline tank model is first updated to include capsules of a hypothetical PCM and then reintegrated into the power tower plant system model. Implementation of a single PCM inside the tank does not yield significant energy storage gains because of an inherent tradeoff between the thermodynamic quality (*i.e.*, melting temperature and heat of fusion) of the added latent heat and its utilization in storage operations. This problem may be circumvented with a cascaded filler structure composed of multiple PCMs with their melting temperatures tuned along the tank height. However, the benefit of a cascade structure is highly sensitive to appropriate selection of the PCM melting points relative to the thermocline tank operating temperatures.

CHAPTER 1. INTRODUCTION

Diminishing fossil fuel reserves and escalating impacts of anthropogenic climate change due to greenhouse gas emissions have led to an unprecedented global interest in renewable sources of energy. A prominent candidate among these emerging technologies is the conversion of sunlight to electricity. This conversion is performed either directly with solar cells (using the photovoltaic effect) or indirectly with the concentration of sunlight to generate high temperature heat, which then supports a thermodynamic power cycle. This indirect approach, known as concentrating solar power (CSP), is most practical for electricity generation at a large commercial scale. In a CSP plant, arrays of reflective surface area or mirrors focus direct sunlight onto a receiver surface located at the focal point of concentration. A heat transfer fluid (HTF) absorbs this radiation as sensible heat and then transports it from the solar receiver to the power block. The fluid exits the power block at an energy-depleted or cold state and returns to the receiver to sustain the conversion process. While environmentally benign, practical application of CSP is constrained to very sunny locations that receive at least 1800 kWh_t/m^2 of direct insolation per year [1]. North Africa, the Middle East, as well as the southwest United States all offer excellent sites.

For a fixed ground location, the instantaneous position of the sun is described by the solar azimuth and solar altitude angles. As the sun travels across the sky, a CSP collector system of mirrors must traverse at least one of these angles to sustain concentration of direct normal irradiance over a given day. Line-focus collectors traverse a single angle; point-focus collectors traverse both angles. The collector design is also characterized by the ratio of mirror aperture area to receiver area, termed the concentration ratio. Point-focus collectors exhibit much higher concentration ratios (and

thus higher operating temperatures) but require more sophisticated tracking mechanisms. Multiple techniques for both line-focus and point-focus have emerged in recent decades for commercial CSP applications and are categorized into four distinct methods: parabolic trough, compact linear Fresnel reflector, power tower, and Stirling dish receiver.

Parabolic trough collectors are a line-focus technique in which arrays of parabolic-shaped mirrors reflect incident sunlight onto a horizontal receiver tube, located along the focal point of the parabola. As a single-axis solar tracker, the mirrors are typically oriented along a north-south axis to track the transient change in solar azimuth angle, maximizing daily concentration at the expense of seasonal concentration. The receiver is composed of an absorber tube (coated in wavelength-selective paint to maximize solar absorption) and a surrounding vacuum glass jack to dampen convection and emissive radiation losses to the surroundings. The absorber tube also acts as a piping network to both heat and transport HTF across the array of mirrors until final delivery to the power block. The first commercial implementation of the parabolic trough concept was the nine Solar Electric Generating Systems (SEGS) plants constructed by Luz International in the Mojave Desert between 1985 and 1991. Each plant remains in operation today, with a combined power output of 353.8 MW_e [2]. The parabolic trough concept has since become the most prevalent CSP collection technology with numerous commercial plants throughout the United States and Europe.

A compact linear Fresnel reflector offers a cheaper line-focus method in which the parabolic trough concept is mimicked with a series of long segmented flat mirrors [3]. The mirrors are installed at equal elevation but adjusted to different angular orientations in order to approximate a parabola. Independent rotation of the mirrors also enables a fixed focal point in space and thus a stationary receiver tube. Economic savings arise from the use of flat mirrors in place of curved surfaces. Mirror installation near the ground also alleviates wind loads that are detrimental to alignment. Operational compact linear Fresnel plants are so far limited to 5 MW_e output at present, but retain promise for further development.

For point-focus collection, a central receiver or power tower design includes thousands of individual heliostats that concentrate sunlight onto a stationary receiver installed at the top of a tower. Heliostats are mirrors that do not track the position of the sun but instead track the vector that bisects the immediate angle created by the sun, the mirror, and the receiver. The heliostats achieve point-focus via two-axis rotation in both the azimuth and altitude directions. The benefit is an increased concentrated heat flux relative to line-focus, allowing for hotter receiver temperatures and thermodynamic efficiency gains in the power block. The 10 MW$_e$ Solar One pilot plant near Barstow, CA was the first large-scale implementation of power tower technology, in operation from 1982 to 1988 [4]. Since then, large-scale power tower facilities include the retrofitted Solar Two (in operation from 1996 to 1999), the 5 MW$_e$ Sierra SunTower in Lancaster, CA, the 11 MW$_e$ Planta Solar 10 and 20 MW$_e$ Planta Solar 20 plants in Spain, and the 19.9 MW$_e$ Gemasolar Thermosolar plant in Spain [5].

A Stirling dish receiver is an alternative point-focus method composed of a single two-axis tracking paraboloidal surface. The paraboloidal shape, fabricated with a coordinated arrangement of mirror facets, achieves the highest solar concentration ratios and operating temperatures of the four solar harvesting technologies. As with parabolic trough, the focal point of the concentrator is not fixed in space. The very high temperatures associated with dish concentration necessitate use of a Stirling engine with gaseous working fluid in conjunction with a generator at the focal point. Thus unlike the previous solar harvesting technologies, electricity generation occurs directly at the focal point without an intermediate HTF. Despite inherently large thermal conversion efficiencies, use of a paraboloidal reflector and mobile Stirling engine limits the individual unit size. Dish receivers must therefore be operated collectively to supply electricity at a commercial scale. A historic implementation of dish receivers was the 1.5 MW$_e$ Maricopa Solar pilot plant in Peoria, AZ.

Despite the renewable benefit of solar power and the commercial validation of different collector technologies, CSP systems remain inferior to traditional fossil-fuel plants such as coal or natural gas for several reasons. CSP is only viable in areas with adequate solar resources as previously discussed, but also requires contiguous level

terrain for installation of the solar collector field. In contrast, fossil fuel combustion does not incur such geographical limitations. With respect to operation, a current state-of-the-art power tower plant may exhibit an annual capacity factor of 0.48 and a levelized cost of electricity (LCOE) of 15 ¢/kWh$_e$ [6]. Future natural-gas fired plants, however, are projected to provide a capacity factor of 0.87 and an LCOE of 6.71 ¢/kWh. Reason for this plant performance gap includes the high capital and maintenance costs associated with solar collection as well as the inherent variation of sunlight across multiple time scales. The diurnal cycle of sunlight requires CSP plants to undergo daily startup and shutdown procedures in response to nighttime conditions. In addition, random cloud transients can subject nominal daytime operation to sporadic losses in solar irradiance and destabilize the corresponding electricity generation.

The United States Department of Energy has attempted to spur dramatic and near-term improvements in CSP plant performance with a stated LCOE goal of 6 ¢/kWh by 2020 [7]. This target cost is estimated to achieve the desired grid parity between CSP and fossil fuel in the United States, but carries several major engineering challenges in order to be realized. Key challenges include higher operating temperatures to boost thermal efficiency in the power block, a transition to alternative working fluids that both increase efficiency and minimize on-site water consumption, and novel thermal energy storage systems to improve plant capacity factor.

All current CSP plants operate a conventional steam Rankine cycle, where heat addition and rejection both occur across the vapor dome of the working fluid and carry a phase change between liquid and vapor. This isothermal condition limits condensation of the turbine exhaust to temperatures near the external ambient. Without a large temperature difference, effective heat rejection to the ambient commonly involves a condensing fluid with high heat capacity, such as water. Such large-scale water consumption for cooling is not viable in arid regions common to CSP and necessitates a transition to dry heat rejection with air. Solar Rankine cycles can be operated with dry cooling but suffer corresponding losses in cycle efficiency. Therefore, next-generation power blocks must apply alternative working fluids that support dry cooling and also

exhibit good thermal-to-electric conversion efficiencies. A promising low-cost candidate is supercritical carbon dioxide.

For parabolic troughs and power towers, practical delivery of heat to the power block restricts selection of the HTF to materials that remain liquid at very high temperatures, *i.e.*, synthetic oils and molten salts. A comparison of liquid operating temperatures for suitable commercial fluids is illustrated in Figure 1.1 [8]. Synthetic oils such as Therminol VP-1 are an expedient design option as they remain in liquid phase under ambient temperatures. However, high vapor pressures limit stable liquid operation of such oils to temperatures below 400 °C, constraining the overall plant performance. Considerable gains in thermal efficiency are possible with a transition to molten nitrate salt mixtures, which remain in stable liquid states up to 600 °C. Furthermore, molten salts are low-cost, nonflammable, and nontoxic. Commercial salt mixtures include solar salt (60 wt.% $NaNO_3$, 40 wt.% KNO_3), HITEC (53 wt.% KNO_3, 40 wt.% $NaNO_2$, 7 wt.% $NaNO_3$), and HITEC XL (48 wt.% $Ca(NO_3)_2$, 45 wt.% KNO_3, 7 wt.% $NaNO_3$). However, these eutectic mixtures all exhibit melting points above ambient; varying from 120 °C to 220 °C [8]. Salt-based systems must therefore include methods of freeze prevention and recovery in order to maintain the HTF at acceptable temperatures and to minimize component damage in the event of solidification. Various metals also exhibit excellent high temperatures in the liquid region, but may not be practical options at present due to material cost and chemical reactivity.

Increasing the capacity factor of a CSP plant requires the addition of either fossil-fuel backup generation or thermal energy storage capability. Backup generation is undesirable as it diminishes the renewable nature of the plant and heightens the environment impact, undermining the original motivations for operating a CSP plant. A more attractive solution is to upgrade the power plant with thermal energy storage capabilities. In practice, the power plant captures excess solar energy during periods of peak irradiance, stores the excess as heat, and later dispatches the heat to the power block during periods of low sunlight. Realization of this concept requires an overdesign of the solar collection system to facilitate excess energy capture as well as an on-site storage volume to contain the corresponding heat. While this adds to the already high capital and

maintenance costs, storage capability is essential for CSP plants to replicate the output performance of conventional fossil-fuel plants. A variety of design concepts exist for thermal energy storage in CSP plants and are summarized in Chapter 2. Of these concepts, a dual-media molten-salt thermocline tank offers the potential for storage at the lowest cost [8]. Despite this economic advantage, the thermal and structural stability of the thermocline concept are not well-understood and require detailed investigation.

1.1   Objectives

The objective of this work is to advance understanding of molten-salt thermocline tank design and operation necessary for commercial applications. A multiscale numerical approach is applied to investigate thermocline performance at both a device level for comprehensive short-term (daily) analysis and at a system level for reduced-order long-term (annual) analysis. Initial investigation of the storage concept is performed at a device level with a multidimensional two-temperature computational fluid dynamics (CFD) model; formulated to study the daily thermal and structural behavior of the tank in response to various boundary conditions. In previous work, application of this modeling approach was subject to impractical tank geometries and over-conservative storage performance metrics. The present work rectifies these deficiencies with an investigation of first and second law based metrics for cyclic tank operation and a parameter study of granulated filler sizes and external heat loss conditions.

In addition to thermal performance, the structural stability of the thermocline concept remains a design concern due to a potential failure mode known as thermal ratcheting. Thermal ratcheting is a progressive outward expansion of the tank wall initiated by repeated thermal cycling and consequent reorientation of the internal filler material. The expansions or ratchets accumulate over time until an eventual tank rupture. The established CFD model for thermocline tanks is extended to predict hoop stress along the tank wall and assess the likelihood for ratcheting phenomena. A thermal and mechanical simulation of an experimental thermocline tank operated at the historic Solar One power tower plant is conducted to validate the modeling approach.

While CFD simulations provide detailed and multidimensional thermal solutions for thermocline tanks, the associated computing time and resources prohibit integration of the storage model into a complete system model of a CSP plant. As a result, the model tank geometry remains subject to arbitrary boundary conditions that may not reflect realistic tank response to daily solar collection and steam generation procedures. A new reduced-order model of a thermocline tank is therefore developed to provide thermal solutions at much lower computational cost. The new model is then combined with separate solar collection and power block models to form a system-level model of a molten-salt power tower plant. Recorded measurements of direct normal irradiance serve as input to the plant model, enabling simulation of realistic and long-term operation. The behavior of the thermocline tank within this power plant is then monitored to confirm its viability as a practical storage concept.

The influence of a thermocline energy storage system on the surrounding CSP plant is proportional to its volume. For a fixed turbine size, larger tanks offer increased energy capacity and can boost net electricity production but also incur greater capital costs for construction. This tradeoff between plant output and plant expenditure is characterized by the levelized cost of electricity. Applying the previously developed system model, a parametric study of solar multiple and thermocline tank energy capacity is conducted to map the attainable LCOE values with thermocline energy storage and to identify economic optima. The modeling campaign is then repeated with conventional two-tank storage to quantify the economic difference between storage methods at a system level.

Despite the financial benefits of a thermocline tank relative to other storage methods, the concept remains a sensible heat device and thus exhibits low energy density. Commercial tanks require large diameters to store sufficient quantities of high-temperature heat, increasing the potential for both maldistribution of flow inside the tank and thermal ratcheting phenomena. A possible design modification to reduce tank size is the substitution of internal rock with a phase-change material or PCM, which provides a high-density latent-heat storage mechanism. The previous reduced-order thermocline model is updated to replace the conventional rock filler with a bed of encapsulated PCM.

This model is then reintegrated into the power tower plant model to continue the system-level perspective. A parametric study of the PCM heat of fusion and melting temperature is conducted to identify potential optima. Plant performance with a conventional rock-filled thermocline tank provides a baseline for design comparison.

1.2   Organization of Thesis

Chapter 2 provides an overview of literature relevant to thermal energy storage for concentrating solar power applications. Chapter 3 presents a thermal simulation of molten-salt thermocline tanks under daily cyclic operation, with a specific focus on the influence of internal filler size and external heat losses. Chapter 4 extends this thermal model with a mechanical simulation of the thermocline tank wall to investigate thermal ratcheting potential. Chapter 5 discusses a new reduced-order model of energy transport in a thermocline tank that is experimentally validated and computationally inexpensive. The model is then integrated into a new system-level model of a molten-salt power tower plant to investigate storage behavior under long-term and realistic operation. In Chapter 6, a parametric study of solar multiple and thermocline tank size is performed with the system model to identify minimum levelized cost obtainable with thermocline energy storage. Chapter 7 updates the storage and system models to investigate the viability of a latent-heat-augmented thermocline tank. Chapter 8 summarizes the contributions of the thesis and outlines areas for future research.
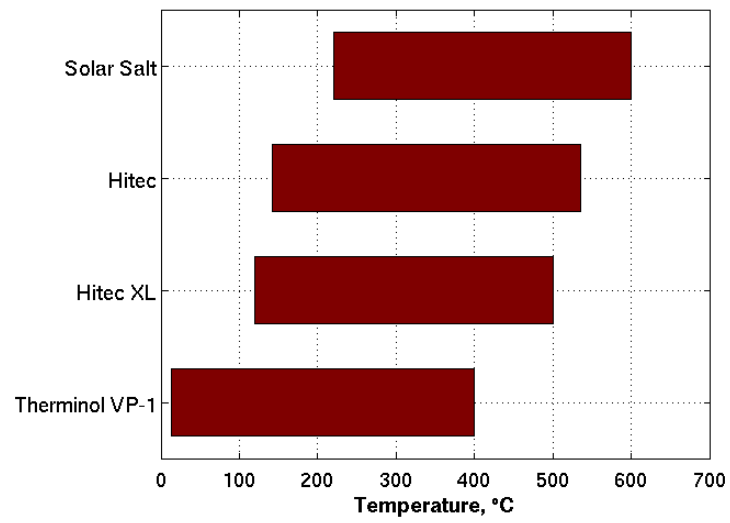
Figure 1.1. Liquid operating temperature spans of commercial heat transfer fluids applied in CSP applications [8].

CHAPTER 2. LITERATURE REVIEW

2.1   Thermal Energy Storage for Concentrating Solar Power

Energy storage is essential for concentrating solar power plants to decouple daily power production from intermittent solar collection. The conversion of sunlight to high-temperature heat in CSP systems provides an inherent compatibility with thermal energy storage devices. Such thermal energy storage technologies exploit one or more of three distinct mechanisms: sensible heat, latent heat, and thermochemical reactions. In thermochemical storage, the heat generated from solar concentration is used to promote a reversible endothermic reaction. The absorbed heat is stored in the chemical bonds of the reaction products at high energy density. To recover this heat, the reverse exothermic reaction is induced through catalysis. Kreetz and Lovegrove [9,10] investigated the dissociation of ammonia as a storage reaction for CSP systems, affirming the concept with a 15 kW_t experimental reactor in conjunction with a dish collector. Outside of this work, thermochemical storage has experienced limited development due to the due to the design complexities and high costs involved at the scale of a commercial CSP system [11].

2.1.1   Latent Heat Storage

CSP systems with latent heat storage use the collected thermal energy to induce a solid-liquid transition in a phase change material (PCM). Storage at this transition temperature also exhibits high energy density, proportional to the enthalpy or heat of fusion of the PCM. When the stored heat is recovered, the PCM reverts to its solid phase. As with thermochemical storage, the transition process must occur within the operational temperature span of the CSP system. While no existing CSP plant applies latent heat

storage, nitrate salts are often proposed for the PCM for their suitable melting temperatures and low material cost. However, these salts also exhibit low thermal conductivities which impede the rate of heat exchange and reduce storage capability. Recent studies have investigated several methods to improve the thermal performance of PCM storage systems.

Steinmann *et al*. [12] examined multiple heat exchanger designs to enhance heat transfer between sodium nitrate ($NaNO_3$) PCM and steam working fluid. A sandwich structure composed of PCM with imbedded graphite fins was reported to be the most feasible and reliable design among the options considered. Laing *et al*. [13,14] later demonstrated this sandwich structure at a laboratory scale with an 8.51 kWh_t test module and again with a larger prototype as part of a 1 MWh_t combined latent and sensible heat storage system for parabolic trough plants. Shabgard *et al*. [15] investigated the inclusion of embedded heat pipes to enhance heat transfer between PCM storage and CSP heat transfer fluid. The authors developed a thermal network model to simulate multiple flow configurations and heat pipe orientations. Simulations with potassium nitrate (KNO_3) as PCM validated the inclusion of heat pipes to improve thermal performance. Robak *et al*. [16,17] modified this network model to investigate the impact of simpler gravity-driven thermosyphons embedded within the PCM. An economic study by the authors indicated the storage concept to be cost competitive with traditional sensible heat storage systems used in current CSP plants.

While use of latent heat storage can be enhanced through optimized storage designs, it should be noted that heat exchange with both the CSP heat transfer fluid and the steam working fluid still occur at the fixed melting temperature of the PCM. Given that both the HTF and steam exhibit a sensible temperature change, interaction with the PCM induces pinch points which may result in excessive exergy destruction. A potential remedy to this second law penalty is to layer multiple PCMs of different melting temperature in order to approximate a sensible storage response and mitigate the influence of pinch points, known as cascaded latent heat storage. Aceves [18] developed a simple analytic model of a latent heat storage system to simulate the use of cascaded PCMs. Michels and Pitz-Paal [19] constructed an experimental heat exchanger filled

with oil HTF on the tube side and three different PCMs on the shell side and reported greater utilization of latent heat over a uniform PCM structure in the heat exchanger.

2.1.2 Sensible Heat Storage

The most established method of thermal energy storage for CSP plants is via sensible heat as it carries less cost and complexity than the thermochemical or latent heat methods previously described. In practice, thermal energy in the HTF is used to induce either a temperature increase in a separate material or is retained in an excess volume of the HTF itself. The amount of energy stored is proportional to the heat capacity of the selected storage material and the temperature difference between hot and cold HTF. As sensible systems do not exhibit a phase change, studies have investigated both solid and liquid materials for CSP applications.

In solid sensible storage, hot HTF convects heat to a bulk material of large thermal mass. The hot solid mass contains this thermal energy until it is later recovered by cold HTF. Concrete is an attractive material selection due to its low material cost, but its low thermal conductivity is detrimental to heat exchange with the HTF [11]. Laing *et al*. [20,21] examined concrete with a combination of numerical simulation and scaled experiments and reported it to be a suitable storage option. As an alternative to concrete, Py *et al*. [22] proposed the implementation of recycled asbestos containing waste for solid storage. A material comparison with concrete revealed similar heat capacity but an order-of-magnitude reduction in cost.

At present, sensible heat in liquid media is the only thermal energy storage method applied in commercial CSP plants. However, this application varies with respect to liquid selection, system integration method, and storage design. As was discussed in Chapter 1, CSP heat transfer fluids are currently limited to synthetic oils and molten salts. Commercial salt mixtures provide engineering benefits such as increased liquid temperature and low material cost, but also exhibit freeze points far above ambient ($\geq$ 120 °C). Solidification and melting of the salt is destructive to the piping network and necessitate freeze prevention systems in the CSP infrastructure. This danger may also be

alleviated with the implementation of novel salt mixtures that exhibit lower melting temperatures. Wang *et al*. [23] reported a melting point of 99 °C for a eutectic salt mixture of Li, Na, K nitrates and Na nitrite. Raade and Padowitz [24] reported a melting point of 65 °C with a eutectic salt mixture of Li, N, Na, Cs, and Ca nitrates.

System integration of the liquid storage system refers to its operation relative to the solar collection system, and employs either a direct or an indirect scheme. Indirect integration isolates the collector flow loop from the energy storage system and requires energy transfer across a heat exchanger. The collector HTF and storage do not have physical contact and thus need not be the same. In contrast, direct integration eliminates this heat exchanger with collection and storage exposed to the same liquid volume. Thermal losses associated with the heat exchange are also removed and permit higher plant thermal efficiencies. For both integration methods, liquid storage is operated either with a two-tank system or a single-tank thermocline system.

A two-tank storage system maintains extra volumes of hot and cold liquid in separate tanks. Under indirect integration, these tanks are connected through one side of a heat exchanger installed in the collection loop. The system is energized or charged by transferring liquid from the cold tank to the hot tank, absorbing heat from the hotter HTF inside the intermediate heat exchanger. To deplete or discharge the storage system, the flow path is reversed and the stored heat is transferred back from the hot liquid to colder HTF inside the heat exchanger. For direct integration, the hot and cold tanks are not connected but are installed separately in the collection loop, illustrated in Figure 2.1a [25]. As seen, the hot tank is installed between the outlet of the collector field and the inlet to the power block. The corresponding cold tank is installed between the outlet of the power block and the inlet to the collection field. To charge the storage system, HTF from the collector field enters the hot tank at a higher flow rate than that at which HTF is dispatched from the tank to the power block, increasing the internal fluid volume. The volume of HTF located in the cold tank is simultaneously depleted (sent to the solar receiver) in order to sustain the flow rate difference. To discharge the system, the system flow rates are adjusted such that the hot tank is emptied and the cold tank is filled with salt exiting the power block.

The two-tank storage concept was first demonstrated at the Solar Two molten-salt power tower plant near Barstow, CA [26]. For parabolic trough plants, Kearney *et al*. [8] evaluated the economic impact of two-tank storage with molten salt and reported a maximum 18.5% reduction in LCOE over a baseline plant with synthetic oil HTF and no storage. Given this technical and economic validation, the two-tank storage concept has since been implemented in several commercial CSP plants worldwide. Recent tank studies include a combined thermal, structural, and economic design tool developed by Gabbrielli and Zamparelli [27]. Zaversky *et al*. [28] developed a transient thermal model of molten-salt tanks to predict external heat losses.

2.2   Single-tank Thermocline Energy Storage

Despite the current prevalence of two-tank storage, it should be noted that the installed cold tank provides no energy benefits to the CSP plant (necessary only for mass balance of the molten salt HTF) and thus adds a substantial physical and cost redundancy to the plant infrastructure. Significant capital cost savings may be realized by instead storing the excess hot and cold molten salt together inside one volume, as is done in a single-tank or thermocline energy storage system. Stable thermal stratification of the two fluid regions is maintained by buoyancy forces corresponding to density differences between hot and cold salt. As a result, cold molten salt remains in the lower portion of the tank while hot salt remains in the upper portion. An intermediate and narrow layer of large temperature gradient develops at the interface of the hot and cold volumes, known as the thermocline or heat-exchange region. The vertical position of this sigmoid-shaped profile varies in time as the thermocline tank is repeatedly filled with either hot or cold salt. An inexpensive granulated material (*e.g.*, rock) fills a majority of the tank to minimize the required salt volume and to mitigate mixing forces detrimental to the thermal stratification. Heat exchange to this solid occurs through forced convection with the surrounding salt. As an unconsolidated porous medium, conduction pathways in the solid are highly constricted and do not disrupt thermal stratification inside the tank. With sensible storage in both the molten-salt HTF and the solid filler, the thermocline tank is termed a dual-media storage system.

Selection of the rock filler is not trivial as the porous bed must exhibit long-term compatibility with both molten salt and cyclic temperature fluctuations. Pacheco *et al.* [29] immersed multiple rock candidates in HITEC XL molten salt for several hundred thermal cycles between 290 °C and 400 °C. Of the tested materials, quartzite, taconite, and silica sand were observed to be the most wear-resistant, with quartzite rock and silica sand being preferable due to low material costs. Brosseau *et al.* [30] extended this work with 10,000 thermal cycles over a wider temperature span of 285 °C and 450 °C. Quartzite rock and silica sand were again observed to tolerate the immersion process with minimal deterioration. Calvet *et al.* [31] recently proposed a post-industrial ceramic waste known as Cofalit as an alternative filler, citing low material cost, increased morphology control, and long-term compatibility with Solar Salt.

As with the two-tank design, a thermocline tank is either installed within the collection loop (direct integration) or isolated with an additional heat exchanger (indirect integration). A schematic diagram of a power-tower plant with a direct-integrated thermocline system is illustrated in Figure 2.1b [25]. To charge the tank, hot salt is supplied at the top while cold salt is pumped out from the bottom. The heat-exchange region then travels downward until it reaches the tank floor, indicating the thermocline tank is at its energy capacity. To discharge the tank, the flow direction is reversed such that cold salt enters at the bottom while hot salt is pumped out from the top. The discharge continues until the heat-exchange region travels back to the top and the volume of hot salt is exhausted. Implementation of a thermocline tank has been estimated to carry a 15 − 33% reduction in storage costs over the prevailing two-tank option [6,29] , sparking extensive interest in tank design and performance.

The earliest demonstration of thermocline storage was with a 182 MWh$_t$ tank installed at the historic Solar One 10 MW$_e$ power tower plant near Barstow, CA [4,32–34]. The tank measured 18.2 m in diameter and was filled with Caloria HT-43 mineral oil and granite rock to a height of 12.4 m. High vapor pressure constrained the maximum oil temperature to 304 °C and limited storage operations to auxiliary steam generation. The thermocline tank satisfied its design specifications but was retired after rupture and fire damage initiated by an accidental ignition of the internal oil. Pacheco *et al.* [29] later

constructed an experimental 2.3 MWh$_t$ thermocline tank to demonstrate storage with molten salt HTF and quartzite rock/silica sand filler. Thermal stratification inside the tank was observed to withstand both cyclic flow conditions and stagnant standby periods.

The elevated temperature and large scale of CSP systems has limited a majority of thermocline tank studies to analytic and computational models. Pomeroy [35] proposed a design procedure to mitigate destratification in a porous bed of liquid sodium HTF and iron spheres. Bharathan and Glatzmaier [36] conducted a multidimensional computational fluid dynamics (CFD) simulation of forced convection between molten salt and a solid quartzite sphere. Afrin *et al*. [37] performed a parametric study of distribution manifold designs with CFD simulation to investigate flow maldistribution inside the porous bed. Qin *et al*. [38] developed analytic stability criterions to prevent viscous channeling between hot and cold molten salt. Bayon and Rojas [39] recently developed a simple one-dimensional single-phase model, assuming thermal equilibrium between the liquid and solid filler, and proposed a design equation to optimize thermocline tank height.

A majority of thermocline tank simulations have applied two-temperature models, where separate energy transport equations are formulated for the liquid and solid phases. Van Lew *et al*. [40] developed such a thermocline tank model from the one-dimensional Schumann equations [41]. Numerical solutions were obtained via the method of characteristics and required minimal computational times. The storage efficiency of cyclic charge and discharge processes was reported to increase with tank height and reduced filler size. The authors then built a laboratory-scale tank to verify the model accuracy, composed of synthetic oil and river pebbles [42,43]. Experimental charge and discharge data were observed to exhibit acceptable agreement with simulations. Li *et al*. [44] extended the computational analysis to construct generalized performance charts as well as a thermocline tank design algorithm to optimize storage effectiveness. Valmiki *et al*. [45] later updated the model to study tank performance in conjunction with a parabolic trough solar collector. Xu *et al*. [46] studied the validity of a lumped capacitance assumption for the solid filler and developed effective convection coefficients to correct for large Biot numbers.

Yang and Garimella [47–49] developed a more comprehensive model of mass, momentum, and two-temperature energy transport inside the thermocline porous bed. Thermal diffusion inside the bed was characterized with an effective thermal conductivity in the liquid-phase energy equation; diffusion in the solid phase was neglected due to particle contact resistance. Solutions were obtained with commercial CFD software, enabling investigation of multidimensional tank geometries and nonadiabatic tank wall boundary conditions. The authors conducted a parametric study of thermocline tank height, filler diameter, and molten-salt discharge power to optimize tank discharge efficiency for both adiabatic and nonadiabatic tank walls. The authors later extended the adiabatic wall analysis to simulate a complete charge-discharge cycle and developed a general correlation of storage efficiency for varying Reynolds number and cycle duration.

Xu *et al*. [50,51] applied a similar multidimensional tank geometry and CFD analysis to perform a sensitivity study of forced convection and thermal diffusion inside the thermocline porous bed. Application of multiple correlations for convection and effective thermal conductivity did not significantly influence tank discharge behavior. The authors later updated the energy transport equations with a more detailed dispersion-concentric model, eliminating the assumption of lumped capacitance in the solid filler particles. The resultant temperature distributions inside the solid were reported to be negligible for small particle sizes.

Kolb and Hassani [52] investigated thermocline tank performance at a system-level with a TRNSYS model of 1 MW_e Saguaro parabolic trough plant in Red Rock, AZ. The authors simulated annual plant performance without storage and again with the addition of a 30 MWh_t synthetic oil-filled thermocline tank. Inclusion of thermocline storage was reported to almost double annual plant capacity factor from 23% to 42%. Kolb [53] later repeated this system-level analysis with a comparison of molten-salt two-tank and thermocline tank energy storage for the 50 MW_e Andasol parabolic trough plant in Spain. The two storage systems exhibited almost identical annual plant output, attributed to viability of transitional temperatures inside the thermocline for sliding-pressure operation of the turbine.

As a sensible-heat concept, thermocline tanks exhibit low energy densities and thus require large tank diameters. A proposed design modification to reduce tank size is the substitution of the internal rock with encapsulated pellets of phase change material (PCM), adding a high-density latent-heat mechanism to the tank assembly. Pendyala *et al*. [54] investigated the encapsulation process and presented a fabrication technique for self-assembly of liner coating around the PCM. Archibold *et al*. [55] developed a two-dimensional finite-volume model of a spherical capsule to study the internal phase change with sodium nitrate PCM. At a device level, Felix Regin *et al*. [56] developed a finite-difference model of an encapsulated PCM storage tank for solar water-heating applications. Nithyanandam *et al*. [57] later developed a finite-volume model of a latent-heat thermocline tank with capsulated PCM filler for molten-salt CSP plants.
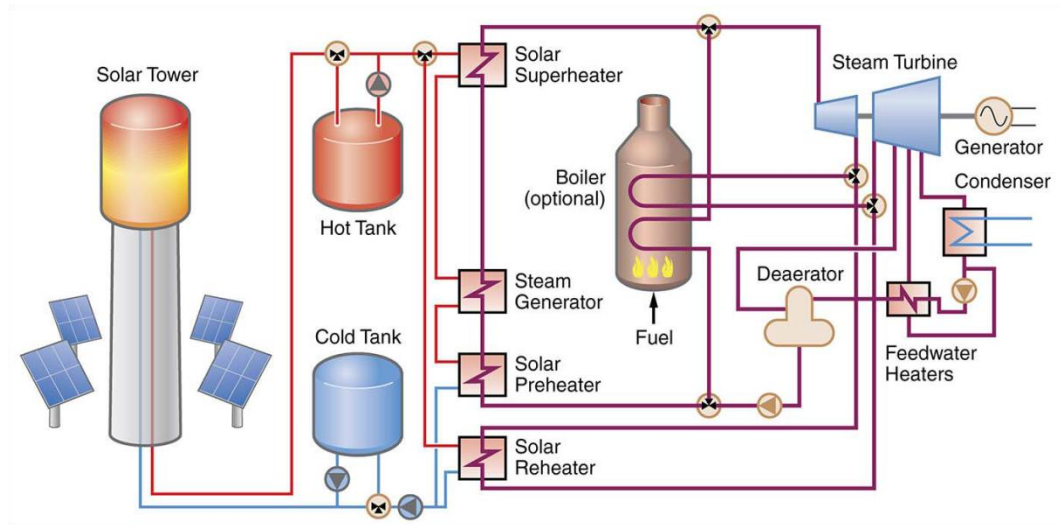
(a)
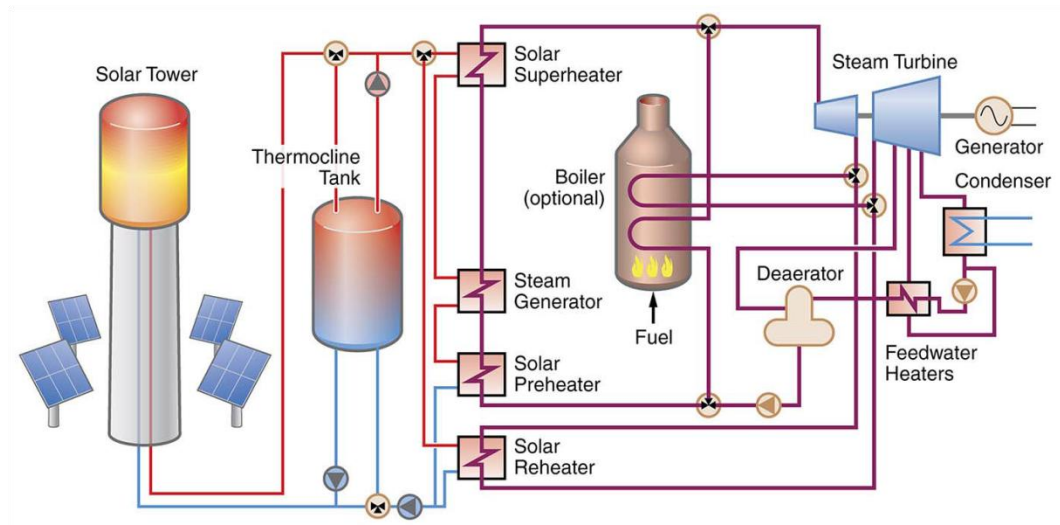
(b)

Figure 2.1. Diagram of a concentrating solar power plant with (a) direct two-tank storage and (b) direct thermocline storage (reproduced from [25]).

CHAPTER 3. SECOND LAW ANALYSIS OF MOLTEN-SALT THERMOCLINE
ENERGY STORAGE

Material in this chapter was published in *Solar Energy* [58].

3.1   Introduction

Dual-media molten-salt thermocline tanks have been the subject of extensive simulation in recent years due to their potential as a low-cost storage option for concentrating solar power. However, many of these previous simulations enforced an ad hoc temperature cut-off criterion on the tank outflow to mitigate the discharge of nonideal salt temperatures below the hot operating limit [47–49]. In these studies, only salt at temperatures above 95% of the total operating span was designated as useful for power production. For example, if the temperature span between the hot and cold limits is 100 K, only molten salt within 5 K of the hot limit is considered viable for steam generation in the CSP plant Rankine cycle. An alternative approach to this ad hoc criterion is to monitor the quality of the outflow using the thermodynamic definition of exergy. Unlike energy, exergy is not subject to a conservation law and can be destroyed. This destruction is proportional to the generation of entropy inside the tank as defined by the second law of thermodynamics.

In this chapter, a numerical simulation of a dual-media thermocline tank is conducted to investigate the recovery of energy and exergy during cyclic storage operations.   A parametric study of the porous bed granule diameter and external convection losses quantifies the respective influence on both the first and second law efficiencies of the thermocline storage cycle. These results are then compared to the previous 95% outflow temperature criterion applied in the literature.

3.2   Numerical Model

3.2.1   Problem Description

A diagram of the thermocline tank geometry is illustrated in Figure 3.1. The tank of diameter d is filled with a porous bed of granulated filler to a height h. Adjacent to the top and bottom of the porous fillerbed are two distributors of height $h' = 0.05h$, free of any filler. Hot and cold fluid enters and exits the tank through two tubular ports of diameter $d' = 0.1d$ extending from the distributors. The open distributor regions serve to diffuse the turbulent tube flow at the port inlet evenly into the tank fillerbed, preventing the formation of radial temperature gradients in the stratified fluid. In reality, this distribution is achieved through the use of pipe manifolds imbedded within the porous region. Such manifolds are not axisymmetric and drastically increase the computational resources necessary to model the thermocline tank. The open distributor regions considered here simplify the numerical approach and maintain axisymmetric flow conditions.

The molten-salt heat transfer fluid inside the thermocline tank is HITEC (53 wt.% KNO_3, 40 wt.% $NaNO_2$, 7 wt.% $NaNO_3$), in operation between 250 °C and 450 °C. For thermal transport analysis, the specific heat is approximated as constant at 1561.7 J/kg-K. Density, viscosity, and thermal conductivity are characterized with temperature-dependent functions (degrees Celsius) derived from experimental data [47,59]:

$$\rho_l = 1938 - 0.732(T_l - 200) \tag{3.1}$$

$$k_l = -6.53 \times 10^{-4}(T_l - 260) + 0.421 \tag{3.2}$$

$$\mu = \exp\left[-4.343 - 2.0143(\ln(T_l) - 5.011)\right]. \tag{3.3}$$

The porosity of the solid filler is fixed at 0.22 in accordance with experimental observation for quartzite rock and silica sand mixture [29]. To simplify analysis, the filler is represented as a quartzite bed with a single effective diameter. The solid density and specific heat are fixed to 830 kg/m^3 and 2500 J/kg-K [47], while thermal conductivity is derived from quartz materials. Thermal diffusion between the solid granules is neglected in the model due to the small contact area and high contact

resistance between particles. However, the solid granules still influence diffusion in the surrounding molten salt, characterized by the following correlation for effective thermal conductivity [60]:

$$k_{eff} = k_l \frac{1 + 2\beta\phi + \left(2\beta^3 - 0.1\beta\right)\phi^2 + \phi^3 0.05 e^{4.5\beta}}{1 - \beta\phi} \tag{3.4}$$

where $\phi = 1 - \varepsilon$ and $\beta = \left(k_s - k_l\right)/\left(k_s + 2k_l\right)$.

During storage operations, the heat-exchange region travels up and down the height of the tank in response to charge and discharge operations. However, the velocity of this region is not equal to the velocity of the internal molten-salt fluid flow but a function of the bed porosity and volumetric heat capacities of the two storage mediums. Yang and Garimella [49] reported this function as a ratio of the heat-exchange and fluid velocities:

$$C_0 = \frac{v}{u_{l,h}} = \frac{\rho_{l,h} C_{P,l}}{\varepsilon \rho_{l,h} C_{P,l} + \left(1 - \varepsilon\right)\rho_s C_{P,s}}. \tag{3.5}$$

For the present mixture of HITEC molten salt and quartzite rock, this velocity ratio is 1.23.

3.2.2   Governing Equations

Mass and momentum transport of molten salt inside the thermocline tank are governed as follows, with momentum flux in the porous bed governed by Darcy's Law with the Brinkman-Forchheimer extension:

$$\frac{\partial\left(\varepsilon\rho_l\right)}{\partial t} + \nabla \cdot \left(\rho_l \mathbf{u}\right) = 0 \tag{3.6}$$

$$\frac{\partial\left(\rho_l \mathbf{u}\right)}{\partial t} + \nabla \cdot \left(\rho_l \frac{\mathbf{u}\mathbf{u}}{\varepsilon}\right) = -\varepsilon\nabla p + \nabla \cdot \tilde{\boldsymbol{\tau}} + \varepsilon\rho_l \mathbf{g} - \varepsilon\left(\frac{\mu}{K}\mathbf{u} + \frac{F}{\sqrt{K}}\rho_l |\mathbf{u}|\mathbf{u}\right). \tag{3.7}$$

In the momentum transport equation, the stress deviator tensor is defined as $\tilde{\boldsymbol{\tau}} = 2\mu\tilde{\mathbf{S}} - \frac{2}{3}\mu\,\mathrm{tr}\left(\tilde{\mathbf{S}}\right)$, where $\tilde{\mathbf{S}} = \frac{1}{2}\left(\nabla\mathbf{u} + \left(\nabla\mathbf{u}\right)^T\right)$ is the rate of strain tensor. The spatial

gradient of the thermocline tank in polar coordinates is $\nabla = \mathbf{e_r}\frac{\partial}{\partial r} + \mathbf{e_\theta}\frac{1}{r}\frac{\partial}{\partial\theta} + \mathbf{e}_x\frac{\partial}{\partial x}$. However, the axisymmetric nature of the thermocline tank geometry eliminates all velocities and functional dependencies in the circumferential direction. The porous bed permeability and inertial coefficient are defined as follows [61,62]:

$$K = \frac{d_s{}^2\varepsilon^3}{175(1-\varepsilon)^2} \tag{3.8}$$

$$F = \frac{1.75}{\sqrt{150\varepsilon^3}}. \tag{3.9}$$

For energy transport inside the porous bed, separate equations are formulated for the molten salt (subscripted l) and quartzite filler (subscripted s) to model thermal non-equilibrium between the two fluid and solid:

$$\frac{\partial\left[\varepsilon\rho_l C_{P,l}(T_l - T_c)\right]}{\partial t} + \nabla\cdot\left[\rho_l\mathbf{u}C_{P,l}(T_l - T_c)\right] = \nabla\cdot\left(k_{eff}\nabla T_l\right) + \mu\Phi + h_i(T_s - T_l) \tag{3.10}$$

$$\frac{\partial\left[(1-\varepsilon)\rho_s C_{P,s}(T_s - T_c)\right]}{\partial t} = -h_i(T_s - T_l). \tag{3.11}$$

Eq. (3.10) and Eq. (3.11) remain coupled by source term associated with the convective heat exchange between the molten salt and solid filler. This interstitial forced convection is modeled with the Wakao and Kaguei correlation for porous media [63]:

$$\mathrm{Nu}_i = 6(1-\varepsilon)\left(2 + 1.1\mathrm{Re}^{0.6}\mathrm{Pr}^{1/3}\right). \tag{3.12}$$

As previously stated, thermal diffusion is limited to the fluid energy equation via the effective thermal conductivity of the dual-media mixture. Nondimensional terms associated with the tank geometry and internal molten-salt flow are defined as: $X = \dfrac{x}{h}$,

$$R = \frac{r}{h}, \quad \Psi = \frac{u_0 t_0}{d_s}, \quad \tau = \frac{t}{t_0}, \quad \Theta = \frac{T - T_c}{T_h - T_c}, \quad \mathrm{Re} = \frac{\rho_l u d_s}{\mu}, \quad \mathrm{Pr} = \frac{\mu C_{P,l}}{k_l}, \quad \mathrm{Nu}_i = \frac{h_i d_s{}^2}{k_l},$$

$$\mathrm{Ec} = \frac{u^2}{C_{P,l}(T_h - T_c)}, \quad \mathrm{Da} = \frac{h^2}{K}.$$

Also of interest is the entropy generation inside the thermocline tank. Unlike the transport variables considered hitherto, entropy is not a conserved property and exhibits generation in response to irreversible processes inside the porous medium, *i.e.*, heat transfer between phases, thermal diffusion, and viscous dissipation:

$$\dot{S}_{gen}''' = \frac{h_i(T_s - T_l)^2}{T_s T_l} + \frac{k_{eff}(\nabla T_l)^2}{T_l^2} + \frac{\mu \Phi}{T_l} \geq 0. \tag{3.13}$$

In accordance with the second law of thermodynamics, entropy generation is always nonnegative. A derivation of Eq. (3.13) is provided in Appendix C, updated from a previous derivation in [58]. The corresponding destruction of exergy inside the porous medium is proportional to this generation:

$$\dot{X}_{des}''' = T_0 \cdot \dot{S}_{gen}'''. \tag{3.14}$$

3.2.3 Boundary Conditions

To charge the thermocline tank, hot molten salt enters the top distributor port at a fixed velocity and temperature:

$$U_{top}' = \left(\frac{d}{d'}\right)^2 (\mathbf{u}_h \cdot \mathbf{e}_z) \qquad T_{top} = T_h.$$

Simultaneous to the hot inflow, cold molten salt exits the tank via the bottom distributor. To discharge the tank, flow is reversed such that cold molten salt enters the tank at the bottom distributor port at a fixed velocity and temperature:

$$U_{bot}' = \left(\frac{d}{d'}\right)^2 (\mathbf{u}_c \cdot \mathbf{e}_z) \qquad T_{bot} = T_c.$$

The entering velocity of the cold molten salt is proportionally less than the prior hot inflow due to the increased density of the cold salt.

A no-slip condition is enforced at the internal wall of the tank (see Appendix D for additional discussion of flow behavior in a porous bed). External heat losses along the external wall surface are governed by forced convection with the ambient air:

$$k_l \frac{\partial T_l}{\partial r}\bigg|_w = -h_w \left(T_l - T_\infty\right). \tag{3.15}$$

The convection coefficient along the tank wall, determined using the Churchill and Bernstein correlation [64], is a function of wind velocity and air properties at film temperature. The influence of the steel tank wall is accounted for as a thermal resistance. Radiation to the environment is neglected as the external tank surface is assumed to be reradiating.

3.2.4   Solution Procedure

The model fillerbed and distributor geometries are discretized into a structured nonuniform mesh, with a maximum nondimensional cell size of $\Delta X = \Delta R = 0.1$. The governing mass, momentum, and energy equations of the molten salt are discretized with the finite-volume method and solved with the CFD software, FLUENT [65]. Spatial discretization of the internal convective fluxes is performed with a second-order upwind scheme. Transient discretization is performed with a first-order implicit method and a nondimensional time step of $\Delta \tau = 1.2 \times 10^{-4}$. Grid and time-step independence were previously verified by Yang and Garimella [49]. Pressure-velocity coupling is achieved with the PISO algorithm [66]. User-defined functions (UDFs) are implemented to solve the co-located solid rock temperature Eq. (3.11) at each cell. The solution at each time step is considered converged when all dimensionless residuals reduce to less than 10^{-4}.

Prior to computation, the entire thermocline tank geometry is initialized to the cold molten-salt temperature. The tank is then subjected to an average day of operation with half cycle durations (t_0) of 12 hours; hot salt is supplied at the top for 12 hours and then discharged for another 12 hours. It should be noted that the initial isothermal condition is not representative of a physical thermocline tank. Successive cycling of the tank model is therefore necessary to generate a more realistic initial condition. After a

sufficient number of storage cycles, the tank converges to a periodic temperature response with each charge and discharge process.

After convergence to periodicity, the storage performance of the simulated thermocline tank is quantified with three separate cyclic efficiencies: first law, second law, and the *ad hoc* 95% outflow temperature criterion applied by Yang and Garimella [47]. The first and second law efficiencies relate the outflow of energy and exergy during discharge to the preceding inflow of energy and exergy during charge:

$$\eta_I = \frac{E_{out,\,dis}}{E_{in,\,chg}} \tag{3.16}$$

$$\eta_{II} = \frac{X_{out,\,dis}}{X_{in,\,chg}}. \tag{3.17}$$

In contrast, the outflow temperature criterion efficiency is defined by omitting all molten-salt energy with a nondimensional temperature below 0.95:

$$\eta_{I,95} = \frac{E(\Theta_l > 0.95)_{out,dis}}{E_{in,chg}}. \tag{3.18}$$

By definition, the outflow temperature cutoff-based efficiency in Eq. (3.18) is always less than the first law efficiency in Eq. (3.16).

The energy and exergy entering the thermocline during charge are both fixed according to the known velocity boundary conditions. To assess the thermal usefulness of the molten salt leaving the tank, additional UDFs in the CFD model record the energy and exergy discharged from the tank distributor ports after every time step. The sums of the values determine the net energy and exergy delivered from the tank outflow. The complete UDF code for the thermocline tank model is located in Appendix E.

3.3   Numerical Results

Computational models similar to the last section are present in the literature [47,49], but these previous thermocline studies did not enforce any practical constraints

on tank height. In reality, the maximum liquid level inside a thermocline tank is limited by the underlying tank foundation and soil bearing capacity. The current study constrains the height of the porous bed to 12 m to satisfy this constraint, feasible with a sufficient tank foundation [25]. The model tank diameter is also fixed to 12 m. The velocity of molten salt entering the tank is determined from a design algorithm and efficiency model developed by Yang and Garimella [49]. For an effective granule diameter of 5 cm and a nondimensional bed height $H = h/(u_0 t_0)$ equal to the normalized heat-exchange velocity (C_0), the inlet Reynolds number and length ratio (Ψ) of the porous bed are 13.9 and 194, respectively. For this scenario, the applied design algorithm predicts a storage efficiency of 0.790 for the 95% outflow temperature criterion.

Under the fixed thermocline tank dimensions, a parametric study of the internal granule diameter and external convection losses is conducted. Yang and Garimella [47] reported that reducing the granule diameter improves the storage performance as it shortens the axial span of the heat-exchange region, but limited their analysis to a minimum diameter of 5 cm. Smaller diameters may provide additional improvement albeit with an increased pressure drop across the porous bed. The current study investigates three effective granule diameters (5 cm, 1 cm, and 2 mm) to map this potential tradeoff between interstitial heat transfer and pressure drop. It should be noted that the Reynolds numbers and tank length ratios corresponding to the smaller diameters are outside the limits of the cyclic performance model presented in [49], precluding *a priori* calculation of the storage efficiency.

External convection losses enforced along the thermocline tank wall are informed by wind speeds representative of locations associated with CSP facilities, *i.e.*, Barstow, CA [67]. The tank geometry is subject to two wall conditions (a) an adiabatic boundary condition corresponding to no losses and (b) a nonadiabatic boundary condition equivalent to an external wind speed of 11.2 m/s at an ambient temperature of 25 °C. For the loss condition, an effective Nusselt number of 4260 is applied to include the thermal resistance posed by the steel tank wall, composed of stainless steel 347 [25] at a thickness of 2 cm. The addition of a thermal insulation layer to mitigate loss effects is omitted to

represent a worst case scenario for storage performance. In conjunction with the three granule diameters of interest, a total of six thermocline cases are simulated and summarized in Table 3.1.

It should be noted that the relative importance of viscous dissipation with respect to fluid energy transport, Eq. (3.10), and entropy generation, Eq. (3.13), may be assessed with the following nondimensional relation [68]:

$$N_v = \frac{\text{Ec} \cdot \text{Pr}}{\text{Da}}.$$
(3.19)

For porous media flows with N_v much less than unity, viscous effects are negligible. In the current thermocline tank study, the tank size and molten-salt velocities result in values on the order of 10^{-21}. As such, viscous effects can be considered small and are omitted from the analysis.

3.3.1   Temperature and Velocity Fields

Temperature profiles corresponding to the cyclic operation of the adiabatic thermocline tank are plotted in Figure 3.2 for all three filler diameters. The width of the heat-exchange region inside each tank case is measured as the distance spanned by 99% of the total temperature difference:

$$0.005 \leq \frac{T_l - T_c}{T_h - T_c} \leq 0.995.$$
(3.20)

As seen, the heat-exchange region for the 2 mm granule filler extends from 0.07 to 0.60 of the nondimensional bed height at the midpoint of the charging process ($\tau = 0.5$). At the same time instant, the larger 5 cm granules exhibit a wider region that extends from 0.11 to 0.77. The benefit of the thinner heat-exchange region achieved with the smaller granules include greater energy storage at the end of the charge ($\tau = 1$), which then prolongs outflow of hot molten salt during the subsequent discharge process ($1 < \tau < 2$). However, the width of the heat-exchange region is almost identical between the 2 mm

and 1 cm filler sizes, indicating a limit on thermal stratification inside the dual-media mixture.

In addition to heat transfer, the granules diameters also exhibit different pressure drops, which scales the pumping power required to sustain fluid through the porous bed. This characteristic pressure drop is defined at the end of the discharge half cycle ($\tau = 2$), when the majority of the thermocline tank is filled with cold molten salt at maximum density. Under the adiabatic boundary condition, the 5 cm bed exhibits a pressure drop of 40.8 Pa/m, the 1 cm bed exhibits a pressure drop of 146 Pa/m, and the 2 mm bed exhibits a pressure drop of 2320 Pa/m. This dramatic increase with reduced size is a consequence of the reduced bed permeability, governed by Eq. (3.8), which scales with diameter squared. Given the previous improvement in thermal stratification for smaller diameters, selection of appropriate filler size is therefore dependent on both desired storage efficiency and available pumping power.

The multidimensional behavior of the thermocline tank is illustrated in Figure 3.3, which plots the adiabatic thermocline tank filled with 1 cm granules during the discharge process. The flow, illustrated with streamlines, travels upward as cold molten salt enters at the bottom distributor port and hot salt exits at the top distributor port. In this scenario, thermal stratification and molten-salt velocity remain well organized throughout the process (see Appendix D). For comparison, Figure 3.4 plots the same thermocline tank discharge process but with the nonadiabatic wall condition. The addition of external convection losses disturbs the thermal stratification by cooling salt located along the tank wall. Secondary buoyancy forces then act on this cooled salt to disrupt the fluid streamlines by inducing flow reversal and radial velocities.

3.3.2   Outflow Temperature Profiles

The outflow temperatures exhibited during thermocline tank discharge are plotted in Figure 3.5 for all six tank scenarios. As expected, the three adiabatic cases (illustrated with solid lines) sustain the hottest outflow through the discharge as no stored heat is lost to the surroundings. In the nonadiabatic cases (illustrated with dashed lines), small but

immediate decreases in outflow temperature occur following the onset of discharge. These declines later become significant in the last half ($\tau > 1.5$) when the heat-exchange region approaches the top distributor port. The addition of external convection reduces the internal energy content of the tank and protracts the heat-exchange region, leading to an earlier depletion of the hot salt supply.

Through most of the discharge process, smaller granules sustain hotter outflow temperatures than the larger granules under equivalent tank wall conditions. Reason for this is again due to the thinner heat-exchange region achieved with small granules, which enables a larger ratio of the tank volume to be filled with hot molten salt and extends the duration of high-temperature outflow. A thinner heat-exchange region also carries larger temperature gradients which then results in a more rapid decline of outflow temperature after the hot supply is exhausted. In the nonadiabatic tanks, this decline eventually leads to colder outflow temperatures for $d_s = 2$ mm compared to $d_s = 5$ cm. However, this phenomenon is limited to near completion of the discharge half-cycle and thus smaller diameters should remain preferable to sustain high thermal quality outflow in the aggregate.

3.3.3   Cyclic Storage Performance

The storage efficiencies achieved under the applied thermocline operation cycle are listed in Table 3.1 for each tank scenario. Included in the table are the first law efficiency, second law efficiency, and the 95% outflow temperature efficiency. As in the previous sections, thermocline tanks with adiabatic wall conditions yield the best performance for all three efficiency metrics. When external losses are present, the energy and exergy inside the tank is reduced, preventing full recovery of energy and exergy supplied during the charge process. Reducing granule diameter also improves efficiency by sustaining more the tank volume at the hot temperature for subsequent discharge. However, the tanks filled with 2 mm and 1 cm granules exhibit similar first and second law efficiencies, again indicating a practical limit on thermal stratification and storage performance. While the second law efficiency is always less than the first law efficiency,

this disparity remains minimal for the three adiabatic tank wall cases but increases with the addition of external convection losses. Given that exergy accounts for the usability of energy, the second law efficiency is therefore more sensitive to the effects of convection and provides a better indication of the resultant tank behavior.

Among the three efficiency definitions, application of the 95% outflow temperature criterion repeatedly results in the lowest performance value. One exception is the adiabatic tank filled with 2 mm granules (case 1), whose outflow temperature remained above the cutoff throughout the discharge, yielding an efficiency equal to the first law efficiency. For the adiabatic tank filled with 5 cm granules (case 5), the 95% criterion efficiency is 0.840 and exceeds the value of 0.790 predicted by the cyclic efficiency model discussed in Section 3.3.1. It should be noted that [49] [monitored the delivery of molten salt at the limit of the dual-media porous bed, below the top distributor region. This approach was not suitable for the current study as the inclusion of wind losses generates recirculation zones at this interface (seen in Figure 3.4), adding large uncertainty to the analysis of energy and exergy transfer. The inflow and outflow of the tank are instead evaluated at the surrounding distributor ports, where recirculation does not occur. However, inclusion of the distributor regions effectively increases the considered tank height and generates storage cycle efficiency greater than the model prediction.

As with the second law efficiency, the outflow temperature criterion-based efficiency is subject to large decreases for nonadiabatic tanks. External losses generate small but immediate drops in outflow temperature at the start of discharge, seen in Figure 3.5. This temperature drop-off inhibits sustained delivery of hot molten salt with $\Theta >$ 0.95, resulting in temperature-criterion efficiencies as low as 0.426. Because of this sharp decline compared to the previous first and second law efficiency definitions, the Θ > 0.95 stipulation for molten salt outflow is an overly conservative thermocline tank design metric. As indicated by the second law efficiency, molten-salt outflow below this temperature remains serviceable for the power block. Instead of rejecting this colder outflow, the Rankine cycle should be compliant with the lower-quality molten salt to continue steam generation and power output at reduced thermal efficiency, known as

sliding-pressure operation. A practical example of this capability is the power block within SEGS VI parabolic trough plant, which can operate with the HTF being as much as 90 K below the nominal design point [52].

3.4   Chapter Summary

A numerical simulation of dual-media thermocline tanks is conducted to investigate the influence of granule diameter and external heat losses. Tanks filled with small granules exhibit thinner heat-exchange regions than tanks with larger granules. This reduction improves the thermal stratification of the molten salt and yields higher outflow temperatures during discharge. The thermocline efficiency (both first and second law) is consequently greater for the smaller granule diameters. However, a trade-off exists between thermocline storage performance and increased pumping power required for fluid flow to overcome the reduced fillerbed permeability. The 2 mm granules exhibit an order-of-magnitude increase in pressure drop relative to the 1 cm granules, but provide diminishing gains in storage performance. Therefore the 1 cm filler diameter is the most practical size for large-scale dual-media thermocline tanks among the cases considered.

The addition of external convection at the tank wall is observed to distort thermal stratification and fluid streamlines inside the thermocline porous bed, resulting in colder outflow temperatures during discharge and reduced storage cycle efficiencies. These efficiency penalties are most severe in the outflow temperature criterion-based efficiency, but this is demonstrated to be an overly conservative performance metric. Alternative determination of the first and second law cycle efficiencies eliminate the need for *ad hoc* thermal analysis applied in previous thermocline studies.

Table 3.1. Case summary of thermocline tank cycle efficiencies (first law, second law, and temperature criterion) for different granule diameters and convection loss conditions.

Case	d_s [cm]	Nu_w	η_I	η_{II}	$\eta_{I,95}$
1	0.2	0	0.975	0.975	0.975
2	0.2	4260	0.940	0.923	0.748
3	1	0	0.975	0.974	0.964
4	1	4260	0.921	0.893	0.597
5	5	0	0.966	0.961	0.840
6	5	4260	0.903	0.868	0.426
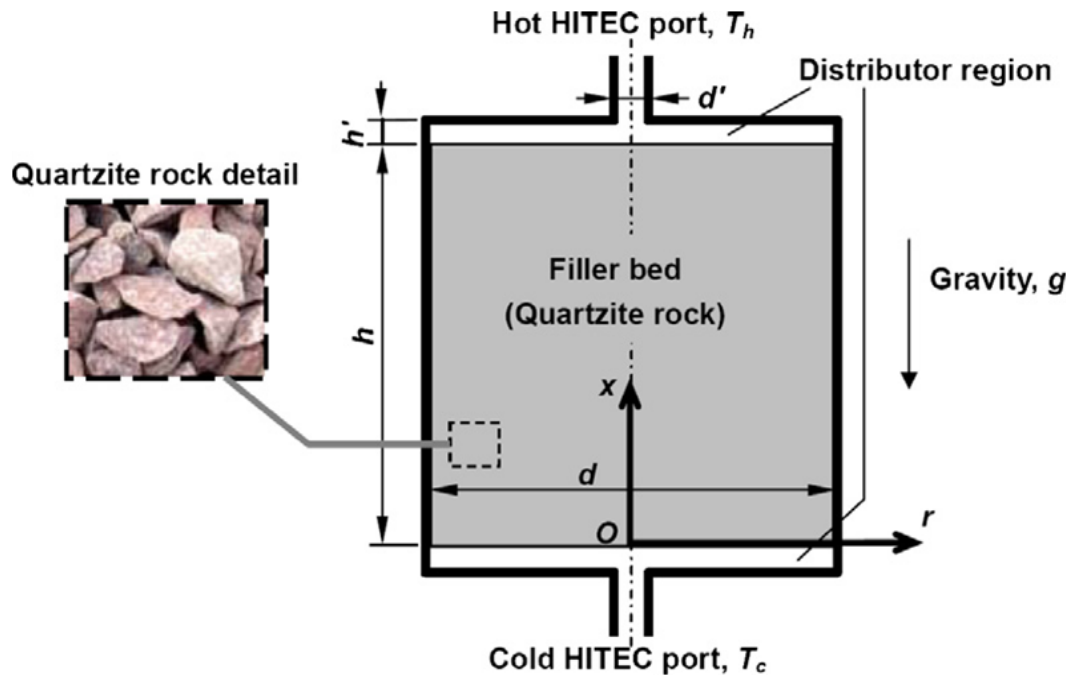
Figure 3.1. Illustration of a dual-media thermocline tank thermal energy storage system composed of molten-salt fluid and quartzite rock filler. Distributor regions are included to generate uniform velocity fields inside the porous region. Hot molten salt is supplied and extracted at the top distributor port; cold molten salt is supplied and extracted at the bottom distributor port.
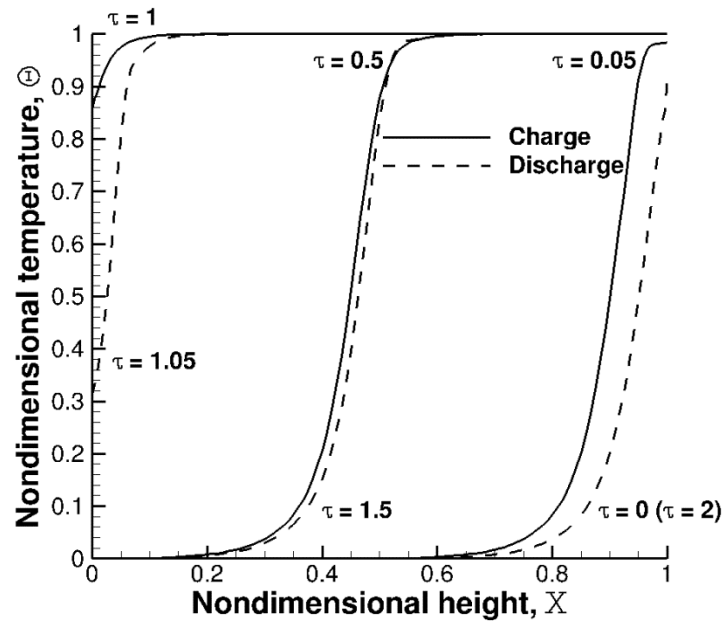
(a)
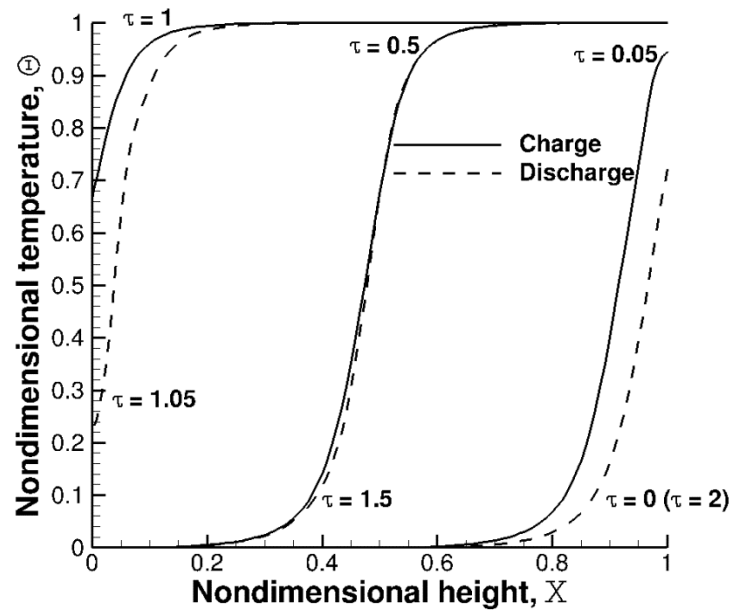
(b)

Figure 3.2. Molten-salt temperature profiles during a charge-discharge cycle of the thermocline tank with an adiabatic wall condition. Profiles are plotted for three different granule diameters: (a) $d_s = 2$ mm, (b) $d_s = 1$ cm, (c) $d_s = 5$ cm.
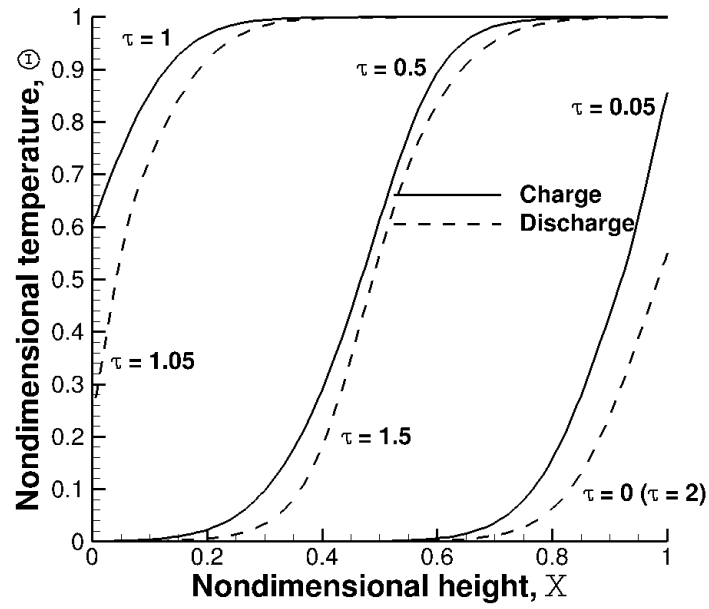
Figure 3.2. continued.
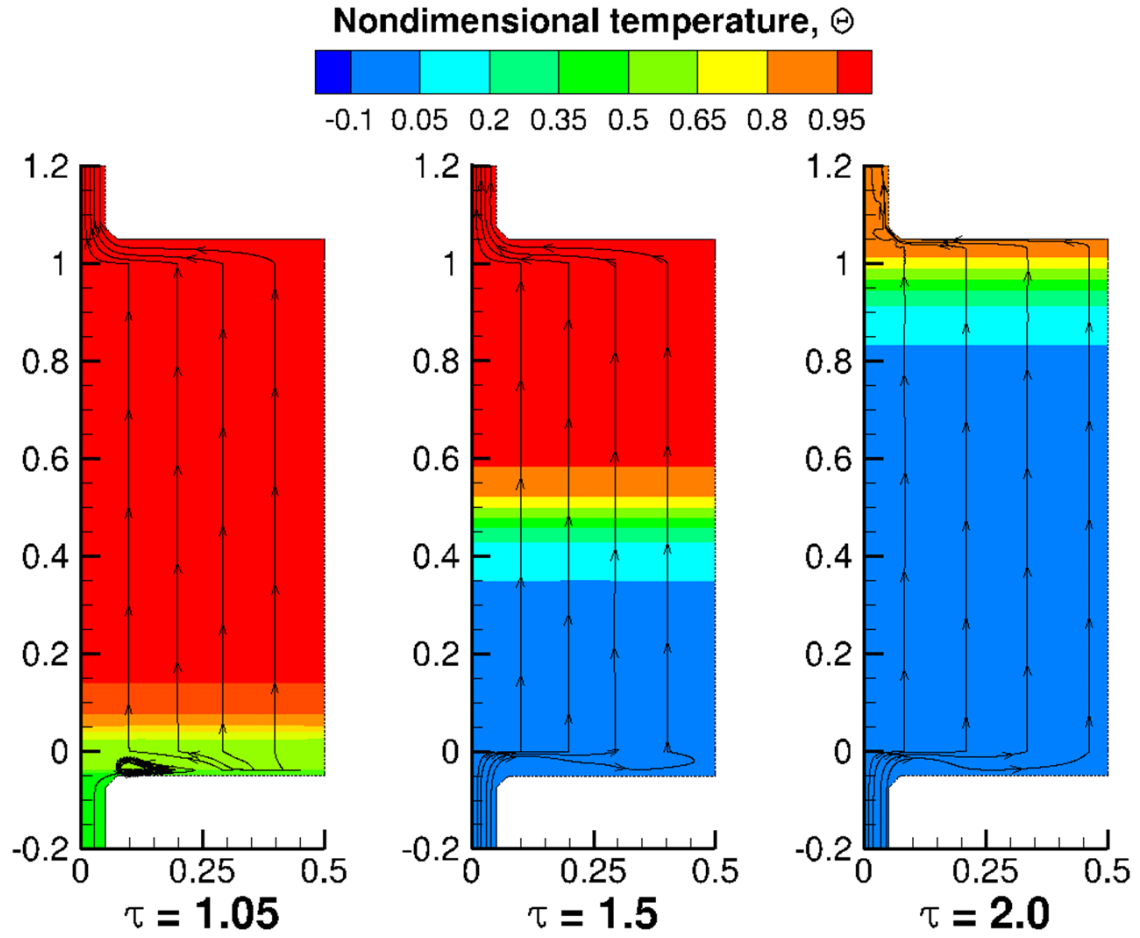
Figure 3.3. Temperature contours and flow streamlines during a discharge of the thermocline tank with an adiabatic tank wall. The porous region (filled with 1 cm granules) extends from 0 to 1 along the nondimensional tank height.
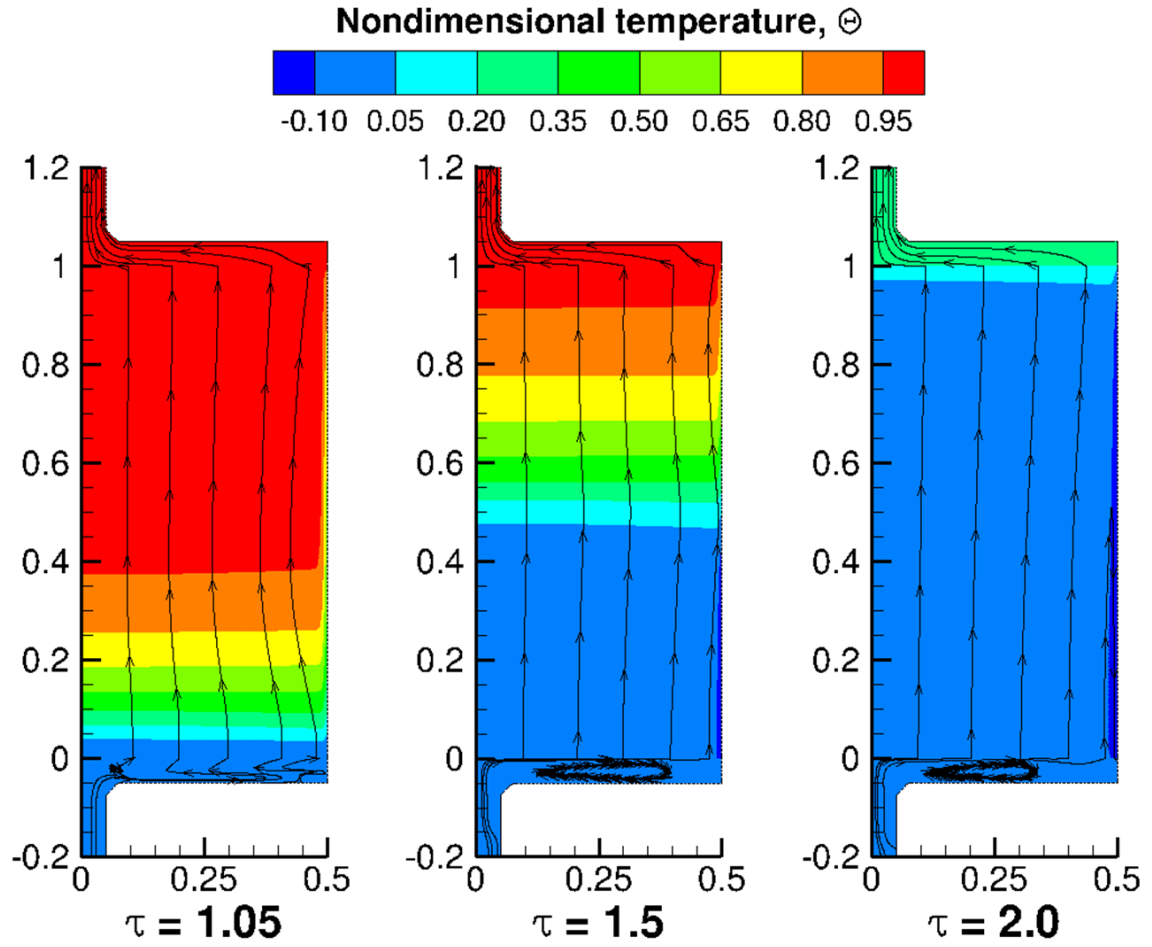
Figure 3.4. Temperature contours and flow streamlines during a discharge of the thermocline tank with external convection ($Nu_w = 4260$) along the tank wall. The porous region (filled with 1 cm granules) extends from 0 to 1 along the nondimensional tank height.
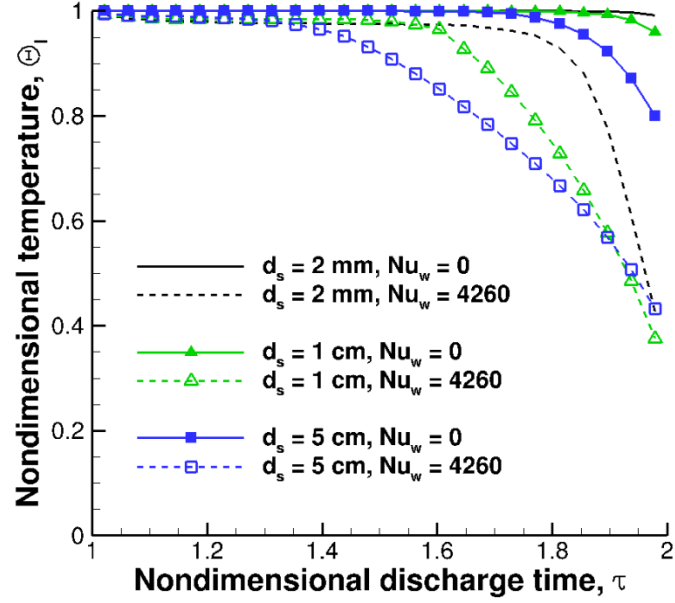
Figure 3.5. Molten-salt outflow temperature during the thermocline tank discharge process. The solid lines represent the adiabatic boundary condition at the tank wall. The dashed lines represent the nonadiabatic convection condition at the tank wall.

CHAPTER 4. NUMERICAL CHARACTERIZATION OF THERMAL RATCHETING
POTENTIAL IN A THERMOCLINE TANK

Material in this chapter was published in *Applied Energy* [69], *ASME Journal of Solar Energy Engineering* [70], and presented at the *2011 ASME Conference on Energy Sustainability in Washington D.C.* [71].

4.1   Introduction

Dual-media thermocline tanks offer low-cost thermal energy storage for CSP power plants but the structural stability of the tank wall remains a critical design concern. As the tank is repeatedly filled with hot and cold heat transfer fluid, both the tank wall and internal rock filler will exhibit corresponding temperature fluctuations along the height of the tank. The physical interaction between the wall and the internal rock filler is a function of the disparity in material coefficients of thermal expansion. For example, if the thermal expansion of the tank wall exceeds that of the filler, an annular gap develops between the materials when the tank is heated during a charge process. The granulated filler then reorients or slumps to fill this gap. After this reorientation, the tank wall has "ratcheted" to a new diameter and can no longer contract to its original shape process due to the resistance posed by the rearranged filler. During the subsequent discharge process when the tank is cooled, a portion of the thermal strain generated from the charge process converts to mechanical strain and carries a corresponding amount of stress. If this stress exceeds the yield strength of the wall material, the wall plastically deforms to prevent full recovery of the thermal strain in successive cycles. These tank operations then become subject to an accumulation of ratchets and the possibility for catastrophic tank failure.

Characterization of thermal ratcheting involves a complex interaction of thermal transport and solid mechanics that has not been widely studied for thermocline-based energy storage tanks. This chapter develops an integrated analysis of the thermal and mechanical behavior of thermocline tanks to improve understanding of ratcheting potential. As in the previous chapter, the porous-media flow and heat transfer inside the tank are simulated by a two-temperature model to account for the different thermal properties of the filler material and the molten salt. Heat transfer inside the added composite tank wall is a function of external heat losses and the internal molten-salt flow. The corresponding thermomechanical stress is quantified using both finite-element analysis and simple analytical strain relations. A parametric study of the tank wall design and external heat loss conditions is first performed to identify methods to mitigate ratcheting potential. The modeling approach is then validated with a simulation of the thermocline tank installed at the historic Solar One power tower plant to compare with reported tank wall stress data.

4.2   Numerical Model

4.2.1   Problem Description

A representation of the thermocline tank geometry is provided in Figure 4.1. The internal structure, composition, and governing transport equations are identical to the model presented in Chapter 3. HITEC molten salt and quartzite are again selected as the heat transfer fluid and solid filler, respectively. However, the present tank is updated with a complex wall consisting of multiple layers [27,72]: an inner firebrick layer for thermal insulation (1), a steel shell layer for mechanical support (2), and an outer layer of ceramic fiber (3) for corrosion protection and thermal insulation. The tank assembly also includes a liner material to inhibit leakage of the molten salt through the porous firebrick, but is neglected study due to relative thinness. Thermal transport properties of the two insulation materials and structural shell are listed in Table 4.1.

The operating temperature span of the HITEC is 293 °C to 450 °C, representative of an advanced molten-salt parabolic trough plant. Corresponding material property data

for the salt and quartzite rock are located in Chapter 3. The thermocline tank is constructed on top of a water-cooled concrete foundation [27], characterized with a Dirichlet boundary condition of 90 °C at the bottom tank surface. The remaining side and top walls are exposed to ambient air at a fixed temperature of 27 °C. The corresponding convection and radiation losses are characterized as follows:

$$k_3 \left. \frac{\partial T_3}{\partial r} \right|_w = -h_w \left(T_w - T_\infty \right) - \varepsilon_{rad,w} \sigma_{rad} \left(T_w^{\ 4} - T_\infty^{\ 4} \right). \tag{4.1}$$

Energy transport through the composite wall is function of thermal diffusion, with contact resistance at the interfaces (firebrick and steel, steel and ceramic) assumed to be negligible.

4.2.2   Structural Analysis

To assess the interaction between the thermocline tank wall the internal filler, the current study assumes the solid quartzite granules as cohesionless (no resistance to slumping) and infinitely rigid (immune to mechanical deformation). The end result is a conservative approximation of the true bed behavior such that the incident wall stresses are proportional to the magnitude of temperature fluctuations associated with the steel layer. The associated radial deformation of the wall is a function of the thermal strain:

$$\varepsilon_T(x,r) = \alpha \left[T_2(x,r) - T_0 \right]. \tag{4.2}$$

When the steel is heated to a maximum temperature during the storage cycle, the local thermal strain also exhibits a maximum value. Thermal stratification inside the tank causes this strain and its associated time of occurrence to vary along the axial tank height. Given that the internal filler granules do not prevent outward expansion of the tank wall, the mechanical strain at this condition is zero. It should be noted that strain interactions with the surrounding insulation layers are neglected as they do not provide structural support to the tank assembly. Under the cohesionless and infinite rigidity assumptions, the wall cannot contract from this local expanded radius and the maximum amount of strain remains constant in the circumferential direction. When the tank is later cooled,

this inability to contracts converts a portion of the thermal strain to mechanical strain. When the steel layer is coldest during the storage cycle, the local thermal strain is at a minimum and the mechanical strain is at a maximum. The stress distribution resulting from this mechanical strain is governed by Hooke's Law:

$$\varepsilon_M(x,r) = \frac{1}{E_M}\left[\sigma_{11} - \nu_P(\sigma_{22} + \sigma_{33})\right]. \tag{4.3}$$

While the weight of the fillerbed and the heat transfer fluid exert some pressure on the tank wall, the resultant stresses are small in comparison to the stress associated with the permanently expanded tank radius. Thus the functional dependence of mechanical strain in Eq. (4.3) may be simplified to a single principal stress, *i.e.*, the hoop stress. If this hoop stress exceeds the yield strength of the steel, the resultant plastic deformation prevents full recovery of the original thermal strain. The total strain value increases with future cycles, enabling the hoop stress to further increase until an eventual tank rupture. Thus to ensure prevention of thermal ratcheting, the maximum stress at a given location along the tank wall (governed by the maximum temperature fluctuation) should not exceed the material yield strength:

$$\sigma_{max}(x,r) = \alpha E_M\left[T_{2,max}(x,r) - T_{2,min}(x,r)\right]. \tag{4.4}$$

The coefficient of thermal expansion, modulus of elasticity, yield strength, and Poisson's ratio are assigned values typical of steels: 0.00001 K^{-1}, 200 GPa, 200 MPa, and 0.3, respectively.

4.2.3 Solution Procedure

Solution to the governing transport equations of the thermocline tank are obtained with FLUENT CFD software [65], identical to the procedure outlined in Chapter 3. The porous bed, distributor, and wall geometries are discretized in to a total of 15,750 cells for finite-volume computation. Prior to simulation, the entire domain is initialized to the hot temperature limit of 450 °C. Consecutive discharge and charge processes are performed until the tank domain exhibits the desired periodic thermal response. After

this periodicity is observed in the thermal solution, the vertical temperature profile of the steel shell is extracted at multiple time instants throughout the simulated storage cycle. The limiting temperatures at each discrete cell location are then organized into two composite profiles that represent the maximum and minimum temperature observed along the steel during one full cycle. Under the stated assumptions for the granular bed, the maximum temperature profile defines the fixed radial shape and position of the thermocline tank wall in response to thermal expansion. The minimum temperature profile then determines the largest hoop stress associated with the tank wall's inability to contract around the reoriented porous bed.

Calculation of this hoop stress is first performed with commercial finite-element analysis software, ANSYS 12.1 [73]. The vertical steel shell is discretized in to deformable solid 2-dimensional elements with a size of $\Delta x/h = 0.00173$. The composite maximum temperature profile is first enforced along the vertical direction to simulate the expected radial deflection. It should be noted that the magnitude of this deflection is small and assumed to be decoupled from the internal fluid flow. The resultant deflection is then fixed and the steel geometry is updated with the composite minimum temperature profile to simulate and output the resultant hoop stress. As an alternative to this approach, the hoop stress may also be determined from the composite profiles with Eq. (4.4). This approach neglects the nonradial principal stresses but is less computationally intensive.

4.3   Results and Discussion

The current study considers seven different thermocline tank cases to investigate ratcheting potential for different external heat loss conditions and composite wall thicknesses, summarized in Table 4.2. In all cases, the height and diameter of the internal filler region are both fixed at 12 m to maintain similarity with respect to tank operation. In cases 1–4, the tank wall configurations are held constant while the convection coefficient alternates between 5 and 10 W/m^2-K and the surface emissivity alternates between 0.5 and 1. In cases 5–7, the external heat loss parameters are held constant while the individual thicknesses of the composite wall layers are modified. As previously

discussed, development of thermal periodicity in each tank case requires a minimum of five full (discharge and charge) cycles. Both the discharge and charge half-cycles extend for six hours of flow time.

4.3.1 Temperature and Velocity Fields

Thermal results for the case 1 thermocline tank are plotted in Figure 4.2 for three separate time instants during the discharge half-cycle. Early in the discharge ($\tau = 0.513$), hot molten salt fills the upper half of the interior tank volume. As the discharge progresses, this salt is extracted from the top distributor port and the hot supply is eventually exhausted at the end ($\tau = 6.516$). The applied convection and radiation losses cool the surrounding composite tank wall as well as molten salt located near the wall. As was discussed in Chapter 3, buoyancy forces associated with this incidental temperature decrease act to disrupt the vertical uniformity of the fluid flow. As seen in Figure 4.2, these effects are most prominent away from the heat-exchange region where the temperature gradients are minimal under nominal conditions. Swirl patterns first occur at the top of the tank in the hot supply volume, but eventually decay as the heat exchange travels upward. However, the corresponding growth of the underlying cold salt volume results in new vortices at the end of the discharge process.

The vertical temperature distribution of the steel layer is plotted in Figure 4.3, including multiple time instants throughout the full storage cycle to illustrate the transient thermal behavior. As with the internal molten-salt volume, the steel exhibits a periodic response with charging and discharging. However, the steel experiences a temporal phase shift with this response due to the thermal mass of the composite wall structure. The amplitude of temperature fluctuation is at a maximum near the midpoint of the tank height, attributed to the repeated presence of the heat-exchange region (which buffers the hot and cold salt) at this location. Near the distributors, temperature change is instead minimal because the traversal of the heat-exchange region does not extend to the upper and lower extremes of the fillerbed.

4.3.2 Thermocline Tank Wall Stress

Hoop stress in the thermocline tank wall is determined from the steel shell temperature profiles obtained in the thermal simulation. As previously discussed, this computation is performed using two separate methods: (1) FEA simulation of the steel shell, and (2) analytic calculation of stress with Eq. (4.4). Predicted stress values for the case 1 tank are plotted in Figure 4.4 using both methods for comparison. This hoop stress is normalized with respect to the steel yield strength:

$$\omega = \frac{\sigma}{\sigma_y} \, . \tag{4.5}$$

As seen, the two approaches yield almost identical results. The second approach is therefore adopted for the remaining tank cases due to its simplicity.

The normalized stress predictions for all seven cases are plotted in Figure 4.5. In cases 1 – 4, the maximum hoop stress is inversely proportional to the external heat loss at the tank wall surface. Among these cases, case 2 experiences the greatest heat loss and exhibits the lowest peak stress value. Case 3 experiences the least heat loss but exhibits the highest peak stress value. This behavior is a result of the combined sensitivity of the composite tank wall temperatures to both heat losses and cyclic storage operations. Greater losses reduce the sensitivity of the wall to the internal molten-salt fluctuations and thus dampen temperature cycles along the steel shell. However, it should also be noted that the four cases exhibit normalized peak stress values between 0.407 and 0.424. Thus plastic deformation is not predicted to occur and low heat losses remain preferable to maximize storage performance.

While the first four thermocline tank cases do not exhibit yielding, additional reductions in stress increase the factor of safety associated with thermal ratcheting potential. This factor may be critical in the event of unexpected temperature changes or other unforeseen circumstances. The remaining three cases serve to investigate this benefit by modifying the individual thicknesses of the firebrick, steel shell, and external ceramic layer. The external heat losses conditions remain fixed to values applied in case 1. Of these different composite wall geometries, case 5 experiences the lowest peak

stress with a normalized value of 0.129. This tank includes a thicker firebrick layer, which further diminishes the sensitivity of the steel to the temperature fluctuations of the internal molten salt. The case 6 tank wall design also exhibits a reduced stress profile, resulting from its increased steel thickness which diffuses temperature gradients and fluctuations along the shell.

Opposite to the behavior of the internal firebrick insulation and steel shell, the external ceramic insulation reduces the wall hoop stress with a reduction in thickness. A thinner ceramic layer increases the steel sensitivity to the external heat losses, which in turn decrease the sensitivity the molten-salt cycles. Data for case 7 illustrates this effect, where the ceramic thickness is halved and results in a normalized peak stress of 0.391. However, this peak stress is only 5% less than what is observed with the default composite wall design (case 1), thus thick external insulation remains preferable to maximize the total amount of insulation and mitigate unwanted thermal losses.

4.4   Model Validation

Results from the previous composite wall analysis could not be validated against real data as the multilayer concepts proposed in [27,72] were not experimentally verified. It is therefore necessary to simulate a real thermocline tank with known dimensions, operating temperatures, and wall stresses in order to validate the prescribed approach for predicting tank wall stresses. Such information is available in the published literature for the 182 MWh_t thermocline tank operated as part of the Solar One facility [4,32–34]. Chapter 2 provides a detailed review of this particular thermocline tank. The tank was filled with Caloria HT-43 mineral oil in combination with granite rock as the solid filler and operated between 204 °C and 304 °C.

As the first large-scale CSP plant in operation, the entire Solar One facility was subjected to extensive instrumentation and data collection. For the installed thermocline tank, this data includes temperatures profiles during storage operations as well as stresses along the tank wall. Structural tank analysis is repeated to simulate the conditions of this historic thermocline tank in an effort to both validate the modeling approach described in

Section 4.2 and to determine whether the tank was susceptible to thermal ratcheting behavior.

4.4.1 Problem Description

Simulation of the Solar One thermocline tank considers model geometry informed by published technical drawings [33,34], and illustrated in Figure 4.6. The tank wall is composed of carbon steel ASTM 537 class 2 with a 9.1 m inner radius and constructed above 0.6 m base layer of concrete. In the original tank, this wall included discrete sections of different thickness, varying from 2.89 cm at the bottom to 0.79 cm near the top. For simplicity, the present model geometry is fixed to an intermediate and uniform thickness of 2 cm. This steel layer is surrounded on the side with a 0.3 m layer of fiberglass insulation and on the top with a 0.6 m layer of calcium silicate. Unlike the previous analysis, no internal insulation was included.

Inside the tank, the porous bed is composed of two distinct sizes (sand and rock) which are stratified along the tank height. Starting from the tank floor, these stratified regions include a 0.3 m layer of sand, a 1.1 m layer of rock, a 10.5 m mixture of sand and rock, and a final 0.5 m layer of rock. The remaining tank volume above this bed is filled with nitrogen gas as ullage to protect the flammable oil, assumed to be a quiescent fluid. For numerical simulation, the size of the granite sand and rock are fixed to effective diameters of 0.2 cm and 5 cm, respectively. For the mixture layer, a weighted average diameter of 0.46 cm is assumed. The bed porosity is fixed at 0.22 for the mixture layer and increased to 0.4 for the pure sand or rock layers. Table 4.3 lists the thermal properties of the solids and nitrogen gas.

During a charge process, hot Caloria oil enters at the top of the filler region at a temperature of 304 °C while colder oil exits at the bottom. For the reverse discharge, cold Caloria enters at the bottom at 204 °C while the above hot oil exits from the top. The density, kinematic viscosity, and thermal conductivity of the oil are known functions of temperature (degrees Celsius) [32]:

$$\rho_l = -0.713T_l + 871.1 \tag{4.6}$$

$$\nu = 0.0452 \left(T_l^{-1.943} \right) \tag{4.7}$$

$$k_l = -0.00014 T_l + 0.125. \tag{4.8}$$

The original thermocline tank included upper and lower distributor manifolds, embedded in the monodisperse rock layers, to transport oil to and from the tank as needed. In the present study, these distributors are represented with two thin regions of mass and energy generation within the rock layers. During a simulated charge process, oil mass and energy are generated inside the upper rock layer while oil mass and energy are simultaneously removed in the lower rock layer, producing the desired fluid flow across the porous bed. For the discharge process, the signs of the mass and energy generation are switched to produce the reverse flow condition. The FLUENT thermal solution is modified with user-defined source terms to enforce the artificial generation and destruction of mass and energy. The complete UDF file for the Solar One thermocline tank model is located in Appendix F.

Oil transport inside the thermocline tank model is informed with documented charge and discharge processes to simulate the original performance. One such operation was charge performed a charge process conducted on May 19, 1983 [33]. The mass flow of the entering hot oil lasted approximately nine hours and is plotted in Figure 4.7. Due to the large physical scale of Solar One, these flow rate measurements were plagued by leaks and subject to inaccuracies, estimated to induce a 15 − 20% positive bias [34]. The recorded oil flow rate is subjected to a 20% reduction to correct for this bias, also plotted in Figure 4.7. For the nine-hour charge simulation, this corrected rate is averaged to define a simple fixed volumetric flow rate. From the artificial distributor volume enforced in the model geometry, this flow rate equate to a mass generation rate of 1.804 kg/m^3-s. An equivalent mass generation rate is applied in the opposing distributor volume during the discharge process. The corresponding energy generation in the distributors is proportional to the mass generation:

$$\dot{E}'''_{gen} = \dot{m}'''_{gen} C_{P,l} \left(T_l - T_c \right). \tag{4.9}$$

As in the real tank, charging and discharging is separated by durations of standby where the oil is not actively transported through the tank. These model standbys extend for 15 hours to formulate a complete storage cycle duration of 48 hours.

Mass, momentum, and energy transport of the oil inside the thermocline tank is governed by the same equations as the previous molten-salt tanks under investigation. The tank wall is also subject to both convection and radiation losses to the surroundings with Eq. (4.1). The applied convection coefficient and ambient temperature are estimated from historic weather data for May 1983 in Barstow, CA [74]; 2.2 W/m^2-K and 21 °C, respectively. The tank surface emissivity is fixed to 0.9. The floor of the cement base (which did not include embedded water tubes is assumed to be adiabatic. Wall stress prediction is identical to the methodology discussed in Section 4.2.2.

4.4.2 Numerical Results

Similar to the previous ratcheting analysis, repeated storage cycles are simulated until the thermocline tank geometry observes a periodic thermal response. The resultant temperature profiles along the steel shell throughout the two-day cycle are plotted in Figure 4.8. These profiles are plotted at three-hour intervals for both the charge (hours 3, 6, and 9) and the discharge (hours 27, 30, 33) processes. Also included are the temperature profiles observed at the end of both standbys (hours 24 and 48). As seen, the largest temperature fluctuations occur between 1 m and 9 m along the tank height, indicating the repeated travel path of the internal heat-exchange region between the hot and cold oil. Time-independent composite profiles of the maximum and minimum observed temperatures along the shell are extracted from this data to conduct to the wall deformation analysis.

Results of the finite-element tank wall simulation are plotted in Figure 4.9. An increased plateau of hoop stress is observed from 2 m to 8 m along the height of the steel shell, corresponding to the previous plot of temperature fluctuation. Outside the travel path of the heat-exchange region, the steel is exposed to relatively isothermal oil and thus

exhibits greater thermal and structural stability. Small increases in stress at the upper limit of the tank wall are attributed to edge effects.

The original thermocline tank included strain gages at various tank heights and azimuth angles. Horizontal stress data recorded from these strain gages in June 1984 [34] are included in Figure 4.9. While the general trend of the model stress predictions agrees with the experiment data, discrepancies at different locations are attributed to the idealized nature of the CFD model (given that the original tank was never operated in such a consistent and periodic fashion) and to the large uncertainties reported for the physical gage readings, up to 142 MPa. This uncertainty is included in Figure 4.9 as error bars. The original operators acknowledged this uncertainty and attributed to the scale, complexity, and novelty of the Solar One facility. However, gages located between 0.6096 m and 1.219 m were reported to yield the most consistent and valid readings. Within this region, the measured horizontal stress exhibits a maximum of 190 MPa, a 6.8% deviation from the maximum stress of 177 MPa predicted with the tank model. Model data at 0.3408 m, 5.486 m, and 12.5 m are also within the range of uncertainty for the strain gages at these locations. Given this reasonable similarity in datasets, it may be inferred that the developed modeling approach adequately predicts hoop stress along the thermocline tank wall.

The minimum yield strength of the steel, 414 MPa, is also plotted in Figure 4.9 to assess the tank's potential for thermal ratcheting. As seen, this strength exceeds all the recorded stresses (both numerical and strain gage), indicating a successful prevention of plastic deformation required for ratchet accumulation. The uncertainty in gage data reported at 1.524 m does exceed the yield strength, but the tank did not fail from ratcheting during its operational lifetime and implies an acceptable stress level at this location.

It must be reiterated that the present model is limited to cyclic charging and discharging of the Solar One thermocline tank geometry. When the tank undergoes a complete shutdown or startup, while rare, temperature variations in the tank wall may increase by a factor of almost three. In such a scenario, the infinite rigidity

approximation applied for the internal granules becomes overly conservative and predicts excessive hoop stress values. In reality, the solid filler will exhibit some finite amount of volume change due to combined thermal expansion and mechanical interaction with its surroundings. As the amplitude of wall temperature variation increases, the change in granulated filler volume also increases and the filler behavior further deviates from the infinite rigidity model. A comprehensive and detailed model of the granular physics inside the tank is therefore needed in conjunction with the thermal model to adequately model such a startup or shutdown procedure.

4.5   Chapter Summary

A combined thermal and mechanical model is developed to investigate thermal ratcheting potential in a thermocline tank wall. Assuming the internal filler granules to be cohesionless and infinitely rigid, hoop stress in the tank wall is readily determined from the periodic temperatures profiles in the steel. Initial simulation is performed with a composite tank wall structure composed of internal and external thermal insulation. Hoop stress in the intermediate steel shell is a direct consequence of temperature fluctuations generated by the cyclic charge and discharge operation of the thermocline tank. The magnitude of this stress is observed to dampen with reduced sensitivity to the cyclic behavior, either through increased external heat losses or thicker internal insulation between the filler and steel. As heat losses degrade energy storage inside the tank, adequate internal insulation is the optimal method to minimize ratcheting potential.

Validation of the mechanical model is performed with a subsequent simulation of the thermocline tank operated at the Solar One power tower plant, which included strain gages along the tank wall. Data recorded with the most reliable gages agrees with the local simulated stresses to within 13 MPa or 6.8%. Both datasets were less than the minimum yield strength of the tank wall steel and thus avoided potential for plastic deformation and thermal ratcheting phenomena. This localized agreement with recorded data indicates that the mechanical model is suitable to assess thermal ratcheting potential in dual-media thermocline tanks. However, model accuracy and versatility can be

improved with additional sub-models related to the internal granular physics, eliminating the infinite rigidity approximation associated with the current work.

Table 4.1. Thermal transport properties of the thermocline tank composite wall.

Material	k [W/m-K]	ρ [kg/m^3]	C_P [J/kg-K]
Firebrick	1	2000	1000
Steel	60	8000	430
Ceramic	1	1000	1000

Table 4.2. Summary of the thermocline tank wall structural parameters and heat loss conditions.

Case	h_w [W/m^2-K]	ε_w	δ_1 [cm]	δ_2 [cm]	δ_3 [cm]
1	5	1	10	2	5
2	10	1	10	2	5
3	5	0.5	10	2	5
4	10	0.5	10	2	5
5	5	1	20	2	5
6	5	1	10	4	5
7	5	1	10	2	2.5

Table 4.3. Thermal transport properties of the Solar One thermocline tank materials.

Material	k [W/m-K]	ρ [kg/m^3]	C_P [J/kg-K]	Reference
Carbon steel	47.0	7850	475	[75]
Calcium silicate	0.080	250	840	[75]
Fiberglass	0.038	32	835	[76]
Cement	0.720	1860	780	[76]
N$_2$ Ullage	0.043	0.585	1070	[76]
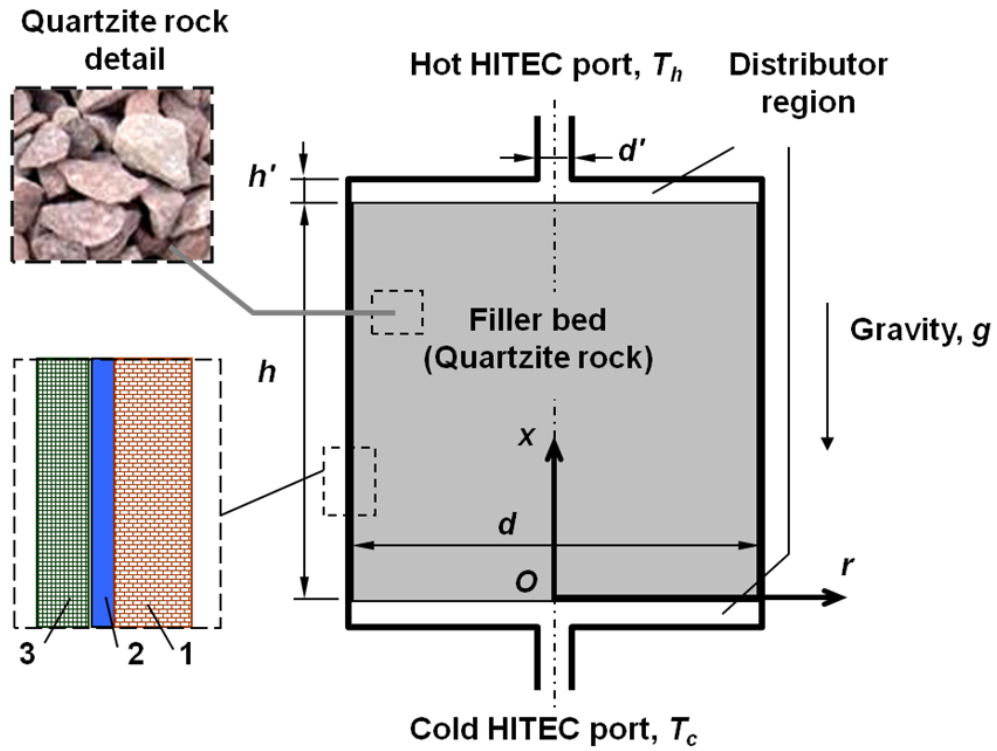
Figure 4.1. Illustration of a thermocline tank with a composite wall consisting of internal firebrick insulation (1), steel (2), and ceramic external insulation (3).
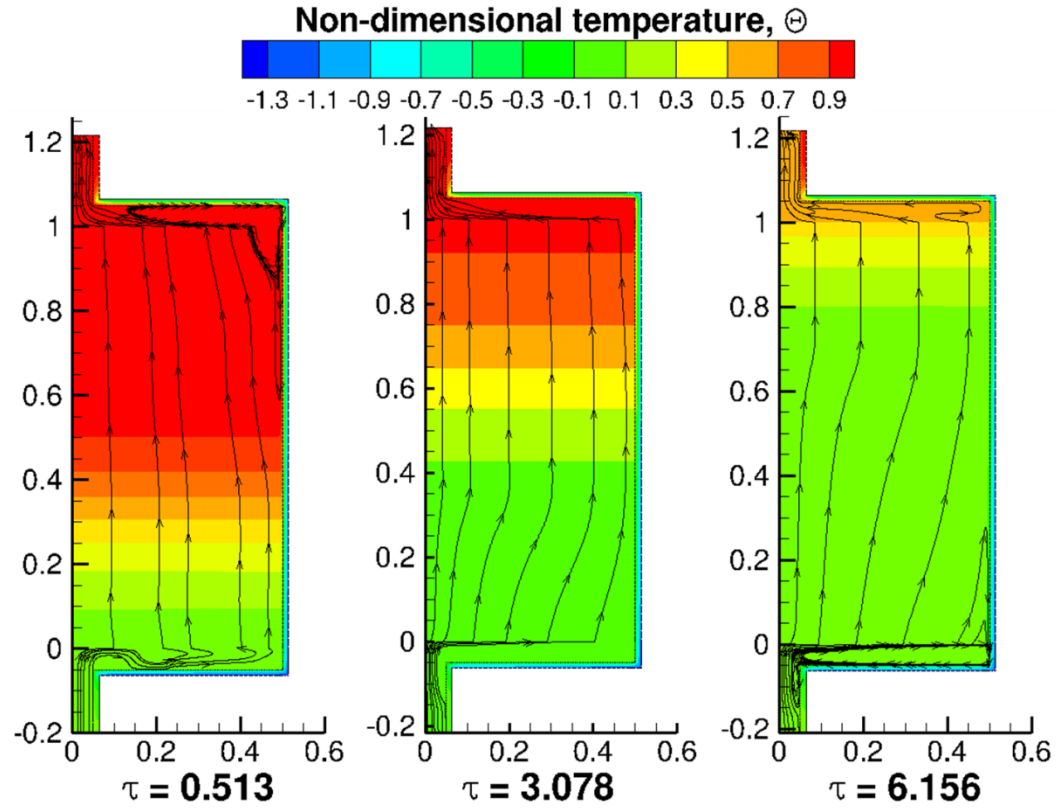
Figure 4.2. Nondimensional temperature contours and flow streamlines of the case 1 thermocline tank at early ($\tau = 0.513$), midpoint ($\tau = 3.078$), and end ($\tau = 6.156$) stages of the discharge process.
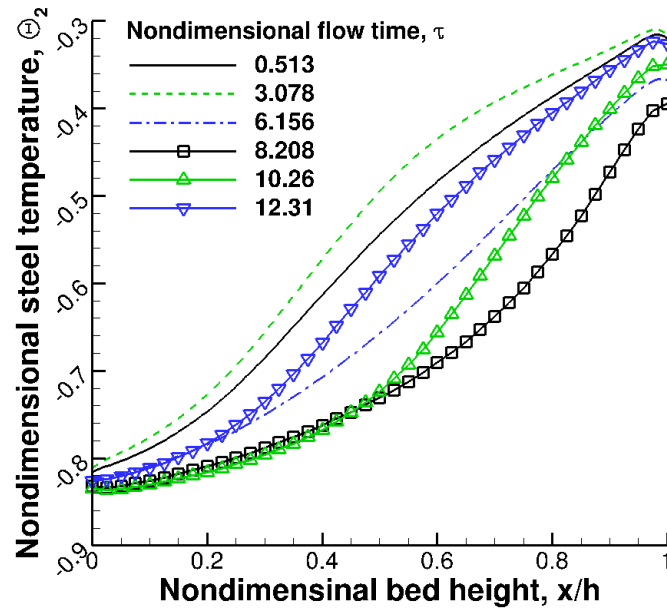
Figure 4.3. Nondimensional temperature profiles along the steel layer of the composite thermocline tank wall for case 1. The periodic temperature response corresponds to the cyclic charging and discharging of the thermocline tank with hot and cold molten salt.
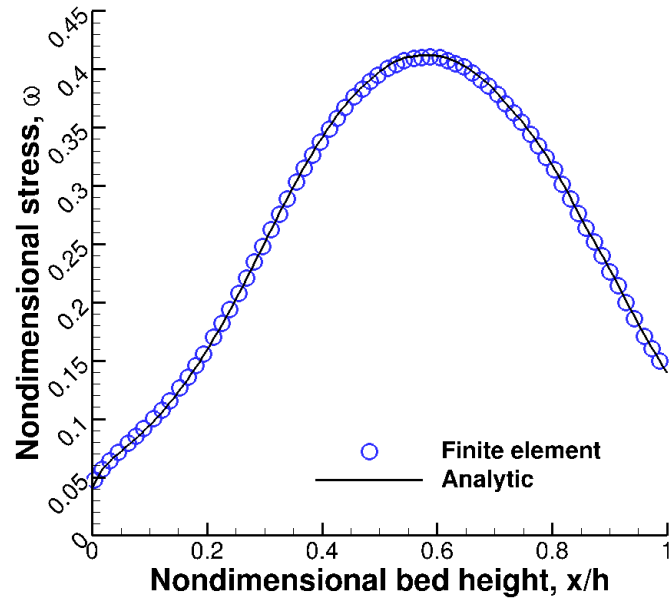
Figure 4.4. Maximum hoop stress predictions along the thermocline tank steel layer for case 1. Stress is determined with both finite element analysis and analytic stress relations and exhibits good agreement between methods.
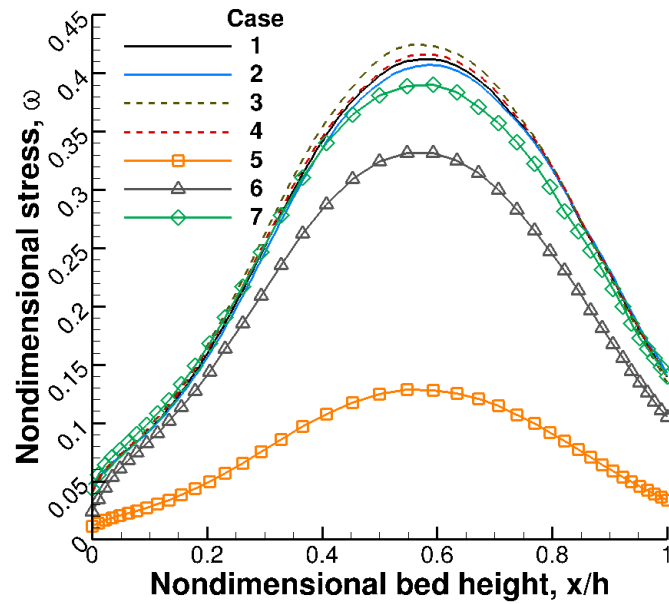
Figure 4.5. Maximum hoop stress predictions along the thermocline tank steel layer for all seven cases. The lowest stress profile is observed with case 5, which includes the thickest amount of internal thermal insulation between the steel layer and tank interior.
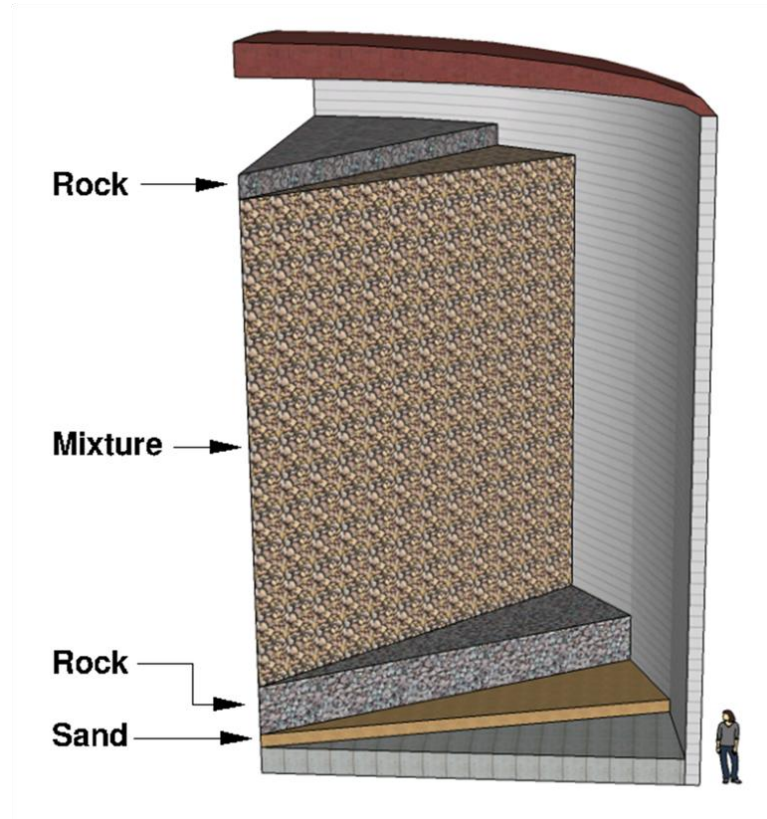
Figure 4.6. Cutaway representation of the 182 MWh$_t$ thermocline tank operated at the Solar One power tower plant. The porous bed was composed of monodisperse layers of rock and sand as well as intermediate layer of mixed rock and sand.
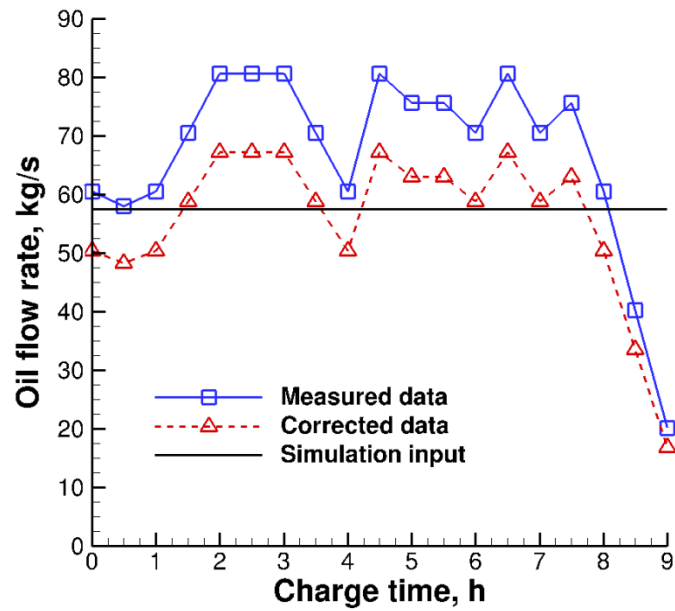
Figure 4.7. Mass flow rate of Caloria HT-43 mineral oil during a thermocline tank charge process. A 20% reduction in the measured data is needed to correct for system biases. For simplicity, the tank simulation assumes a fixed flow rate corresponding to the time average of the corrected data.
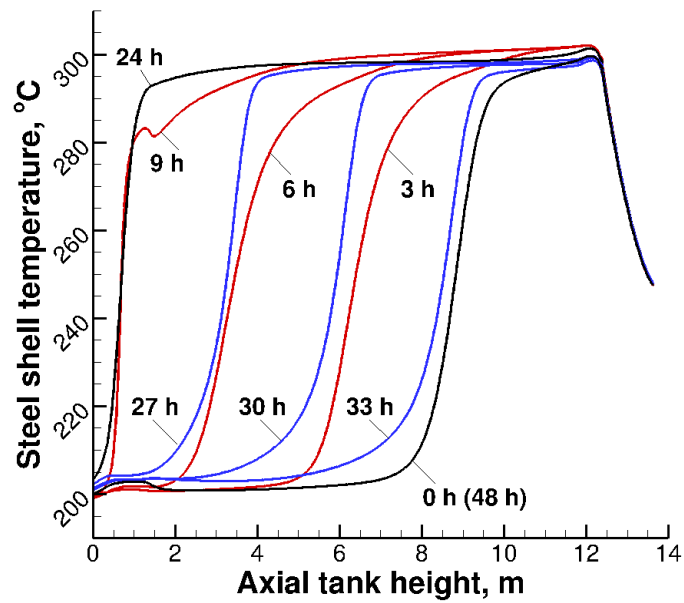
Figure 4.8. Steel wall temperature profiles observed throughout the simulated 48-hour storage cycle. The largest temperature variation (between 0.5 and 9 m) corresponds to the travel path the heat-exchange region inside the thermocline tank.
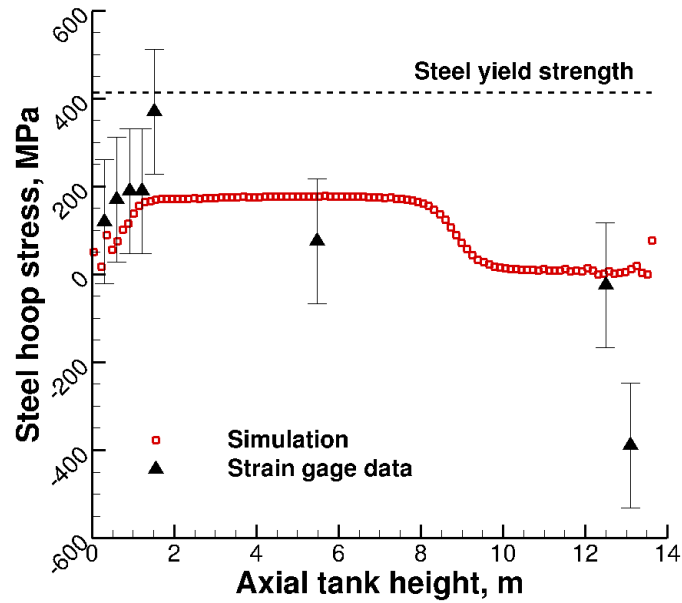
Figure 4.9. Hoop stress along the Solar One thermocline tank wall, including reported strain gage measurements and model predictions. Both datasets are below the yield strength of the steel (represented by the dashed line), indicating the ratcheting phenomena did not occur along the tank wall.

CHAPTER 5. SYSTEM-LEVEL SIMULATION OF A CONCENTRATING SOLAR POWER PLANT WITH THERMOCLINE ENERGY STORAGE

Material in this chapter was published in *Applied Energy* [77].

5.1   Introduction

Comparison of the thermocline tank simulations in the preceding chapters along with other models presented in the literature illustrates a persistent tradeoff between model complexity and computing cost. Tank analysis performed with computational fluid dynamics software [47–51,58,69] provides comprehensive and multidimensional solutions, but require long calculation times. In contrast, simplified energy transport models derived from the Schumann equations [40,44] can be solved quickly, but may sacrifice some amount of accuracy. These past modeling efforts have also been limited to a device-level analysis where charge and discharge processes are governed by arbitrary and idealized flow conditions. In actuality, control of a thermocline tank is informed by the immediate sunlight conditions and surrounding CSP plant infrastructure.

The following chapter addresses the above deficiencies with a new user-generated thermocline tank model that is both comprehensive and computationally inexpensive. The model is first validated against published experimental data and then integrated into a system-level simulation of a molten-salt power tower plant. This system model serves to govern the thermocline tank in response to realistic solar collection and power production. Solar collection is itself informed by an entire meteorological year of recorded sunlight data. Plant capacity factor and thermocline storage effectiveness are monitored throughout the simulated year to assess the influence of the thermocline tank on power production as well as long-term sustainment of thermal stratification inside the tank.

5.2   Thermocline Tank Model

A diagram of the molten-salt thermocline tank is illustrated in Figure 5.1. The tank is operated with a commercial molten nitrate salt mixture (60 wt.% $NaNO_3$, 40 wt.% KNO_3) as the heat transfer fluid. The salt is liquid above 220 °C; however, the enforced operating range is 300 – 600 °C to avoid inadvertent salt freezing in the plant infrastructure. This temperature span exceeds that of current power tower plants, which operate between 290 °C and 565 °C, but is assumed to be achievable through advancements in solar receiver performance. Physical properties of the salt in the liquid phase are known functions of temperature (degrees Celsius) [78,79]:

$$\rho_l = 2090 - 0.636 T_l \tag{5.1}$$

$$k_l = 0.443 + 1.9 \times 10^{-4} T_l \tag{5.2}$$

$$\mu = 0.022714 - 1.20 \times 10^{-4} T_l + 2.281 \times 10^{-7} T_l^2 - 1.474 \times 10^{-10} T_l^3 . \tag{5.3}$$

The specific heat of the molten salt is relatively constant with temperature and is approximated to have a constant value of 1520 J/kg-K. Over the operating temperature span, this value exhibits a maximum deviation of 1.7% versus reported data [79]. For the quartzite rock filler, density, specific heat, and thermal conductivity are all assumed constant: 2500 kg/m^3, 830 J/kg-K, and 5 W/m-K, respectively [47,80]. The porosity of the quartzite rock bed is fixed at 0.22 based on past experimental observation [29].

Given the inherent molten-salt density variation with temperature, a thermocline tank cannot be treated as a control volume. The liquid level inside the tank rises when the tank is filled with hot salt and falls when the tank is filled with cold salt. Therefore, an additional volume of molten salt must be maintained above the quartzite rock to prevent dryout of the porous region. Past thermocline studies in the literature have neglected the inclusion and influence of this "liquid heel" in order to achieve a tacit control volume condition for numerical simulation. In contrast, the current study includes simulation of both the porous region and the liquid heel, as discussed in the following sections.

5.2.1 Porous Region

Fluid and solid energy transport in the porous region are governed by the following conservation equations:

$$\frac{\partial\left[\varepsilon\rho_l C_{p,l}\left(T_l - T_c\right)\right]}{\partial t} + \nabla\cdot\left[\rho_l \mathbf{u} C_{p,l}\left(T_l - T_c\right)\right] = \nabla\cdot\left(k_{eff}\nabla T_l\right) + h_i\left(T_s - T_l\right) \tag{5.4}$$

$$\frac{\partial\left[\left(1 - \varepsilon\right)\rho_s C_{p,s}\left(T_s - T_c\right)\right]}{\partial t} = -h_i\left(T_s - T_l\right). \tag{5.5}$$

Spatial discretization of the filler region is neglected as the temperature in each solid rock is assumed to be homogeneous. Thermal diffusion between the solid filler rocks is also assumed to be negligible due to inter-particle contact resistance. However, thermal diffusion in the fluid region is influenced by the rock and is represented with the Gonzo [60] correlation for effective thermal conductivity, Eq. (3.4). The energy transport equations are also couple by interstitial forced convection between the molten salt and quartzite rock. The associated convection coefficient is determined with the Wakao and Kaguei [63] correlation, Eq. (3.12).

For simplification, the thermocline tank is assumed to be well-insulated and to experience laminar and plug flow throughout the filler bed (*i.e.*, any maldistribution of molten salt entering from the tubing manifolds is negligible). As a result, Eq. (5.4) reduces to a one-dimensional formulation along the axial direction. The molten-salt and solid filler temperatures are also normalized with respect to the hot and cold temperature limits:

$$\Theta = \frac{T - T_c}{T_h - T_c}. \tag{5.6}$$

Energy transport in the porous region reduces to the following differential equations:

$$\frac{\partial\left(\varepsilon\rho_l C_{p,l}\Theta_l\right)}{\partial t} + \frac{\partial\left(\rho_l \mathbf{u} C_{p,l}\Theta_l\right)}{\partial x} = \frac{\partial}{\partial x}\left(k_{eff}\frac{\partial\Theta_l}{\partial x}\right) + h_i\left(\Theta_s - \Theta_l\right) \tag{5.7}$$

$$\frac{\partial\left[(1-\varepsilon)\rho_s C_{p,s}\Theta_s\right]}{\partial t}=-h_i\left(\Theta_s-\Theta_l\right).\tag{5.8}$$

As previously discussed, all material properties are either constant or known functions of temperature. The remaining variables include the fluid and solid temperatures as well as the fluid velocity (u) in the convection term of Eq. (5.7). With two equations and three unknowns, an additional relationship is needed to obtain a unique temperature solution. Yang and Garimella [47] reported an inherent relationship between the speed of the heat-exchange region and the velocity of the molten salt entering the porous bed:

$$v=\frac{\rho_{l,in}C_{p,l}}{\varepsilon\rho_{l,in}C_{p,l}+(1-\varepsilon)\rho_s C_{p,s}}u_{in}.\tag{5.9}$$

However, this relationship between fluid velocity and the resulting vertical shift of the heat-exchange region is not limited to the porous-bed inlet and can be reformulated for any bed location where molten-salt density and velocity are known. Eq. (5.9) is combined with an alternative formulation at an arbitrary axial location inside the bed to yield the following:

$$u_x=\frac{\varepsilon\rho_{l,x}C_{p,l}+(1-\varepsilon)\rho_s C_{p,s}}{\varepsilon\rho_{l,in}C_{p,l}+(1-\varepsilon)\rho_s C_{p,s}}\frac{\rho_{l,in}}{\rho_{l,x}}u_{in}.\tag{5.10}$$

Eq. (5.10) reveals an inherent relationship between the fluid density field and the velocity field inside the porous bed, independent of time. Thus the thermocline fluid velocity can be determined throughout the porous bed without an explicit calculation of mass or momentum conservation.

Solution to the reduced-order energy transport model in the porous bed region is obtained via a finite-volume method. The temporal term is discretized with a first-order implicit method. Spatial discretization of the convective flux term is accomplished with the quadratic flux limiter, a quasi-second-order local extrema-diminishing scheme. Picard iteration is implemented to resolve the nonlinearity in Eq. (5.7) as well as the interstitial convection coupling with Eq. (5.8). The resultant algebraic equations are then

solved at each time step with a tridiagonal matrix algorithm written in C. Iterations at each time step proceed until the nondimensional residual error reduces to less than 10^{-6}.

Under a charge process, molten salt is supplied to the thermocline liquid heel at 600 °C. A portion of this salt then enters the underlying porous bed, as explained in the next section. Cold liquid exits the bottom of the tank, and is solved for with an outflow boundary condition. In the discharge process, the salt reverses direction and enters the bottom of the bed at 300 °C. An outflow condition is again used to solve the corresponding exit of hot salt from the top of the porous bed into the liquid heel. Thermal diffusion between the porous bed and liquid heel is represented with a Dirichlet boundary condition informed by the instantaneous heel temperature, as discussed in the next section. As previously stated, the tank top and side walls are assumed to be well-insulated and adiabatic. For simplicity, the bottom of the porous region is also assumed to be adiabatic.

5.2.2   Liquid Heel

Variations in molten-salt density with temperature generate the potential for dryout of the thermocline porous bed. Dryout must be avoided during storage operations as it would reduce the available energy storage capacity of the granular bed and may also inhibit extraction of hot molten salt from the tank. A liquid heel is therefore maintained at the top of the thermocline tank to prevent dryout of the underlying porous region. In reality, the sigmoid temperature profile along the height of the porous region will extend into this additional volume when the tank approaches a fully-discharged state. However, the height of the heel is not fixed and varies in response to the internal energy content of the tank, prohibiting straightforward analysis with a finite-volume approach. As a conservation approximation, the liquid heel is instead assumed to be an isothermal mass. The mass and energy of the heel are known at each time step as an outcome of the porous region model and surrounding CSP component models, discussed in later sections. The mean temperature of the heel is then calculated from the molten-salt specific heat:

$$T_{heel} = T_c + \frac{E_{heel}}{m_{heel}C_{P,l}} .$$
<div align="right">(5.11)</div>

This heel temperature informs not only energy transport with the underlying porous region but also represents the temperature of salt available for steam generation in the CSP plant power block.

5.2.3   Model Validation

The accuracy of the thermocline tank model is verified by comparing predicted results for a 2.3 MWh$_t$ molten-salt tank constructed by Sandia National Laboratories against experimental measurements [29]. The tank measured 6.1 m in height and 3 m in diameter, filled with a mixture of quartzite rock and silica sand to a bed height of 5.2 m. The bed porosity was reported to be 0.22. The measured temperature distribution in the tank during a two-hour discharge process is plotted in Figure 5.2. The authors did not report a molten-salt flow rate or an initial temperature condition, which are needed inputs to a simulation of the tank. However, the heat-exchange region plotted in Figure 5.2 is observed to travel up the thermocline tank at a rate of 2 m per hour. Using Eq. (5.9), this travel rate for the heat-exchange region corresponds to cold molten salt entering the porous bed at a velocity of 0.436 mm/s. A linear curve is then fit to the heat-exchange region of earliest measured temperature profile plotted in Figure 5.2 to provide an initial temperature condition.

With this estimated inlet velocity and initial temperature profile, the tank discharge is simulated, and the predicted molten-salt temperatures are included in Figure 5.2 for comparison with the experimental data. This simulation is performed both with the established CFD model developed in a prior study [47] and with the reduced-order finite-volume model described in the sections above. The internal filler is approximated as a bed of quartzite rock with an effective diameter of 1.5 cm. The reduced-order model is discretized with an axial cell length (Δx) of 2.2 cm and a time step (Δt) of 3 seconds. Temperature results with a finer cell length and time step of 1.1 cm and 2 seconds, respectively, agreed with the coarser discretization to within 0.3% and verified grid

convergence. The molten-salt temperature results for both CFD and reduced-order thermocline modeling approaches are included in Figure 5.2. The instantaneous temperature profiles are seen to exhibit good agreement with the reported data throughout the entire two-hour discharge operation. As previously stated, temperature in each solid rock is assumed to be homogeneous (*i.e.*, a lumped capacitance). The validity of this assumption is indicated by the Biot number of the quartzite rock:

$$\text{Bi} = \frac{h_i d_s}{6 k_s} = \frac{\text{Nu}_i}{36(1 - \varepsilon)} \frac{k_l}{k_s}. \tag{5.12}$$

During the 2-hour discharge, the rock exhibits a maximum Biot number of 0.139. While this value exceeds the conventional limit of 0.1 for lumped capacitance, it should be noted that the local thermal non-equilibrium between molten-salt and quartzite is on the order of 1 K. Given that the overall temperature span of the thermocline tank is greater than 100 K, lumped capacitance is an acceptable assumption for the solid region.

It should be also noted that simulation with the reduced-order model is two orders of magnitude faster than the CFD model and did not require the use of a commercial software package. With a validated and low-cost model, study of the thermocline tank is now extended to the system level, in order to investigate the storage performance in response to actual sunlight data and typical solar power plant operation.

5.3   Molten-salt Power Tower Plant Model
5.3.1   Steam Rankine Cycle

As previously mentioned, existing CSP plants achieve power production with a traditional steam Rankine cycle. Hot molten salt generates the necessary superheated steam through a series of heat exchangers (preheater, evaporator, and superheater). In the current study, the steam then travels through a Rankine cycle composed of a non-reheat turbine and a single open feedwater heater for deaeration of the working fluid. The design, illustrated in Figure 5.3, is taken from the power block operated at the Solar Two power tower plant [26].

At nameplate or rated conditions, superheated steam enters the turbine at a temperature and pressure of 538 °C and 125 bar (12.5 MPa), respectively (state 1). A portion of the steam (y) exits the first turbine stage and is sent to the feedwater heater at an intermediate pressure while the remaining steam enters a second turbine stage (state 2). The steam exiting this turbine (state 3) is condensed across the vapor dome at 0.1 bar (10 kPa) and exits the condenser as saturated liquid (state 4). This saturated liquid is then pumped into the feedwater heater (state 5) and mixes with the first turbine stage exhaust. The mixture exits the feedwater heater as saturated liquid (state 6) and is again pumped to 125 bar (state 7). The water then enters the molten-salt heat exchangers and returns to the turbine inlet state as superheated steam. Pressure drops across the various heat exchanger elements are assumed to be negligible. Figure 5.4 shows the corresponding temperature-entropy diagram for the rated cycle operation. The turbine and pump machinery are both assumed to exhibit an isentropic efficiency of 0.9 at rated load, resulting in a gross first-law cycle efficiency of 41.2%. Parasitic power consumption within the solar plant requires an overdesign of the power block, fixed at 10.3% for the current study [81]. Therefore, a desired net work output of 100 MW_e requires a gross output of 111.5 MW_e and a corresponding heat input of 270.9 MW_t for steam generation.

In addition to the rated performance, the combination of the Rankine cycle with a molten-salt thermocline tank also allows for derated operation in response to any salt delivered from the tank at temperatures below the hot design limit of 600 °C. This reduction in exergy is carried through the corresponding steam generation and reduces the turbine inlet temperature. Power production is sustained so long as the thermodynamic cycle adjusts in response to the decrease in steam quality. Known as sliding-pressure operation, the cycle mass flow rates and pressures are both lowered to accommodate the reduced turbine temperature in this mode of operation, explained as follows.

The pressure drop across each of the turbine stages exhibits the following relationship with variable mass flow rate [82]:

$$\frac{\dot{m}^2}{\dot{m}_0^{\,2}} = \frac{p_{in}^{\,2} - p_{out}^{\,2}}{p_{in,0}^{\,2} - p_{out,0}^{\,2}} \tag{5.13}$$

where $p_{1,0}$ and $p_{2,0}$ are the turbine pressures at rated conditions. The isentropic efficiencies of the turbine and pump machinery are also influenced by off-peak performance. Spelling *et al.* [83] characterized the derated turbine efficiency as a function of turbine speed and enthalpy change:

$$\eta_{turb} = \eta_{turb,0} - 2\left(\frac{\omega_{turb}}{\omega_{turb,0}} \sqrt{\frac{\Delta h_{s,0}}{\Delta h_s}} - 1 \right)^2 . \tag{5.14}$$

Both turbine stages are assumed to be constant speed in the current study. For the pump performance, Lippke [82] reported the following relationship between efficiency and mass flow rate:

$$\frac{\eta_p}{\eta_{p,0}} = 2\frac{\dot{m}_p}{\dot{m}_{p,0}} - \left(\frac{\dot{m}_p}{\dot{m}_{p,0}} \right)^2 . \tag{5.15}$$

Additional assumptions are necessary to solve the remaining cycle state points for derated operation. The condenser pressure is constrained to 0.1 bar (10 kPa) for all cycle conditions. Water always exits the condenser and feedwater heater as saturated liquid. The amount of superheat at the turbine inlet is assumed to remain fixed at 210 K. The preheater also maintains a fixed inlet temperature of 230 °C via recirculation of saturated liquid ($x = 0$) from the evaporator. Under these constraints, the entire derated cycle is solved with a user-generated MATLAB script, provided in Appendix G. Shutdown occurs when the derated operation reduces to 30% of the rated gross output, 33 MW$_e$. The steam turbine inlet temperature associated with this minimum derated condition is 463 °C. The corresponding temperature-entropy diagram is included in Figure 5.4. The assumption of a fixed turbine superheat results in an increase in steam quality at the exit of the second turbine stage from 0.842 at rated output to 0.890 at the 30% output limit.

5.3.2   Steam Generation

As stated in the previous section, generation of steam with hot molten salt occurs by means of three heat exchangers: a preheater, evaporator, and superheater. At design conditions, molten salt enters the superheater at 600 °C and exits the preheater at 300 °C. Water enters the preheater at 230 °C, converts to steam in the evaporator at 328 °C, and exits the superheater at 538 °C. The overall heat transfer coefficients for these heat exchangers are taken from the Solar Two power block [26] and are listed in Table 5.1. The individual thermal power required for each component is determined from the water vapor dome, and is also included in Table 5.1. The design surface area for the preheater and superheater are then determined from the log mean temperature difference (LMTD). For the heat exchanger with fluid streams undergoing phase change, *i.e.*, the evaporator, the design surface area is determined using the NTU method. Discussion of these methods is provided in [76]. Figure 5.5 shows the temperature response of the molten salt and steam inside each of the heat exchangers as a function of the available surface area.

For derated operation at reduced temperatures, the overall heat transfer coefficient for each heat exchanger becomes a function of the adjusted molten-salt and steam mass flow rates [84]:

$$\frac{U}{U_0} = \left(\frac{\dot{m}_l}{\dot{m}_{l,0}}\right)^{0.8} \left(\frac{\dot{m}_{wat}}{\dot{m}_{wat,0}}\right)^{0.8} \left(\frac{\dot{m}_{l,0}{}^{0.8} + \dot{m}_{wat,0}{}^{0.8}}{\dot{m}_l{}^{0.8} + \dot{m}_{wat}{}^{0.8}}\right). \tag{5.16}$$

The plant model also allows molten salt exiting the preheater at 300 °C to recirculate upstream of both the superheater and the evaporator to prevent flow of any saturated mixture outside the evaporator. A plot of the temperature response for 30% derated turbine output is included in Figure 5.5. The hot molten-salt temperature necessary for this minimum output is 473 °C; thus any molten salt below this temperature is not utilizable for power production and will not be discharged from the thermocline tank. It should also be noted that the required preheater surface area must decrease to sustain the desired exit salt temperature of 300 °C during derated operation. This variable area could be implemented in practice with a shell and tube heat exchanger that includes a tubing

manifold. For derated operation, valves in the manifold close a select number of tubes within the heat exchanger and reduce the surface area available for convection.

For combination with the thermocline tank model, the heat exchanger and Rankine cycle models are simplified with polynomial expressions determined from linear regression. These expressions are algebraic relationships between the molten-salt hot supply temperature, molten-salt flow rate in the steam generators, and the gross turbine output power, W (when salt available from the thermocline tank is above 473 °C). The polynomial curve fits obtained from linear regression are listed below, and are specific to the current problem statement:

$$\frac{W}{W_0} = -1.706(\Theta_{heel})^3 + 4.406(\Theta_{heel})^2 - 2.031(\Theta_{heel}) + 0.3307 \qquad (5.17)$$

$$\frac{\dot{m}_{HX}}{\dot{m}_{HX,0}} = -0.5976(\Theta_{heel})^3 + 0.399(\Theta_{heel})^2 + 1.431(\Theta_{heel}) - 0.2325 . \qquad (5.18)$$

The temperature of the molten-salt liquid heel inside the thermocline tank (from which hot salt is delivered to the steam generators) therefore determines both the gross turbine output power and required mass flow rate of molten salt in the power block.

Prior to any daily turbine output being achieved, both the steam generators and the turbine must be conditioned for power production through a multistage process known as startup. This includes warming of the heat exchangers, synchronization of the turbine with the generator, and ramp-up to rated gross output. During the heat exchanger warming and turbine synchronization stage, the thermocline tank supplies hot molten salt to the power block in an amount equivalent to the minimum thermal input (30% load), but with no work output. After synchronization is complete, the turbine initiates power production with a linear ramp-up to rated operation.

The required time intervals for these actions are dependent on the initial turbine temperature, which is itself a function of the length of time since the previous shutdown [85]. For simplicity, this temperature is classified under three states – hot, warm, and cold. The turbine is designated as hot for up to 12 hours after a shutdown, after which it

degrades to a warm condition. After 72 hours of shutdown, the turbine further degrades to a cold condition. Table 5.2 lists the process times for each turbine temperature state.

5.3.3 Solar Collection

For the current study, concentrating and harvesting of direct sunlight is assumed to be performed with a central receiver or power tower design. A field of dual-axis heliostats follows the position of the sun and reflects the direct normal irradiance (DNI) onto an elevated receiver. From the thermocline tank, molten salt enters the receiver at 300 °C and exits at 600 °C. The corresponding mass flow rate of molten salt is then a function of the power incident on the receiver. In reality, some fluctuation in the exit temperature does result from the lag in the adjustment of the mass flow rate with varying DNI. However, these events were brief due to a combination of temperature feed-back control and irradiance feed-forward control [26] and are omitted from the present system study.

Both the heliostat field and solar receiver are sized with DELSOL [81], a power tower design tool developed by Sandia National Laboratories. For a user-defined solar multiple (ratio of sunlight collected at noon on summer solstice relative to the rated thermal input to the power cycle) and solar receiver shape, DELSOL solves for the optimum heliostat field and then computes the corresponding solar collector efficiency as a function of solar position (see Appendix G). The current study constrains the individual heliostat size to a height of 9.93 m and a reflection surface area of 95.45 m^2, default values in DELSOL. For a solar multiple of 2.3, the corresponding heliostat field solution includes 1,170,000 m^2 of reflector area surrounding a tower of height 194.7 m. The solar receiver atop this tower is an external receiver design with a diameter of 21 m and a height of 18 m, rated to a maximum thermal power of 623 MW_t.

Transient simulation of the solar receiver is performed with SOLEGY [86], a power tower performance model also developed by Sandia National Laboratories. A year-long dataset of direct sunlight serves as input to the model. The current study applies DNI measurements recorded near Barstow, CA at 15-minute intervals from January 1 to December 31 of 1977. This selected dataset is attractive for its excellent

annual insolation of 2700 kWh$_t$/m^2, high granularity, and prior application in other power tower studies [85]. At each 15-minute interval, SOLERGY calculates the current solar collector efficiency and then solves for the thermal power absorbed by the molten salt traveling through the solar receiver (see Appendix G). The receiver is simulated for the entire year of operation, independent of the thermocline tank and power block systems. The mass flow rate varies in response to the collected thermal power such that exiting salt temperature is maintained at 600 °C:

$$\dot{m}_{rec} = \frac{P_{rec}}{C_{P,l}\left(T_h - T_{rec,in}\right)}.$$
(5.19)

The solar receiver inlet temperature is governed by the mixture of salt exiting both the thermocline tank and power block heat exchangers.

5.3.4   Model Integration

In the current study, the molten-salt thermocline tank is desired to provide the power tower plant with six hours of thermal energy storage. The maximum energy capacity of the tank should clearly exceed this condition to accommodate simultaneous containment of salt at cold and transitional temperatures. Sizing of the storage system is informed by a previous design study of thermocline tanks by the Electric Power Research Institute [25], which applied an approximate overdesign of 40% for the tank volume. The study also concluded that the molten-salt liquid level should not exceed 39 feet (11.9 m) to stay within the maximum bearing capacity of the soil with a typical foundation. The height of the model quartzite bed is therefore fixed to 11 m to provide additional volume for the liquid heel above the bed. With the given energy densities of the molten salt and quartzite rock, a thermocline tank diameter of 36.3 m is required to satisfy the requisite energy capacity and volumetric overdesign. The effective diameter of the quartzite rock granules inside the tank is assumed to be 1 cm [58].

The three component models (solar collection, thermocline tank, and power block) are integrated to generate a system model of a 100 MW$_e$ power tower plant and interact as follows. During daylight hours, sunlight is concentrated onto the solar receiver as

previously simulated by SOLERGY. Molten salt absorbs this radiation as sensible heat and is then delivered to the thermocline tank heel. When the tank contains enough energy to sustain two hours of steam generation in the plant heat exchangers, hot salt is sent from the tank heel to the power block to initiate turbine startup. After startup is complete, the turbine is conditioned for rate power production. Cold salt exiting the power block either returns to the solar receiver or to the bottom of the tank, as dictated by mass balance in the solar collection loop.

It is again noted that no provision for a bypass loop is included between the solar receiver and the power block, and all heat and mass transport in the power plant is routed through the thermocline tank. The thermocline tank operating condition (charge, discharge, or standby) and corresponding salt flow direction is therefore dependent on the immediate disparity in molten-salt mass flow rate between the power block, Eq. (5.18), and the solar receiver, Eq. (5.19). For example, when the receiver provides hot salt at a faster rate than is necessary in the power block, the thermocline tank is charged with the excess. Conversely, when the power block requires more flow than the amount provided by the receiver, the tank undergoes a discharge to make up the difference. A standby condition with stagnant molten salt (*i.e.*, no net flow inside the porous bed) occurs when the discharging tank is depleted of all usable energy.

For prolonged charge processes, the salt exiting the bottom of the thermocline tank will begin to increase in temperature as the transitional heat-exchange region reaches the tank floor. This exiting warm salt also generates a temperature increase at the solar receiver inlet, then resulting in a proportional mass flow rate increase to maintain an exit hot temperature of 600 °C, governed by Eq. (5.19). However, cold salt exiting the bottom of the thermocline tank is limited to a maximum allowable temperature of 400 °C to prevent both overcharging of the storage system and overheating of the solar receiver. At this exit temperature, the thermocline tank is declared to be at energy capacity and transitions to a forced standby condition. With no more available storage, the solar receiver can only collect enough energy to satisfy the Rankine cycle steam generation. Heliostats are defocused away from the receiver and some amount of sunlight available for collection must be forgone: this amount of energy is known as thermal energy discard.

The forced tank standby persists until the solar receiver power output decays near sunset and the energy-saturated tank can then be discharged to sustain the rated power production.

Under ideal clear sky conditions on a given day, the thermocline tank would energize to its capacity, go into standby, and finally discharge near sunset following shutdown of the solar receiver. In reality, random cloud transients will lead to sporadic DNI losses during daylight hours. Therefore additional care must be taken in the operation of the thermocline tank to avoid chaotic flow direction changes and consequent wear on the turbine. In the operation considered in the current study, dispatch of hot molten salt from the thermocline tank to the power block is prohibited until the turbine is guaranteed to operate for at least two hours. Prior to turbine startup, the system model checks both the energy content of the tank as well as receiver performance in the immediate future (already known from the SOLERGY solution) to ensure that this condition on the turbine is satisfied. The authors assume that in practice, plant operators are capable of making similar near-term receiver predictions from weather forecasts. As a result, rapid on-off toggling of either the thermocline tank or the Rankine cycle is avoided.

5.4   Results and Discussion
5.4.1   Power Tower Plant

At the onset of the power plant simulation, the thermocline tank fillerbed and liquid heel are both initialized to the cold molten-salt temperature limit of 300 °C. The fillerbed geometry is discretized with a cell length of 2.2 cm (500 cells) and a time step of 3 seconds; grid independence at this resolution was already verified with the previous simulation of a small-scale thermocline tank. As stated before, the performance of the heliostat field and solar receiver is first simulated in SOLERGY using a meteorological year of sunlight data reported near Barstow, CA. The amount of thermal power collected by the solar receiver then serves as an input to the integrated thermocline tank and power

block models for each time step of simulation. This integrated system model is solved with a user-generated C script, provided in Appendix G.

Simulation of the assembled power tower plant yields a complete year of performance data. A subset of this year-long operation is plotted in Figure 5.6, including results for the solar receiver power, thermocline energy storage, and gross turbine output for five days centered on the summer solstice, June 19 to 23. The daily plant behavior represented in the figure is explained as follows. After sunrise, the heliostat field and solar receiver activate and the collected solar power increases from zero. This initial heat collected is sent to the thermocline tank. When the stored energy inside the tank is sufficient for steam generation, the power block undergoes startup procedures, after which the turbine reaches its rated output. As the day progresses, the collected power increases to the 623 MW_t rating of the solar receiver, with the excess energy collected being sent to the thermocline tank. Close to sunset, the receiver power begins to decrease until the solar collection system must shutdown for the night. The thermocline tank is then discharged to sustain turbine output into the night. When the thermocline tank energy nears depletion, colder molten salt is supplied to the steam generators and the turbine transitions to derated output until an eventual shutdown.

The receiver data plotted in Figure 5.6 exhibit consistent daily performance, corresponding to minimal cloud influence for the selected days. A cloud transient did occur on day 172 of the year, indicated by noise in the receiver power near sunset and an early turbine shutdown relative to the other days. Also of interest is the repeated step decrease in the receiver power that occurs near sunset for the other days plotted in the figure. This reduction occurs when the solar receiver has collected enough excess thermal energy to saturate the thermocline tank, marked by molten salt exiting the bottom of the thermocline tank at 400 °C. The tank goes into standby and the solar receiver can only collect thermal energy for steam generation, deviating from the receiver performance predicted by SOLERGY. This deviation quantifies the amount of thermal energy lost due to the lack of additional storage capacity. It should be noted that an economically optimized plant may have a storage system which discards some energy during the peak of the summer, but is heavily utilized during the rest of the year.

For a seasonal perspective, the plant capacity factor is calculated for each month and plotted in Figure 5.7. Capacity factor (CF) is the ratio of total turbine output over time to the theoretical maximum corresponding to constant output at rated load:

$$CF = \frac{1}{W_0 t_0} \int_0^{t_0} W(t) dt \, . \tag{5.20}$$

Monthly capacity factor is largest in the summer due to the seasonal variation in DNI available for collection, with a maximum value of 0.696 observed for July. With respect to the entire year, the power tower plant generates a total net output of 465.4 GWh$_e$ and exhibits an annual capacity factor of 0.531. The overall solar-to-electric efficiency of the power tower plant is defined as the ratio of the net work output to the theoretical maximum amount of sunlight collected (annual solar resource × total heliostat area), and achieves a value of 0.147.

The contribution of the thermocline tank to plant performance is observed by repeating the simulation of the power tower plant without a thermal energy storage system. The corresponding monthly capacity factors without storage are included in Figure 5.7. As expected, absence of energy storage results in a significant drop in monthly capacity factor relative to the case with a thermocline tank. Year-long operation without storage reduces the annual capacity factor to 0.273 from 0.531 and the solar-to-electric efficiency to 0.076 from 0.147. The simulated thermocline tank was able to store over eight hours of useable heat during operation, which exceeded the originally desired six hours of storage. Thus the 40% overdesign for the tank size applied from the EPRI design study is shown to be larger than necessary, under the assumptions of the present work.

5.4.2   Thermocline Tank

While the capacity factor reveals the impact of the thermocline tank over time, the usefulness of the thermal energy that passes through the storage subsystem for steam generation is quantified by the storage effectiveness, defined as the ratio of utilizable heat delivered from the tank to the maximum heat available:

$$\varepsilon_{tank} = \frac{\int \dot{m}_{HX} \, C_{P,l} \left(T_{heel} - T_c \right) dt}{\int P_{rec} \, dt + E_{init}} \, .$$

(5.21)

Utilizable heat refers to the available molten salt at sufficient temperature (exergy) for steam generation. The maximum available heat is the total amount of thermal energy delivered to the tank as hot molten salt from the solar receiver plus the initial energy content inside the tank. The monthly storage effectiveness values are plotted in Figure 5.8. The effectiveness remains above 99% throughout the year, indicating that over 99% of thermal energy delivered to the tank from the solar receiver each month is later recovered for steam generation.

The excellent effectiveness of the thermocline tank is attributed to the regular (daily) and consistent use of the stored energy during operation, as indicated by the short time duration of standby periods when flow is stagnant inside the tank. During the year-long plant simulation, the tank experienced 615 separate instances of standby, of which 98.2% were less than 24 hours in duration. This indicates that the tank was operated either in charge or discharge mode on a daily basis throughout the meteorological year. The benefit of this daily operation is a limited residence time of hot molten salt inside the thermocline tank, mitigating the extent of thermal diffusion between the hot salt and the underlying cold salt. Thus for the diurnal cyclic behavior of thermoclines in solar plants, factors that would be detrimental to maintaining thermal stratification inside the tank and would inhibit storage performance over long-term application were found not to play a significant role over the chosen year with the DNI data for Barstow, CA. The thermocline tank is therefore concluded to be a viable thermal energy storage option for use in a solar power plant under such conditions.

The impact of the thermocline tank on power production is a function of its size and energy storage capacity. As previously discussed, thermal energy discard occurs when the thermocline tank becomes saturated with hot salt and is unable to store additional heat. Figure 5.8 includes a plot of thermal energy discarded each month, normalized with respect to the amount of sunlight available for collection. As with the plant capacity factor, thermal energy discard displays a strong seasonal dependence

corresponding to the variation of DNI received. Winter months receive the least amount of sunlight and thus do not exhibit saturation of thermocline tank on a regular basis. In contrast, summer months experience frequent saturation and exhibit the largest amount of thermal energy discard. During the year, a total of 223 days experience energy saturation of the thermocline tank. The annual thermal energy discard associated with this saturation and subsequent heliostat defocusing is 176 GWh_t or 13.7% of the total energy collected by the solar receiver.

An optimal amount of thermal energy discard likely exists for a given solar power plant and energy storage system. If storage saturation and thermal energy discard occurs on a near-daily basis, the storage volume is likely undersized relative to the solar collection system, and this reduces the potential revenue of the solar plant. On the other hand, if thermal energy discard is never observed, the storage volume may be oversized and carry an excessive capital cost. Further investigation and optimization of the thermocline tank is therefore needed to quantify trade-offs in plant cost and annual revenue as a function of tank size.

The validity of the adiabatic tank wall assumption made in the present simulation is assessed by estimating the annual heat loss relative to the total amount of energy delivered to the tank from the solar receiver. The EPRI thermocline tank design study proposed mineral wool insulation ($k = 0.2$ W/m-K) at a thickness of 23 inches (0.584 m) for high-temeprature storage tanks [25]. The annual average temperature and wind speed in Barstow, CA in 1977 were 20.1 °C and 4.94 m/s, respectively. For the maximum tank temperature of 600 °C, this external boundary condition generates an average convection heat loss of 203 kW_t through the mineral wool. The annual energy loss due to this convection is 1775 MWh_t, or 0.138% of the total hot energy supplied to the thermocline tank from the solar receiver over the year. Given this very low percentage of expected loss, the original adiabatic tank wall assumption is deemed to be acceptable.

5.4.3   System Model Comparison

In addition to solar receiver performance, thermal energy storage and power production may also be modeled in SOLERGY. It is of interest to compare the simulated plant output from the current study with predictions from SOLERGY. Table 5.3 includes the annual outputs of the 100 MW$_e$ power tower plant as predicted by the current study, along with SOLERGY results for both two-tank and thermocline storage systems of equivalent size. As seen in the table, SOLERGY predicts identical plant performance for either the two-tank and thermocline tank storage options. Comparison of the current study and the SOLERGY simulation also shows reasonable agreement, exhibiting a 2.34% difference in annual net turbine output. This difference may be attributed to the lack of molten-salt temperature control in the thermocline tank sub-model implemented in SOLERGY. In the current study, the temperature of salt leaving the bottom of the tank is limited to 400 °C to avoid compromising the heat-exchange region, but this prevents the tank from reaching its maximum energy capacity. In contrast, SOLERGY does not consider such temperature limits and thus over predicts the thermal energy storage performance in a thermocline tank. This added capacity manifests as greater power production and explains the somewhat larger annual turbine output in Table 5.3.

It should be noted that SOLERGY and the current system model both apply a sun-following control, which means the turbine is activated whenever sufficient energy is available from storage. In reality, the economic value of electricity is a function of variable time-of-day sale prices and will influence the choice of when the turbine is operational. An alternative plant control strategy would be to delay power production until the most lucrative hours of the day (*e.g.*, weekday afternoons) in order to maximize the annual revenue. However, delaying power production may then lead to an increased occurrence of storage saturation and related thermal energy discard. This potential trade-off between maximizing power production and maximizing revenue is another area of further investigation.

5.4.4   Expanded Temperature Span

Given that the present model of a CSP plant does consider molten-salt temperatures, it is also of interest to investigate the system-level influence of the defined operating temperature span. The molten-salt HTF freezes at 220 °C, thus the cold temperature limit in the previous analysis may be reduced to increase the sensible heat capacity of the salt and the thermocline tank. The present system model is therefore modified with an expanded operating span of 250 – 600 °C to identify any potential benefits. It should be noted that this expansion also alters the molten-salt flow rate inside both the solar receive and the steam generators. As before, a 100 K temperature increase is permitted at the floor of the thermocline tank before a saturation condition is triggered.

With the expanded temperature span, a similar annual plant output (464 GWh$_e$) as the original model can be achieved but with a 7.4% reduction in the thermocline tank diameter (33.6 m). This tank reduction results from the increased heat capacity of the HTF and may also carry substantial capital cost savings. However, as the cold temperature limit approaches the salt freezing point, more stringent controls become necessary to ensure solidification is averted in the CSP plant infrastructure.

5.4.5   Thermocline Structural Stability

Along with long-term thermal reliability, a thermocline tank must also exhibit structural stability in response to the repeated cycling during the charge-discharge cycles with hot and cold salt. The tank is also packed with quartzite rock; such quartz-based materials exhibit a change in crystal structure near 573 °C. As this inversion point and the corresponding volumetric expansion are within the applied molten-salt operating temperature range, heating the tank to the maximum hot temperature may lead to large hoop stresses in the surrounding tank wall. Previous structural models for thermocline tanks [69] did not operate above this critical temperature and may not be applicable. Experimental observation as well as further study of granular mechanics inside the thermocline tank is needed to ensure that the tank wall can sustain this quartzite phase change.

To increase safety, the dual-media thermocline tank concept can also be modified either with lower maximum operating temperatures or by use of alternative filler materials. Filler selection for the solid rock calls for both low cost and physical stability under repeated thermal cycling. In addition to quartzite, Pacheco *et al.* [29] reported successful application of iron ore taconite pellets with molten salt. However, physical property data for taconite are not readily available in the literature and require further study. Additional materials not considered in [29] should also be explored.

5.5   Chapter Summary

A numerical model for molten-salt thermocline tank operation has been developed to provide accurate simulation of mass and energy transport at low computing cost and without reliance on commercial CFD software. The thermal model is integrated into a system-level simulation of a 100 MW$_e$ power tower plant to assess thermocline tank performance under realistic and long-term operating conditions. Operation of the plant model is informed by a meteorological year of sunlight data recorded near Barstow, CA in 1977. The molten-salt thermocline tank, sized to provide six hours of thermal energy storage, increased the annual plant capacity factor to 0.531 with excellent year-long storage effectiveness exceeding 99%. This good performance results from the regular and consistent utilization of the stored energy in the tank during year-long plant operation, limiting the residence time of hot salt inside the tank and the corresponding loss of thermal stratification that would result. Comparison of the model developed in this work with the results from SOLERGY showed excellent agreement. The 2.34% difference observed between the results for annual turbine output is attributed to the absence of temperature control in the SOLERGY thermocline tank model, which results in over-prediction of storage performance.

Table 5.1. Heat exchanger design data for the power block steam generators.

Heat exchanger	Thermal power [MW]	U [W/m^2-K]	A_{HX} [m^2]
Preheater	57.3	1940	580
Evaporator	128	1392	1042
Superheater	85.1	911	850

Table 5.2. Power block startup times for different turbine temperature states [85].

Hours after shutdown	Turbine temperature	Warming and synchronization [min]	Ramp up [min]
<12	Hot	15	25
12 – 72	Warm	60	100
>72	Cold	110	160

Table 5.3. Comparison of annual solar receiver energy collection and net turbine output between the current study and SOLERGY for a 100 MW$_e$ power tower plant.

Model	Solar receiver [GWh$_t$]	Turbine net [GWh$_e$]
Current study	1281	465
SOLERGY (thermocline)	1326	476
SOLERGY (two-tank)	1326	476
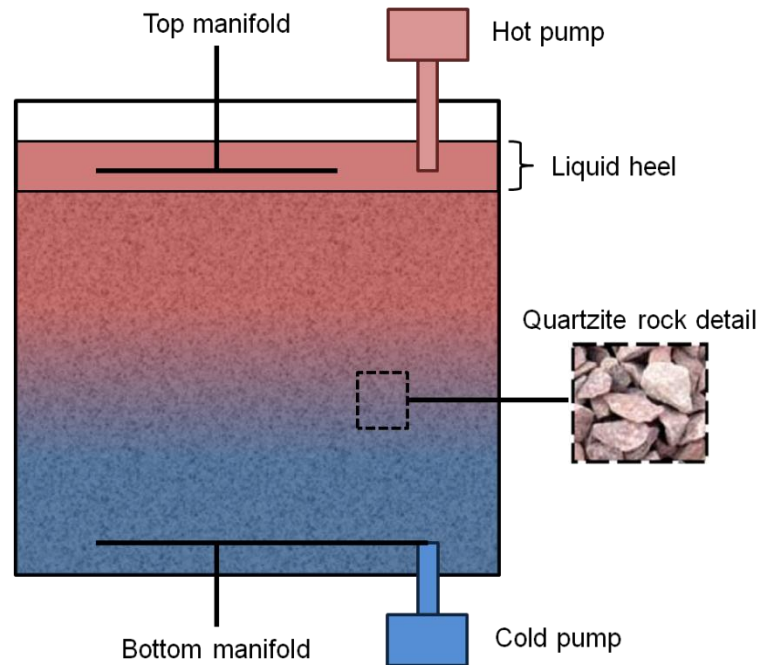
Figure 5.1. Illustration of a dual-media thermocline tank composed molten salt and quartzite rock. A liquid heel of molten salt is maintained above the bed to prevent dryout. Hot salt is supplied at the liquid heel through the top manifold and is extracted via the hot pump. Cold salt enters the porous bed through the bottom manifold but is also extracted through the manifold via the cold pump.
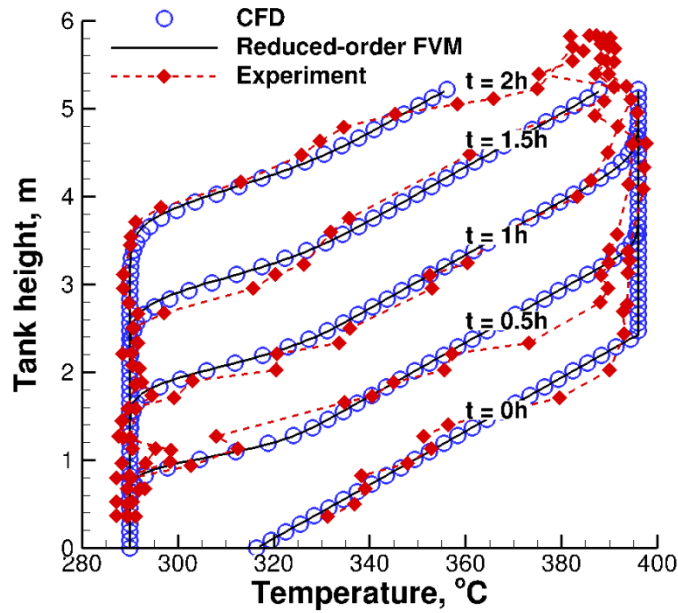
Figure 5.2. Temperature response of a 2.3 MWh$_t$ molten-salt thermocline tank undergoing discharge. Numerical simulation is performed with two separate approaches: detailed computational fluid dynamics simulation, and a reduced-order finite-volume method. Experimental temperature data reported for the tank [29] are included for model validation.
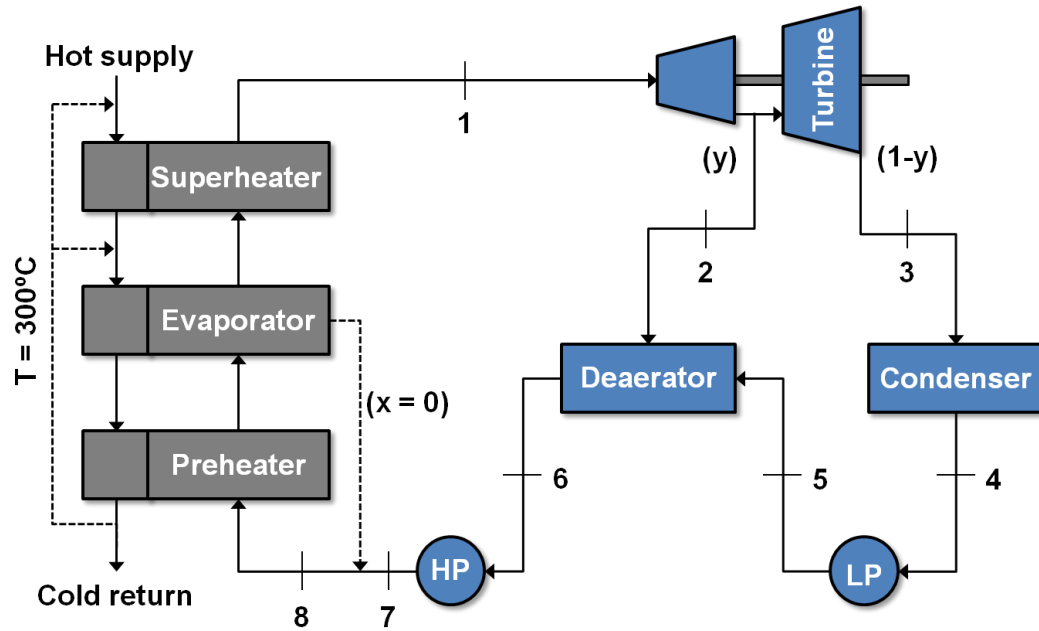
Figure 5.3. Schematic drawing of the plant steam generators and Rankine power cycle. The Rankine cycle includes a two-stage non-reheat turbine and a single open feedwater heater for deaeration of the working fluid. LP is the low-pressure pump and HP is the high-pressure pump. During power production, hot molten salt enters the superheater and exits the preheater at a cold temperature.
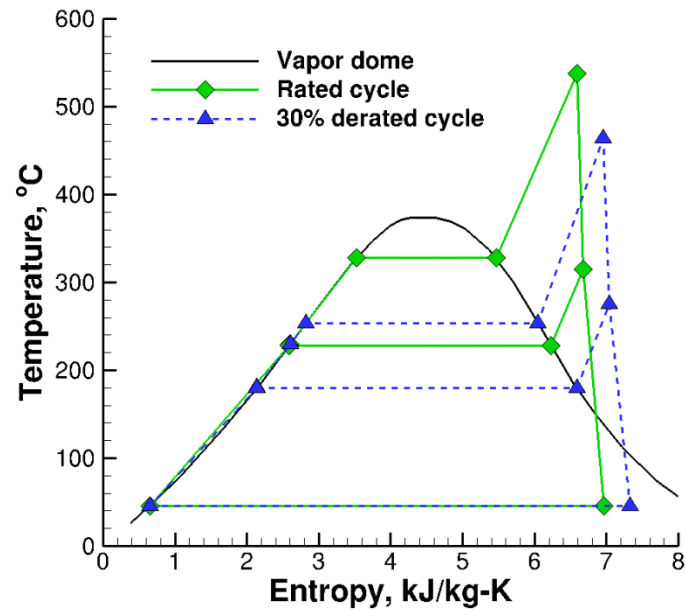
Figure 5.4. Temperature-entropy diagram of the steam Rankine cycle. The solid lines illustrate operation with at rated turbine output, while the dashed lines illustrate operation at a minimum derated operation mode of 30% gross output.
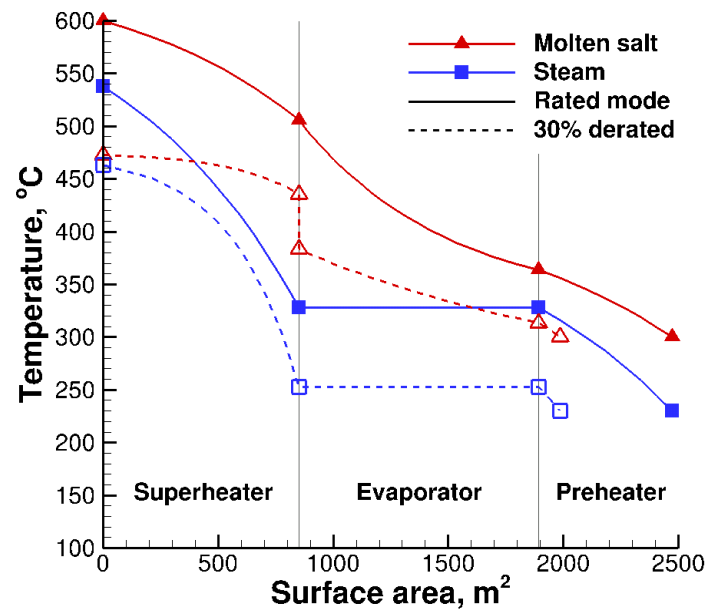
Figure 5.5. Temperature plot of molten salt and steam working fluid inside the power block heat exchangers. The solid lines illustrate the temperature response at rated output; the dashed lines illustrate the response at 30% derated operation.
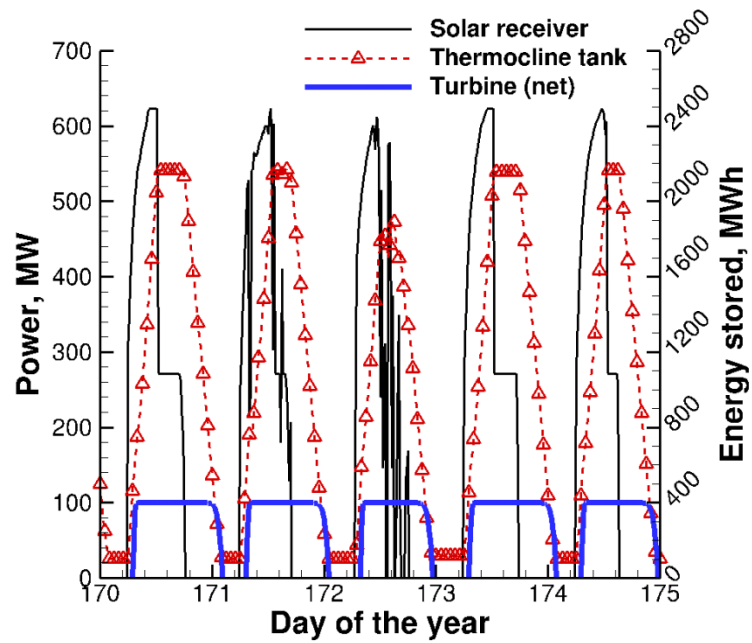
Figure 5.6. Power tower plant performance during June 19 – 23. Solar receiver power and net turbine output are plotted on the left y-axis; thermal energy stored in the thermocline tank is plotted on the right y-axis. The inclusion of the thermocline tank sustains power production each day after nighttime shutdown of the solar receiver. Step decreases in the receiver power correspond to saturation of the thermocline tank and consequent heliostat defocusing.
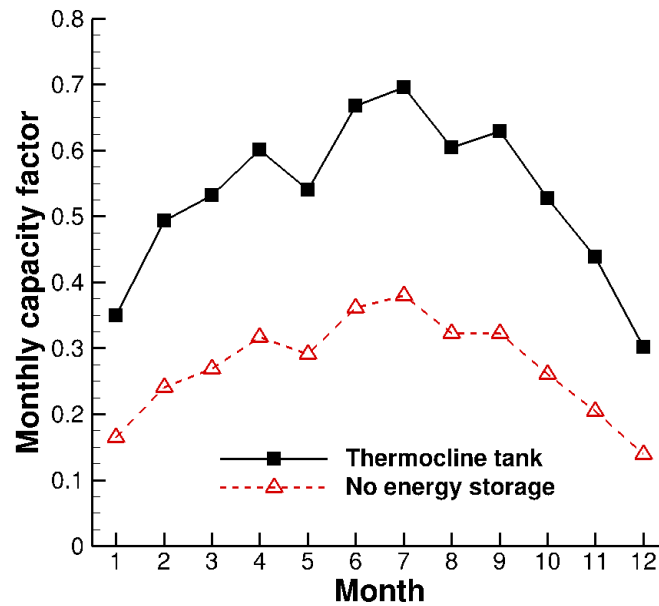
Figure 5.7. Power plant capacity factors observed for each month of operation. The solid line illustrates the plant performance; the dashed line illustrates the plant performance without the inclusion of any thermal energy storage.
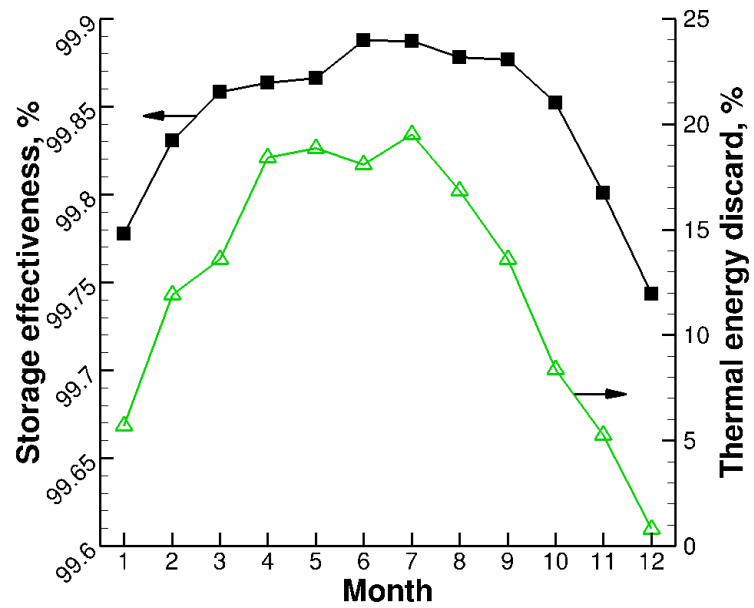
Figure 5.8. Monthly thermocline storage effectiveness and plant thermal energy discard. Discard is normalized with respect to the amount of sunlight available for collection each month.

CHAPTER 6. ECONOMIC OPTIMIZATION OF A CONCENTRATING SOLAR
POWER PLANT WITH THERMOCLINE ENERGY STORAGE

Material in this chapter was published in *ASME Journal of Solar Energy Engineering* [87]
and presented at the *2013 ASME Conference on Energy Sustainability in Minneapolis,
MN* [88].

6.1 Introduction

The contribution of a thermocline tank storage system in a CSP plant is directly
related to its energy capacity or overall size. For a fixed power plant rating, larger tanks
yield an increased annual output but require greater capital cost for construction. It
should also be noted that the amount of thermal energy available for storage is a function
of the power plant solar multiple (maximum solar collector power at noon on summer
solstice relative to the thermal power require to run the power cycle). Increasing the solar
multiple allows to be collected but at the financial expense of the additional heliostats
required. These tradeoffs between power production and plant expenditure are
characterized by a levelized cost of electricity. A minimum levelized cost indicates the
optimum solar multiple and thermocline tank size for the CSP plant design.

The following chapter performs a system-level simulation of a molten-salt power
tower plant with thermocline tank energy storage in order to optimize annual economic
performance. Thermal simulation of the power plant (solar collectors, thermocline tank,
and power block) is identical to the model presented in Chapter 5. The system model is
extended to quantify the levelized cost of electricity associated with year-long operation.
A parametric study of the thermocline tank size and solar multiple is then performed to
identify a minimum cost. Additional metrics of interest include the annual plant capacity
factor and thermal energy discard.

6.2   Economic Analysis

The economic viability of a power plant is characterized by its levelized cost of electricity (LCOE), or the required power price in ¢/kWh$_e$ needed to offset the entire plant expenditure within its operational lifetime [85,89]:

$$LCOE = \frac{TCC \cdot FCR + FOM}{A_y \cdot CF \cdot 8760} + VOM \, . \tag{6.1}$$

Total capital cost (TCC) is the combined direct and indirect costs required for plant construction per rated kilowatt of electric output (¢/kW$_e$). An annual fixed charge rate (FCR) is the percentage of capital cost that must be repaid during each year of operation. The current study assumes an FCR of 7.5% and a plant lifetime of 30 years, based on previous economic analyses of power tower plants in the literature [85]. The cost per unit energy is dependent on the annual electric output from the plant. This output is governed by the annual plant availability (A_y), assumed to be 0.9 according to previous plant predictions [6], and the capacity factor (CF), which is the ratio of power production to the theoretical maximum, *i.e.*, continuous operation at rated load.

Direct capital costs include all tangible resources necessary to build the plant, including site improvements, heliostats, tower, solar receiver, energy storage, power block, balance of plant infrastructure, as well as a contingency to accommodate any unforeseen expenditures. Indirect capital costs include plant design, land, and sales taxes. For the current study, the required land area for the solar plant is assumed to be a circle defined by the radial distance from the central tower to the farthest heliostat. In addition to capital, power plants incur expenditures associated with operation and maintenance. These include fixed operation and maintenance (FOM) costs that are dependent on plant size and variable (VOM) costs that are dependent on electricity generation.

A summary of the various capital and operation costs for a molten-salt power tower plant are taken from System Advisor Model ver. 2012.11.30, a financial model for CSP plant performance developed by the National Renewable Energy Laboratory [90], and listed in Table 6.1. However, with a molten-salt thermocline tank implemented in place of the conventional two-tank storage option, the default capital cost of thermal

energy storage is reduced from \$27/kWh$_t$ to \$20/kWh$_t$ to reflect the financial benefit realized [85]. It should also be noted that the solar tower and solar receiver costs do not exhibit a direct scaling with power, but are determined by the following functions reported in System Advisor Model:

$$\$_{tow} = 1.927 \times 10^6 \exp\left[\frac{h_{tow} + 0.5(h_{hel} - h_{rec})}{8.85}\right] \tag{6.2}$$

$$\$_{rec} = 1.262 \times 10^8 \left(\frac{\pi\, d_{rec}\, h_{rec}}{1571}\right)^{0.7}. \tag{6.3}$$

6.3   Results and Discussion

Annual plant simulation is performed for a 100 MW$_e$ solar power tower plant. The plant size (*i.e.*, number of heliostats in the surrounding field) is dictated by the solar multiple, which is varied from 1 – 4 in the current study. The optimized power plant dimensions for each solar multiple (SM) of interest are determined with DELSOL, a power tower design tool developed by Sandia National Laboratories [81], and summarized in Table 6.2. In all cases, the default heliostat size (height of 9.93 m and a reflection area of 95.45 m^2) is applied by DELSOL. While a solar multiple of 1 implies that no excess sunlight is ever collected during plant operation, inclusion of a storage system is still useful to buffer power production from transient fluctuations in DNI. For each solar plant size, the energy capacity of the thermocline tank is varied from 6 – 20 hours of available storage time. A volumetric overdesign equivalent to an additional half hour of storage is included in all tanks sizes to accommodate the presence of transitional temperatures below the hot design limit. The actual energy capacity of each tank size is the product of this adjusted storage time and the power block heat input at the rated load of 270.9 MW$_t$.

While the energy capacity of each thermocline tank size is known, the corresponding tank shape remains subject to multiple design constraints. Given the density of the molten salt and quartzite bed, the liquid level inside the thermocline tank

cannot exceed 39 feet (11.9 m) to satisfy the bearing capacity of the underlying soil with a typical foundation [25]. The height of each thermocline tank design is fixed at 11 m to accommodate the liquid heel, with the requisite energy capacity achieved through scaling of the tank diameter, as summarized in Table 6.3. However, the necessary diameters for tank sizes with storage capacity exceeding 14 hours are larger than a practical tank limit of 160 feet (48.8 m) reported in a previous design study [25]. For these cases, thermocline energy storage is assumed to include two smaller tanks operating in parallel.

Prior to each solar plant simulation, the thermocline tank fillerbed and liquid heel are both initialized to the cold molten-salt temperature limit of 300 ℃. The fillerbed geometry is discretized with 500 cells along the axial height and a time step of 3 seconds; model accuracy was previously verified with temperature data reported in the literature [29,77]. Prior to storage simulation, the thermal performance of the heliostat field and solar receiver is first simulated in SOLERGY applying the meteorological-year sunlight data reported near Barstow, CA. The instantaneous power collected by the molten salt in the receiver then serves as input to the thermocline tank and power block models for each time step of simulation. As in the previous chapter, the molten salt flow rate through the solar receiver is adjusted to maintain a fixed exit temperature of 600 ℃. With the SOLERGY results, each plant design and thermocline tank size is then simulated for a full year of operation from January 1 to December 31. The influence of the thermocline tank on annual plant performance is characterized in terms of thermal energy discard, plant capacity factor, storage effectiveness, and LCOE.

6.3.1   Thermal Energy Discard

For prolonged charge processes, cold molten salt exiting the bottom of the thermocline tank will begin to increase in temperature as the transitional heat-exchange region travels to the tank floor. When this warmed salt enters the solar receiver, an increased receiver mass flow rate is assumed so that the exit hot temperature may be maintained at 600 ℃. To prevent overcharging of the storage system, the salt exiting at the tank floor is limited to a maximum allowable temperature of 400 ℃. When this

occurs, the thermocline tank is designated to be at energy capacity and transitions to a forced standby condition. With no more available storage capacity, the solar receiver can only collect enough energy to satisfy the Rankine cycle steam generation. In effect, the mass flow rate of hot molten salt supplied to the thermocline tank is reduced to exactly balance the hot flow to the steam generators, producing no overall energy addition of energy to the tank. Heliostats are defocused away from the receiver and some amount of sunlight available for concentration must be forgone; this is known as thermal energy discard. The forced tank standby persists until the solar receiver power output decays near sunset and the energy-saturated tank can then be discharged to sustain rated power production.

A plot of annual thermal energy discard for each solar multiple and thermocline tank size is provided in Figure 6.1. Values are normalized with respect to the total amount of sunlight available for collection. As expected, the magnitude of annual discard increases with solar multiple. No thermal energy discard is observed with a solar multiple of 1 for any thermocline tank size, because the plant never collects more sunlight than is needed to operate the power block. In contrast, the larger-sized plants are able to collect excess sunlight, increasing the use of the thermocline tank and leading to instances of storage saturation. As tank size increases, saturation becomes less frequent and the amount of energy discarded for the year converges to zero.

For solar multiples of 3 and 4, it is observed that the rate of convergence slows with increasing tank size. As such, zero thermal energy discard is not observed within the span of tank sizes simulated in the current study. It should be noted that both of these plant designs are large enough to sustain 24-hour power production during weather periods of high insolation. When this occurs, increasing the thermocline tank size carries diminishing returns for reducing thermal energy discard as the power block is already operating at maximum performance. Therefore, a thermocline tank size big enough to achieve zero annual discard is not practical for large solar multiples.

6.3.2 Capacity Factor

When thermal energy discard is reduced as a result of increasing storage size, more thermal power is collected in the solar receiver and converted to work output. The annual work output of a power plant is characterized by its capacity factor. Capacity factors for the current study are plotted in Figure 6.2. As expected, this factor increases with solar multiple (due to more thermal energy collected) and tank size (due to more thermal energy stored). It should be noted that the maximum potential work output is also function of the amount of sunlight collected by the receiver. Each solar multiple therefore exhibits a maximum obtainable capacity factor independent of thermal energy storage capability:

$$CF_{max} = \frac{1}{24 \cdot 365} \left(\frac{\eta_{cyc} \eta_{par} Q_{rec}}{W_{net}} \right). \tag{6.4}$$

The capacity factor limits for solar multiples from $1 - 4$ are 0.266, 0.531, 0.806, and 1.09, respectively. The last value exceeds unity and indicates that a solar multiple of 4 may collect more sunlight than what is needed for continuous year-long power production. In reality, capacity factor cannot exceed unity and the maximum for SM = 4 is therefore reduced to 1. The capacity factor data in Figure 6.2 are normalized with respect to the theoretical maximums for each solar multiple and plotted in Figure 6.3.

As expected, the normalized capacity factor increases with thermocline tank size because less thermal energy is discarded and more of it is converted to net work output. When the discarded thermal energy reduces to zero, the model data converge to a maximum as observed for the solar multiples of 1 and 2. As discussed in the previous section, solar multiples of 3 and 4 discard energy for all simulated tank sizes and thus do not exhibit a converged maximum.

It is observed that the maximum normalized capacity factor for SM = 2 (0.983) exceeds the corresponding maximum for SM = 1 (0.941). This is due to the inability of the SM = 1 plant design to collect excess sunlight during daylight hours, which then prolongs the daily turbine shutdown periods to an excess of 12 hours. As a result, the majority of power block operations require warm turbine startups, which consume more

thermal energy than hot startups. Thus a greater fraction of collected energy is lost to startup in the SM = 1 design than in the SM = 2 design and reduces the normalized capacity factor.

6.3.3   Storage Effectiveness

As stated previously, the thermocline tank walls are considered well insulated, and are subjected to an adiabatic boundary condition, *i.e.*, no heat is lost from the tank to the surroundings. Without heat loss, the efficiency of the tank remains unity at all times. However, the quality of thermal energy in thermocline storage is not constant as the internal tank temperatures vary with time, including the molten-salt temperatures supplied to the power block. Thus, the storage performance of the tank can instead be characterized by an effectiveness metric, as for a heat exchanger. For a thermocline tank, storage effectiveness is defined as the ratio of utilizable heat delivered from the tank to the maximum amount of heat available:

$$\varepsilon_{tank} = \frac{\int \dot{m}_{HX} \, C_{P,l} \left(T_{heel} - T_c \right) dt}{\int P_{rec} \, dt} \, . \tag{6.5}$$

The annual thermocline tank storage effectiveness is plotted in Figure 6.4 each simulation case. All of the simulated tanks exhibit annual storage effectiveness values greater than 99%, indicating that almost all of the thermal energy delivered to the tank from the solar receiver is recovered for steam generation in the power block. Despite adiabatic boundary conditions, the effectiveness exhibits a small loss due to the generation and sustainment of the heat-exchange region between the hot and cold volumes inside the tank. Thus the molten-salt thermocline tank is a viable thermal energy storage option for long-term operation in a CSP plant, independent of its size.

It should be noted that storage effectiveness is not independent of the time duration of assessed in Eq. (6.5). At shorter durations, the tank is more sensitive to degradation of the thermocline from thermal diffusion and results in lower effectiveness

values than that for the yearlong condition applied in Figure 6.4. Thermocline effectiveness values at shorter month-long intervals are addressed in Chapter 5.

6.3.4 Levelized Cost of Electricity

With known plant expenditures and annual capacity factor predictions, the LCOE for each thermocline tank case is calculated with Eq. (6.1) and plotted in Figure 6.5. The SM = 1 plant design does not exhibit a cost optimum but instead shows a linear increase in cost with thermocline tank size. Without excess solar collection, the thermocline tank for this design size cannot provide a significant benefit to annual power production and only adds to the plant capital cost. It should also be noted that the SM = 1 design yields the largest electricity cost among the 100 MW_e power tower plant designs, verifying that lack of storage utilization is not practical for year-long plant operation. The SM = 2 plant design exhibits a minimum LCOE of 13.4 ¢/kWh_e with a thermocline tank size of 10 hour capacity. This size yields almost no thermal energy discard, and thus larger tanks provide little additional benefit and a linear cost increase similar to the SM = 1 plant design is observed. Further, for lower amounts of storage hours (*e.g.,* ≤ approximately 10.5 h), plants with an SM = 2 represent the lowest cost option of the four SM values.

Greater solar multiples indicate potential for further levelized cost reductions. A solar multiple of 3 exhibits a minimum cost of 12.2 ¢/kWh_e with a thermocline tank size of 16 hour capacity. However, a larger multiple of 4 exhibits a minimum cost of 13.2 ¢/kWh_e with a thermocline tank size of 20 hour capacity. This increase in cost is explained by the diminishing returns in annual power production observed for increasing solar multiple. At the minimum levelized costs, the capacity factors for the SM = 3 and SM = 4 cases are 0.742 and 0.837, respectively. While the larger solar multiple can provide more annual power, the gain is not sufficient to offset the increase in capital costs required. Thus a solar multiple of 3 and a thermocline storage capacity of 16 hours are found to exhibit an economic optimum for a 100 MW_e molten-salt power tower plant among the cases considered.

The optimum electricity cost of 12.2 ¢/kWh$_e$ identified in this work indicates the extent of cost reduction possible by implementing thermocline energy storage in a power tower plant. However, this minimum does not meet the target price of 6 ¢/kWh$_e$ identified by the U.S. Department of Energy SunShot Initiative [7]. The reason for this discrepancy is illustrated in Figure 6.6, which plots the individual contributions of the power tower plant to the levelized cost. The heliostat field is seen to remain a significant capital expenditure and constitutes almost 30% of the total LCOE under the applied economic conditions. The current study is limited to an investigation of thermocline tank size and plant solar multiple. While a thermocline tank offers a useful alternative to two-tank storage, optimization of thermal energy storage alone is not sufficient to achieve domestic grid parity with fossil fuels in the cost of electricity from solar plants. Additional plant improvements outside of thermal energy storage (*e.g.*, heliostat cost reduction) are essential for future power tower plant design.

6.3.5   Two-Tank Comparison

Despite the inability of thermocline energy storage to achieve grid parity for CSP technologies, the concept remains less expensive than conventional two-tank storage methods. It is therefore of interest to repeat the power tower plant case study with two-tank storage and quantify the direct economic benefit. In this scenario, the energy capacity is sized equal to the maximum capacity of the previous thermocline tank geometries. The year-long simulation is then conducted with SOLERGY for each solar multiple and energy storage size to solve for the annual turbine outputs and levelized costs. The disparity in LCOE between thermocline and two-tank systems of equal capacity is plotted in Figure 6.7. The plotted lines correspond to each solar multiple of interest and terminate at the minimum LCOE achieved; larger storage sizes being impractical and thus omitted from the graph.

For large solar multiple and small storage sizes, implementation of two-tank storage generates cheaper electricity than an equivalent thermocline tank despite the higher capital cost. In this circumstance, the economic benefit of additional storage capacity is large. Given that a thermocline tank loses some of its capacity due to the

heat-exchange region, the two-tank system yields a small increase in turbine output which offsets the higher cost. As the applied storage size increases, the benefits of increased capacity diminish and thermocline tanks become preferable (*i.e.*, the two-tank system begins to carry a more severe economic penalty). However, the disparity in LCOE between the two storage methods is less than 1 ¢/kWh$_e$ for all practical cases investigated. Furthermore, while a thermocline tank achieves a minimum LCOE of 12.2 ¢/kWh$_e$, a two-tank system provides a marginally greater cost of 12.4 ¢/kWh$_e$. So although a thermocline tank is preferentially cheaper, this benefit does not necessarily translate into substantial LCOE savings due to the inherent reduction in storage performance with stratification.

6.4   Chapter Summary

A numerical simulation of a 100 MW$_e$ solar power tower plant is conducted to optimize annual performance as a function of thermocline tank size and plant solar multiple. Thermal energy discard associated with thermocline storage saturation is a strong function of the applied solar multiple. However for increasing thermocline tank size, less energy is discarded but is instead collected and stored for later power production, as indicated by the annual capacity factor. All tank sizes exhibit high annual storage effectiveness and illustrate the viability of the thermocline tank as a component of future CSP plants.

Economic analysis of the power tower plant indicates a minimum levelized cost of electricity for a solar multiple of 3 and thermocline tank energy capacity of 16 hours in the 100 MW$_e$ plant. While larger plants produced more electricity annually, the gain is insufficient to offset the added capital costs. The levelized cost of 12.2 ¢/kWh$_e$ associated with this minimum exceeds the target price of 6 ¢/kWh$_e$, indicating that additional cost reductions outside of thermal energy storage are necessary in a power tower plant to achieve domestic grid parity with fossil fuels. A subsequent plant model comparison with conventional two-tank storage also indicates that the capital savings

obtained with a thermocline tank are divorced from system-level reductions in LCOE due to inherent losses in energy storage capacity with thermal stratification.

Table 6.1. Cost parameters for a molten-salt power tower plant [90]. Capital cost for thermocline energy storage is taken from [85].

Cost	Type	Value	Units
Site improvements	Direct	20	$/m^2
Heliostats	Direct	180	$/m^2
Balance of plant	Direct	350	$/kW$_e$ (gross)
Power block	Direct	850	$/kW$_e$ (gross)
Energy storage	Direct	20	$/kWh$_t$
Tower	Direct	Eq. (6.2)	$
Receiver	Direct	Eq. (6.3)	$
Contingency	Direct	7	% of DCC
Plant design	Indirect	11	% of DCC
Land	Indirect	10000	$/acre
Sales tax	Indirect	4	% of DCC
Fixed	Operating	65	$/kW$_e$-yr
Variable	Operating	0.003	$/kWh$_e$

Table 6.2. 100 MW$_e$ power tower plant dimensions as a function of desired solar multiple [81].

SM	h_{tow} [m]	h_{rec} [m]	d_{rec} [m]	Mirror area [km^2]	Land area [km^2]
1	137.5	15	10	0.488	3.34
2	187.5	18	18	0.994	6.21
3	225	21	21	1.53	8.95
4	250	23	23	2.12	11.0

Table 6.3. Summary of thermocline energy capacity and corresponding tank diameter. A practical diameter limit of 48.8 m is enforced, requiring two tanks operating in parallel for large energy capacities.

Energy capacity [h]	Tank diameter [m]	Number of tanks
6	31.9	1
8	36.5	1
10	40.6	1
12	44.2	1
14	47.7	1
16	35.9	2
18	38.1	2
20	40.1	2
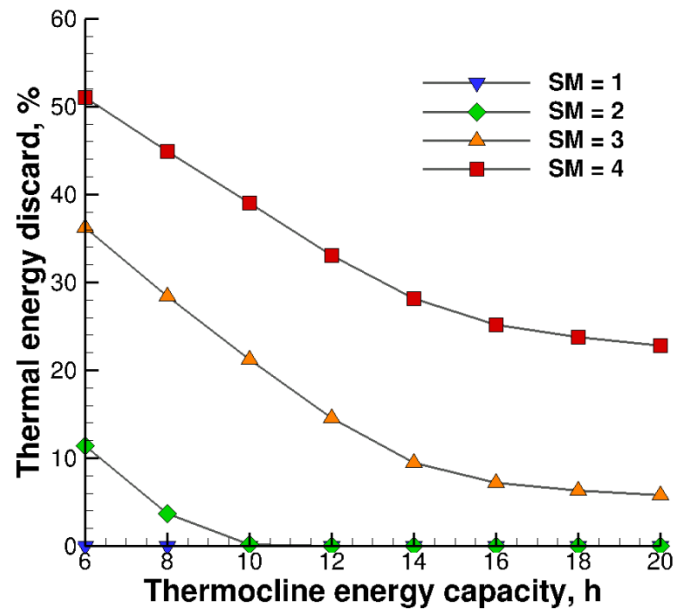
Figure 6.1. Annual solar thermal energy discarded due thermocline tank energy saturation, normalized with respect to the total amount of sunlight available for collection. Plant performance corresponds to weather data recorded near Barstow, CA, for the year 1977.
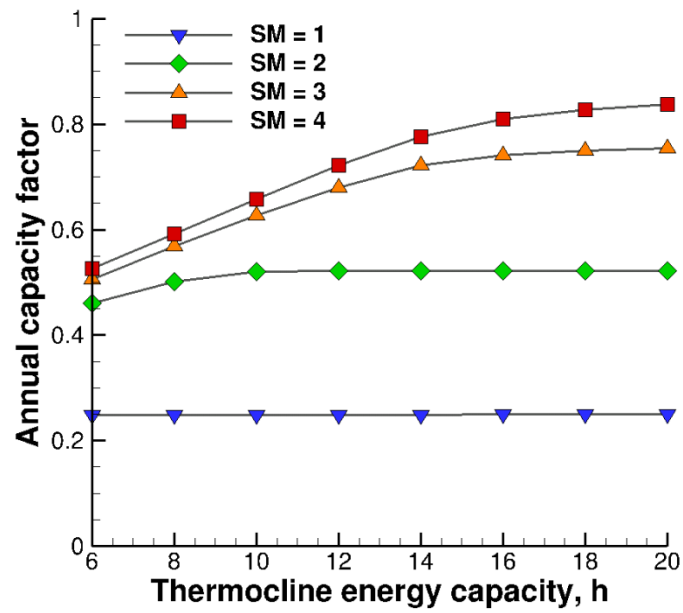
Figure 6.2. Annual power tower plant capacity factor. Plant output increases with both solar multiple and thermocline tank energy capacity.
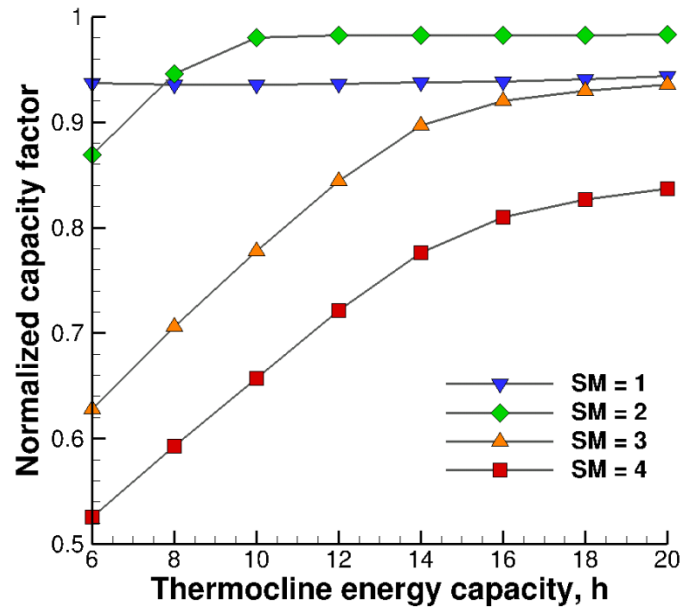
Figure 6.3. Annual capacity factor normalized with respect to the theoretical maximum for each plant solar multiple.
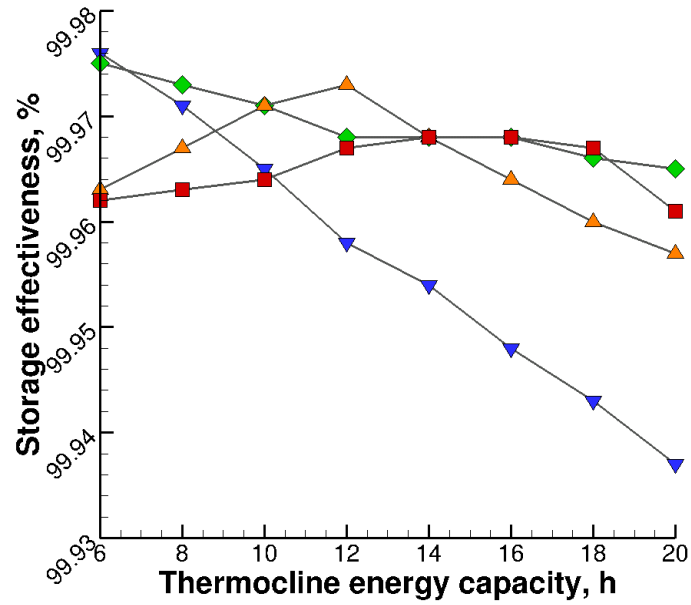
Figure 6.4. Annual thermocline storage effectiveness. All cases exhibit values above 99%, validating the thermocline storage concept for implementation in long-term CSP applications.
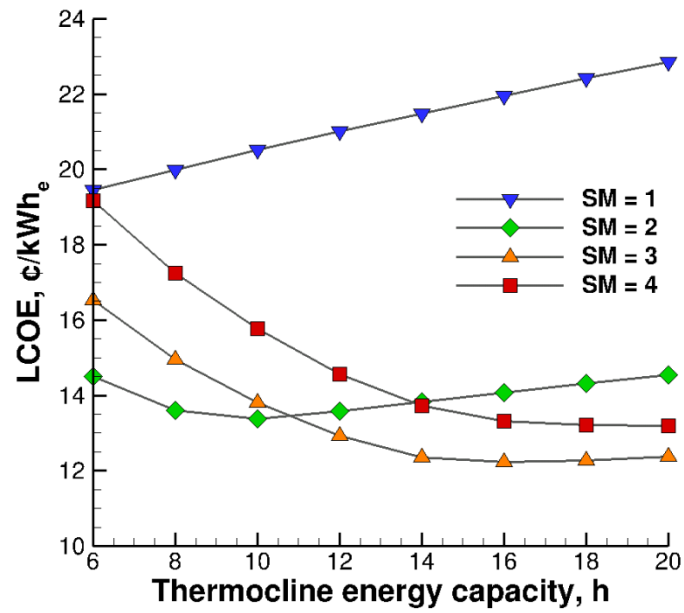
Figure 6.5. Levelized cost of electricity for a 100 MW$_e$ power tower plant with thermocline energy storage. Minimum LCOE is observed at a solar multiple of 3 and thermocline energy capacity of 16 hours.
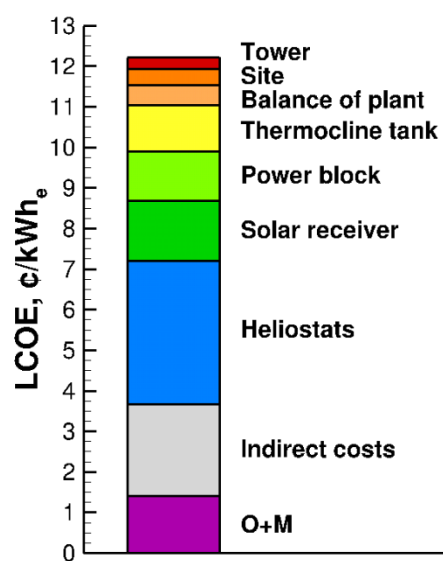
Figure 6.6. Individual power tower plant costs at the minimum LCOE of 12.2 ¢/kWh$_e$. Heliostats exhibit the largest plant capital cost and require improvement to achieve grid parity with fossil fuel.
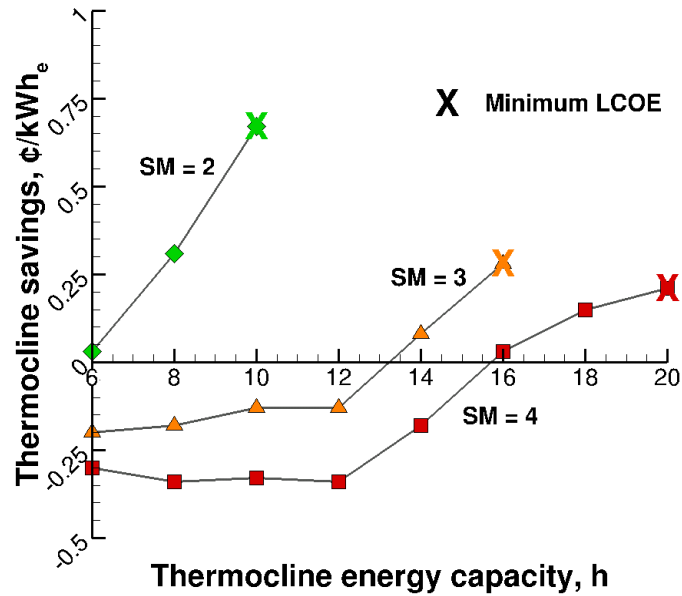
Figure 6.7. Levelized cost of electricity savings associated with thermocline energy storage in place of an equal sized two-tank system. Thermocline benefits are largest near the optimum LCOE for each solar multiple. Away from this point, the improved storage performance of the two-tank system offsets the increased capital cost.

CHAPTER 7. LATENT HEAT AUGMENTATION OF THERMOCLINE ENERGY
STORAGE FOR CONCENTRATING SOLAR POWER

Material in this chapter is under review for possible publication in *Applied Energy* [91].

7.1   Introduction

Despite its low capital cost and successful technical demonstration of the concept, the dual-media thermocline tank presents several design challenges that continue to inhibit commercialization. As a device that stores energy solely by sensible heat, the low energy density of the molten-salt and rock volume requires large tank diameters to store sufficient quantities of high-temperature heat (the tank height itself is constrained by the bearing capacity of the underlying soil). A large tank diameter is undesirable as it increases the potential for both maldistribution of fluid flow inside the porous bed and thermal ratcheting (see Chapter 4). A design modification that has been proposed for reducing the tank size (by increasing energy density) is a substitution of the internal filler rock with a phase-change material (PCM). During storage operations, the PCM undergoes repeated melting and solidification in response to forced convective heat exchange with the surrounding molten-salt flow, contributing an additional latent heat storage mechanism inside the tank. For practical implementation, small volumes of PCM are encapsulated in a protective liner to prevent physical mixing with the salt. The tank is then filled with these capsules to mimic the unconsolidated porous structure of the conventional rock filler.

Computational study of the latent heat thermocline tank has not been performed to date at the power plant system level, *i.e*., in conjunction with solar collection and power production processes. Given the diurnal and seasonal intermittency of the available sunlight, this system-level perspective is essential to the understanding of how the storage

tank behaves in the context of actual CSP plant operation. The present work addresses this need with a new finite-volume simulation of a latent heat thermocline tank, replacing the quartzite rock with a bed of encapsulated phase-change material. This storage model is then integrated into a system model of a 100 MW$_e$ molten-salt power tower plant. The objective of the system modeling effort is to ascertain the viability of the latent heat thermocline concept for CSP applications. A parametric study of the PCM melting temperature and heat of fusion serves to identify the optimal ranges of values that would maximize the annual power plant output. System performance with a conventional rock-filled (sensible heat-based) thermocline tank of equal size serves as the benchmark for comparison.

7.2 Numerical Model

An illustration of the latent heat thermocline tank is provided in Figure 7.1. The tank interior includes a dual-media porous region, composed of molten salt and PCM capsules, as well as a liquid heel of salt above the capsules. For the current study, molten salt is represented with a commercial eutectic mixture known as solar salt (60 wt.% NaNO$_3$, 40 wt.% KNO$_3$) which operates between 300 °C and 600 °C. Physical properties of the salt are known functions of temperature [78,79]. The specific heat is relatively constant across the stated temperature span and is approximated with an average value of 1520 J/kg-K.

To facilitate direct comparison with thermocline tanks that use conventional sensible heat filler materials, a hypothetical PCM filler is considered with density, specific heat, and thermal conductivity equivalent to those of quartzite rock: 2500 kg/m^3, 830 J/kg-K, and 5 W/m-K, respectively [47,80]. In reality, phase-change materials suitable for latent heat storage tend to have lower thermal conductivities as well as densities that vary with temperature. The current study neglects these material deficiencies of PCMs in order to provide an objective and abstracted assessment of the storage capacity added by the latent heat mechanism. Cyclic phase change is governed by the heat of fusion (h_{fs}) and the melting temperature of the material, which are treated

as user-defined inputs. The protective capsule liner surrounding the PCM is assumed to be thin and any thermal resistance posed is neglected. Thermal energy storage in both the porous PCM-filled bed and the pure liquid heel are explained in the following sections.

7.2.1 Porous Region

Mass and momentum transport of molten salt inside the thermocline porous bed are governed by the following equations:

$$\frac{\partial \varepsilon \rho_l}{\partial t} + \nabla \cdot (\rho_l \mathbf{u}) = 0 \tag{7.1}$$

$$\frac{\partial \rho_l \mathbf{u}}{\partial t} + \nabla \cdot \left(\rho_l \frac{\mathbf{u}\mathbf{u}}{\varepsilon} \right) = -\varepsilon \nabla p + \nabla \cdot \tilde{\boldsymbol{\tau}} + \varepsilon \rho_l \mathbf{g} + \varepsilon \left(\frac{\mu}{K} \mathbf{u} + \frac{F}{\sqrt{K}} \rho_l |\mathbf{u}| \mathbf{u} \right). \tag{7.2}$$

It should be noted that thermocline tanks generally exhibit low fluid velocities, approximating laminar, plug-flow conditions. Under these flow conditions, the momentum equation simplifies to the Darcy-Forchheimer equation.

Energy transport in the porous region is formulated with separate equations for the liquid molten salt (subscript *l*) and the PCM filler (subscript *s*):

$$\frac{\partial \left[\varepsilon \rho_l C_{P,l} (T_l - T_c) \right]}{\partial t} + \nabla \cdot \left[\rho_l \mathbf{u} C_{P,l} (T_l - T_c) \right] = \nabla \cdot \left(k_{eff} \nabla T_l \right) + h_i (T_s - T_l) \tag{7.3}$$

$$\frac{\partial \left[(1 - \varepsilon) \rho_s C_{P,s} (T_s - T_c) \right]}{\partial t} = -h_i (T_s - T_l) + \frac{\partial \left[(1 - \varepsilon) \rho_s L_{fs} \right]}{\partial t}. \tag{7.4}$$

Thermal diffusion is neglected in Eq. (7.4) as the temperature in each PCM capsule is assumed to be uniform. The porous structure influences diffusion in the surrounding molten salt that is characterized by an effective thermal conductivity calculated from a correlation [60]. Forced convection between the molten salt and PCM capsule is characterized with the Wakao and Kaguei correlation [63].

A second transient source term is included in Eq. (7.4) to represent the cyclic melting and solidifying of the PCM filler. The current study applies the enthalpy method

developed by Voller and Prakash [92], where the latent thermal energy (L_{fs}) contained by the PCM is proportional to its solid fraction (F_s):

$$L_{fs} = h_{fs}(1 - F_s). \tag{7.5}$$

For numerical stability, the PCM solid fraction is assumed to vary linearly between the solidus $(T_{sol} = T_m - e)$ and the liquidus $(T_{liq} = T_m + e)$ temperatures over a small mushy region (in which both liquid and solid phases exist in equilibrium) half span temperature range e of 1 K:

$$F_s = \begin{cases} 1 & T_s \leq T_{sol} \\ \dfrac{T_{liq} - T_s}{2e} & T_{sol} < T_s \leq T_{liq} \\ 0 & T_s > T_{liq} \end{cases} \tag{7.6}$$

The thermocline tank wall is assumed to be well-insulated, which simplifies Eq. (7.3) to a one-dimensional formulation along the axial direction. To nondimensionalize the governing energy equations, the molten-salt and PCM temperatures are normalized with respect to the hot and cold operating limits:

$$\Theta = \frac{T - T_c}{T_h - T_c}. \tag{7.7}$$

The transport equations are solved using a finite-volume discretization of the porous bed along the axial direction. The molten-salt velocity field along the discretized porous bed is determined from mass conservation with Eq. (7.1). The energy transport equations are then converted to algebraic relationships as follows. A first-order implicit method is applied for discretization of the temporal terms. The convective flux term in the fluid energy transport, Eq. (7.3), is discretized with the quadratic flux limiter, a quasi-second-order local extrema-diminishing scheme. A Picard iteration scheme is implemented to resolve nonlinearity in Eq. (7.3) as well as the forced convection coupling with Eq. (7.4). The resultant equations are then solved at each time step with a tridiagonal matrix algorithm written in C. This algorithm is repeated for up to 75 iterations or until the nondimensional residual error reduces to less than 10^{-6}. Validation

of the thermal model and the solution technique were previously demonstrated in Chapter 5 with a simulation of the 2.3 MWh$_t$ thermocline tank constructed by Sandia National Laboratories [29,77].

Boundary conditions for the continuity and energy equations are informed by the prevalent mode of tank operation. During a charge process, hot molten salt from the liquid heel (discussed in the next section) enters the top of the porous bed at a uniform velocity. At the same time, cold salt exiting the floor of the bed is simulated with an outflow boundary condition. During the reverse discharge process, uniform cold salt is supplied to the bottom of the bed. An outflow boundary condition is then applied for the hot salt exiting the top of the porous bed. Thermal diffusion from the liquid heel to the underlying porous bed is treated with a Dirichlet condition equal to the current temperature of the heel. Another Dirichlet condition is enforced at the tank floor, with a fixed temperature equal to the cold operating limit.

7.2.2 Liquid Heel

Given that the molten-salt density decreases with temperature, the thermocline tank cannot realistically be modeled as a control volume. A pure molten-salt region must therefore be maintained above the porous bed (*i.e.*, the PCM capsules) to prevent dryout in the porous region. As in the preceding chapters, the heel is approximated as an isothermal region, where temperature is determined from the known mass and energy content, Eq. (5.11). During daylight hours, the solar receiver supplies hot molten salt to this heel at 600 °C. When the heel warms to a temperature hot enough to support power production, salt is extracted from the heel for steam generation in the Rankine cycle heat exchangers. Mass and energy transport between the heel and the underlying porous bed again depends on the tank operating mode as discussed in the previous section.

7.2.3 System Model

The low computing cost of the thermocline model allows for integration into a system-level model of a CSP plant. Such a model was previously developed in Chapter 5

for a molten-salt power tower plant with sensible heat thermocline storage and is summarized here. The power tower plant is desired to provide a net turbine output of 100 MW$_e$ at a solar multiple of 2.3. The surround-style heliostat field and solar receiver are sized with DELSOL [81]. The model field includes 1,170,000 m^2 of reflector area and a receiver tower height of 194.7 m. The solar receiver atop this tower is an external cylinder design with a diameter of 21 m and a height of 18 m. Sunlight data for collector analysis are taken from direct normal irradiance (DNI) measurements near Barstow, CA, selected for its excellent annual insolation of 2700 kWh$_t$/m^2. This dataset includes recorded DNI at 15-minute intervals from January 1 to December 31 of 1977.

From the available sunlight data, incident thermal power reflected onto the solar receiver and absorbed by the molten salt is calculated with SOLERGY [86]. The mass flow rate inside the receiver is controlled in response to changes in DNI such that molten salt always exits the receiver at 600 °C. No storage bypass line is included between the solar receiver and Rankine cycle heat exchangers; thus all molten salt exiting the receiver is directed to the liquid heel of the thermocline tank. Once the tank is charged to sufficient energy content, hot salt is extracted from this heel and sent to the power block. Detailed discussion of the power block (heat exchangers and steam Rankine cycle) and its operation is presented in Chapter 5.

Derated power output via sliding-pressure operation is allowed down to 30% of rated gross output, associated with a molten-salt supply temperature of 473 °C ($\Theta = 0.58$). It should also be noted that the bottom of the thermocline tank is limited to a maximum exit temperature of 400 °C ($\Theta = 0.33$) to prevent overheating of the solar receiver. Thus, any salt region that is between these temperature limits within the tank constitutes a thermal dead zone that is not useful for either solar collection or steam generation.

7.3 Results and Discussion

A system-level study of a 100 MW$_e$ molten-salt power tower plant is now conducted with the latent-heat-augmented thermocline concept to quantify the plant performance benefits over a conventional sensible heat thermocline. As previously

discussed, this one-to-one comparison is enabled by implementing a bed of (hypothetical) phase-change material with sensible transport properties equivalent to quartzite rock. The latent transport properties, *viz.*, heat of fusion and melting temperature, are varied to determine their influence on storage and plant performance. The magnitude of the heat of fusion inside the PCM is expressed relative to the *fixed* sensible heat capacity as an inverse Stefan number:

$$\frac{1}{\text{Ste}} = \frac{h_{fs}}{C_{P,s}\left(T_h - T_c\right)}. \tag{7.8}$$

The current study investigates three inverse Stefan numbers: 0 (*i.e.*, quartzite rock), 0.25, and 0.5. The heats of fusion corresponding to the nonzero inverse Stefan numbers are 62.25 kJ/kg and 124.5 kJ/kg, respectively. Relative to actual candidate PCMs, these properties represent lower and conservative values for latent heat storage. The PCM is also investigated at five different melting temperatures within the operating span of the molten salt; 315 °C ($\Theta = 0.05$), 375 °C ($\Theta = 0.25$), 450 °C ($\Theta = 0.5$), 525 °C ($\Theta = 0.75$), and 585 °C ($\Theta = 0.95$). The different porous bed conditions investigated are summarized in Table 7.1.

Simulation of each thermocline filler bed composition is performed in conjunction with the power-tower system model. In all models, the tank is sized to contain eight hours of *sensible* heat, plus an additional half-hour overdesign, totaling 2300 MWh$_t$. The volumetric overdesign is needed to accommodate both the requisite amount of sensible heat and the underlying cold and transitional temperatures associated with the heat-exchange region. As in the preceding chapters, the height of the porous bed is fixed to 11 m. The PCM capsules are sized to an effective diameter of 1 cm and assumed to form a 0.22 porosity bed. Given the sensible energy densities of the molten salt and filler material, the thermocline tank requires a diameter of 36.5 m to satisfy the required storage capacity. With the tank sized to a fixed sensible heat capacity, the latent heat of the PCM filler adds either 388 MWh$_t$ (1/Ste = 0.25) or 766 MWh$_t$ (1/Ste = 0.5) to the maximum storage capacity. The benefit of this supplement should then manifest in a greater annual energy storage inside the tank, and thus a greater annual turbine output.

Prior to storage and power block simulation, the year-long performance of the heliostat field and solar receiver are first calculated with SOLERGY using recorded sunlight data. The thermocline tank porous bed and liquid heel are then both initialized to the cold temperature limit of 300 °C. The porous bed geometry is discretized with a cell length of 1.1 cm (1000 cells) along the axial direction and a time step of 3 seconds. Each tank design is then subjected to a full year of operation, informed by the SOLERGY solar receiver data. The influence of supplemental latent heat capacity in the thermocline tank on CSP plant performance is monitored with respect to annual capacity factor, thermal energy discard, and utilization of the storage energy capacity.

7.3.1   Annual Plant Performance

The annual plant capacity factors for all 11 thermocline filler cases are plotted in Figure 7.2a. The baseline quartzite-filled tank (case 1) exhibits an annual capacity factor of 0.533. A majority of the PCM-filled tanks have similar values to quartzite, implying minimal impact from the addition of latent heat. PCMs with low melting temperatures ($\Theta_m = 0.05, 0.25$) result in a slight increase relative to quartzite, while PCMs with high melting temperatures ($\Theta_m = 0.75, 0.95$) show a slight decrease. The intermediate melting temperature of $\Theta_m = 0.5$ exhibits the largest decrease, which worsens with increased heat of fusion (*i.e.*, latent heat capacity), represented by the inverse Stefan number of the PCM. For all other PCM melting points, variation of the material heat of fusion does not influence annual power production.

The annual discard of thermal energy from the solar collector due to saturation of the thermocline storage capacity is plotted in Figure 7.2b. As previously discussed, storage saturation occurs when cold salt exiting the tank floor increases to 400 °C. The discard is normalized with respect to the total sunlight available to provide insight on how well the thermocline tank is sized relative to the surrounding power plant. During a year of operation, the conventional thermocline tank (case 1) discards 11.6% of the available sunlight. As with capacity factor, this performance is not benefitted by the addition of supplemental latent heat. PCMs with low melting temperature exhibit a slight decrease in discard relative to quartzite, while the high melting temperatures perform

almost identically to quartzite. The intermediate melting temperature of $\Theta_m = 0.5$ again presents the worst-case condition with an increased annual discard up to 25.5%.

A comparison of Figure 7.2a and Figure 7.2b illustrates a complementary trend between thermal energy discard and capacity factor. When discard increases, less thermal energy is harnessed by the thermocline tank and power block, leading to the observed reduction in electricity generation as expected. The model data reveal that the addition of latent heat (at no change in sensible heat capacity) to the thermocline filler material does not provide substantial benefits with respect to CSP plant performance. Instead, a majority of the PCM fillers result in a decrease in capacity factor, indicating that a *larger* thermocline tank would be required to match the plant performance achieved with conventional quartzite rock. While the latent heat provided by the PCM filler increases the available total storage capacity potential, the addition also appears to hinder the ability of the thermocline tank to harness this capacity.

7.3.2 Thermocline Tank Utilization

During CSP plant operation, the utilization of the thermocline tank is indicated by the energy content inside the tank relative to its theoretical energy capacity (the amount of heat stored if the entire molten-salt and filler volumes are heated to the hot operating limit of 600 °C). The theoretical energy capacity is not observed in practice due to the constant presence of the heat-exchange region inside the tank. The actual maximum utilization is observed when the thermocline tank reaches its saturation condition and is prevented from accepting any additional excess heat from the solar receiver. Figure 7.3 illustrates this maximum utilization for all 11 filler conditions, corresponding to when the tank becomes saturated during plant operation. While these tank saturations occur multiple times throughout the year, the amount of thermal energy stored at this condition varies by less than 1% for the same tank between instances. Utilization of sensible heat and latent heat in the porous bed are calculated and plotted separately to isolate the influence of the added phase change:

$$U_{sen} = \frac{1}{h} \sum_{j=1}^{N} \frac{\left(\varepsilon \rho_l C_{P,l} \Theta_l + (1-\varepsilon) \rho_s C_{P,s} \Theta_s \right)_j \Delta x}{\varepsilon \rho_l C_{P,l} + (1-\varepsilon) \rho_s C_{P,s}} \tag{7.9}$$

$$U_{lat} = \frac{1}{h} \sum_{j=1}^{N} (1 - F_s)_j \Delta x. \tag{7.10}$$

As seen in Figure 7.3a, the conventional quartzite-filled thermocline tank utilizes up to 93.8% of the sensible heat capacity. For the PCM fillers, maximum utilization varies with respect to both melting temperature and heat of fusion. While the latent thermal energy capacity is unrelated to the sensible heat capacity of the tank, the phase change process does influence heat transfer between the molten salt and the PCM filler. PCM fillers with low melting temperature result in greater sensible heat storage than quartzite and further improve with increased heat of fusion. In contrast, PCM fillers with intermediate or high melting temperatures enable less sensible heat storage than quartzite and further degrade with increased heat of fusion, explained in the next section. The worst-case-performance is observed for the intermediate normalized PCM melt temperature of 0.5, which only utilizes 75.1% of the available sensible heat capacity among the cases considered.

Maximum utilization of the latent heat inside the thermocline tank is plotted in Figure 7.3b. Unlike the sensible heat capacity, the magnitude of latent heat available inside the tank is not fixed but is proportional to the user-defined PCM heat of fusion. The conventional quartzite rock filler (case 1) provides no latent heat and is thus omitted from the figure. The remaining cases illustrate a large variation with respect to the PCM melt properties. While low melting temperatures achieve 100% utilization (indicating that all PCM converts to a liquid phase), this performance deteriorates with increasing melting point and heat of fusion. For the highest melting temperature and heat of fusion condition (case 11), the PCM-filled thermocline tank only utilizes 9.4% of the available latent heat capacity at saturation.

The trends observed in Figure 7.3b indicate that as the thermodynamic quality of the PCM increases (*i.e.*, a higher melting point or heat of fusion), the ability of the thermocline tank to harness the available latent heat decreases. This behavior explains

why the PCM-filled tanks did not significantly outperform a quartzite-filled tank of equal size with respect to net power production (Figure 7.2a) or annual thermal energy discard (Figure 7.2b). The latent heat thermocline tank only stores more thermal energy than a quartzite-filled tank when the PCM filler melts at low temperatures; however, at such low temperatures this additional latent heat energy is not viable for steam generation. At higher PCM melting points, the supplemental energy capacity added by latent heat is offset by the reduction in actual phase change.

7.3.3 Heat-exchange Region

The poor utilization of latent heat at high PCM melting points is explained by the behavior of the heat-exchange region inside the porous bed. As discussed before, the heat-exchange region travels up and down the height of the tank in response to cyclic charging and discharging of the system. For a conventional sensible heat thermocline tank, the relation between the heat-exchange region travel rate and the inlet velocity of the molten salt is obtained from an energy balance on the region [47]:

$$v_{sen} = \frac{\rho_{l,in}C_{P,l}}{\varepsilon\rho_{l,in}C_{P,l} + (1-\varepsilon)\rho_s C_{P,s}} u_{in}. \tag{7.11}$$

In the current study, the travel rate of sensible heat exchange between the molten salt and filler is 1.19 times the entering hot salt velocity (u_{in}) during a charge process. A similar energy balance can be formulated for a latent heat-exchange region; however, the influence of phase change is dissimilar between the charging and discharging processes in the tank, necessitating separate formulations. In the charging mode, hot molten salt enters at the top of the porous bed and melts the surrounding PCM. The travel rate of this melt front is expressed as follows:

$$v_{lat,chg} = \frac{\rho_{l,in}C_{P,l}}{\varepsilon\rho_{l,in}C_{P,l} + (1-\varepsilon)\rho_s C_{P,s}\left[1 + \dfrac{1}{\text{Ste}}\left(\dfrac{T_h - T_c}{T_h - T_{sol}}\right)\right]} u_{in}. \tag{7.12}$$

Inspection of Eq. (7.12) reveals that the travel rate of the melt front slows with either increased heat of fusion (nondimensionalized as the inverse Stefan number) or as the solidus temperature approaches the hot operating limit. For the lowest melting point and heat of fusion (case 2), the charging melt front travels at a rate of 0.99 times the velocity of the hot molten salt, while for the highest melting point and heat of fusion (case 11), the travel rate is only 0.15 times the salt velocity. It should be noted that heat exchange in the region of the tank below the solidus temperature remains subject to the faster sensible heat transfer rate governed by Eq. (7.11). This disparity in travel rates deconstructs the porous-bed heat transfer into two separate regions.

Figure 7.4 illustrates this deconstruction with a plot of molten-salt temperature profile inside the case 5 porous bed during a charge process. Below the solidus point, the salt exhibits a sigmoid-shaped temperature profile typical of quartzite-filled thermocline tanks [49,58]. Above this point, the salt exhibits a delayed step increase in temperature, corresponding to the slower travel rate of the melt front. The remaining sensible heat exchange at temperatures above the phase change $\left(T > T_{liq}\right)$ is not governed by Eq. (7.11) but is instead constrained by the underlying melt front, producing the observed step increase. The axial separation of the two heat-exchange zones is also illustrated in Figure 7.4 with a plot of the thermal non-equilibrium or temperature difference between the molten salt and PCM filler. The separation results in an intermediate span of molten salt and PCM in equilibrium at the solidus temperature. As charging progresses, this axial span continues to grow until the leading sensible heat front reaches the tank floor and triggers a saturation condition.

Analogous behavior occurs during the tank discharge process. Cold molten salt enters at the bottom of the porous bed and recovers the latent heat inside the surrounding PCM, solidifying the material. The travel rate of this solidification front is expressed as follows:

$$
v_{lat,dis} = \frac{\rho_{l,in} C_{P,l}}{\varepsilon \rho_{l,in} C_{P,l} + (1-\varepsilon)\rho_s C_{P,s}\left[1 + \dfrac{1}{\text{Ste}}\left(\dfrac{T_h - T_c}{T_{liq} - T_c}\right)\right]} u_{in} .
\tag{7.13}
$$

Eq. (7.13) shows that the latent heat exchange again slows with increased heat of fusion but also as the liquidus temperature approaches the cold operating limit. This indicates that while tanks with low PCM melting temperatures can utilize the entire latent heat capacity during a charge process, the subsequent recovery during a discharge process decreases in response to the slower return rate of the solidification front up the height of the tank.

These trends again illustrate that latent heat thermocline tanks suffer a tradeoff between thermodynamic quality of the PCM filler and corresponding utilization. High melting temperatures (Θ_m = 0.75, 0.95) can support steam generation but exhibit the largest disparity in travel rate between latent and underlying sensible heat exchange during a charge process, resulting in poor utilization. Low melting temperatures (Θ_m = 0.05, 0.25) enable 100% utilization of the latent heat capacity but cannot support steam generation. However, the corresponding distortion in temperature profile inside the tank enables more sensible heat storage than the baseline quartzite, as seen in Figure 7.5. This small gain explains the minor increase in annual plant output with low-melting PCM relative to the quartzite-filled tank. The remaining melting temperature considered (Θ_m = 0.5) falls in the dead zone of the thermocline tank temperature gradient: too cold to support steam generation in the power block and too hot for return of surrounding molten salt to the solar receiver. As a result, the isothermal region between the advancing sensible heat exchange and the lagging latent heat exchange acts as a choke on the storage capability of the thermocline tank. The corresponding tank stores less heat than the quartzite-filled tank of equal size and enables less power output at a system level.

7.3.4   Cascaded Latent Heat Thermocline Tank

The preceding analysis revealed that a latent heat thermocline tank filled with a single phase-change material is unable to substantially outperform a quartzite rock bed with respect to storage capacity or system-level output; however, this barrier may be circumvented with a modified graded filler structure composed of multiple PCMs, each exhibiting a differing melting temperature. In this concept, the capsules are organized

inside the tank such that the melting temperature increases with axial height; such a tank will be referred to as a cascaded latent heat thermocline tank. Materials with low melting points are located near the bottom while materials with high melting temperatures are located near the top. The different PCMs would be expected to complement each other and result in a latent heat thermocline tank that stores more high-quality heat than a quartzite-filled tank of equal size.

The system-level modeling analysis is now extended to investigate the storage performance of a cascaded latent heat thermocline tank. The finite-volume model of the tank porous bed is first segmented into three equal-volume layers along the vertical direction, each composed of a PCM with different melting temperature. Applying the same five user-defined melting points from the previous analysis, a total of eight different cascaded PCM combinations are simulated, as summarized in Table 7.2. The heat of fusion is fixed at 124.5 kJ/kg (1/Ste = 0.5) for all layers in all cases. As before, each tank model is integrated into the system model and simulated in response to a full year of CSP plant operation. The annual plant performance data (capacity factor and thermal energy discard) are plotted in Figure 7.6 along with the baseline data for a quartzite-filled tank.

A majority of the cascade structure demonstrate marginal gains over quartzite, as was observed with the previous uniform structures with low melting points. The case D structure exhibits the lowest plant output, with a 20.7% discard of thermal energy and an annual capacity factor of 0.469, less than the output achieved with a quartzite-filled tank of equal size. The largest gains are observed with case E, which exhibits only 1.1% discard of thermal energy and an annual capacity factor of 0.584. This annual output equates to an additional 45.2 GWh$_e$ or 9.7% increase over implementation of a quartzite-filled tank of equal size. Given that the original motivation for PCM filler is to reduce thermocline tank size, the case E structure can also support a 16% reduction in tank diameter to match the plant output achieved with quartzite rock filler.

The variation in plant performance for different cascade combinations is explained by the temperature disparity in melting points between the three PCM layers. Among the combinations considered, case D exhibits the largest disparity from top to

bottom (270 K) and achieves the lowest plant output. In contrast, case E exhibits the smallest disparity (150 K) and achieves the greatest plant output. The three melting points in case E are also near the mean of the molten-salt temperature span, enabling similar latent heat exchange rates between charging, Eq. (7.12), and discharging, Eq. (7.13). While this similarity is desired, the melting points of the top and bottom layers must still remain outside the molten-salt thermal dead zone to avoid the choking phenomenon observed in the previous section with a uniform bed of $\Theta_m = 0.5$. Therefore, an optimal three-layer cascaded latent heat thermocline tank should include a top PCM layer that melts slightly above the molten-salt hot supply threshold and a bottom PCM layer that melts slightly below the cold return threshold.

Since particular designs of the cascade latent heat thermocline show improvement in energy storage over a conventional quartzite rock bed, it is reiterated that the current study applies a hypothetical PCM with a high thermal conductivity of 5 W/m-K. Suitable candidates for phase change materials (such as nitrate and carbonate salts) exhibit much lower conductivities on the order of 0.5 W/m-K, which would induce large temperature gradients inside the capsule and inhibit energy transfer with the surrounding heat transfer fluid. Additional consideration must also be directed towards the cost and physical stability of the encapsulated PCM. Long-term compatibility of the capsules with hot and cold molten salt should be verified with immersion tests similar to previous investigations of quartzite rock [29]. The economic benefit of the latent heat mechanism, either from increased plant revenue or from cost savings with tank size reduction, must also justify any material and fabrication expenses related to encapsulation.

7.4   Chapter Summary

A new computational model using a finite-volume method is developed to simulate mass and energy transport inside a thermocline tank filled with encapsulated phase-change material. A hypothetical PCM is applied to enable a one-to-one comparison with conventional quartzite rock filler. The storage model is then integrated into a system-level model of a 100 MW$_e$ molten-salt power tower plant to inform storage behavior with

realistic solar collection and steam generation processes. A parametric study of hypothetical PCM melt properties is conducted with this system model to ascertain the viability of latent heat as a replacement for quartzite rock.

Thermocline tanks filled with only a single PCM exhibit a persistent tradeoff between the thermodynamic quality of the PCM and the corresponding utilization of the added latent heat inside the tank. Low melting temperatures are well-utilized with complete phase change, but provide marginal energy benefits for steam generation in the power block. In contrast, high melting temperatures can support steam generation but are not utilized to a sufficient extent. This trend is an inherent limitation of energy transfer inside a dual-media thermocline tank. Modification of the porous bed with a cascaded PCM structure increases the utilization of the latent heat and can provide significant improvement over conventional quartzite rock filler. For a user-defined PCM heat of fusion of 124.5 kJ/kg (1/Ste = 0.5), a three-layer cascade structure yields either a 9.7% increase in annual power output or a 16% decrease in thermocline tank diameter relative to a quartzite-filled tank; however, this benefit remains highly sensitive to the selected melting points relative to the temperature thresholds for tank supply (steam generation) and tank return (solar heating).

Table 7.1. Case summary of inverse Stefan number and melting temperature for PCM filler in a latent heat thermocline tank.

Case	1/Ste	Θ_m
1	0	N/A
2	0.25	0.05
3	0.25	0.25
4	0.25	0.5
5	0.25	0.75
6	0.25	0.95
7	0.5	0.05
8	0.5	0.25
9	0.5	0.5
10	0.5	0.75
11	0.5	0.95

Table 7.2. Case summary of melting temperatures (Θ_m) in a three-layer cascade structure for a latent heat thermocline tank. All PCMs are assumed to have a latent heat that corresponds to an inverse Stefan number of 0.5.

Case	Top layer	Middle layer	Bottom layer
A	0.75	0.25	0.05
B	0.95	0.25	0.05
C	0.75	0.5	0.05
D	0.95	0.5	0.05
E	0.75	0.5	0.25
F	0.95	0.5	0.25
G	0.95	0.75	0.05
H	0.95	0.75	0.25
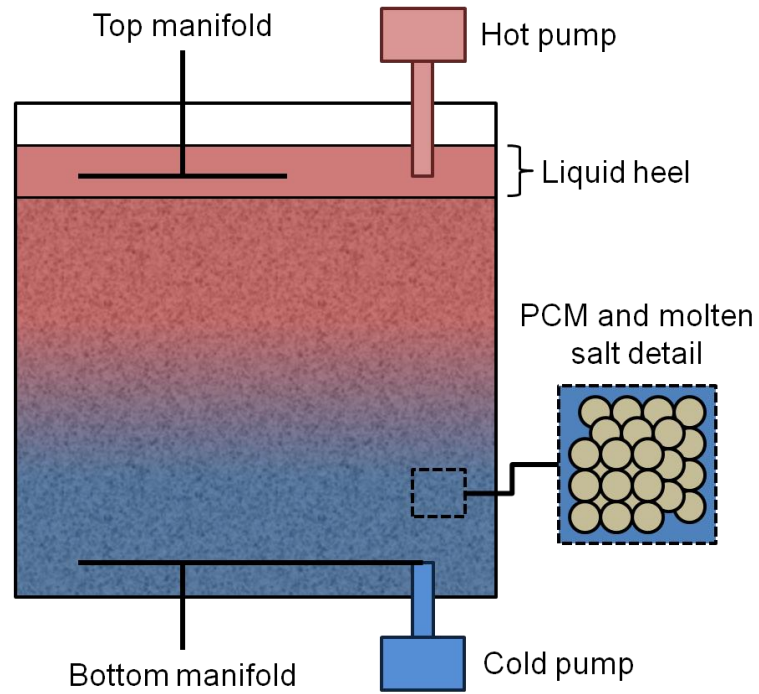
Figure 7.1. Schematic illustration of a molten-salt latent-heat-augmented thermocline tank, including the porous bed with encapsulated PCM and the pure liquid heel. Hot salt is supplied at the liquid heel through the top manifold and is extracted via the hot pump. Cold salt enters the porous bed through the bottom manifold but is also extracted through the manifold via the cold pump.
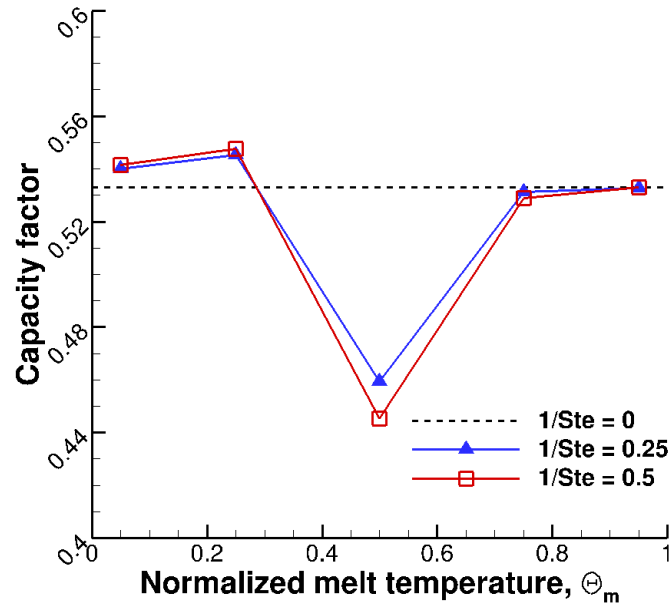
(a)
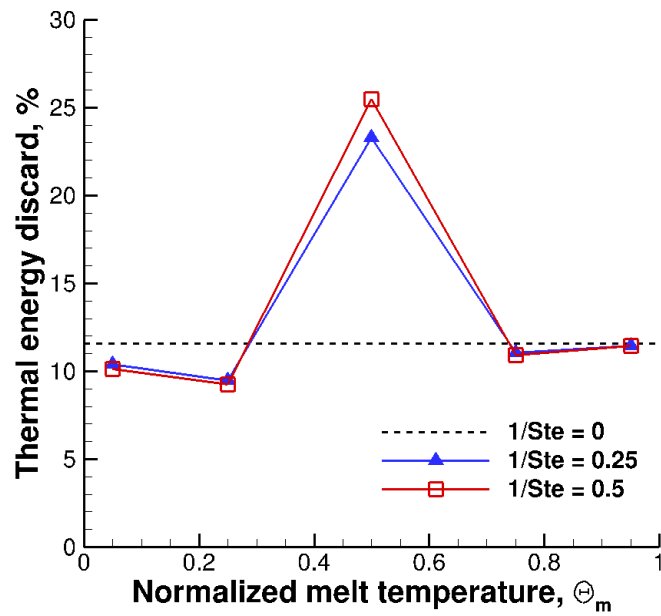
(b)

Figure 7.2. Annual power tower plant performance with respect to PCM melting temperature: (a) capacity factor and (b) thermal energy discard. The dashed lines illustrate a conventional quartzite-filled tank with no latent heat capacity.
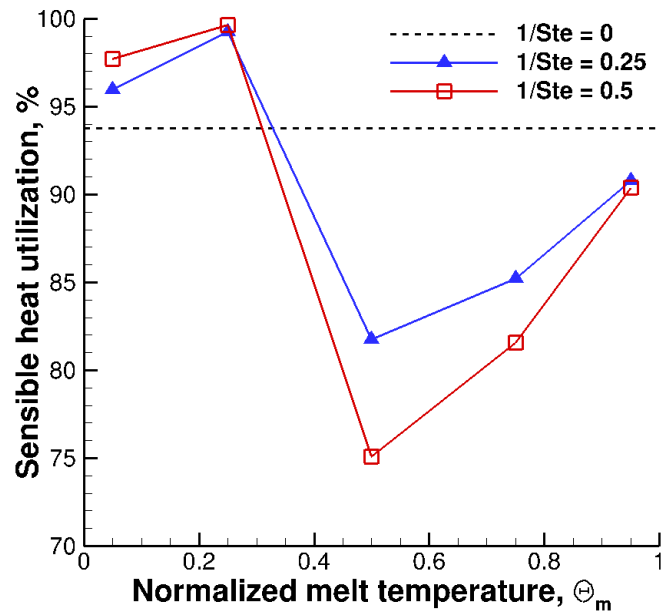
(a)
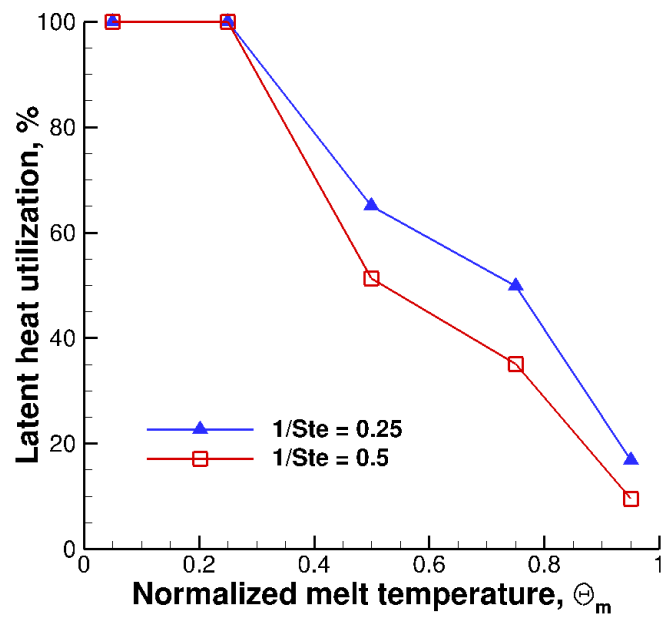
(b)

Figure 7.3. Maximum utilization of thermal energy capacity (corresponding to tank saturation for a single day during year-long simulation) with respect to the PCM melting temperature: (a) sensible heat and (b) latent heat.
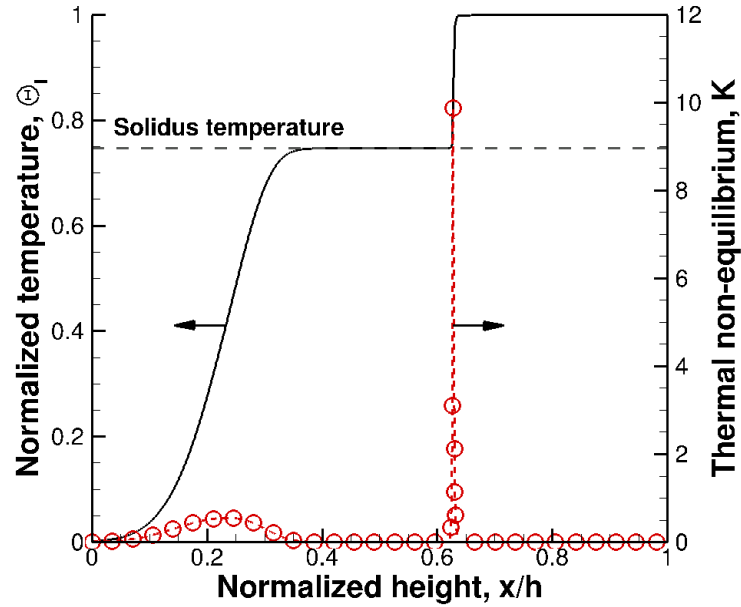
Figure 7.4. Molten-salt temperature profile for case 5 ($1/Ste = 0.25$, $\Theta_m = 0.75$) during a charge process. Below the solidus temperature, heat exchange between the molten salt and filler is sensible. Above the solidus temperature, the influence of latent heat distorts the temperature profile and results in a second heat-exchange region. These two regions are distinguished by the magnitude of thermal non-equilibrium between the molten salt and filler, plotted on the second y-axis.
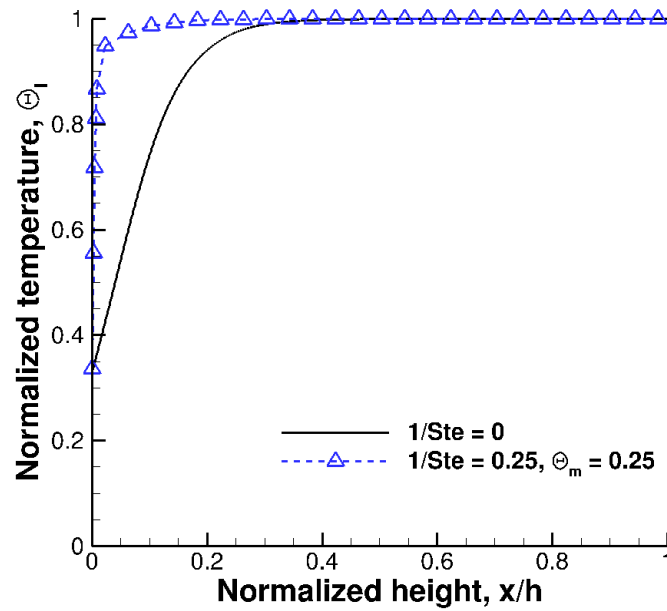
Figure 7.5. Normalized molten-salt temperature profiles inside the thermocline tank at saturation for case 1 (quartzite rock) and case 3 ($1/Ste = 0.25$, $\Theta_m = 0.25$). The step increase in temperature above the melting region enables the PCM-filled tank to store more sensible heat at saturation than quartzite (provided the melting temperature is below the molten salt return threshold), indicated by the higher temperatures observed near the floor of the thermocline tank.
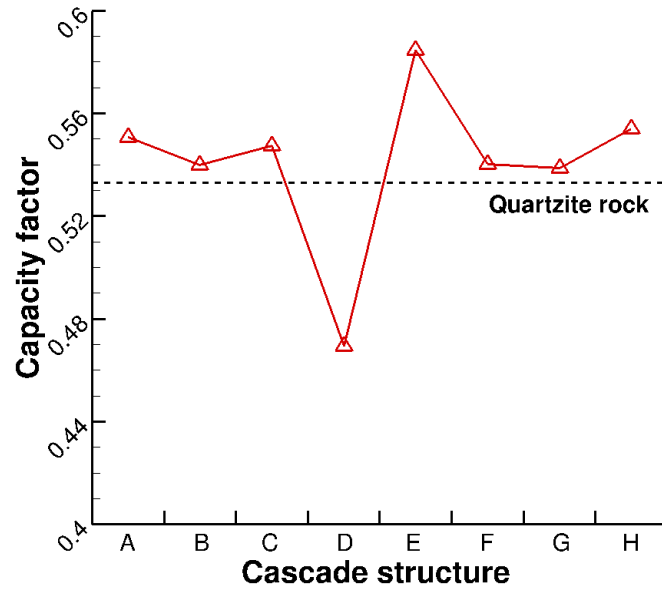
(a)
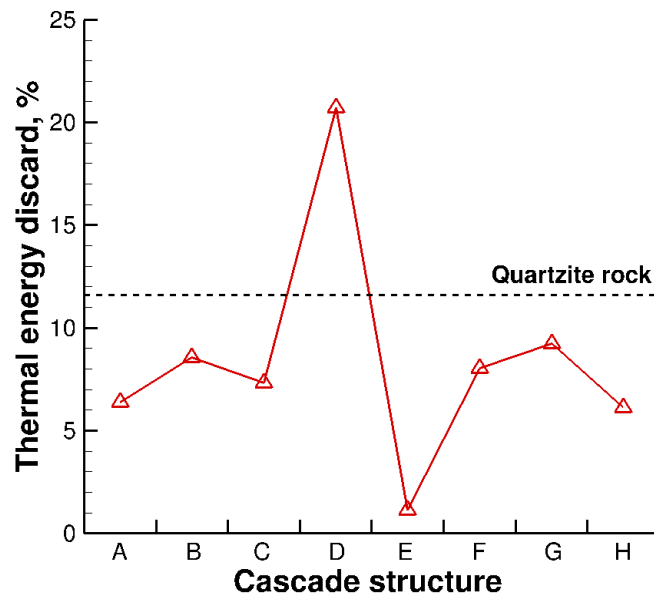
(b)

Figure 7.6. Annual power tower plant performance with a cascaded latent heat thermocline tank: (a) capacity factor and (b) thermal energy discard. Substantial benefits only occur when the top and bottom melting points are close to the respective threshold molten-salt supply and return temperatures, represented by case E.

CHAPTER 8. CONCLUSIONS AND FUTURE WORK

The principal objective of this work was to advance understanding of the design and control of thermocline storage for concentrating solar power plants. The key findings are summarized below, along with suggestions for future work.

8.1   Conclusions

In Chapter 3, a multidimensional computational fluid dynamics model of a dual-media molten-salt thermocline tank is presented to simulate thermal energy storage under repeated charge and discharge operations. The model builds upon previous work in the literature, with an expanded study of internal filler size and a consideration of practical limitations on tank height. Reducing the size of the internal filler results in a narrower heat-exchange region but also lowers the bed permeability, generating a tradeoff between thermal storage performance and required pumping power. Among the cases considered, a filler diameter of 1 cm is found to be a design optimum as it achieves similar storage performance as smaller granules but does not incur an excessive pressure drop. A common storage metric for thermocline tanks that enforces an arbitrary 95% temperature cut-off on usable tank outflow is also found to be too conservative as a portion of stored molten salt below this temperature limit should be viable for steam generation in the power block.

Chapter 4 continues this computational approach to instead examine the structural stability of the thermocline tank wall under repeated storage cycles. The established thermal solution informs a new mechanical model to predict the wall hoop stress generated by cyclic transport of hot and cold molten salt. An adverse cycling effect known as thermal ratcheting may occur if this stress exceeds the yield strength of the tank wall. For analysis, the porous bed is assumed to exhibit infinite rigidity and no cohesion,

such that the resultant wall stress is proportional to the amplitude of the wall temperature fluctuations. A parametric study of a composite tank wall design illustrates that the inclusion of thermal insulation between the bed and the tank wall best prevents thermal ratcheting by decoupling the transient thermal response of the tank wall from the internal cyclic storage operations. As model validation, a subsequent simulation of the thermocline tank installed at the historic Solar One power tower plant illustrates reasonable agreement between the predicted stress values and recorded strain gage data.

In Chapter 5, a new reduced-order model of energy transport in a thermocline tank is developed to avoid the high computing cost associated with the CFD approach applied in the Chapters 3 and 4. The model is solved with a user-generated finite-volume approach; validated with published temperature data from a previous thermocline tank experiment and providing thermal solutions two orders-of-magnitude faster than that of commercial CFD software. The low-cost storage model is then integrated into a system-level model of a 100 MW_e molten-salt power tower plant, enabling the simulated thermocline tank to be informed with realistic solar collection and power production processes. The resultant plant capacity factor and tank storage effectiveness observed with a year of recorded sunlight data verify that a thermocline tank is a suitable storage concept for long-term operation in a CSP plant.

Chapter 6 extends analysis of the 100 MW_e system model to obtain an economic perspective of the annual plant operation. A parametric study of the power tower solar multiple and the thermocline tank size is conducted to identify the minimum levelized cost of electricity obtainable. Among the cases considered, a solar multiple of 3 and a thermocline storage capacity of 16 hours achieve a minimum levelized cost of 12.2 ¢/kWh_e. This value exceeds the target power purchase price of 6 ¢/kWh_e and indicates that optimization of thermal energy storage alone will not achieve grid parity with fossil fuels. Furthermore, operation of conventional two-tank storage exhibits only slightly larger levelized costs than an equal-sized thermocline, implying that the capital savings associated with a thermocline are divorced from significant reductions in electricity prices.

Chapter 7 updates the reduced-order thermocline tank model with a substitution of the internal rock filler for an encapsulated phase change material. The updated storage model is then reintegrated into the established system-level model to assess the benefit of the added latent heat storage mechanism for different PCM melting temperatures and heats of fusion. For a hypothetical PCM, inclusion of a single melting temperature inside the thermocline tank does not yield substantial storage or plant output gains over the conventional solid filler. At low melting temperatures (relative to the molten-salt operating span), the latent heat is well-utilized inside the tank but is not useful for steam generation in the power block. In contrast, high melting temperatures support steam generation but the latent heat capacity inside the tank is not sufficiently utilized to outperform a pure sensible heat tank of equal size. This limitation may be circumvented with a cascaded PCM structure composed of multiple melting temperatures along the tank height, but improvement is shown to be highly sensitive to the selection of melt points relative to the thermocline operating temperatures.

8.2   Suggested Future Work

8.2.1   Thermocline Energy Storage

An imperative next step for molten-salt thermocline energy storage is large-scale experimental demonstrations of the concept. One such demonstration was previously conducted by Sandia National Labs with a 2.3 MWh_t tank [29], but this system has since been mothballed with little documentation outside of a single discharge process (see Figure 5.2). A new experimental tank, outfitted with thermocouples and strain gages, would therefore provide a wealth of unprecedented information on actual thermocline behavior. Key points of interest include the influence of different flow fields on thermal stratification, the impact and mitigation of external heat losses, and the stability of wall hoop stress after multiple storage cycles.

The ability of a thermocline tank to store and deliver heat is a strong function of the flow uniformity maintained across the porous bed. While the bed itself helps to dampen flow aberrations via permeability restrictions, significant nonuniformities can

still result from either external heat losses or flow maldistribution. This then leads to radial temperature gradients that smear the desired thermal stratification along the height of the tank. While heat losses to the surroundings can be resolved with thermal insulation, additional study is needed to optimize the impact of insulation with respect to tank performance and cost. The other loss factor, flow maldistribution, is a consequence of poorly designed tubing manifolds inside the thermocline tank. Future work must both design and demonstrate suitable manifolds that are capable of supplying molten salt across a large tank diameter at uniform velocity. The bottom manifold design must also withstand crushing or clogging from the filler material above.

Quartzite rock has proven to be a successful filler candidate for molten-salt thermocline tanks, but the material exhibits a crystal phase transition near 573 °C and may not be suitable for next-generation power tower plants with operating temperatures ≥ 600 °C. Reason for this concern is the large volume change at this transition, which may lead to unacceptable hoop stresses or thermal ratcheting effects along the tank wall. Alternative solid filler candidates should therefore be explored to replace and preferably improve upon quartzite rock. Taconite has been shown to be compatible with molten salt, but is more expensive than quartzite and lacks detailed property data. Given the low material cost of quartzite, practical filler substitution is likely limited to other rocks or waste materials such that the capital cost benefits of the dual-media thermocline concept are retained. New granular physics models are also needed to improve simulation of bed deformation inside the thermocline tank during cyclic storage operations and further understanding of thermal ratcheting potential.

Apart from structural stability, alternative filler materials (either solid or phase change) are also desired to increase the thermal energy density of thermocline storage and reduce the overall tank size. However, it should be noted that substitution of quartzite with denser materials to boost the volumetric heat capacity may be counterproductive due to tank height limitations governed by the underlying foundation and soil bearing capacity. For solid materials, focus should instead be spent on larger specific heat capacities. For latent heat enhancement, suitable phase change materials must form a cascade structure that complies with the operating temperatures of the CSP

plant as discussed in Chapter 7. Even if such a cascade can be assembled, the practicality of using encapsulated PCMs as thermocline filler remains to be demonstrated. Pertinent tasks include feasible and scalable encapsulation processes, verification of long-term compatibility with a thermally cycled molten-salt environment, and economic justification for the replacement of already proven solid fillers.

8.2.2   System-level Modeling

The molten-salt power tower plant model developed in Chapters 5 – 7 operates under a turbine dispatch strategy known as sun following; electricity is produced whenever sufficient thermal energy is available from storage, independent of the current grid demand. As such, the installed thermocline tank primarily serves to extend power production beyond sunset and into nighttime. In reality, a CSP plant should respond to grid demand and dispatch peak power during the most lucrative hours of the day (*e.g.*, weekday afternoons) in order to maximize the economic value of the turbine output. A more sophisticated control strategy is therefore needed in the system model to account for time-of-day electricity prices and target thermocline tank operations to yield the maximum plant revenue. However, a consequence of delayed dispatching is that the thermocline tank will hold high temperature heat for longer periods of time and may suffer increased heat losses or stratification smearing as a result. Thus, additional operating procedures should remain in place to ensure that excessive exergy losses do not occur inside the tank.

All system-level simulations conducted in the preceding chapters were informed with the same year of recorded sunlight data from Barstow, CA in 1977. While this specific dataset is attractive for its high annual insolation and 15-minute granularity, the system model should also be exposed to sunlight data from other locations to gauge the influence of geography on both the power plant output and the thermocline storage performance. Certain plant sites with prolonged cloudiness may be particularly unsuitable to thermocline storage given the sensitivity of the tank to unwanted thermal diffusion during periods of plant shutdown or tank standby.

A final modification to the system-level analysis is an update for potential future increases in maximum operating temperature. If a heat transfer fluid with an operating temperature above 600 °C can be implemented in a power tower plant, potential plant benefits include a higher Carnot efficiency and a transition to a more efficient supercritical steam Rankine cycle. A new power block model should therefore be developed to simulate the performance of the supercritical cycle and to investigate operation within the power tower system model. The plant analysis should further demonstrate the viability of the thermocline concept as an energy storage device and also quantify the electric and economic benefits obtainable with a supercritical cycle.

LIST OF REFERENCES

LIST OF REFERENCES

[1]   H. Müller-Steinhagen, 2010, "From megawatt to gigawatt: new developments in concentrating solar thermal power," Proceedings of the 14th International Heat Transfer Conference, Washington D.C.

[2]   J. A. Duffie, and W. A. Beckman, 2006, Solar Engineering of Thermal Processes, John Wiley & Sons.

[3]   D. R. Mills, and G. L. Morrison, 2000, "Compact linear Fresnel reflector solar thermal powerplants," Sol. Energy, **68**, pp. 263–283.

[4]   L. G. Radosevich, 1988, Final report on the power production phase of the 10MWe solar central receiver pilot plant, SAND87-8022, Sandia National Laboratories.

[5]   National Renewable Energy Laboratory, 2012, "Concentrating solar power projects: power tower projects," http://www.nrel.gov/csp/solarpaces/ power_tower.cfm.

[6]   G. J. Kolb, C. K. Ho, T. R. Mancini, and J. A. Gary, 2011, Power tower technology roadmap and cost reduction plan, SAND2011-2419, Sandia National Laboratories.

[7]   U.S. Department of Energy, 2012, SunShot Vision Study, DOE/GO-102012-3037.

[8]   D. W. Kearney, U. Herrmann, P. Nava, B. Kelly, R. Mahoney, J. Pacheco, R. Cable, N. Potrovitza, D. Blake, and H. Price, 2003, "Assessment of a Molten Salt Heat Transfer Fluid in a Parabolic Trough Solar Field," ASME J. Sol. Energy Eng., **125**, pp. 170–176.

[9]   H. Kreetz, and K. Lovegrove, 2002, "Exergy analysis of an ammonia synthesis reactor in solar thermochemical power system," Sol. Energy, **73**, pp. 187–194.

[10]   K. Lovegrove, A. Luzzi, I. Soldiani, and H. Kreetz, 2004, "Developing ammonia based thermochemical energy storage for dish power plants," Sol. Energy, **76**, pp. 331–337.

[11]   U. Herrmann, and D. W. Kearney, 2002, "Survey of thermal energy storage for parabolic trough power plants," ASME J. Sol. Energy Eng., **124**, pp. 145–152.

[12] W. D. Steinmann, D. Laing, and R. Tamme, 2010, "Latent heat storage systems for solar thermal power plants and process heat applications," ASME J. Sol. Energy Eng., **132**, p. 021003.

[13] D. Laing, T. Bauer, D. Lehmann, and C. Bahl, 2010, "Development of a thermal energy storage system for parabolic trough power plants with direct steam generation," ASME J. Sol. Energy Eng., **132**, p. 021011.

[14] D. Laing, C. Bahl, T. Bauer, D. Lehmann, and W. D. Steinmann, 2011, "Thermal energy storage for direct steam generation," Sol. Energy, **85**, pp. 627–633.

[15] H. Shabgard, T. L. Bergman, N. Sharifi, and A. Faghri, 2010, "High temperature latent heat thermal energy storage using heat pipes," Int. J. Heat Mass Transf., **53**, pp. 2979–2988.

[16] C. W. Robak, T. L. Bergman, and A. Faghri, 2011, "Enhancement of latent heat energy storage using embedded heat pipes," Int. J. Heat Mass Transf., **54**, pp. 3476–3484.

[17] C. W. Robak, T. L. Bergman, and A. Faghri, 2011, "Economic evaluation of latent heat thermal energy storage using embedded thermosyphons for concentrating solar power applications," Sol. Energy, **85**, pp. 2461–2473.

[18] S. M. Aceves, H. Nakamura, G. M. Reistad, and J. Martinez-Frias, 1998, "Optimization of a class of latent thermal energy storage systems with multiple phase-change materials," ASME J. Sol. Energy Eng., **120**, pp. 14–19.

[19] H. Michels, and R. Pitz-Paal, 2007, "Cascaded latent heat storage for parabolic trough solar power plants," Sol. Energy, **81**, pp. 829–837.

[20] D. Laing, W. D. Steinmann, M. Fiß, R. Tamme, T. Brand, and C. Bahl, 2008, "Solid media thermal storage development and analysis of modular storage operation concepts for parabolic trough power plants," ASME J. Sol. Energy Eng., **130**, p. 011006.

[21] D. Laing, D. Lehmann, M. Fiß, and C. Bahl, 2009, "Test results of concrete thermal energy storage for parabolic trough power plants," ASME J. Sol. Energy Eng., **131**, p. 041007.

[22] X. Py, N. Calvet, R. Olives, A. Meffre, P. Echegut, C. Bessada, E. Veron, and S. Ory, 2011, "Recycled material for sensible heat based thermal energy storage to be used in concentrated solar power plants," ASME J. Sol. Energy Eng., **133**, p. 031008.

[23] T. Wang, D. Mantha, and R. G. Reddy, 2013, "Novel low melting point quarternary eutectic system for solar thermal energy storage," Appl. Energy, **102**, pp. 1422–1429.

[24] J. W. Raade, and D. Padowitz, 2011, "Development of molten salt heat transfer fluid with low melting point and high thermal stability," ASME J. Sol. Energy Eng., **133**, p. 031013.

[25] Electric Power Research Institute, 2010, Solar thermal storage systems: preliminary design study, 1019581, EPRI.

[26] J. E. Pacheco, 2002, Final test and evaluation results from the Solar Two project, SAND2002-0120, Sandia National Laboratories.

[27] R. Gabbrielli, and C. Zamparelli, "Optimal design of a molten salt thermal storage tank for parabolic trough solar power plants," ASME J. Sol. Energy Eng., **131**, p. 041001.

[28] F. Zaversky, J. Garcia-Barberena, M. Sanchez, and D. Astrain, 2013, "Transient molten salt two-tank thermal storage modeling for CSP performance simulations," Sol. Energy, **93**, pp. 294–311.

[29] J. E. Pacheco, S. K. Showalter, and W. J. Kolb, 2002, "Development of a molten-salt thermocline thermal storage system for parabolic trough plants," ASME J. Sol. Energy Eng., **124**, pp. 153–159.

[30] D. Brosseau, J. W. Kelton, D. Ray, M. Edgar, K. Chisman, and B. Emms, 2005, "Testing of thermocline filler materials and molten-salt heat transfer fluids for thermal energy storage systems in parabolic trough power plants," ASME J. Sol. Energy Eng., **207**, pp. 109–116.

[31] N. Calvet, J. C. Gomez, A. Faik, V. V. Roddatis, A. Meffre, G. C. Glatzmaier, S. Doppiu, and X. Py, 2013, "Compatibility of a post-industrial ceramic with nitrate molten salts for use as filler material in a thermocline storage system," Appl. Energy, **109**, pp. 387–393.

[32] Honeywell Energy Resources Center, 1977, Solar pilot plant, phase 1. Preliminary design report volume 5. Thermal storage subsystem, SAN1109-87, Sandia National Laboratories.

[33] McDonnell Douglas Astronautics Company, 1986, 10 MWe solar thermal central receiver pilot plant mode 5 (test 1150) and mode 6 (test 1160) test report, SAND86-8175, Sandia National Laboratories.

[34] S. E. Faas, L. R. Thorne, E. A. Fuchs, and N. D. Gilbertsen, 1986, 10 MWe solar thermal central receiver plant: thermal storage subsystem evaluation - final report, SAND86-8212, Sandia National Laboratories.

[35] B. D. Pomeroy, 1979, "Thermal energy storage in a packed bed of iron spheres with liquid sodium coolant," Sol. Energy, **23**, pp. 513–515.

[36]   D. Bharathan, and G. C. Glatzmaier, 2009, "Progress in thermal energy storage modeling," Proceedings of the ASME 2009 3rd International Conference on Energy Sustainability, San Francisco, CA.

[37]   S. Afrin, E. Cordero, S. De La Rosa, V. Kumar, D. Bharathan, G. C. Glatzmaier, and Z. Ma, 2012, "Computational analysis of pipe flow distributor for a thermocline based thermal energy storage system," Proceedings of the ASME 2012 6th International Conference on Energy Sustainability, San Diego, CA.

[38]   F. G. F. Qin, X. Yang, Z. Ding, Y. Zuo, Y. Shao, R. Jiang, and X. Yang, 2012, "Thermocline stability criterions in single-tanks of molten salt thermal energy storage," Appl. Energy, **97**, pp. 816–821.

[39]   R. Bayon, and E. Rojas, 2013, "Simulation of thermocline storage for solar thermal power plants: from dimensionless results to prototypes and real-size tanks," Int. J. Heat Mass Transf., **60**, pp. 713–721.

[40]   J. T. Van Lew, P. Li, C. L. Chan, W. Karaki, and J. Stephens, 2011, "Analysis of heat storage and delivery of a thermocline tank having solid filler material," ASME J. Sol. Energy Eng., **133**, p. 021003.

[41]   T. E. W. Schumann, 1929, "Heat transfer: a liquid flowing through a porous prism," J. Frankl. Inst., **208**, pp. 405–416.

[42]   W. Karaki, P. Li, J. Van Lew, M. M. Valmiki, C. Chan, and J. Stephens, 2011, "Experimental investigation of thermal storage processes in a thermocline storage tank," Proceedings of the ASME 2011 5th International Conference on Energy Sustainability, Washington D.C.

[43]   M. M. Valmiki, W. Karaki, P. Li, J. Van Lew, C. Chan, and J. Stephens, 2012, "Experimental investigation of thermal storage processes in a thermocline tank," ASME J. Sol. Energy Eng., **134**, p. 041003.

[44]   P. Li, J. Van Lew, W. Karaki, C. Chan, J. Stephens, and Q. Wang, 2011, "Generalized charts of energy storage effectiveness for thermocline heat storage tank design and calibration," Sol. Energy, **85**, pp. 2130–2143.

[45]   M. M. Valmiki, P. Li, and C. Chan, 2012, "Parametric study simulating the daily operation of a thermocline thermal storage system," Proceedings of the ASME 2012 6th International Conference on Energy Sustainability, San Diego, CA.

[46]   B. Xu, P. Li, and C. L. Chan, 2012, "Extending the validity of lumped capacitance method for large Biot number in thermal storage application," Sol. Energy, **86**, pp. 1709–1724.

[47]   Z. Yang, and S. V. Garimella, 2010, "Thermal analysis of solar thermal energy storage in a molten-salt thermocline," Sol. Energy, **84**, pp. 974–985.

[48] Z. Yang, and S. V. Garimella, 2010, "Molten-salt thermal energy storage in thermoclines under different environmental boundary conditions," Appl. Energy, **87**, pp. 3322–3329.

[49] Z. Yang, and S. V. Garimella, 2013, "Cyclic operation of molten-salt thermal energy storage in thermoclines for solar power plants," Appl. Energy, **103**, pp. 256–265.

[50] C. Xu, Z. Wang, Y. He, X. Li, and F. Bai, 2012, "Sensitivity analysis of the numerical study on the thermal performance of a packed-bed molten salt thermocline thermal storage system," Appl. Energy, **92**, pp. 65–75.

[51] C. Xu, X. Li, Z. Wang, Y. He, and F. Bai, 2013, "Effects of solid particle properties on the thermal performance of a packed-bed molten-salt thermocline thermal storage system," Appl. Therm. Eng., **57**, pp. 69–80.

[52] G. J. Kolb, and V. Hassani, 2006, "Performance analysis of thermocline energy storage proposed for the 1 MW Saguaro solar trough plant," Proceedings of the ASME International Solar Energy Conference, Denver, CO.

[53] G. J. Kolb, 2011, "Evaluation of annual performance of 2-tank and thermocline thermal storage systems for trough plants," ASME J. Sol. Energy Eng., **133**, p. 031023.

[54] S. Pendyala, P. Sridharan, S. Kuravi, C. K. Jotshi, M. K. Ram, M. Rahman, E. Stefanakos, and D. Y. Goswami, 2012, "Macroencapsulation of sodium nitrate for thermal energy storage in solar thermal power," Proceedings of the ASME 2012 6th International Conference on Energy Sustainability, San Diego, CA.

[55] A. R. Archibold, M. M. Rahman, D. Y. Goswami, and E. L. Stefanakos, 2012, "Parametric investigation of the melting and solidification process in an encapsulated spherical container," Proceedings of the ASME 2012 6th International Conference on Energy Sustainability, San Diego, CA.

[56] A. Felix Regin, S. C. Solanki, and J. S. Saini, 2009, "An analysis of a packed bed latent heat thermal energy storage system using PCM capsules: Numerical investigation," Renew. Energy, **34**, pp. 1765–1773.

[57] K. Nithyanandam, R. Pitchumani, and A. Mathur, 2012, "Analysis of a latent thermocline energy storage system for concentrating solar power plants," Proceedings of the ASME 2012 6th International Conference on Energy Sustainability, San Diego, CA.

[58] S. M. Flueckiger, and S. V. Garimella, 2012, "Second-law analysis of molten-salt thermal energy storage in thermoclines," Sol. Energy, **86**, pp. 1621–1631.

[59] Coastal Chemical Co., 2010, "HITEC heat transfer salt," http://www.coastalchem.com.

[60] E. E. Gonzo, 2002, "Estimating correlations for the effective thermal conductivity of granular materials," Chem. Eng. J., **90**, pp. 299–302.

[61] V. Beckermann, and R. Viskanta, 1988, "Natural convection solid/liquid phase change in porous media," Int. J. Heat Mass Transf., **31**, pp. 35–46.

[62] S. Krishnan, J. Y. Murthy, and S. V. Garimella, 2004, "A two-temperature model for analysis of passive thermal control systems," ASME J. Heat Transf., **126**, pp. 628–637.

[63] N. Wakao, and S. Kaguei, 1982, Heat and Mass Transfer in Packed Beds, Gordon Beach, New York.

[64] S. W. Churchill, and M. Bernstein, 1977, "A correlating equation for forced convection from gases and liquids to a circular cylinder in crossflow," ASME J. Heat Transf., **99**, pp. 300–306.

[65] Fluent Inc., 2012, "Fluent User's Guide, Lebanon, NH."

[66] R. I. Issa, 1986, "Solution of implicitly discretized fluid flow equations by operator splitting," J. Comput. Phys., **62**, pp. 40–65.

[67] National Climate Data Center, 2011, http://www.ncdc.noaa.gov.

[68] D. A. Nield, 2000, "Resolution of a paradox involving viscous dissipation and non-linear drag in a porous medium," Transp. Porous Media, **41**, pp. 349–357.

[69] S. Flueckiger, Z. Yang, and S. V. Garimella, 2011, "An integrated thermal and mechanical investigation of molten-salt thermocline energy storage," Appl. Energy, **88**, pp. 2098–2105.

[70] S. M. Flueckiger, Z. Yang, and S. V. Garimella, 2012, "Thermomechanical simulation of the Solar One thermocline storage tank," ASME J. Sol. Energy Eng., **134**, p. 041014.

[71] S. M. Flueckiger, Z. Yang, and S. V. Garimella, 2011, "Thermocline energy storage in the Solar One power plant: An experimentally validated thermomechanical investigation," Proceedings of the ASME 2011 5th International Conference on Energy Sustainability, Washington D.C.

[72] G. J. Kolb, and U. Nikolai, 1988, Performance evaluation of molten salt theraml storage systems, SAND87-3002, Sandia National Laboratories.

[73] ANSYS Inc., 2012, "ANSYS User's Guide, Lebanon, NH."

[74] Weather Underground, 2011, "History for Daggett-Barstow, CA," http://www.wunderground.com/history/airport/KDAG/1983/5/19/DailyHistory.html?req_city=Barstow&req_state=CA&req_statename=California.

[75] Online Materials Information Resource - Matweb, 2013, http://www.matweb.com/.

[76] F. P. Incropera, and D. P. DeWitt, 2002, Fundamentals of Heat and Mass Transfer, John Wiley & Sons.

[77] S. M. Flueckiger, B. D. Iverson, S. V. Garimella, and J. E. Pacheco, 2014, "System-level simulation of a solar power tower plant with thermocline thermal energy storage," Appl. Energy, **113**, pp. 86–96.

[78] D. A. Nissen, 1982, "Thermophysical properties of the equimolar mixture NaNO3-KNO3 from 300C to 600C," J. Chem. Eng. Data, **27**, pp. 269–273.

[79] J. E. Pacheco, M. E. Ralph, J. M. Chavez, S. R. Dunkin, E. E. Rush, C. H. Ghanbari, and M. W. Matthews, 1995, Results of molten salt panel and component experiments for solar central receivers, SAND94-2525, Sandia National Laboratories.

[80] J. Cote, and J.-M. Konrad, 2005, "Thermal conductivity of base-coarse materials," Can. Geotech. J., **42**, pp. 61–78.

[81] B. L. Kistler, 1986, A user's manual for DELSOL3, SAND86-8018, Sandia National Laboratories.

[82] F. Lippke, 1995, Simulation of the part-load behavior of a 30 MWe SEGS Plant, SAND95-1293, Sandia National Laboratories.

[83] J. Spelling, M. Jocker, and A. Martin, 2012, "Thermal modeling of a solar steam turbine with a focus on start-up time reduction," ASME J. Eng. Gas Turbines Power, **134**, p. 013001.

[84] A. M. Patnode, 2006, "Simulation and performance evaluation of parabolic trough solar power plants," MSME Thesis, University of Wisconsin-Madison.

[85] G. J. Kolb, 2011, An evaluation of possible next-generation high-temperature molten-salt power towers, SAND2011-9320, Sandia National Laboratories.

[86] M. C. Stoddard, S. E. Faas, C. J. Chiang, and J. A. Dirks, 1987, SOLERGY, SAND86-8060, Sandia National Laboratories.

[87] S. M. Flueckiger, B. D. Iverson, and S. V. Garimella, "Economic optimization of a concentrating solar power plant with molten-salt thermocline storage," ASME J. Sol. Energy Eng., (accepted for publication).

[88] S. M. Flueckiger, B. D. Iverson, and S. V. Garimella, 2013, "Simulation of a concentrating solar power plant with molten-salt thermocline storage for optimized annual performance," Proceedings of the ASME 2013 7th International Conference on Energy Sustainability, Minneapolis, MN.

[89] National Renewable Energy Laboratory, 2013, "Simple levelized cost of energy (LCOE) calculator," http://www.nrel.gov/analysis/.

[90] National Renewable Energy Laboratory, 2012, "System Advisor Model, Ver. 2012.11.30," https://sam.nrel.gov/.

[91] S. M. Flueckiger, and S. V. Garimella, 2013, "Latent heat augmentation of thermocline energy storage for concentrating solar power - a system-level assessment," (in review).

[92] V. R. Voller, and C. Prakash, 1987, "A fixed grid numerical modelling methodology for convection-diffusion mushy region phase-change problems," Int. J. Heat Mass Transf., **30**, pp. 1709–1719.

[93] B. D. Iverson, S. M. Flueckiger, and B. Earhart, 2011, "Trough heat collection deformation and solar intercept impact," Proceedings of SolarPACES 2011, Granada, Spain.

[94] R. W. Bradshaw, J. G. Cordaro, and N. P. Siegel, 2009, "Molten nitrate salt development for thermal energy storage in parabolic trough solar power systems," Proceedings of the ASME 2009 3rd International Conference on Energy Sustainability, San Francisco, CA.

[95] J. W. Raade, and D. Padowitz, 2010, "Development of molten salt heat transfer fluid with low melting point and high thermal stability," Proceedings of SolarPACES 2010, Perpignan, France.

[96] G. J. Kolb, C. Ho, B. D. Iverson, T. A. Moss, and N. P. Siegel, 2010, "Freeze-thaw tests of trough receivers employing a molten salt working fluid," Proceedings of the ASME 2010 4th International Conference on Energy Sustainability, Phoenix, AZ.

[97] B. D. Iverson, S. T. Broome, and N. P. Siegel, 2010, "Temperature dependent mechanical property testing of nitrate thermal storage salts," Proceedings of SolarPACES 2010, Perpignan, France.

[98] B. D. Iverson, J. G. Cordaro, and A. M. Kruizenga, 2011, "Thermal property testing of nitrate thermal storage salts in the solid-phase," Proceedings of the ASME 2011 5th International Conference on Energy Sustainability, Washington D.C.

[99] Schott Solar, 2011, "Material properties of stainless steel 321H."

[100] F. Burkholder, and C. Kutscher, 2009, Heat loss testing of Schott's 2008 PTR70 parabolic trough receiver, NREL/TP-550-45633, National Renewable Energy Laboratory.

[101] S. M. Flueckiger, S. V. Garimella, and E. A. Groll, 2012, "Numerical study of supercritical CO2 convective heat transfer in advanced Brayton cycles for concentrated solar power," Proceedings of the ASME 2012 6th International Conference on Energy Sustainability, San Diego, CA.

[102] E. J. Parma, S. A. Wright, M. E. Vernon, D. D. Fleming, G. E. Rochau, A. J. Suo-Anttila, A. Al Rashdan, and P. V. Tsvetkov, 2011, Supercritical CO2 direct cycle gas fast reactor (SC-GFR) concept, SAND11-2525, Sandia National Laboratories.

[103] R. Chacartegui, J. M. Muñoz de Escalona, D. Sánchez, B. Monje, and T. Sánchez, 2011, "Alternative cycles based on carbon dioxide for central receiver solar power plants," Appl. Therm. Eng., **31**, pp. 872–879.

[104] V. Dostal, P. Hejzlar, and M. J. Driscoll, 2006, "The supercritical carbon dioxide power cycle: comparison to other advanced power cycles," Fission React., **154**, pp. 283–301.

[105] S. A. Wright, R. F. Radel, M. E. Vernon, G. E. Rochau, and P. S. Pickard, 2010, Operation and analysis of a supercritical CO2 Brayton cycle, SAND2010-0171, Sandia National Laboratories.

[106] S. S. Pitla, D. M. Robinson, E. A. Groll, and S. Ramadhyani, 1998, "Heat transfer from supercritical carbon dioxide in tube flow: a critical review," Int. J. HVAC Refrig. Res., **4**, pp. 281–301.

[107] A. J. Ghajar, and A. Asadi, 1986, "Improved forced convective heat-transfer correlations for liquids in the near-critical region," AIAA J., **24**, pp. 2030–2037.

[108] B. Hubacher, 2003, "Experimental and theoretical performance analysis of carbon dioxide compressors," MSME, Purdue University.

[109] S. Holloway, W. T. Horton, E. A. Groll, D. Sherman, and M. Albertin, 2010, "Experimental performance of a prototype carbon dioxide compressor," Proceedings of the International Compressor Engineering Conference, Purdue University, IN.

[110] R. Span, and W. Wagner, 1996, "A new equation of state for carbon dioxide covering the fluid region from the triple-point temperature to 1100 K at pressures up to 800 MPa," J. Phys. Chem. Ref. Data, **25**, pp. 1409–1596.

[111] V. Vesovic, W. A. Wakham, G. A. Olchowy, J. V. Sengers, J. T. R. Watson, and J. Millat, 1990, "The transport properties of carbon dioxide," J. Phys. Chem. Ref. Data, **19**.

[112] S. V. Patankar, and D. B. Spalding, 1972, "A calculation procedure for heat, mass and momentum transfer in three-dimensional parabolic flows," Int. J. Heat Mass Transf., **15**, pp. 1787–1806.

[113] B. E. Launder, and D. B. Spalding, 1974, "The numerical computation of turbulent flows," Comput. Methods Appl. Mech. Eng., **3**, pp. 269–289.

APPENDICES

Appendix A.   Parabolic Trough Heat Collection Element Deformation

The material in this appendix was presented at *SolarPACES 2011 in Granada, Spain* [93]. It has been authored in partnership with Sandia National Laboratories, a multi-program laboratory managed and operated by Sandia Corporation, a wholly owned subsidiary of Lockheed Martin Corporation, for the U.S. Department of Energy's National Nuclear Security Administration under contract DE-AC04-94AL85000. Experimental work discussed herein was performed by Dr. Brian D. Iverson and Mr. Brian Earhart.

A.1.   Introduction

Transition to molten-salt heat transfer fluid in concentrated solar power plants is attractive due to the potential for thermal energy storage and higher operating temperatures, increasing both the capacity factor and thermal efficiency of the plant. However, concerns exist regarding the use of molten salt in parabolic trough collectors including the potential of salt solidification and recovery from freezing in the event of total power failure. Lower melting point salt formulations have been developed that would essentially provide increased time before the initiation of solidification [94,95]. Delay of the onset of freezing can be effective assuming a timely power restoration and essentially mitigates the risk of such a solidification event occurring. Regardless, any salt that has a solidification temperature above ambient temperature would still have some level of risk in its usage.

The potential for a freeze event necessitates an understanding of freeze event recovery and the possible detrimental effects associated with returning to normal operation. To this end, Sandia National Laboratories has constructed a test facility to expose trough heat collection elements to conditions experienced during solidification and melting cycles. Early experiments indicated the possibility of tube deformation and initiated a series of studies to quantify and characterize the bending behavior [96]. In an effort to model the system and stress imparted by the expanding salt, studies were

performed to obtain mechanical and thermal properties for three salt formulations (with melting temperatures from 90 – 220 °C) in the solid-phase [97,98]. These works included results for unconfined compressive strength, indirect tensile strength, Young's modulus, Poisson's ratio, coefficient of thermal expansion, thermal conductivity and specific heat.

Reliable deflection models are essential to predict deflection of the absorber tube as a result of various thermal and structural loads. To establish these models, initial analysis is limited to empty tubes without molten salt. In this chapter, deformation of an empty absorber tube exposed to sun heating is measured with an experimental test facility. Analytic and numerical models are then constructed to predict deflection, validated with the experimental results.

A.2. Experimental Facility

Figure A.1 illustrates the test facility constructed at Sandia National Laboratories for performing solidification/melt cycling on receiver tubes. The receiver tube or heat collection element is composed of a stainless steel absorber tube surrounded with a glass envelope. The interstitial volume is nominally under vacuum to minimize thermal losses from the absorber. The mounting system mimics the LS-2 trough design (applied at the SEGS III-VII plants) with comparable moment arms to allow axial expansion of trough receiver tubes with change in temperature (see Figure A.1 for dimensions). The approximately 4 m absorber is constrained with two collars (4.27 m apart) fixed near the risers, connecting to bracket arms attached to the ground. The east bracket is fixed in the vertical direction at the base while the west bracket is free to rotate at two pin joints. Impedance heating circuitry and equipment has been included in the facility as a means to preheat/heat the receiver tube. Standpipes at either end of the receiver tube mimic the orientation of the flex hoses at the end of an operational solar collector assembly when modules are in a stow position. These standpipes are heavily insulated with multiple wraps of Superwool Plus (8 lb). Thermocouples (at positions indicated in Figure A.1) monitor temperature throughout a test cycle. As the internal thermocouples are

cantilevered from their entry point in the standpipe, their radial position is not guaranteed. Tube position is measured relative to the glass enclosure and compared to its initial position to determine deformation change using optical techniques.

A.3.   Empty Tube Deflection

Deflection analysis of the Schott PTR70 absorber tube began with a baseline case of an empty tube exposed to direct sunlight. Experimental investigation followed the thermal and optical methods outlined in the previous section. A numerical simulation of this scenario was composed of two distinct models, thermal and structural, and validated with experimental data. The thermal model simulates the transient response of the absorber tube exposed to direct sunlight. Temperature fields at discrete time points are then imported into the structural model to calculate the resultant deflection due to thermal expansion. While the glass cover is excluded from the model geometry, the thermal influence is replicated with boundary conditions discussed below. Assuming the influence of solar altitude to be negligible, a vertical symmetry plane is defined through the middle of the tube assembly along the east-west axis. Temperature-dependent thermal and mechanical properties for absorber tube (stainless steel 321H) are listed in Table A.1 [99].

A.3.1. Thermal Model

Prior to exposure to direct sunlight, the experimental test setup (and corresponding models) begin at a uniform initial temperature of 9 °C. The heat flux incident on the absorber surface is derived from the direct normal insolation (DNI) measurements associated with the test setup. For a test performed on April 27, 2011 from 11:00 am to 3:00 pm MST, the average incident DNI was 1065 W/m^2. The actual flux received by the absorber tube is reduced by the surface solar absorptivity (0.95) and varies with the circumferential position due to cosine losses, which generate a nonuniform heat flux along the upper half of the absorber. To simulate this phenomenon, the incident heat flux profile is divided into three, 30° intervals (Figure A.2a). From

vertical to 30°, the model absorber receives a heat flux of 966.2 W/m^2; from 30° to 60 °, the incident flux is 707.3 W/m^2; and from 60° to 90° the flux is 258.9 W/m^2. The total flux incident on the tube is equal to the integration of these regions. The extent of these fluxes is limited to the span of the glass cover, approximately 3.91 m. In addition to heating from incident sunlight, a portion of received energy is rejected to the colder surroundings. The loss per unit length associated with this heat rejection (within ±10 W/m) for a Schott PTR70 absorber was modeled by Burkholder and Kutscher as a function of the absorber temperature, T_{abs} (measured in °C) [100]:

$$q' = 0.141 T_{abs} + 6.48 \times 10^{-9} T_{abs}{}^4. \qquad (A.1)$$

For a measured ambient temperature of 14 °C, this function is approximated by an absorber emissivity of 0.06 (see also [100]) and a convection coefficient of 0.05 W/m^2-K. Heat loss in the standpipe and mounting regions are simulated with a 5 W/m^2-K convection coefficient. Thermal transport across pin joints in the brackets is neglected as the convective losses in the standpipe account for any transport through the bracket arms and collars. Heat exchange inside the empty absorber tube is simulated with blackbody radiation.

The thermal solution is calculated with ANSYS 13.0 Workbench [73], a commercial finite-element solver. The model geometry is meshed with 51161 elements (reducing the element count yields identical results). The temperature response at the midpoint of the absorber tube is plotted in Figure A.2b along with thermocouple data measured inside the center of the tube. The two data sets show a similar temperature response in time with a final numerical convergence to 288 °C at the top of the tube in the center of the length. Disparity between the thermocouple and model during the heating process may be attributed to position uncertainty of the thermocouple inside the absorber. Due to the circumferentially varying heat flux, the bottom of the absorber converges to a lower temperature of 276 °C.

A.3.2. Structural Model

With a higher temperature along the tube top relative to the bottom, the absorber tube bends upward from the corresponding disparity in thermal expansion. The maximum vertical deflection is calculated from the solved temperature field using both analytical and numerical models, described below.

1. Analytical approach:

The change in length at both the top and bottom of the absorber tube is known from the coefficient of thermal expansion of the absorber material, stainless steel 321H. To simplify the calculation, the top and bottom temperatures are assumed constant along the length of the tube. From the results of the thermal simulation, this approximation is appropriate for the tube region inside the glass cover. The disparity in expansion between the top and bottom is solved with the following equation, where the cold receiver length inside the glass cover is 3.91 m:

$$\Delta L_{abs} = \alpha L_{abs0} \left(T_{top} - T_{bot} \right).$$
(A.2)

Approximating the resultant deformation as parabolic (illustrated in Figure A.3), a second-order equation is fit to the deflection as a function of the length disparity. Three boundary conditions are required to construct the second-order equation, described as follows. First, the slope at the ends of the deflected tube (parabola) is approximated from trigonometry as half the length disparity, divided by the tube diameter. Second, the slope at the point of maximum deflection (assumed to be the midpoint) is zero. Third, the horizontal length between the east-west ends of the parabola is assumed to be equal to the nominal receiver length. The second-order fit is then fully defined and solved for the maximum vertical deflection, illustrated below:

$$\Delta y = \frac{\Delta L_{abs}}{2d_{abs}} \left(x - \frac{x^2}{L_{abs0}} \right)$$
(A.3)

$$\Delta y_{max} = \frac{\Delta L_{abs}}{8d_{abs}} L_{abs0}.$$
(A.4)

It should be noted that gravity induces sag in the tube when suspended in a horizontal position, reducing the amount of upward deflection. This sag is modeled by the deflection of a pinned-pinned Euler-Bernoulli beam exposed to a distributed load (tube weight per unit length):

$$\Delta y_{sag} = \frac{-5(\rho A g)L_{pin}^{4}}{384 E_M I}. \tag{A.5}$$

The length of tube exposed to gravitational sag (L_{pin}) is equal to the distance between the two collars, 4.27 m. The cross-sectional area and the second moment of area are both fixed by the absorber dimensions, 427 mm^2 and 247000 mm^4, respectively. Young's modulus of the absorber steel decreases with temperature, which induces more sagging as the tube is heated. Summing thermal expansion and gravitational effects yields an analytic estimate of the vertical position of the absorber tube during heating.

2. Numerical approach:

To avoid lengthwise temperature uniformity and an implicit parabolic deformation assumptions associated with the previous approach, the complete assembly mesh and thermal solution are imported into a structural model solved with ANSYS 13.0 Workbench. As before, gravity must be applied as an inertial load on the model geometry to account for the inherent sagging of the tube.

Solutions for the analytically and numerically obtained deflections are plotted in Figure A.4 along with experimental data from three consecutive days of test with sun heating. The experimental data is measured as the distance between the external radii of the absorber and glass cover. The difference between the nominal separation distance (between the absorber and glass) and the measured gap defines the vertical deflection of the absorber. Eccentricity is accounted for by adjusting the initial position of the unheated absorber tube by the expected gravity sag. This correction value is then applied to each deflection measurement.

As seen in Figure A.4, the analytic and numerical deflection data agree to within 2.1 mm throughout the heating process. Prior to heating, both approaches predict initial

sag (due to tube weight only) between -2.8 and -2.9 mm. Correcting the experimental data to this initial downward deflection yields reasonable agreement between the measurement and models, validating the two methodologies for an empty tube. The large deflection early in the heating process is attributed to the initial temperature disparity generated by the nonuniform heat flux. As the process continues, heat diffuses from the upper half of the absorber to the bottom half, reducing the temperature disparity and upward bending. Parallel to this, stiffness of the absorber decreases with temperature and generates more sagging. At the beginning of the next day's tests the tube has returned to its initial position indicating that the deflection was elastic (yield strength is approximately 180 MPa at 200 °C).

While experimental data and the analytic approach only determine the vertical deflection of the absorber tube midpoint, the numerical method allows for the deflection to be solved along the entire length of the tube. This deflection profile is plotted in Figure A.5. The ends of the profile indicate the location of the collars. Also plotted is a second-order curve fit of the deflection, which matches the profile with a regression value of 0.996. Thus, the assumption of a parabolic profile in the analytic deflection model is adequate.

A.4.   Summary

Trough receiver tubes have been shown to deform under loading as well as asymmetric heating conditions. In particular, when circumferential temperature gradients are established, tube deformation can be dramatic. Analytic and numeric models have been developed to predict this deflection. For an empty absorber tube exposed to sun heating, tube deformation remains elastic. Extension of this deflection analysis with salt-filled tubes and corresponding influence on solar collection is presented in [93].

Table A.1. Thermal and mechanical properties of stainless steel 321H [99].

T [°C]	α [μm/m]	E [GPa]	σ_y [MPa]
20	-	198	235
100	16.3	192	201
200	16.9	183	181
300	-	-	172
400	17.8	167	162
500	-	-	152
600	-	-	142
700	18.7	142	-
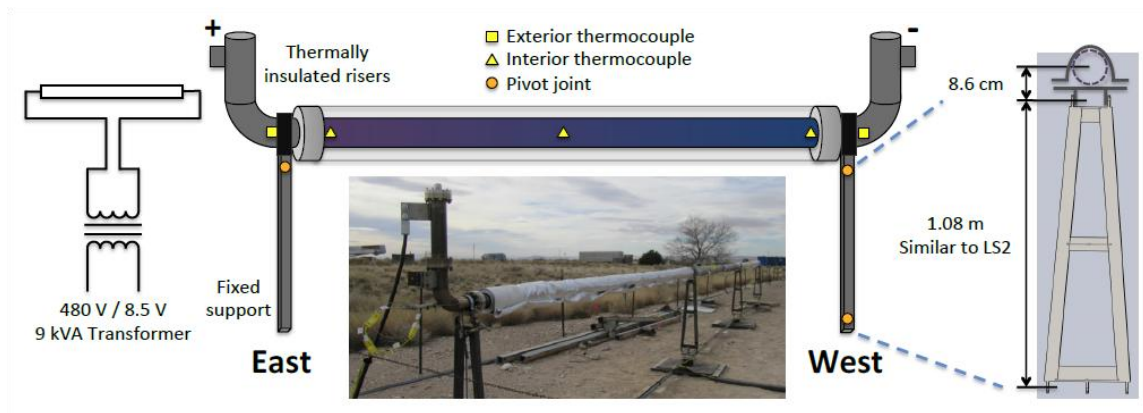
Figure A.1. Depiction of the test facility for solidification/melt cycles on trough heat collection elements.
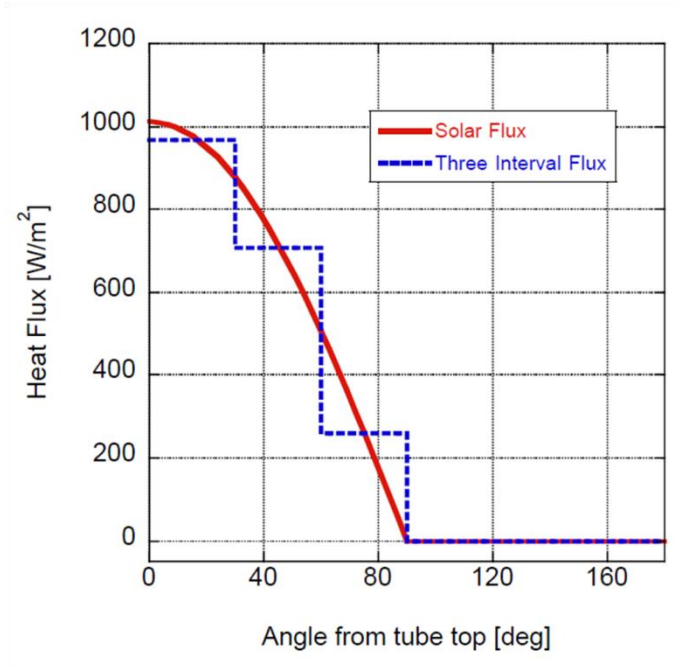
(a)
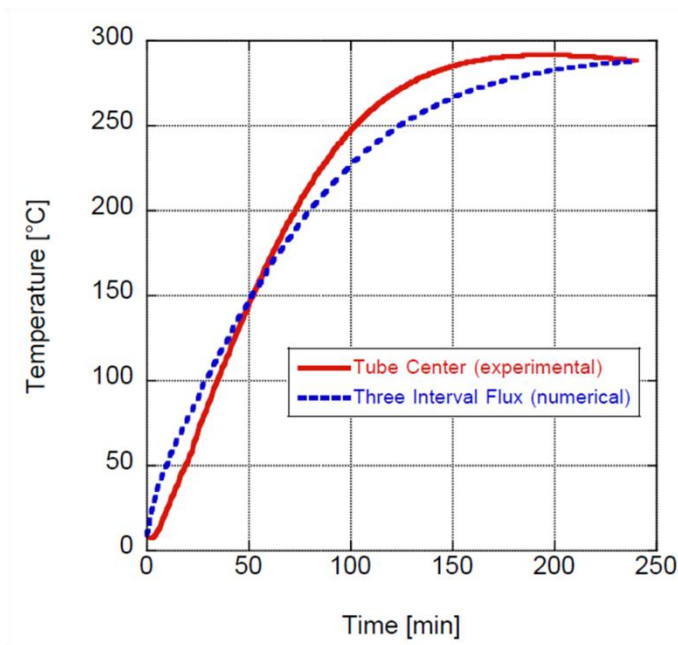
(b)

Figure A.2. (a) Simulation incident heat flux along the absorber tube surface. (b) Experimental and simulated temperature response of empty absorber tube with sun heating. Thermocouple location is inside the absorber tube at the lengthwise midpoint; numerical model temperature location is the top and center of the tube.
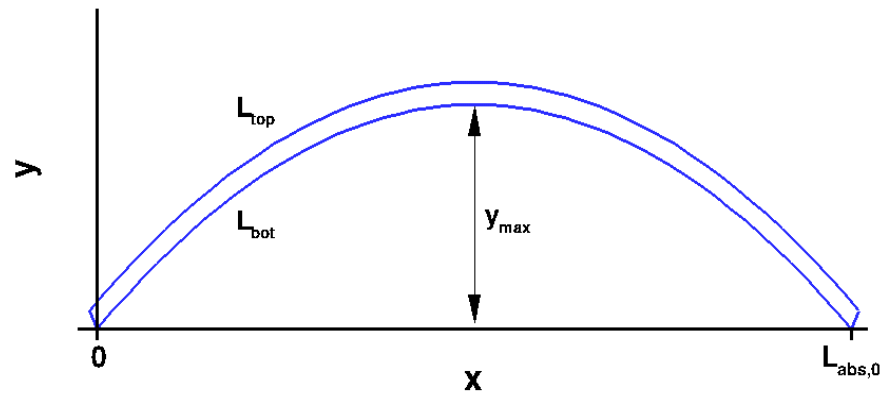
Figure A.3. Illustration of absorber tube parabolic deflection (not to scale).
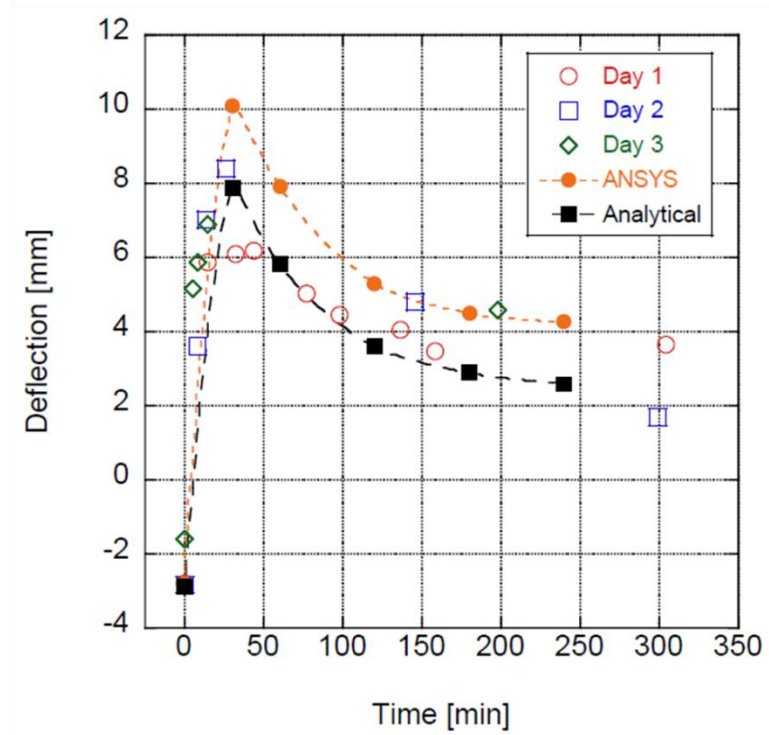
Figure A.4. Vertical deflection of the empty absorber tube due to sun heating (measurement error ±1.5 mm). Zero deflection is defined as the ideal tube position without thermal expansion bending or gravitational sagging.
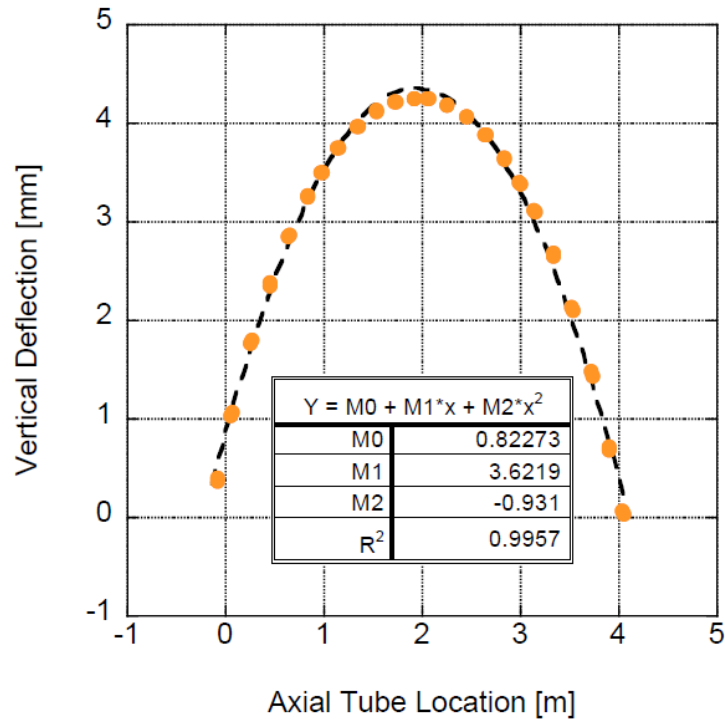
Figure A.5. Axial tube profile along the top of the tube (Day 1) obtained from numerical modeling indicates that the deformed position can be represented well with a parabolic profile.

Appendix B.   Characterization of Carbon Dioxide Convection Heat Transfer for
Supercritical Brayton Cycles

Material in this appendix was presented at the *2012 ASME Conference on Energy
Sustainability in San Diego, CA* [101].

B.1.   Introduction

Concentrating solar power (CSP) plants typically operate a conventional steam Rankine cycle for power production, where heat addition and rejection occur across the water vapor dome and carry an associated phase change. Condensation of the turbine exhaust is therefore limited to an isothermal state near the ambient temperature. Without a large temperature difference, effective heat rejection to the ambient commonly involves a condensing fluid with high heat capacity, *i.e.*, water. This condenser water usage is detrimental to CSP deployment as practical plant sites with ample sunlight largely consist of arid regions, such as the U.S. Southwest or the Saharan desert. Next-generation CSP power blocks require alternative working fluids that both support dry cooling but also provide thermal-to-electric conversion efficiencies above present systems. One such low-cost alternative is supercritical carbon dioxide (sCO$_2$). Supercritical fluids exist in a thermodynamic state above the critical temperature and pressure; 31.1 °C and 7.38 MPa for carbon dioxide, respectively. Above this state point, carbon dioxide is outside the vapor dome and does not exhibit a discrete phase change between liquid and vapor. All heating and cooling is therefore sensible and carries an associated temperature change.

A supercritical working fluid transitions the CSP power block from a Rankine cycle to a Brayton cycle as all heat transfer processes are sensible. Without condensation, the turbine exhaust temperature moves away from ambient and thus exhibits a greater temperature differential for waste heat rejection to the surroundings. As such, the Brayton cycle can better accommodate dry cooling with air in place of water, satisfying the stated objective of minimizing water consumption in CSP. Furthermore, the hotter exhaust temperature enables recuperation via preheating the compressor discharge, increasing the overall thermal efficiency. Additional efficiency gains are attainable

through cycle modifications such a split-flow recompression [102,103]. Table B.1 provides a summary of simulated performance data reported for different sCO_2 Brayton cycles using recompression enhancements. Beyond thermal performance, Dostal *et al.* [104] also performed an economic comparison of different working fluids and reported a 29% reduction in capital for a direct sCO_2 Brayton cycle compared to an indirect steam Rankine cycle for nuclear power applications.

One major challenge associated with supercritical fluids is the intense nonlinear variation of thermal transport properties near the thermodynamic critical point. These property variations smooth out away from the critical point but still must be considered for realization of a commercial sCO_2 Brayton cycle. Wright *et al.* [105] constructed a small-scale sCO_2 test loop to investigate compression effects near the critical point and to model cycle component performance. In addition to turbomachinery studies, advancement of sCO_2 heat exchangers is also essential for commercialization. Classical duct-flow correlations for convection are not a suitable basis for design with supercritical fluids given the large property variation. For circular tubes, this property variation manifests in both the axial and radial directions and yields dissimilar performance between heating and cooling. A majority of past studies have limited focus to cooling loads for the development of transcritical carbon dioxide HVAC systems [106]. Studies of heating loads, necessary for power generation cycles, are not widely reported in the literature. From the scant experimental data available, Ghajar and Asadi [107] proposed the following Nusselt number correlation for sCO_2 in turbulent duct flow:

$$\text{Nu} = 0.025\,\text{Re}^{0.8}\,\text{Pr}^{0.417}\left(\frac{\rho_w}{\rho_b}\right)^{0.32}\left(\frac{\overline{C}_P}{C_{P,b}}\right)^{0.4} \tag{B.1}$$

$$\overline{C}_p = \frac{i_w - i_b}{T_w - T_b}. \tag{B.2}$$

Experimental results upon which Eq. (B.1) is based were limited to pressures and temperatures below 10.8 MPa and 110 °C, respectively. A combined numerical and experimental study of supercritical carbon dioxide duct flow under heating is conducted to investigate this correlation. The basis of the experimental investigation is a modified

hot gas bypass load stand. Numerical simulation of this setup is performed in parallel with a computational fluid dynamics model. Experiment data and model results are then compared with the published Nusselt number correlations to assess their validity.

B.2. Experimental Analysis
B.2.1. Test Facility

Generation of carbon dioxide in the supercritical region is achieved using a hot gas bypass load stand. The hot gas bypass cycle is similar to a vapor compression cycle, but modified to eliminate need for external heat input. The cycle state points are illustrated in a pressure-enthalpy diagram shown in Figure B.1. Superheated carbon dioxide enters the compressor at state 1 and exits at state 2 in the supercritical region. The discharge is throttled to an intermediate pressure (state 2a) and then split into two separate flows. One flow path is condensed across the vapor dome to subcooled liquid (state 3) and then throttled to the suction pressure (state 4). The remaining flow bypasses the condenser and is throttled to the compressor suction pressure in the superheated region (state 5). The two flows are remixed to generate the desired compressor suction condition and close the loop. This mixing process returns the condenser-cooled outflow back across the vapor dome and eliminates the need for an evaporator within the cycle.

The physical load stand is shown in Figure B.2, previously constructed for experimental study of various carbon dioxide compressor designs [108,109]. In the present study, a DORIN TCS 362-4D compressor is applied for all experiments. Heat rejection across the vapor dome is performed with two tube-in-tube heat exchangers in parallel. Tap water serves as the condensing fluid. Cycle state points are controlled with metering valves installed downstream of the compressor and within both the bypass and condenser lines. The state points are monitored with Omega T-type thermocouple probes and Omega pressure transducers that output to a LabVIEW VI. The compressor mass flow rate is also monitored with a Micro Motion flow meter.

It should be noted that the carbon dioxide flow is subject to some contamination from oil (CPI Engineering synthetic lubricant EXP-1926) escaping the compressor. An

oil separator installed at the intermediate pressure, shown in the top left corner of Figure B.3, prevents exposure of the condenser and bypass lines to this oil. The oil exits the bottom of the separator and is returned back to the compressor. Observation of the oil concentration in the compressor discharge flow is made with a sight glass installed in the oil return line.

For convective heat transfer measurement in the supercritical region, the hot gas bypass load stand is modified with a heat test section downstream of the compressor. A detailed schematic of the modified setup is shown in Figure B.3. A second bypass line is installed around the heated test section to enable user control of the mass flow in the experiment tube. The flow rate is controlled with a metering valve at the inlet of the test section and monitored with a Micro Motion flow meter. Omega T-type thermocouple probes, installed at the inlet and exit of the test section, monitor the bulk or mean fluid temperature rise. Static mixers are installed upstream of both probe locations to disrupt thermal boundary layers in the carbon dioxide flow and ensure measurement of the desired mean fluid temperature. Downstream of the test section, the flow recombines with the second bypass line and completes the original compression cycle.

The heated test section is composed of 0.5 inch (1.27 cm) diameter stainless steel 304 tubing, 36 inches (91.44 cm) in length. The tube thickness is 0.028 inches (0.0711 cm). Ten Omega 30-gauge thermocouple beads are attached with epoxy along the tube surface at 9 cm increments. The tube and thermocouple assembly is encapsulated with a gap pad thermal interface and an aluminum annulus. Two lengths of Omega FGS051-100 heater tape are then coiled around the aluminum to provide the electric heat input. A 1 kW Sorenson power supply controls the heater tape voltage and current. The underlying gap pad and aluminum serve to diffuse variations along the heater tape and provide uniform heat flux into the stainless tube.

Measure of the convective heat transfer coefficient is conducted as follows. The hot gas bypass load stand is first activated and set to the user-defined compressor suction and discharge pressures. The power supply for the heater tape is then activated and set to the desired thermal power. The heated test section is designated to be at steady state

when the rate of temperature change for 10 minutes is less than 1 K/hour. Data is then recorded for 5 minutes. For convection analysis, the external surface temperature data is corrected from the known tube dimensions and thermal conductivity to obtain the internal surface temperature:

$$T_{sur}(x) = T_{ext}(x) - q'' \frac{r_{sur}}{k} \ln(r_{ext}/r_{sur}).$$ (B.3)

For convection with uniform heating, the mean fluid enthalpy increase across the test section is linear. This linear profile is defined by the inlet and outlet enthalpy; calculated from the pressure and temperature data and the Span and Wagner equation of state for carbon dioxide [110]. The corresponding mean temperature profile may not be linear due to the variable specific heat of the supercritical fluid but is determined from the enthalpy response and known pressure with the carbon dioxide equation of state.

It should be noted that the thermal power absorbed by the carbon dioxide is less than the applied electric power due to heat losses through test section insulation:

$$q_{loss} = q_{elec} - \dot{m}(i_{out} - i_{in}).$$ (B.4)

As a result, the heat flux through the tube (q'') is power absorbed by the carbon dioxide divided by the internal surface area of the tubular test section (324 cm^2). With known temperature data and heat flux, the convective heat transfer coefficient is solved at each surface thermocouple location:

$$h_w(x) = \frac{q''}{T_{sur}(x) - T_b(x)}.$$ (B.5)

The corresponding Nusselt number profile is then calculated as follows:

$$\mathrm{Nu}(x) = \frac{2r_{sur}h_w(x)}{k(x)}.$$ (B.6)

Supercritical carbon dioxide thermal conductivity is determined from the known pressure and temperature [111]. While the test facility obtains a steady-state response, the measurement data retains some uncertainty governed by the accuracy of the applied

sensors. Measurement accuracies for the thermocouples, pressure transducer, and mass flow meter are listed in Table B.2.

B.2.2. Experimental Results

A total of six different supercritical convection experiments are conducted with the modified hot gas bypass load stand. The carbon dioxide flow conditions and electric power for each test case are summarized in Table B.3. Convection coefficient are then calculated along the tube and converted to nondimensional Nusselt numbers and plotted in Figure B.4. Also plotted (as dashed lines) are the corresponding Nusselt numbers as predicted by the Eq. (B.1). As seen, the experiments all exhibit the strongest convection (*i.e*., the largest Nusselt numbers) near the inlet of the heat test section and indicate the presence of a thermally developing region inside the tube. Beyond this initial region, the test cases all converge to lower Nusselt numbers but with distortion near the end of the heated test section. Error bars associated with profiles are omitted from the graph for clarity but the cases exhibit a maximum uncertainty of 17.4% from the various sensor accuracies.

Among the six cases, the highest convection profile is observed with case E while the lowest is observed with case B. This result directly corresponds to the variation in mass flux between the different cases. In contrast, the cases do not exhibit a discernible trend with respect to either pressure or inlet temperature, indicating that the present supercritical convection is not subject to intensive thermal property variation. As result, mass flux is determined to be the most significant influence on forced convection for the current test conditions.

Comparison of the experimental Nusselt numbers and the correlation predictions via Eq. (B.1) reveals a $20 - 50\%$ disparity between the different cases. This large disagreement is outside the estimated measurement uncertainty and raises significant concern about the accuracy of the test data. To investigate the concern, the raw temperature data from case E is plotted in Figure B.5. As seen, the surface temperature does not exhibit a continuous increase with axial location but instead local decreases near

the end of the heated test section. Similar temperature trends occur in the other cases as well. This behavior indicates that a uniform heat flux is not maintained along the length of the tube. Potential causes for this failure include possible air pockets in the aluminum/gap pad heat spreader assembly or nonuniform heat losses through the surrounding thermal insulation. Given the suspect performance of the experimental facility, analysis is now continued with a numerical simulation of the heated test assembly.

B.3. Numerical Analysis

B.3.1. Model Geometry

Simulation of the previous heated test section is now performed with a computational fluid dynamics model. The test section geometry (stainless steel tube and carbon dioxide flow) is modeled with an axisymmetric 2-dimensional representation: buoyancy forces are assumed to be negligible. The test section also assumes hydraulic and thermal steady-state conditions. Mass, momentum, and energy transport in the fluid region are solved for with the following transport equations:

$$\nabla \cdot (\rho \mathbf{u}) = 0 \tag{B.7}$$

$$\nabla \cdot (\rho \mathbf{u}\mathbf{u}) = -\nabla p + \nabla \cdot \tilde{\boldsymbol{\tau}} \tag{B.8}$$

$$\nabla \cdot (\rho \mathbf{u}i) = \nabla \cdot (k\nabla T) - \mathbf{u} \cdot \nabla p + \mu \Phi . \tag{B.9}$$

The spatial gradient of the heated test section in polar coordinates is $\nabla = \mathbf{e_r} \frac{\partial}{\partial r} + \frac{\mathbf{e}_\theta}{r} \frac{\partial}{\partial \theta} + \mathbf{e}_x \frac{\partial}{\partial x}$. The axisymmetric formulation of the test section geometry eliminates all velocities and functional dependencies in the circumferential direction. Thermal transport in the stainless steel tube is resolved with the cylindrical heat diffusion equation. Carbon dioxide enters the tube inlet at a user-defined velocity and temperature. A pressure-outlet boundary condition is enforced at the test section exit.

The tube and fluid geometry are discretized with a structured nonuniform mesh composed of 177,413 cells. The axial cell length (Δx) is 0.5 mm for both the tube and fluid regions. Far from the tube wall boundary, the radial cell length (Δr) of the fluid

region is 0.1 mm. Near the wall, this radial cell length is reduced to 0.00597 mm to resolve the viscous sub-layer of the turbulent boundary layer (for dimensionless wall coordinate y^+ less than five). Additional simulation with a refined mesh of 473,711 cells demonstrates mesh independence with less than 0.15% deviation in temperature fields.

The governing mass, momentum, and energy equations are discretized with the finite-volume method and solved with the commercial CFD software, FLUENT 13.0 [65]. Spatial discretization of the convective fluxes is performed with the second-order upwind scheme. Pressure-velocity coupling of the fluid flow is achieved with the SIMPLE algorithm [112]. Turbulent phenomena are resolved with the k-ε model [113] and enhanced wall functions.

Carbon dioxide properties are determined using the Span and Wagner equation of state along with representative equations for viscosity and thermal conductivity [110,111]. It is not practical to include the entire equation of state in the CFD model due to computational costs and because the current interest is limited to the supercritical region. Instead, localized polynomial curve fits are generated for each thermodynamic and thermal transport property in the pressure and temperature region of interest and then incorporated into the model as user-defined functions (UDFs). The CFD solution is designated as converged when all dimensionless residuals reduce to less than 10^{-5}.

Once a converged solution is obtained, the outflow temperature and velocity profiles are extracted to solve for the mean fluid temperature increase across the heated test section. The radial heat flux and surface temperature at the wall boundary are then extracted to measure the convective heat transfer coefficient along the length of the tube. The corresponding Nusselt number is determined from known tube diameter and local fluid thermal conductivity.

B.3.2. Numerical Results

Given the poor performance of the experimental campaign, a numerical simulation of the heated test section is now performed under conditions typical of the hot gas bypass load stand. Table B.4 provides a parametric overview of the applied pressure,

temperature, and mass flux for these simulations. In all cases, a uniform heat flux of 1.08 W/m^2 is applied at the external tube surface. It should be noted that the thermodynamic state of the sCO_2 supplied to the heated test section is a function of the compressor performance. Thus, the inlet pressure and temperature to the test section are not strictly independent variables: increasing the compressor discharge pressure will increase the discharge temperature. However, some temperature adjustment is retained through user control of the compressor suction superheat (state 1 in Figure B.1).

The Nusselt number associated with case 1 is plotted in Figure B.6 as a function of axial location along the heated test section. Development of the thermal boundary layer leads to initial oscillations in the Nusselt number along the first 0.5 m of the tube. Transition to thermally developed flow occurs beyond this length, indicated by the following derivative condition being satisfied [76]:

$$\frac{\partial}{\partial x}\left[\frac{T_{sur}(x)-T(r,x)}{T_{sur}(x)-T_b(x)}\right]=0 \,. \tag{B.10}$$

Along the developed region, the Nusselt number retains some variation due to the non-constant thermal transport properties of sCO_2. As the mean fluid temperature increases along the length of the tube, these transport properties decrease in value and diminish the convective heat transfer performance. Data in this region are averaged to produce a single representative Nusselt number for each case, as compiled in Table B.4. The uncertainty associated with the averaged value is designated as two standard deviations.

For cases 7, 8, and 13-15, thermal property variations prolonged transition to thermally developed flow beyond the length of the simulated test section. In each case, dynamic viscosity exhibited an inflection with temperature along the length of the tube, at a temperature of 107 °C and 130 °C for 11 MPa and 13 MPa, respectively. This nonlinear behavior delayed the onset of fully developed conditions, such that the entire length of the tube exhibited hydraulic and thermal developing conditions. For the remaining cases, the Nusselt number increases with mass flux as expected. The influence of inlet temperature and pressure is explained by the variation of the Prandtl number. At the applied supercritical conditions, the Prandtl number increases with pressure but

decreases with temperature. Thus, at increased fluid inlet temperatures, the Nusselt number decreases as expected. A similar trend also occurs with increasing pressure, despite the increased Prandtl number. It should be remembered that the compressor discharge pressure and temperature conditions applied to the model are related. Thus, gains in Prandtl number associated with the higher pressure are offset by the corresponding increase in fluid inlet temperature.

In addition to the numerical determination of Nusselt number as described above, the correlation in Eq. (B.1) may be used with thermal property data extracted from the converged CFD solution substituted as inputs. The predicted Nusselt numbers from the correlation for case 1 are included in Figure B.6 as a comparison. In the thermally developed region, the two datasets agree to within 6.5%. The influence of property differences between the mean and surface conditions, expressed by the last two terms of Eq. (B.1), varies between 1 and 5% for all cases. The influence is largest for cases with $G = 200$ kg/m^2-s, where greater temperature differences are sustained between the fluid mean and wall surface temperature.

Comparisons of all CFD simulations to predictions with Eq. (B.1) are summarized in Figure B.7. As with the numerical simulation approach, a single Nusselt number is found from the correlation by averaging data outside the thermal entry region. In all cases, the simulated results agree with the prediction from the correlations to within 15%. The mean absolute error between simulation and prediction is 6.4%, less than the 6.8% average error reported for the correlation [107]. This good agreement implies that the correlation remains accurate outside the limits of the original experimental data (10.8 MPa, 110 °C) upon which it was based.

B.4. <u>Summary</u>

An experimental and numerical study is performed to advance understanding of carbon dioxide convection in the supercritical region, necessary for heat exchanger design in future Brayton power cycles. A hot gas bypass load stand is first modified with an external electric heat source to generate supercritical convection. The carbon dioxide

response is measured with thermocouples at the inlet, outlet, and along the external tube wall surface. A case study of different carbon dioxide flow conditions is performed, including temperatures greater than previous investigations in the literature. However, the experimental data obtained all exhibit large disagreement with a published Nusselt correlation for carbon dioxide. Reason for this is attributed to the inability of the heated test section to obtain a satisfactory uniform heat flux.

A numerical model of the heated test section is then developed to reassess the convective heat transfer of supercritical carbon dioxide. A case study of 18 different flow conditions, comparable to the hot gas bypass load stand capability, is performed. Unlike the previous experiment data, model cases exhibit good agreement with the existing Nusselt number correlation. This agreement extends to pressures and temperatures beyond the basis of the correlation and indicates increased viability for heat exchanger design.

Table B.1. Summary of simulated sCO$_2$ Brayton cycles with recompression reported in the literature.

Parameter	[102]	[103]	[104]
T_{max} [°C]	650	727	600
P_{max} [MPa]	20	22.5	20
η_{turb}	0.93	0.90	0.93
η_{comp}	0.85	0.80	0.88
ε_{HX}	0.97	0.85	0.95
η_{cyc}	0.50	0.43	0.47

Table B.2. Hot gas bypass load stand sensor accuracies.

Sensor	Type	Accuracy
Thermocouple probe	Omega TMQSS-062G-6	±1 K
Thermocouple wire	Omega TT-T-30-SLE	±0.5 K
Pressure transducer	Omega PX32B1-2.5KAV	±0.25% FS
Mass flow meter	Micro Motion DS025S	±0.5%
Power supply	Sorensen DCS80-13E	±0.23 amp

Table B.3. Case summary of convection measurement tests.

Case	P [MPa]	G [kg/m^2-s]	T_{in} [°C]	q'' [W/cm^2]
A	8.01	182	104	0.622
B	9.01	175	106	0.769
C	9.02	181	117	0.609
D	9.02	235	106	0.626
E	9.05	235	107	0.773
F	9.88	194	117	0.621

Table B.4. Summary of simulated heated test section inlet conditions and average Nusselt number obtained. A fixed heat flux of 1.08 W/cm^2 is enforced for all cases. Nusselt numbers designated as (*) did not achieve thermally developed flow inside the model geometry.

Case	P [MPa]	T [°C]	G [kg/m^2-s]	$\overline{Nu}$
1	9	80	200	236±6
2	9	80	400	435±11
3	9	80	600	621±12
4	9	100	200	216±7
5	9	100	400	399±7
6	9	100	600	582±8
7	11	95	200	*
8	11	95	400	*
9	11	95	600	577±14
10	11	115	200	213±2
11	11	115	400	388±2
12	11	115	600	562±2
13	13	110	200	*
14	13	110	400	*
15	13	110	600	*
16	13	130	200	208±1
17	13	130	400	374±1
18	13	130	600	538±1
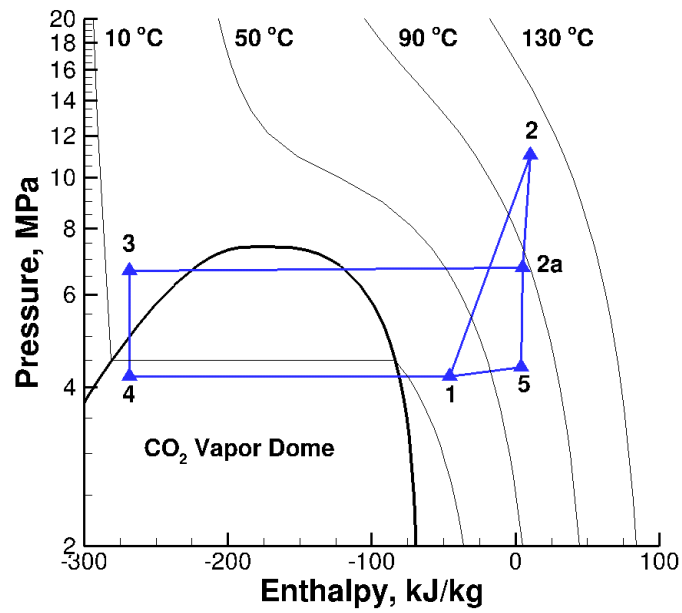
Figure B.1. Example pressure-enthalpy diagram of a carbon dioxide hot gas bypass cycle.
Cycle data is taken from [108].
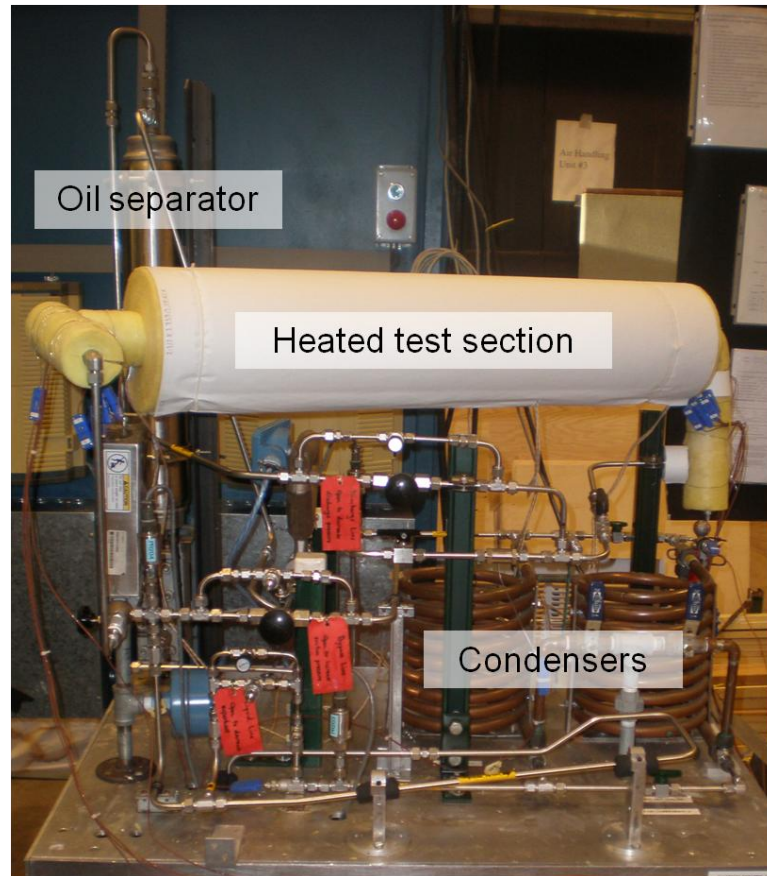
Figure B.2. Carbon dioxide hot gas bypass load stand. The flow loop has been modified with an electric heat source downstream of the compressor to enable supercritical convection measurements.
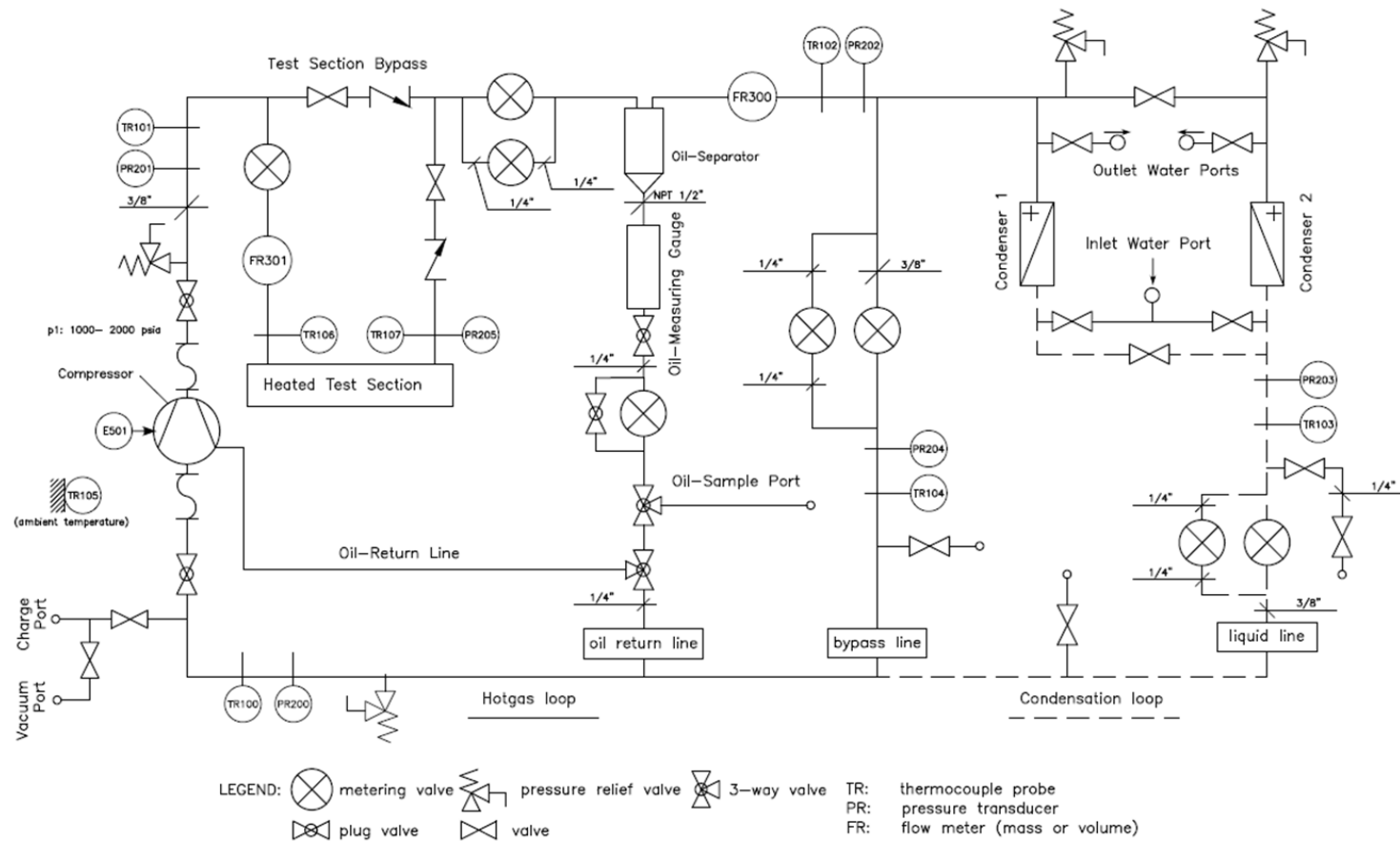
Figure B.3. Flow loop diagram of the carbon dioxide hot gas bypass test stand and heated test section.
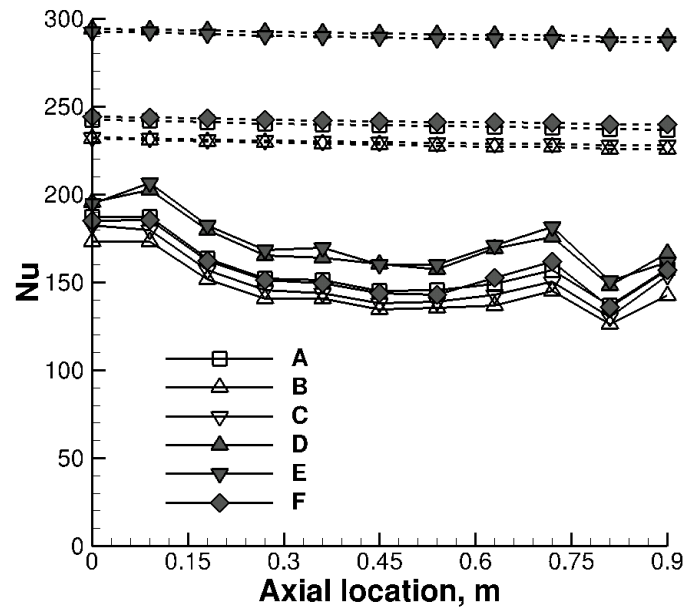
Figure B.4. Experimental Nusselt numbers measured along the heated test section. Also plotted (as dashed lines) are the corresponding correlation predictions for each test case. Measurement uncertainty bars are not plotted for clarity. The data are most strongly influenced by mass flux but exhibit an over 40% deviation from the expect correlation results.
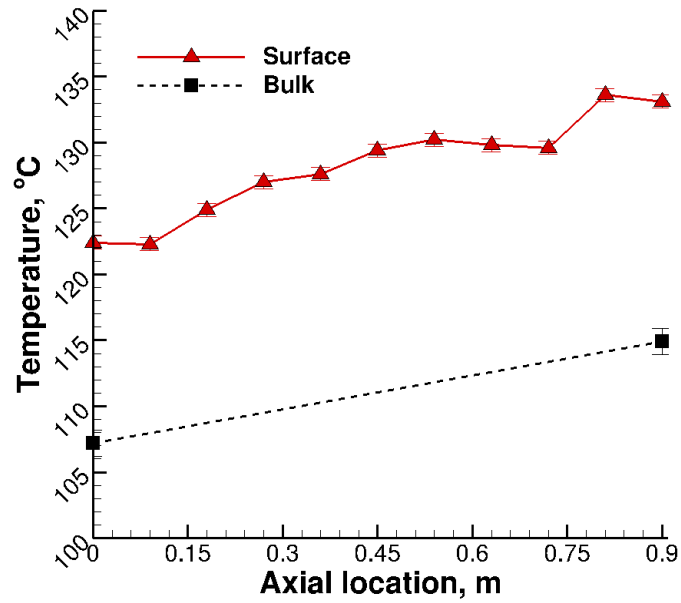
Figure B.5. Raw temperature data recorded for case E test. The external surface temperature does not exhibit a continuous increase along the heated test section and raises concerns about the veracity of uniform heat flux achieved along the tube.
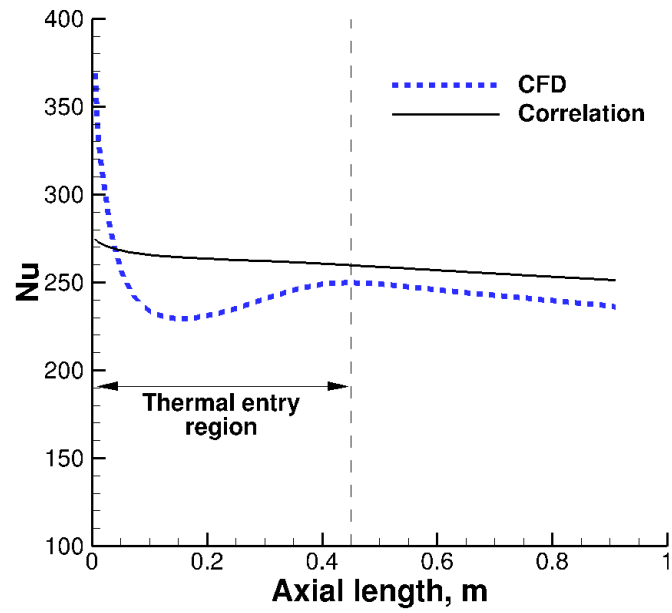
Figure B.6. Nusselt number calculated for case 1 along the axial length of the simulated heated test section. Also plotted for comparison is the Nusselt number prediction from the Ghajar and Asadi correlation [107].
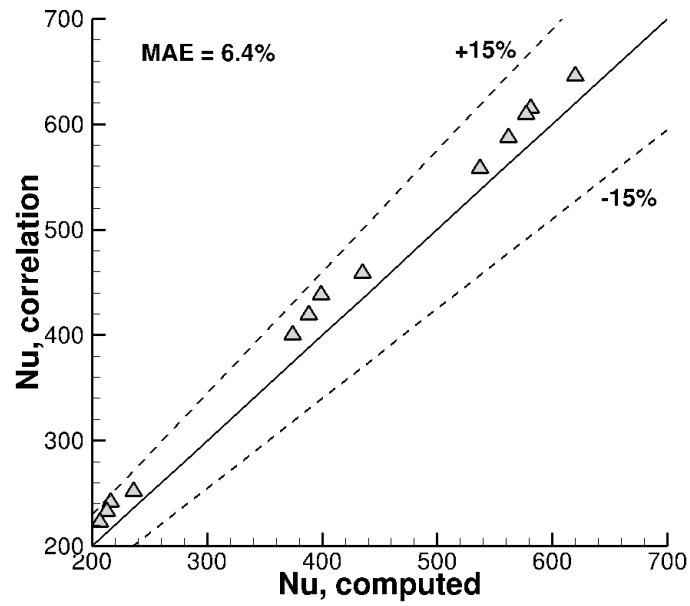
Figure B.7. Comparison of Nusselt numbers computed from the numerical simulation to predictions from the Ghajar and Asadi correlation [107].

Appendix C.   Entropy Generation in an Unconsolidated Porous Medium

In accordance with the second law of thermodynamics, entropy generation in a control volume is governed by the following equation:

$$\dot{S}'''_{gen} = \frac{\partial \rho s}{\partial t} + \nabla \cdot (\rho \mathbf{u} s) - \nabla \cdot \left(\frac{\mathbf{q}}{T}\right) - \frac{\dot{Q}'''}{T_b}.$$
(C.1)

The above equation is recast in non-conservative form by combining the transient and convection terms as a material derivative of entropy:

$$\dot{S}'''_{gen} = \rho \frac{Ds}{Dt} - \nabla \cdot \left(\frac{\mathbf{q}}{T}\right) - \frac{\dot{Q}'''}{T_b}.$$
(C.2)

For incompressible materials, the material derivative of entropy converts to a material derivative of enthalpy. The divergence of heat flux over temperature is also expanded to give:

$$\dot{S}'''_{gen} = \rho \frac{1}{T} \frac{Di}{Dt} + \frac{\nabla \cdot \mathbf{q}}{T} - \frac{\mathbf{q} \cdot \nabla T}{T^2} - \frac{\dot{Q}'''}{T_b}.$$
(C.3)

For a porous medium not in thermal equilibrium, separate generation equations must be considered for the fluid and solid phases. In the case of a dual-media thermocline tank, the solid filler is granulated or unconsolidated. Due to the corresponding contact resistance between particles, thermal diffusion is neglected in the solid phase. However, the solid equation still contributes to thermal diffusion in the liquid region, characterized with an effective thermal conductivity. Both phases include an energy source term associated with the interstitial forced convection between the molten salt and solid rock. It should be noted that this heat exchange occurs across an intermediate boundary temperature (T_b) between the liquid and solid:

$$\dot{S}'''_{gen,l} = \rho_l \frac{1}{T_l} \frac{Di_l}{Dt} + \frac{\nabla \cdot \mathbf{q}}{T_l} - \frac{\mathbf{q} \cdot \nabla T_l}{T_l^2} - \frac{h_i (T_s - T_l)}{T_b}$$
(C.4)

$$\dot{S}'''_{gen,s} = \rho_s \frac{1}{T_s} \frac{\partial i_s}{\partial t} + \frac{h_i(T_s - T_l)}{T_b} \, . \tag{C.5}$$

To simplify the entropy generation equations further, the energy transport equations for both liquid and solid regions are reconsidered:

$$\frac{\partial \rho_l i_l}{\partial t} + \nabla \cdot (\rho_l \mathbf{u} i_l) = -\nabla \cdot \mathbf{q} + \mu \Phi + h_i(T_s - T_l) \tag{C.6}$$

$$\frac{\partial \rho_s i_s}{\partial t} = -h_i(T_s - T_l). \tag{C.7}$$

As with the previous entropy generation, the energy transport equations are recast in non-conservative form to formulate a material derivative of enthalpy:

$$\rho_l \frac{Di_l}{Dt} = -\nabla \cdot \mathbf{q} + \mu \Phi + h_i(T_s - T_l) \tag{C.8}$$

$$\rho_s \frac{\partial i_s}{\partial t} = -h_i(T_s - T_l). \tag{C.9}$$

Equations (C.8) and (C.9) are combined with the entropy generation equations for the respective phases to eliminate the enthalpy terms:

$$\dot{S}'''_{gen,l} = \frac{\mu \Phi}{T_l} + \frac{h_i(T_s - T_l)}{T_l} - \frac{\mathbf{q} \cdot \nabla T_l}{T_l^2} - \frac{h_i(T_s - T_l)}{T_b} \tag{C.10}$$

$$\dot{S}'''_{gen,s} = -\frac{h_i(T_s - T_l)}{T_s} + \frac{h_i(T_s - T_l)}{T_b} \, . \tag{C.11}$$

The total entropy generation inside the porous medium control volume is the sum of the two phases. The dot product of the heat flux and liquid temperature gradient is also expanded to give:

$$\dot{S}'''_{gen} = \frac{h_i(T_s - T_l)^2}{T_s T_l} + \frac{k_{eff}(\nabla T_l)^2}{T_l^2} + \frac{\mu \Phi}{T_l} \geq 0 \, . \tag{C.12}$$

The boundary temperature associated with the interstitial forced convection is canceled out by the summation and does need not be calculated. For thermocline energy storage applications, viscous dissipations are small and may be neglected.

Appendix D.   Flow Resistance in a Dual-media Thermocline Tank

Multi-dimensional simulations of dual-media thermocline tanks (Figure 3.3) exhibit well-organized temperature contours and flow streamlines. The lack of radial effects in the velocity field indicates that a boundary layer does not develop along the surrounding tank wall. Reason for this is the relative flow resistances associated with the tank wall and internal porous bed, explained as follows.

The pressure drop associated with the thermocline tank wall is characterized as laminar flow in a pipe:

$$\left.\frac{\partial P}{\partial x}\right|_{wall} = -\frac{8\mu}{\pi R^4} Q. \tag{D.1}$$

The additional pressure drop associated with flow inside the porous bed is characterized with the Darcy equation:

$$\left.\frac{\partial P}{\partial x}\right|_{bed} = -\frac{\mu}{\pi R^2}\frac{1}{K} Q. \tag{D.2}$$

The total pressure drop inside a dual-media thermocline tank is the combination of these effects:

$$\frac{\partial P}{\partial x} = \left.\frac{\partial P}{\partial x}\right|_{wall} + \left.\frac{\partial P}{\partial x}\right|_{bed} = -\frac{Q\mu}{\pi R^2}\left(\frac{8}{R^2} + \frac{1}{K}\right). \tag{D.3}$$

The permeability K of the packed bed structure is governed by the Kozeny-Carman equation [61]:

$$K = \frac{\varepsilon^3 d_s^{\ 2}}{175(1-\varepsilon)^2}. \tag{D.4}$$

For a filler size of 1 cm and a bed porosity of 0.22, the associated permeability is 10^{-8} m^2. It should also be noted that a large-scale thermocline tank will exhibit a radius R of several meters. Thus the flow resistance associated with the bed ($1/K$) is several orders-of-magnitude greater than resistance associated with the wall ($8/R^2$). As a result,

the influence of the tank wall is negligible and a macro-scale boundary layer is not observed inside the tank.

Appendix E.   FLUENT UDF Script for the Molten-salt Thermocline Tank Model

```c
#include "udf.h"

real Cp_s = 2500.0, rho_s = 830.0;    /*Solid properties*/
real Cp_l = 1561.7;                   /*Fluid specific heat*/
real T_high = 723.0;                  /*High temperature*/
real T_low = 523.0;                   /*Low temperature*/
real T_0 = 298.0;                     /*Reference temperature*/
real bed_porosity = 0.22;             /*Filler bed porosity*/
real dd = 0.05;                       /*Sand diameter*/

int id1 = 2, id2 = 3;                 /*id1 -- fillerbed, id2 -- distributors*/
int top = 12, bot = 11;

/* UDMI 0 - porosity, UDMI 1 - current T2, UDMI 2 - previous T2,
   UDMI 3 - k_eff, UDMI 4 - d_sphere, UDMI 5 - old molten salt T
   UDMI 6 - T1n2, UDMI 7 - T2n2*/

DEFINE_SOURCE (energy_source, c, t, dS, eqn)
{
        real source=0.0;
        real hi, Re, Pr, pp, mu, rho_l, d_sphere;
        real k_l, T1_old, T2_old, uu, dt;

        T1_old = C_UDMI(c, t, 5)-273.0;
        T2_old = C_UDMI(c, t, 2)-273.0;

        /*Update filler material temperature*/
        uu = sqrt(C_U(c, t)*C_U(c, t) + C_V(c,t)*C_V(c,t));
        mu = exp(log(0.013)-2.0143*(log(T1_old)-log(150.0)));
        rho_l = C_R_M1(c, t);         /*old density*/
        d_sphere = C_UDMI(c, t, 4);
        pp = C_UDMI(c, t, 0);
        Re = rho_l * d_sphere * uu / mu;
        k_l = (T1_old-260.0)/(454.4-260.0)*(0.294-0.421)+0.421;
        Pr = mu * Cp_l / k_l;
        hi = k_l*6.0*(1.0-pp)*(2.0+1.1*pow(Re,0.6)*pow(Pr,0.333))/pow(d_sphere,2.0);
        source = hi * (T2_old - T1_old);
        dt = RP_Get_Real("physical-time-step");
        C_UDMI(c, t, 1) = -source * dt / ((1.0 - pp)*rho_s*Cp_s) + C_UDMI(c, t, 2);
        return source;
}
```

```
DEFINE_EXECUTE_AT_END (update_prop)
{
        Domain *d;
        Thread *t;
        FILE *fp, *fp1;
        cell_t c;
        face_t f;
        real pp, T1, T2, k_l, k_s, bb, phi, keff, x[ND_ND], dt, rho_l, T1_new, U1;
        real x1, e1, T1_old, T2_new, T2_old, dS1_dT, dT1_dt, dS2_dT, dT2_dt, dk_dT;
        real a1, A[ND_ND], a_top, part_a, part_b, part_c, part_d, lap_T, vol;
        real q_conv, net_s1=0.0, net_s2=0.0, T1_n2, T2_n2, num, den, d_bb, d_num;
        real d_den, dk1_dT, q_s1, q_s2, uu, mu, Re, Pr, d_sphere, hi, x_in, e_in;
        real x_out, e_out, x_top1, x_bot1, e_top1, e_bot1, flow_time, T_top1, T_s;
        int ns, n_time;
        float tm, s1, x_top, x_bot, e_top, e_bot, T_top;
        dt = RP_Get_Real("physical-time-step");

        /*Store Temperature Gradient in UDSI*/
        d = Get_Domain (1);
        t = Lookup_Thread (d, id1);
        begin_c_loop(c, t)
        {
                C_UDSI(c, t, 0) = C_T_G(c, t)[0];
                C_UDSI(c, t, 1) = C_T_G(c, t)[1];
        }
        end_c_loop(c, t)

        t = Lookup_Thread (d, id1);   /*Filler bed*/
        begin_c_loop(c, t)
        {
                pp = C_UDMI(c, t, 0);
                vol = C_VOLUME(c, t)*2.0*M_PI;
                T1_new = C_T(c, t);
                T1_old = C_UDMI(c, t, 5);
                T1_n2 = C_UDMI(c, t, 6);
                T2_new = C_UDMI(c, t, 1);
                T2_old = C_UDMI(c, t, 2);
                T2_n2 = C_UDMI(c, t, 7);

                T1 = T1_new - 273.0;
                T2 = T2_new - 273.0;
                k_l = (T1-260.0)/(454.4-260.0)*(0.294-0.421)+0.421;
                k_s = (T2-200.0)/200.0*(1.84-1.55)+1.55;
                bb = (k_s - k_l)/(k_s+2.0*k_l);
                phi = 1.0 - C_UDMI(c, t, 0);
```

```
            num = 1.0+2.0*bb*phi+(2.0*pow(bb,3.0)-
0.1*bb)*pow(phi,2.0)+pow(phi,3.0)*0.05*exp(4.5*bb);
            den = 1.0 - bb*phi;
            keff = k_l*num/den;
            C_UDMI(c, t, 3) = keff/pp;    /*Update eff thermal k*/

            /*Entropy Generation in Fillerbed*/
            part_c = keff*NV_MAG2(C_T_G(c, t))/pow(T1_new, 2.0);
            net_s1 += part_c*vol;

            /*Update Temperatures*/
            C_UDMI(c, t, 6) = C_UDMI(c, t, 5); /*Update old  salt T*/
            C_UDMI(c, t, 7) = C_UDMI(c, t, 2); /*Update old filler T*/
            C_UDMI(c, t, 2) = C_UDMI(c, t, 1); /*Update filler T*/
            C_UDMI(c, t, 5) = C_T(c, t);          /*Update molten salt T*/
        }
        end_c_loop(c, t)

        t = Lookup_Thread (d, id2);  /*Distributor zones*/
        begin_c_loop(c, t)
        {
            C_UDMI(c, t, 5) = C_T(c, t); /*Update molten salt T*/
            T1 = C_UDMI(c, t, 5)-273.0;
            k_l = (T1-260.0)/(454.4-260.0)*(0.294-0.421)+0.421;
            keff = k_l;
            C_UDMI(c, t, 3) = keff;                /*Update eff thermal k*/
        }
        end_c_loop(c, t)

        a_top = 0.25*M_PI*pow(1.2, 2);     /*top port area*/
        t = Lookup_Thread (d, top);             /*Thermocline port top*/
        begin_f_loop(f, t)
        {
            T1 = F_T(f, t);
            U1 = F_U(f, t);
            a1 = F_AREA(A, f, t);
            x1 = Cp_l*(T1 - T_0) - T_0*Cp_l*log(T1/T_0);
            e1 = Cp_l*(T1 - T_0);
            rho_l = 1938.0 - 0.732*((T1 - 273.0) - 200.0);
            x_in = rho_l*U1*x1*a1*2.0*M_PI;
            e_in = rho_l*U1*e1*a1*2.0*M_PI;
            x_top1 += x_in;
            e_top1 += e_in;
            T_top1 += T1*a1*2.0*M_PI/a_top;
```

```
        }
        end_f_loop(f, t)

        t = Lookup_Thread (d, bot);                /*Thermocline port bot*/
        begin_f_loop(f, t)
        {
                T1 = F_T(f, t);
                U1 = F_U(f, t);
                a1 = F_AREA(A, f, t);
                x1 = Cp_l*(T1 - T_0) - T_0*Cp_l*log(T1/T_0);
                e1 = Cp_l*(T1 - T_0);
                rho_l = 1938.0 - 0.732*((T1 - 273.0) - 200.0);
                x_out = rho_l*U1*x1*a1*2.0*M_PI;
                e_out = rho_l*U1*e1*a1*2.0*M_PI;
                x_bot1 += x_out;
                e_bot1 += e_out;
        }
        end_f_loop(f, t)

        /*Record entropy generation*/
        flow_time = RP_Get_Real("flow-time");
        n_time = RP_Get_Integer("time-step");

        fp = fopen("d5cm_adiabatic.txt", "r");
        fscanf(fp,"S_1: %f,Xtop: %f,Xbot: %f,Etop: %f,Ebot: %f",&s1,&x_top,&x_bot,
&e_top,&e_bot);
        fclose(fp);

        s1 += net_s1*dt;
        x_top += x_top1*dt;
        x_bot += x_bot1*dt;
        e_top += e_top1*dt;
        e_bot += e_bot1*dt;

        fp = fopen("d5cm_adiabatic.txt", "w");
        fprintf(fp,"S_1: %f,Xtop: %f,Xbot: %f,Etop: %f,Ebot: %f",s1,x_top,x_bot,e_top,e
_bot);
        fclose(fp);

        if(n_time % 1800 == 0)
        {
                fp = fopen("d5cm_adiabatic.txt", "r");

        fscanf(fp,"S_1: %f,Xtop: %f,Xbot: %f,Etop: %f,Ebot: %f",&s1,&x_top,&x_bot,
&e_top,&e_bot);
```

```
        fclose(fp);

        fp1 = fopen("d5cm_adiabatic_perm.txt", "a+");
        tm = flow_time/3600;
        s1 = s1/1000000;
        x_top = x_top/1000000;
        x_bot = x_bot/1000000;
        e_top = e_top/1000000;
        e_bot = e_bot/1000000;
        T_top = T_top1;
        fprintf(fp1,"%f,%f,%f,%f,%f,%f,%f\n",tm,s1,x_top,x_bot,e_top,e_bot,T_top);
        fclose(fp1);
        }
}

DEFINE_ON_DEMAND (initial_prop)
{
        Domain *d;
        Thread *t;
        cell_t c;
        real T1, T2, bb, phi, keff, k_l, k_s, pp;

        d = Get_Domain (1);
        t = Lookup_Thread(d, id1);    /*Fillerbed region*/
        begin_c_loop(c, t)
        {
                C_UDMI(c, t, 0)=bed_porosity; /*porosity*/
                pp = C_UDMI(c, t, 0);
                C_UDMI(c, t, 4) = dd;           /*d_sphere*/
                C_UDMI(c, t, 1) = T_low; /*current T2*/
                C_UDMI(c, t, 2) = T_low; /*previous T2*/
                C_UDMI(c, t, 5) = T_low; /*previous molten salt T*/
                C_UDMI(c, t, 6) = T_low; /*T1 n-2*/
                C_UDMI(c, t, 7) = T_low; /*T2 n-2*/

                T1=C_T(c, t)-273.0;
                T2=C_UDMI(c, t, 2)-273.0;
                k_l=(T1-260.0)/(454.4-260.0)*(0.294-0.421)+0.421;
                k_s=(T2-200.0)/200.0*(1.84-1.55)+1.55;
                bb = (k_s - k_l)/(k_s+2*k_l);
                phi = 1.0 - C_UDMI(c, t, 0);
                keff = k_l*(1.0+2.0*bb*phi+(2.0*pow(bb,3.0)-
0.1*bb)*pow(phi,2.0)+pow(phi,3.0)*0.05*exp(4.5*bb))/(1.0-bb*phi);
                C_UDMI(c, t, 3) = keff/pp;
        }
```

```
        end_c_loop(c, t)

        t = Lookup_Thread (d, id2);   /*Distributor Zones*/
        begin_c_loop(c, t)
        {
                C_UDMI(c, t, 0) = 1.0;          /*porosity*/
                C_UDMI(c, t, 1) = 0.0;
                C_UDMI(c, t, 2) = 0.0;
                C_UDMI(c, t, 4) = 0.0;          /*d_sphere*/
                C_UDMI(c, t, 5) = T_low;    /*previous molten salt T*/
                C_UDMI(c, t, 6) = 0.0;
                C_UDMI(c, t, 7) = 0.0;

                T1=C_UDMI(c, t, 5)-273.0;
                k_l=(T1-260.0)/(454.4-260.0)*(0.294-0.421)+0.421;
                keff = k_l;
                C_UDMI(c, t, 3) = keff;
        }
        end_c_loop(c, t)
        Message("enter solve/set/expert to prevent memory freed\n");
}

DEFINE_ON_DEMAND (initial_textfile)
{
        FILE *fp;
        float s1, x_top, x_bot, e_top, e_bot;
        fp = fopen("d5cm_adiabatic.txt", "w");
        s1 = 0.0; x_top = 0.0; x_bot = 0.0; e_top = 0.0; e_bot = 0.0;
        fprintf(fp,"S_1: %f,Xtop: %f,Xbot: %f,Etop: %f,Ebot: %f",s1,x_top,x_bot,e_top,e
_bot);
        fclose(fp);
}

DEFINE_ON_DEMAND (initial_perm)
{
        FILE *fp1;
        float tm, s1, x_top, x_bot, e_top, e_bot, T_top;
        fp1 = fopen("d5cm_adiabatic_perm.txt", "a");
        fprintf(fp1, "tm, s1, x_top, x_bot, e_top, e_bot, T_top\n");
        tm = 0.0; s1 = 0.0; x_top = 0.0; x_bot = 0.0;
        e_top = 0.0; e_bot = 0.0; T_top = 0.0;
       fprintf(fp1, "%f, %f, %f, %f, %f, %f, %f\n",tm,s1,x_top,x_bot,e_top,e_bot,T_top);
        fclose(fp1);
}
```

```
DEFINE_ON_DEMAND (exergy_report)
{
        Domain *d;
        Thread *t;
        cell_t c;
        FILE *fp;
        real pp, vol, T1, T2, x1, x2, e1, e2, rho_l, net_x=0.0, net_e=0.0;
        float s1, x_top, x_bot, e_top, e_bot;
        fp = fopen("d5cm_adiabatic.txt", "r");
        fscanf(fp,"S_1: %f, Xtop: %f, Xbot: %f, Etop: %f,
Ebot: %f",&s1,&x_top,&x_bot,&e_top,&e_bot);
        fclose(fp);

        Message("Fillerbed Sgen: %f MJ/K\n\n", s1/1000000);
        Message("Fillerbed Xtop: %f MJ\n", x_top/1000000);
        Message("Fillerbed Xbot: %f MJ\n", x_bot/1000000);
        Message("Fillerbed Etop: %f MJ\n", e_top/1000000);
        Message("Fillerbed Ebot: %f MJ\n", e_bot/1000000);

        d = Get_Domain (1);
        t = Lookup_Thread(d, id1);
        begin_c_loop(c, t)
        {
                pp = C_UDMI(c, t, 0);
                vol = C_VOLUME(c, t)*2.0*M_PI;
                T1 = C_T(c, t);
                T2 = C_UDMI(c, t, 1);
                x1 = Cp_l*(T1 - T_0) - T_0*Cp_l*log(T1/T_0);
                x2 = Cp_s*(T2 - T_0) - T_0*Cp_s*log(T2/T_0);
                e1 = Cp_l*(T1 - T_0);
                e2 = Cp_s*(T2 - T_0);
                rho_l = 1938.0 - 0.732*((T1 - 273.0) - 200.0);
                net_x += pp*vol*rho_l*x1 + (1.0-pp)*vol*rho_s*x2;
                net_e += pp*vol*rho_l*e1 + (1.0-pp)*vol*rho_s*e2;
        }
        end_c_loop(c, t)

        t = Lookup_Thread(d, id2);
        begin_c_loop(c, t)
        {
                vol = C_VOLUME(c, t)*2.0*M_PI;
                T1 = C_T(c, t);
                x1 = Cp_l*(T1 - T_0) - T_0*Cp_l*log(T1/T_0);
                e1 = Cp_l*(T1 - T_0);
                rho_l = 1938.0 - 0.732*((T1 - 273.0) - 200.0);
```

```
                net_x += vol*rho_l*x1;
                net_e += vol*rho_l*e1;
        }
        end_c_loop(c, t)
        Message("Thermocline X: %f MJ\n", net_x/1000000);
        Message("Thermocline E: %f MJ\n", net_e/1000000);
}

/*------------------------*/
/*FLUID AND FLOW PROPERTIES*/
DEFINE_PROFILE (porosity, t, i)
{
        cell_t c;
        begin_c_loop (c, t)
        {
                F_PROFILE(c, t, i) = C_UDMI(c, t, 0);
        }
        end_c_loop (c, t)
}

DEFINE_PROFILE (visc_resis, t, i)
{
        real pp, K, source, d_sphere;
        cell_t c;
        begin_c_loop (c, t)
        {
                pp=C_UDMI(c, t, 0);
                d_sphere = C_UDMI(c, t, 4);

                /*permeability*/
                K = pow(d_sphere, 2.0)*pow(pp, 3.0)/(175.0*(1.0-pp)*(1.0-pp));
                source = 1.0 / K;
                F_PROFILE(c, t, i) = source;
        }
        end_c_loop(c, t)
}

DEFINE_PROFILE (inertial_resis, t, i)
{
        real pp, K, F, source, d_sphere;

        cell_t c;
        begin_c_loop (c, t)
        {
                pp=C_UDMI(c, t, 0);
```

```
            d_sphere = C_UDMI(c, t, 4);
            K = pow(d_sphere, 2.0)*pow(pp, 3.0)/(175.0*(1.0-pp)*(1.0-pp));
            F = 1.75 / sqrt(150.0*pow(pp,3.0));
            source = 2.0*F/sqrt(K);
            F_PROFILE(c, t, i)=source;
        }
        end_c_loop(c, t)
}

DEFINE_PROPERTY (cell_viscosity, c, t)
{
        real mu;
        real T1;
        T1 = C_T(c, t)-273.0;
        mu = exp(log(0.013)-2.0143*(log(T1)-log(150.0)));
        return mu;
}

DEFINE_PROPERTY (cell_density, c, t)
{
        real rho_l;
        real T1;
        T1 = C_T(c, t)-273.0;
        rho_l = 1938.0 - 0.732*(T1 - 200.0);
        return rho_l;
}

DEFINE_PROPERTY (thermal_conductivity, c, t)
{
        real keff;
        keff = C_UDMI(c, t, 3);
        return keff;
}
```

Appendix F.   FLUENT UDF Script for the Solar One Thermocline Tank Model

```
#include "udf.h"

real Cp_s = 790.0, rho_s = 2700.0, k_s = 2.2;
real Cp_l = 2400.0;
real T_hot = 577.0; //304 C
real T_cold = 477.0; //204 C
real T_ref = 298.0;

int id1 = 8, id2 = 7, id3 = 6;   //id1 is sand, id2 is rock, id3 is mix
real iso_porosity = 0.4, mix_porosity = 0.22;
real d_sand = 0.002, d_rock = 0.0127, d_mix = 0.0046;
real v_mass, m_chg = 0.0, m_dis = 1.8404;
real rho_hot = 654.3, rho_cold = 725.6;
real Bot1 = 0.665, Bot2 = 0.785, Top1 = 12.28, Top2 = 12.4;

// UDMI 0 - porosity, UDMI 1 - current T2,  UDMI 2 - prev T2,
// UDMI 3 - keff, UDMI 4 - d_sphere, UDMI 5 - Caloria T at the prev timestep
// UDMI 6 - mass_source

DEFINE_SOURCE (energy_source, c, t, dS, eqn)
{
        real source = 0.0;
        real hi, Re, Pr, pp, mu, rho_l, d_sphere, x[ND_ND], ss;
        real k_l, T1_old, T1, T2_old, T2, uu, dt;

        T1_old = C_UDMI(c, t, 5)-273.0;
        T2_old = C_UDMI(c, t, 2)-273.0;
        uu = sqrt(C_U(c, t)*C_U(c, t) + C_V(c,t)*C_V(c,t));
        mu = 67.415*pow(T1_old, -2.083);   //Caloria viscosity
        k_l = -0.00014*T1_old + 0.125;                //Caloria conductivity
        rho_l = C_R_M1(c, t);
        d_sphere = C_UDMI(c, t, 4);
        pp = C_UDMI(c, t, 0);
        Re = rho_l * d_sphere * uu / mu;
        Pr = mu * Cp_l / k_l;
        hi = k_l*6.0*(1.0-pp)*(2.0+1.1*pow(Re,0.6)*pow(Pr,0.333))/pow(d_sphere,2.0);
        source = hi * (T2_old - T1_old);
        dt = RP_Get_Real("physical-time-step");
        C_UDMI(c, t, 1) = -source*dt/((1.0-pp)*rho_s*Cp_s)+C_UDMI(c, t, 2); //cur T2

        C_CENTROID(x, c, t);
        T1 = C_T(c, t);
```

```
        ss = 0.0;

        //Energy source for charging
        /*v_mass = m_chg/rho_hot;
        if(x[0] > Top1 && x[0] < Top2)                      //hot region
                ss = m_chg*Cp_l*(T_hot - T_ref);
        if(x[0] > Bot1 && x[0] < Bot2)
                ss = -v_mass*rho_l*Cp_l*(T1 - T_ref);        //cold region
        //end if*/

        //Energy source for discharging
        v_mass = m_dis/rho_cold;
        if(x[0] > Top1 && x[0] < Top2)                      //hot region
                ss = -v_mass*rho_l*Cp_l*(T1 - T_ref);
        if(x[0] > Bot1 && x[0] < Bot2)
                ss = m_dis*Cp_l*(T_cold - T_ref);   //cold region
        //end if

        C_UDMI(c, t, 6) = source;
        C_UDMI(c, t, 7) = ss;

        source = source + ss;
        return source;
}

DEFINE_SOURCE (mass_source, c, t, ds, eqn)
{
        real source = 0.0;
        real x[ND_ND], rho_l;

        rho_l = C_R_M1(c, t);
        C_CENTROID(x, c, t);

        //Mass source for charging
        /*v_mass = m_chg/rho_hot;
        if(x[0] > Top1 && x[0] < Top2)                  //hot region
                source = m_chg;
        if(x[0] > Bot1 && x[0] < Bot2)                  //cold region
                source = -v_mass*rho_l;
        //end if*/

        //Mass source for discharging
        v_mass = m_dis/rho_cold;
        if(x[0] > Top1 && x[0] < Top2)
                source = -v_mass*rho_l;
```

```
        if(x[0] > Bot1 && x[0] < Bot2)
                source = m_dis;
        //end_if

        return source;
}

DEFINE_EXECUTE_AT_END (update_properties)
{
        Domain *d;
        Thread *t;
        cell_t c;
        real T1, T2, bb, phi, k_l, keff, mu_t, pp;

        d = Get_Domain (1);
        t = Lookup_Thread (d, id1);   //Sand zone
        begin_c_loop(c, t)
        {
                pp=C_UDMI(c, t, 0);
                C_UDMI(c, t, 2)=C_UDMI(c, t, 1);  //previous T2
                C_UDMI(c, t, 5)=C_T(c, t);
                T1=C_UDMI(c, t, 5)-273.0;
        T2=C_UDMI(c, t, 2)-273.0;
                k_l = -0.00014*T1 + 0.125;   //Caloria k
                bb = (k_s - k_l)/(k_s+2.0*k_l);
                phi = 1.0 - C_UDMI(c, t, 0);
                keff = k_l*(1.0+2.0*bb*phi+(2.0*pow(bb,3.0)-
0.1*bb)*pow(phi,2.0)+pow(phi,3.0)*0.05*exp(4.5*bb))/(1.0-bb*phi);
                C_UDMI(c, t, 3) = keff/pp;
        }
        end_c_loop (c, t)

        t = Lookup_Thread(d, id2);    //Rock Zone
        begin_c_loop(c, t)
        {
                pp=C_UDMI(c, t, 0);
            C_UDMI(c, t, 2)=C_UDMI(c, t, 1);  //previous T2
            C_UDMI(c, t, 5)=C_T(c, t);
            T1=C_UDMI(c, t, 5)-273.0;
            T2=C_UDMI(c, t, 2)-273.0;
            k_l = -0.00014*T1 + 0.125;
            bb = (k_s - k_l)/(k_s+2.0*k_l);
            phi = 1.0 - C_UDMI(c, t, 0);
            keff = k_l*(1.0+2.0*bb*phi+(2.0*pow(bb,3.0)-
0.1*bb)*pow(phi,2.0)+pow(phi,3.0)*0.05*exp(4.5*bb))/(1.0-bb*phi);
```

```
                C_UDMI(c, t, 3) = keff/pp;
        }
        end_c_loop (c, t)

        t = Lookup_Thread(d, id3);    //Mixture Zone
        begin_c_loop(c, t)
        {
                pp=C_UDMI(c, t, 0);
                C_UDMI(c, t, 2)=C_UDMI(c, t, 1);  //previous  T2
                C_UDMI(c, t, 5)=C_T(c, t);
                T1=C_UDMI(c, t, 5)-273.0;
                T2=C_UDMI(c, t, 2)-273.0;
                k_l = -0.00014*T1 + 0.125;
                bb = (k_s - k_l)/(k_s+2.0*k_l);
                phi = 1.0 - C_UDMI(c, t, 0);
                keff = k_l*(1.0+2.0*bb*phi+(2.0*pow(bb,3.0)-
0.1*bb)*pow(phi,2.0)+pow(phi,3.0)*0.05*exp(4.5*bb))/(1.0-bb*phi);
                C_UDMI(c, t, 3) = keff/pp;
        }
        end_c_loop (c, t)
}

DEFINE_PROFILE (porosity, t, i)
{
        cell_t c;
        begin_c_loop (c,t)
        {
                F_PROFILE(c, t, i) = C_UDMI(c, t, 0);
        }
        end_c_loop (c, t)
}

DEFINE_PROFILE (visc_resis, t, i)
{
        real pp, K, source, d_sphere;
        cell_t c;

        begin_c_loop (c, t)
    {
                pp=C_UDMI(c, t, 0);  // porosity
                d_sphere = C_UDMI(c, t, 4);

                //permeability
                K = pow(d_sphere, 2.0)*pow(pp, 3.0)/(175.0*(1.0-pp)*(1.0-pp));
                source = 1.0 / K;
```

```
                        F_PROFILE(c, t, i)=source;
                }
        end_c_loop(c, t)
}

DEFINE_PROFILE (inertial_resis, t, i)
{
        real pp, K, F, source, d_sphere;
        cell_t c;

        begin_c_loop (c, t)
        {
                pp=C_UDMI(c, t, 0);
                d_sphere = C_UDMI(c, t, 4);
                K = pow(d_sphere, 2.0)*pow(pp, 3.0)/(175.0*(1.0-pp)*(1.0-pp));
                F = 1.75 / sqrt(150.0*pow(pp,3.0));
                source = 2.0*F/sqrt(K);
                F_PROFILE(c, t, i)=source;
        }
        end_c_loop(c, t)
}

DEFINE_ON_DEMAND (init_properties)
{
        Domain *d;
        Thread *t, *t0, *t1, *tf, *tf1;
        cell_t c, c0, c1;
        face_t f;
        real X[ND_ND];
        real T1, T2, bb, phi, keff, k_l, pp;
        real A[ND_ND], ds, es[ND_ND], A_by_es, dr0[ND_ND], dr1[ND_ND];
        real A_mag, A_n[ND_ND];
        real xc[ND_ND], xf[ND_ND];

        d = Get_Domain (1);
        t = Lookup_Thread(d, id1);    //Sand Region
        begin_c_loop (c, t)
        {
                C_UDMI(c, t, 0)= iso_porosity;        //uniform porosity
                pp=C_UDMI(c, t, 0);
                C_UDMI(c, t, 4)=d_sand; //mixture mean diameter
                C_UDMI(c, t, 1)=T_cold; //current T2
                C_UDMI(c, t, 2)=T_cold; //previous T2
                C_UDMI(c, t, 5)=T_cold; //previous molten salt T
```

```
            T1 = C_T(c, t)-273.0;
            T2 = C_UDMI(c, t, 2)-273.0;
            k_l = -0.00014*T1 + 0.125;
            bb = (k_s - k_l)/(k_s+2*k_l);
            phi = 1.0 - C_UDMI(c, t, 0);
            keff = k_l*(1.0+2.0*bb*phi+(2.0*pow(bb,3.0)-
0.1*bb)*pow(phi,2.0)+pow(phi,3.0)*0.05*exp(4.5*bb))/(1.0-bb*phi);
            C_UDMI(c, t, 3) = keff/pp;
        }
        end_c_loop (c, t)

        t = Lookup_Thread(d, id2);    //Rock Region
        begin_c_loop(c, t)
        {
            C_UDMI(c, t, 0) = iso_porosity; //rock porosity
            pp=C_UDMI(c, t, 0);
        C_UDMI(c, t, 4)=d_rock;  //rock diameter
            C_UDMI(c, t, 1)=T_cold;  //current T2
            C_UDMI(c, t, 2)=T_cold;  //previous T2
          C_UDMI(c, t, 5)=T_cold;  //previous molten salt T

            T1 = C_T(c, t)-273.0;
            T2 = C_UDMI(c, t, 2)-273.0;
            k_l = -0.00014*T1 + 0.125;
            bb = (k_s - k_l)/(k_s+2*k_l);
            phi = 1.0 - C_UDMI(c, t, 0);
            keff = k_l*(1.0+2.0*bb*phi+(2.0*pow(bb,3.0)-
0.1*bb)*pow(phi,2.0)+pow(phi,3.0)*0.05*exp(4.5*bb))/(1.0-bb*phi);
            C_UDMI(c, t, 3) = keff/pp;
        }
        end_c_loop(c, t)

        t = Lookup_Thread(d, id3);    //Mixture Region
        begin_c_loop(c, t)
        {
            C_UDMI(c, t, 0) = mix_porosity; //rock porosity
            pp=C_UDMI(c, t, 0);
            C_UDMI(c, t, 4)=d_mix;  //rock diameter
            C_UDMI(c, t, 1)=T_cold;  //current T2
            C_UDMI(c, t, 2)=T_cold;  //previous T2
            C_UDMI(c, t, 5)=T_cold;  //previous molten salt T

            T1 = C_T(c, t)-273.0;
            T2 = C_UDMI(c, t, 2)-273.0;
            k_l = -0.00014*T1 + 0.125;
```

```
                bb = (k_s - k_l)/(k_s+2*k_l);
                phi = 1.0 - C_UDMI(c, t, 0);
                keff = k_l*(1.0+2.0*bb*phi+(2.0*pow(bb,3.0)-
0.1*bb)*pow(phi,2.0)+pow(phi,3.0)*0.05*exp(4.5*bb))/(1.0-bb*phi);
                C_UDMI(c, t, 3) = keff/pp;
        }
        end_c_loop(c, t)
}

DEFINE_PROPERTY (cell_viscosity, c, t)
{
        real mu, T1;
        T1 = C_T(c, t)-273.0;
        mu = 67.415 * pow(T1, -2.083);
        return mu;
}

DEFINE_PROPERTY (cell_density, c, t)
{
        real rho_l, T1;
        T1 = C_T(c, t)-273.0;
        rho_l = -0.713*T1 + 871.1;
        return rho_l;
}

DEFINE_PROPERTY (thermal_conductivity, c, t)
{
        real keff;
        keff = C_UDMI(c, t, 3);
        return keff;
}

DEFINE_ON_DEMAND (energy_calc)
{
        Domain *d;
        Thread *t;
        cell_t c;
        real x[ND_ND], Vc, pp, T1, T2, rho_l, cur_t = CURRENT_TIME;
        real E_fluid = 0.0, E_solid = 0.0, E_tank = 0.0, E_supply = 0.0;

        d = Get_Domain (1);
        t = Lookup_Thread(d, id2);
        begin_c_loop(c, t)
        {
                Vc = C_VOLUME(c, t);
```

```
            pp = C_UDMI(c, t, 0);
            T1 = C_T(c, t);
            T2 = C_UDMI(c, t, 1);
            rho_l = C_R_M1(c, t);

            E_fluid += pp*rho_l*Cp_l*(T1 - T_cold) * Vc;
            E_solid += (1.0 - pp)*rho_s*Cp_s*(T2 - T_cold) * Vc;
    }
    end_c_loop(c, t)

    t = Lookup_Thread(d, id3);
    begin_c_loop(c, t)
    {
            Vc = C_VOLUME(c, t);
            pp = C_UDMI(c, t, 0);
            T1 = C_T(c, t);
            T2 = C_UDMI(c, t, 1);
            rho_l = C_R_M1(c, t);

            E_fluid += pp * rho_l * Cp_l * (T1 - T_cold) * Vc;
            E_solid += (1.0-pp) * rho_s * Cp_s * (T2 - T_cold) * Vc;
    }
    end_c_loop(c, t)

    E_tank = (E_fluid + E_solid) * 2 * 3.14159;
    E_supply = m_chg *0.2 * 260.155 * cur_t * Cp_l * (T_hot - T_cold);
    printf("Supplied Energy is %g\n", E_supply);
    printf("Thermocline Energy is %g and %g\n", E_tank);
}
```

Appendix G.   Subsystem Models for a Molten-salt Power Tower Plant

G.1.   MATLAB Script for a CSP plant Steam Rankine Cycle

```
%Scott Flueckiger
%July 8, 2012
format short

clc
clear
T = zeros(1,7); P = zeros(1,7); h = zeros(1,7); s = zeros(1,7);

%Enter T(1)
T(1) = 538 + 273.15;

%Fixed Inputs
T1_o = 538 + 273.15;
P(3) = 0.1*100;     %kPa
P(4) = P(3);
x4 = 0;
x6 = 0;
Gross_MW = 111.48;
Gross_o = Gross_MW * 1000000;     %W

%Solve state 4 (does not change)
T(4) = refpropm('T','P',P(4),'Q',0,'water');
h(4) = refpropm('H','P',P(4),'Q',0,'water');
s(4) = refpropm('S','P',P(4),'Q',0,'water');

%Rated cycle inputs
P1_o = 125*100;
%disp('Rated P1 (bar):'); disp(P1_o/100);
n_turb_o = 0.9001;
n_pump_o = 0.9;

%Iterate to solve P2_o?
z = zeros(1,30); f_g = zeros(1,30);
j = 0; a_g = 0.5; err_g = 1;
while err_g > 0.001
        j = j + 1;
        if j < 3
                z(1) = 40*100;     %kPa
                z(2) = 5*100;
        else
```

```
            z(j) = z(j-1) - a_g*f_g(j-1)*(z(j-1) - z(j-2))/(f_g(j-1) - f_g(j-2));
        end
        P6_g = z(j);
        h6_g = refpropm('H','P',P6_g,'Q',0,'water');
        s6_g = refpropm('S','P',P6_g,'Q',0,'water');
        P7_g = P1_o;
        h7s_g = refpropm('H','P',P7_g,'S',s6_g,'water');
        h7_g = h6_g + (h7s_g - h6_g)/n_pump_o;
        T7_g = refpropm('T','P',P7_g,'H',h7_g,'water');
        f_g(j) = T7_g - (230 + 273.15);
        err_g = abs(f_g(j));
end
P2_o = z(j);
disp('Rated P2 (bar):'); disp(P2_o/100);
%disp('T7 error (K):'); disp(err_g);

%Solve design state 1
h1_o = refpropm('H','T',T1_o,'P',P1_o,'water');
s1_o = refpropm('S','T',T1_o,'P',P1_o,'water');
D1_o = refpropm('D','T',T1_o,'P',P1_o,'water');

%Solve design state 2
s2s_o = s1_o;
h2s_o = refpropm('H','P',P2_o,'S',s2s_o,'water');
dhs1_o = h1_o - h2s_o;
h2_o = h1_o - n_turb_o*dhs1_o;
D2_o = refpropm('D','P',P2_o,'H',h2_o,'water');

%Solve design state 5
P5_o = P2_o;
h5s_o = refpropm('H','P',P5_o,'S',s(4),'water');
h5_o = h(4) + (h5s_o - h(4))/n_pump_o;

%Solve design state 6
P6_o = P5_o;
h6_o = refpropm('H','P',P6_o,'Q',0,'water');

y_o = (h6_o - h5_o)/(h2_o - h5_o);
disp('Rated y:'); disp(y_o);

%Solve remaining inputs
T_evp_o = refpropm('T','P',P1_o,'Q',0,'water');
T_sh = T1_o - T_evp_o;

s2_o = refpropm('S','P',P2_o,'H',h2_o,'water');
```

```
s3s_o = s2_o;
h3s_o = refpropm('H','P',P(3),'S',s3s_o,'water');
dhs2_o = h2_o - h3s_o;
h3_o = h2_o - n_turb_o*(h2_o - h3s_o);


m_top_o = Gross_o/(h1_o - h2_o + (1-y_o)*(h2_o - h3_o));
m_bot_o = (1 - y_o)*m_top_o;

disp('T1 (C):'); disp(T(1)-273.15);
%Solve state 1
T_evp = T(1) - T_sh;
P(1) = refpropm('P','T',T_evp,'Q',0,'water');
h(1) = refpropm('H','T',T(1),'P',P(1),'water');
s(1) = refpropm('S','T',T(1),'P',P(1),'water');
D1 = refpropm('D','T',T(1),'P',P(1),'water');


%Guess P2
x = zeros(1,50); f = zeros(1,50);
j = 0; error = 1; alpha = 0.5;
while error > 0.0001
        j = j + 1;
        if j < 3
                x(1) = P2_o - 0.1*100;
                x(2) = 5*100;
        else
                x(j) = x(j-1) - alpha*f(j-1)*(x(j-1) - x(j-2))/(f(j-1) - f(j-2));
        end

        m_ratio_top = sqrt((P(1)^2 - x(j)^2)/(P1_o^2 - P2_o^2));

        %Solve h2
        h2s = refpropm('H','P',x(j),'S',s(1),'water');
        dhs1 = h(1) - h2s;
        %blade1 = m_ratio_top;
        blade1 = 1;
        n_turb1 = n_turb_o - 2*(blade1*(dhs1_o/dhs1)^0.5 - 1)^2;
        h(2) = h(1) - n_turb1*(h(1) - h2s);

        %Solve h5
        P(5) = x(j);
        m_ratio_bot = sqrt((x(j)^2 - P(3)^2)/(P2_o^2 - P(3)^2));
        n_pump2 = n_pump_o*(2*m_ratio_bot - (m_ratio_bot)^2);
        h5s = refpropm('H','P',P(5),'S',s(4),'water');
        h(5) = h(4) + (h5s - h(4))/n_pump2;
```

```matlab
        %Solve h6
        P(6) = P(5);
        h(6) = refpropm('H','P',P(6),'Q',0,'water');

        %Solve error
        y_a = (h(6) - h(5))/(h(2) - h(5));
        y_b = 1 - (1 - y_o)*m_ratio_bot/m_ratio_top;
        f(j) = y_a - y_b;
        error = abs(f(j));
end
y = y_a;

%Solve state 2
P(2) = x(j);
s(2) = refpropm('S','P',P(2),'H',h(2),'water');
T(2) = refpropm('T','P',P(2),'H',h(2),'water');
D2 = refpropm('D','P',P(2),'H',h(2),'water');

%Solve state 3
h3s = refpropm('H','P',P(3),'S',s(2),'water');
dhs2 = h(2) - h3s;
%blade2 = m_ratio_bot;
blade2 = 1;
n_turb2 = n_turb_o - 2*(blade2*(dhs2_o/dhs2)^0.5 - 1)^2;
h(3) = h(2) - n_turb2*(h(2) - h3s);
T(3) = refpropm('T','P',P(3),'H',h(3),'water');
s(3) = refpropm('S','P',P(3),'H',h(3),'water');
q3 = refpropm('Q','P',P(3),'H',h(3),'water');
disp('State 3 Quality:'); disp(q3);

m_top = m_ratio_top*m_top_o;
m_bot = m_ratio_bot*m_bot_o;
Gross = m_top*(h(1) - h(2)) + m_bot*(h(2) - h(3));
Percent = Gross/Gross_o;
disp('% Load:'); disp(Percent*100);

%Solve state 5
T(5) = refpropm('T','P',P(5),'H',h(5),'water');
s(5) = refpropm('S','P',P(5),'H',h(5),'water');

%Solve state 6
T(6) = refpropm('T','P',P(6),'Q',0,'water');
s(6) = refpropm('S','P',P(6),'Q',0,'water');

%Solve state 7
```

```
P(7) = P(1);
h7s = refpropm('H','P',P(7),'S',s(6),'water');
n_pump1 = n_pump_o*(2*m_ratio_bot - (m_ratio_bot)^2);
h(7) = h(6) + (h7s - h(6))/n_pump1;
T(7) = refpropm('T','P',P(7),'H',h(7),'water');
s(7) = refpropm('S','P',P(7),'H',h(7),'water');

%Solve state 8
P(8) = P(7);
T(8) = 230 + 273.15;
h(8) = refpropm('H','T',T(8),'P',P(8),'water');
s(8) = refpropm('S','T',T(8),'P',P(8),'water');

T_C = T - 273.15;
P_bar = P/100;

%Heat exchanger energy balance
h_f = refpropm('H','P',P(1),'Q',0,'water');
h_g = refpropm('H','P',P(1),'Q',1,'water');
Q_pre = m_top*(h_f - h(7));
Q_evp = m_top*(h_g - h_f);
Q_sup = m_top*(h(1) - h_g);
Q_net = Q_pre + Q_evp + Q_sup;
m_pre = m_top*(h(7) - h_f)/(h(8) - h_f);

disp('Q pre (MW):'); disp(Q_pre/1000000);
disp('Q evp (MW):'); disp(Q_evp/1000000);
disp('Q sup (MW):'); disp(Q_sup/1000000);
disp('Q net (MW):'); disp(Q_net/1000000);

disp('m top (kg/s):'); disp(m_top);
disp('m pre (kg/s):'); disp(m_pre);

sa = refpropm('S','T',T(6),'Q',1,'water');
s10 = refpropm('S','T',T_evp,'Q',1,'water');
s9 = refpropm('S','T',T_evp,'Q',0,'water');

s_plot = [s(2),s(3),s(4),s(5),s(6),sa,s(2),s(1),s10,s9,s(8),s(7),s(6)];
T_plot = [T(2),T(3),T(4),T(5),T(6),T(6),T(2),T(1),T_evp,T_evp,T(8),T(7),T(6)]-273.15;
%disp(transpose(s_plot));
%disp(transpose(T_plot));
%plot(s_plot,T_plot);

%n_te = Gross/Q_net;
%disp('Thermal to electric:'); disp(n_te);
```

```
%disp(P(2)/100);
%disp(T(2)-273.15);

parasitic = m_top*(h(7) - h(6)) + m_bot*(h(5) - h(4));
disp('Parasitic:'); disp(parasitic/1000000);
disp('Net power block:'); disp((Gross-parasitic)/1000000);
```

G.2.   DELSOL Scripts for Heliostat Field Design

G.2.1. Input Script to Optimize Heliostat Field Design

```
100 mwt cylindrical receiver
 &BASIC
 iprob=4
 itape=1
 /
 &FIELD
 /
 &HSTAT
 rmirl=.893
 /
 &REC
 iautop=1
 rrecl=0.948
 /
 &NLFLUX
 iflx=1
 iflaut=4
 nxflx=4
 nflxmx=4
 fazmin=0
 fazmax=270
 flxlim(1)=1e+06
 flxlim(2)=1e+06
 flxlim(3)=1e+06
 flxlim(4)=1e+06
 /
 &NLEFF
 etaref=0.4116
 smult=2.3
 /
 &REC
 iautop=1
 rrecl=0.948
```

```
/
&opt
numtht=20
numrec=11
wst=15.0
wend=25.0
numhtw=11
htwend=2.0
numopt=1
poptmn=100e+06
poptmx=100e+06
smult=2.3
iplfl(1)=1
iotape=1
irerun=1
/
&nlflux
iflx=1
iflaut=1
nxflx=4
nflxmx=4
fazmin=0
fazmax=270
flxlim(1)=1.0e+06
flxlim(2)=1.0e+06
flxlim(3)=1.0e+06
flxlim(4)=1.0e+06
/
&nleff
etaref=0.4116
smult=2.3
/
&nlcost
crec1=125e+06
xrec=0
ctow1=1.65e+06
ctow2=0.013
/
&nlecon
/
```

G.2.2. Input Script to Calculate Heliostat Field Efficiency Matrix

performance
```
&BASIC
```

```
iprob=3
itape=3
tdesp=100
/
&FIELD
/
&HSTAT
rmirl=0.893
/
&REC
iautop=1
rrecl=0.948
/
&NLFLUX
iflx=1
iflaut=4
nxflx=4
nflxmx=4
fazmin=0
fazmax=270
flxlim(1)=1e+06
flxlim(2)=1e+06
flxlim(3)=1e+06
flxlim(4)=1e+06
/
&NLEFF
etaref=0.4116
smult=2.3
/
&rec
w=-100.
/
```

G.3.   SOLERGY Script to Solve Transient Receiver Performance

```
THE NAME OF THE INSOLATION FILE IS:
 YEAR= 1985
 1977 data from Aerospace Corp.

 WARNING, THE MEANING OF IFILL=1 AND PMPAR
  HAS BEEN CHANGED.  CALL GREG KOLB (505)-844-1887
 &NMLGEN
 IFOUT   = 50*0,
 ISOUT   = 50*0,
 DELT    = 0.2500000
```

```
/
&NMLLOC
 ALAT   =  34.89700   ,
 ALONG  =  117.0220   ,
 ZONE   =  8.000000   ,
 IFLAGP =        0
/
&NMLCOEF
 NX    =        7,
 ELR   = 0.0000000E+00, 5.000000   , 15.00000   , 25.00000   , 45.00000   ,
65.00000   , 89.50000   ,
 NY    =        7,
 AZR   = 0.0000000E+00, 30.00000   , 60.00000   , 75.00000   , 90.00000   ,
110.0000   , 130.0000   ,
 FR    = 0.0000000E+00, 0.2840000   , 0.4660000   , 0.5620000   , 0.6210000   ,
0.6350000   , 0.6480000   ,
   0.0000000E+00, 0.2810000   , 0.4630000   , 0.5590000   , 0.6190000   ,
0.6340000   , 0.6480000   , 0.0000000E+00,
   0.2770000   , 0.4570000   , 0.5510000   , 0.6130000   , 0.6310000   , 0.6480000   ,
0.0000000E+00, 0.3060000   ,
   0.4610000   , 0.5490000   , 0.6090000   , 0.6290000   , 0.6480000   ,
0.0000000E+00, 0.2680000   , 0.4460000   ,
   0.5410000   , 0.6050000   , 0.6270000   , 0.6480000   , 0.0000000E+00,
0.2990000   , 0.4490000   , 0.5380000   ,
   0.6000000   , 0.6230000   , 0.6480000   , 0.0000000E+00, 0.3030000   ,
0.4450000   , 0.5340000   , 0.5970000   ,
   0.6210000   , 0.6480000
/
&NMLCOLF
 FS    =  1170000.   ,
 TLIML  = 0.0000000E+00,
 TLIMU  =  120.0000   ,
 ELIM   = 0.0000000E+00,
 WSLIM  =  17.90000   ,
 RFLCTY =  1.000000   ,
 NEFWS  =        8,
 WSX   = 0.0000000E+00, 2.000000   , 4.000000   , 6.000000   , 8.000000   ,
10.00000   , 12.00000   ,
   13.40000   ,
 WSEF   = 8*1.000000
/
&NMLRCVR
 EPS   = 0.9480000   ,
 RS    =  622.9600   ,
 ALPHAR = 0.2000000   ,
```

```
 TREQD  =  0.7500000   ,
 EREQD  =  1.100000   ,
 RMF    =  0.1600000   ,
 NXLR   =        7,
 WXLR   = 0.0000000E+00,  2.000000   ,  4.000000   ,  6.000000   ,  8.000000   ,
10.00000   ,  12.00000   ,
 PLXLR  = 7*42.6000      ,
 IFILL  =        2,
 EXFAC  =  0.0000000E+00
 /
 &NMLPIPE
 NXLP   =        9,
 TXLP   = -22.00000   , -4.000000   ,  14.00000   ,  32.00000   ,  50.00000   ,
68.00000   ,  86.00000   ,
   104.0000   ,  122.0000   ,
 YXLP   = 3.4730000E-04, 3.3929999E-04, 3.3129999E-04, 3.2319999E-04,
3.1520001E-04, 3.0710001E-04, 2.9910001E-04,
  2.9110000E-04, 2.8300000E-04
 /
 &NMLTRBN
 TBHWS  =  12.00000   ,
 TBWCS  =  60.00000   ,
 TPFSL  =  270.8500   ,
 TMFS   =  0.3000000   ,
 ESMIN1 =  104.9600   ,
 ESMIN2 =  270.8500   ,
 ESMAX1 =  104.9600   ,
 ESMAX2 =  8125.500   ,
 SDH    =  0.2500000   ,
 SDW    =  1.000000   ,
 SDC    =  1.800000   ,
 RDH    =  0.4000000   ,
 RDW    =  1.700000   ,
 RDC    =  2.700000   ,
 NREPSS =        6,
 NCEPSS =        4,
 REPSS  = 0.2907000   , 0.5239000   , 0.7563000   ,  1.000000   ,
 CEPSS  = 30.00000   ,  40.00000   ,  50.00000   ,  60.00000   ,  70.00000   ,
80.00000   ,
 FEPSS  = 6*0.3482000    , 6*0.3757000    , 6*0.3968000    , 6*0.4116000
 /
&NMLSTRG
 PTSMAX =  622.9600   ,
 PFSMAX =  270.8500   ,
 PTSMIN =  0.0000000E+00,
```

```
PFSMIN =  2.000000    ,
EMAX   =  8125.500    ,
EMIN   =  0.0000000E+00,
ES     =  0.0000000E+00,
A      = 3*0.0000000E+00  ,
CLF    =  0.0000000E+00,
DLF    =  0.1600000    ,
TNKLF  =  0.0000000E+00,
LS     =         1,
REFPC  =  260.0000    ,
TSTCR  =  0.0000000E+00,
ESTCR  =  0.0000000E+00,
TSTDR  =  0.2500000    ,
ESTDR  =  0.0000000E+00,
PWARMC =  375.0000    ,
PWARMD =  37.20000
/
&DISPATCH
IDISP  =         0,
TSTUR  =  1.250000    ,
PSTFR  =  0.1000000    ,
IDF1   =       400,
IDF2   =         0,
NVAC   =         8,
IDYLT1 =       118,
IDYLT2 =       299,
ISUMR1 =       153,
ISUMR2 =       279,
IVAC   =         1,       49,      147,      185,      245,      315,      332,      359,
 2*0,
IWEEK  =         2
/
&PRNTOUT
MFLAG  =         2,
NDAF   =         1,
NDAL   =       365
/
&PRSTIC
PA     = 8.0000001E-07, 2.4000001E-05,  1.100000    , -1.680000    ,  6.580000    ,
0.0000000E+00,  2.410000    ,
   1.150000    ,  1.380000    ,  0.7120000    ,  0.3560000    ,  0.0000000E+00,
1.650000    ,  0.2100000    ,  0.2390000    ,
   0.2750000    ,  0.5370000    ,  0.6080000    ,  1.040000    ,  1.350000    ,  1.180000    ,
0.7280000    ,  0.4690000    ,
```

```
   0.2930000  , 0.2510000  , 10.70000  , 3.000000  , 0.3100000  , 0.2850000  ,
 1.060000  ,
 PAHR  = 1.000000  , 2.000000  , 3.000000  , 4.000000  , 5.000000  ,
 6.000000  , 7.000000  ,
   8.000000  , 9.000000  , 10.00000  , 11.00000  , 12.00000  , 13.00000  ,
 14.00000  , 15.00000  ,
 RCVPAT  = 16*0.0000000E+00  ,
 RCVPAE  = 16*0.0000000E+00
  /
```

Appendix H.   C Script for System-level Simulation of a CSP Plant with Molten-salt Thermocline Energy Storage

```c
#include <stdio.h>
#include <stdlib.h>
#include <math.h>
#include <time.h>
#define max(a,b) a > b ? a : b
#define min(a,b) a < b ? a : b


#define n 500                   //number of thermocline bed cells
#define data 35040              //number of solar receiver data points
double TDMA(double a_x[n],double b_x[n],double c_x[n],double d_x[n],double
phi_x[n]);
double storage(double mass_in, double temp_in);
double density(double temp);
double annual(double hour_tank);
double T_hot = 600;            //Hot temperature limit
double T_cold = 300;           //Cold temperature limit
double pp = 0.22;              //Thermocline porosity
double dt = 3.0;               //Time step
double height = 11.0;          //Thermocline bed height
double cp_l = 1520.0;          //Molten salt specific heat
double cp_s = 830.0;           //Rock specific heat
double rho_s = 2500.0;         //Rock density
double d_s = 0.01;             //Rock diameter
double area;
char min_file[255], day_file[255], bed_file[255], heel_file[255];


double Tmin = 473.0;           //Minimum salt temperature for steam gen
double Pmin = 95.04;           //Minimum receiver power for steam gen
double n_cyc = 0.4116;         //Rated cycle efficiency
double Wnet = 100.0;           //Net electrical output (MW)
double SM = 2.3;               //Solar multiple (defines dynamic folder names)

int main(void) {

        int i;
        double hour_tank;
        //Batch mode
        /*for(i = 0; i < 7; i++){
                hour_tank = 6.0 + 2.0*i;        //tank size h
                annual(hour_tank);
        }*/
```

```c
        hour_tank = 6.0;
        annual(hour_tank);
        return 0;
}

double annual(double hour_tank){
        int i, j, count_max, t_step, step, Flag, Tflag, sat, hot, warm, cold;
        double Eheel, del_E, tstrt, Loss_old, Qdes, Emax, mc0, E_A, rho_h, t_off;
        double t_end, standby, mass_in, Temp_in, dx, t_max, xp[n], Salt[n], Rock[n];
        double Theel, Tbot, rhob, Ttop, diam, rhot, TMtop, TMbot, TM, dm_dt, dE_dt;
        double Tadd, mass_top, mass_bot, mflow[n], time, Tdiff, hour, Prec, mrec;
        double mcyc, Qout, nday, TMs, B, mbot, theta, Trec, Peff, Wgrs, volc, rho1;
        double Eliq, hourt, Esol, Enet, Etank, Eold, mold, mliq, flow, timet, mass1;
        double mass2, rate, Elec, Sunq, Qtnk, Qmax, Qhot, eff, CF, Prat, threq, Rloss;
        double liquid, t_ramp, frac, kheel, diffusion, E_in, E_out;
        float fx[n], fT1[n], fT2[n], fm[n], M_kg, E_MJ, T_ave, DAY[data], PTWF[data];
        clock_t proc;
        FILE *fbed, *fheel, *fp1, *output, *fp2, *CSPout;
        proc = clock();

        //Create dynamic filenames
        sprintf(min_file, "%.0fh_100MW_SM=%.1f_15min.txt", hour_tank, SM);
        sprintf(day_file, "%.0fh_100MW_SM=%.1f_day.txt", hour_tank, SM);
        sprintf(bed_file, "%.0fh_100MW_SM=%.1f_bed.txt", hour_tank, SM);
        sprintf(heel_file,"%.0fh_100MW_SM=%.1f_heel.txt", hour_tank, SM);

        //Size thermocline tank
        Qdes = Wnet/((1.0-0.103)*n_cyc);            //0.103 parasitic term from DELSOL
        Emax = (hour_tank + 0.0)*Qdes*1.4;          //Half hour overdesign
        mc0 = Qdes*1.0e6/(cp_l*(T_hot - T_cold));
        rho_h = 2090 - 0.636*T_hot;
        E_A = (T_hot-T_cold)*(height*(pp*rho_h*cp_l+(1.0-pp)*rho_s*cp_s) +
0.9*rho_h*cp_l)/(1.0e6*3600.0);

        area = Emax/E_A;
        diam = pow(area*4.0/3.14159,0.5)*100.0/(2.54*12.0); //tank diameter in feet

        //Area constraint
        if(diam > 160.0){
                //Single thermocline is too large
                //Operate two thermocline tanks (in parallel!)
                //Model is based on area, not diameter, so nothing changes

                diam = pow(0.5*area*4.0/3.14159,0.5)*100.0/(2.54*12.0);
                printf("Two tanks are required\n");
```

```
}

//Output model overview
printf("\nStorage time is %.1f h (40 percent overdesign)\n", hour_tank);
printf("Maximum storage capacity is %.2f MWh\n", Emax);
printf("Thermocline tank area is %0.2f m2\n", area);
printf("Thermocline tank diameter is %0.2f feet\n", diam);

dx = height/n;
count_max = 365*24*1200;   //1 year

//Initial temperatures
for(j = 0; j < n; j++){
        xp[j]= j*dx + dx/2.0;
        Salt[j] = T_cold;
        Rock[j] = T_cold;
        mflow[j] = 0.0;
}
Tbot = T_cold;
mass_bot = mflow[0];
mcyc = 0.0;

//Generate bed text file
fbed = fopen(bed_file, "w+");
for(j = 0; j < n; j++){
        fx[j] = xp[j];
        fT1[j] = Salt[j];
        fT2[j] = Rock[j];
        fm[j] = mflow[j];

        fprintf(fbed,"%f,",fx[j]);
        fprintf(fbed,"%f,",fT1[j]);
        fprintf(fbed,"%f,",fT2[j]);
        fprintf(fbed,"%f\n",fm[j]);
}
fclose(fbed);

//Generate heel text file
fheel = fopen(heel_file, "w+");
M_kg = 0.57*area*(2090.0 - 0.636*T_cold); //fix initial heel height to 0.57 m
E_MJ = 0.0; T_ave = T_cold;
fprintf(fheel,"%f, %f, %f", M_kg, E_MJ, T_ave);
fclose(fheel);

//Generate summary data file
```

```
        output = fopen(min_file,"w+");
        fprintf(output,"day,hour,Prec,Trec,mrec,mcyc,mbot,mtop,Tbot,Ttop,Theel,Ebed,E
heel,Wgrs,Flag,timet,Tflag\n");
        fclose(output);

        //Generate daily file
        CSPout = fopen(day_file,"w+");
        fprintf(CSPout,"day,Qmax,Qtnk,Qhot,CF,Work,Discard\n");
        fclose(CSPout);

        //Read in Day and PTWF data
        fp1 = fopen("PTWF_100MW_15Jan13.txt", "r");
        for(i = 0; i < data; i++){
                fscanf(fp1,"%f", &DAY[i]);
                fscanf(fp1,"%f", &PTWF[i]);
        }
        fclose(fp1);

        Elec = 0.0; Sunq = 0.0; Qtnk = 0.0; Qmax = 0.0; Qhot = 0.0; Rloss = 0.0;
        tstrt = 0.0; standby = 0.0; Tflag = 0; Loss_old = 0.0; sat = 0;
        t_end = 40.0/60.0; t_off = 0.0; hot = 0; warm = 0; cold = 0;
        //TRANSIENT CSP PLANT ANALYSIS
        for(t_step = 0; t_step < count_max; t_step++){
                time = (t_step)*dt;
                hour = time/3600.0;
                while(hour > 24.0){
                        hour = hour - 24.0;
                }

                //Read in bed (to get floor temps)
                fbed = fopen(bed_file, "r");
                for(j = 0; j < n; j++){
                        fscanf(fbed,"%f,", &fx[j]);
                        fscanf(fbed,"%f,", &fT1[j]);
                        fscanf(fbed,"%f,", &fT2[j]);
                        fscanf(fbed,"%f\n", &fm[j]);
                }
                Tbot = fT1[0];
                Ttop = fT1[n-1];
                fclose(fbed);

                //Call day of the year and current receiver power
                step = floor(time/900.0);
                nday = DAY[step];
                Prec = PTWF[step];
```

```
//Read in heel (to get Theel)
fheel = fopen(heel_file, "r");
fscanf(fheel,"%f, %f, %f", &M_kg, &E_MJ, &T_ave);
Theel = T_ave;
fclose(fheel);
theta = (Theel - T_cold)/(T_hot - T_cold);
Eheel = M_kg*cp_l*(Theel - 300.0)/(1.0e6*3600.0);

//Calculate solar reciever temperature
Trec = T_cold;
mbot = max(-mass_bot, 0.0); //Only non-zero during charge
if(mcyc + mbot > 0.0){
        Trec = (mcyc*T_cold + mbot*Tbot)/(mcyc + mbot);
}

//SOLVE POWER BLOCK MASS FLOW RATE 25Sep12
if(Theel > Tmin){
        //Thermocline heel hot enough to support power block
        if(Theel > 599.8){
                //Rated turbine performance
                mcyc = mc0;
                Wgrs = Wnet/(1.0-0.103);
        }
        else{
                //Derated turbine performance
                mcyc = (-
0.59764*pow(theta,3.0)+0.39901*pow(theta,2.0)+1.4306*theta-0.23253)*mc0;
                Wgrs = -190.20*pow(theta,3.0)+491.16*pow(theta,2.0)-
226.38*theta+36.865;
        }
}
else{
        //Thermocline tank too cold to support power block
        mcyc = 0.0;
        Wgrs = 0.0;
}

//STARTUP CONTROL 3Dec12
if(Tflag == 1 || tstrt > t_end){
        //Turbine is fully activated
        if(Tflag == 0){
                //Count hot, warm, or cold start
                if(t_end > 40.0/60.0){
                        if(t_end > 160.0/60.0){
```

```
                                        cold = cold + 1;
                                }
                                else{
                                        warm = warm + 1;
                                }
                        }
                        else{
                                hot = hot + 1;
                        }
                }
                Tflag = 1;
                tstrt = 0.0;
        }
        else{
                //Turbine is not fully activated
                if(hourt > 1.5 || tstrt > 0.0){
                        //Turbine in startup (expect 2h of storage before rampup);
                        mcyc = Pmin*1.0e6/(cp_l*(Theel - T_cold));
                        Wgrs = 0.0;
                        tstrt = tstrt + dt/3600.0;

                        //Turbine in rampup
                        if(tstrt > (t_end - t_ramp)){
                                frac = 1.0 + 0.7*(tstrt - t_end)/t_ramp;
                                mcyc = mc0*(-
0.080227*pow(frac,2.0)+1.0243*frac+0.055298);
                                Wgrs = Wnet*frac/(1.0 - 0.103);
                        }
                }
                else{
                        //Turbine in shutdown
                        mcyc = 0.0;
                        Wgrs = 0.0;
                }
        }

        //SOLAR RECEIVER FLOW RATE (Tank overcharge control) 29Dec12
        mrec = Prec*1.0e6/(cp_l*(T_hot - Trec));
        if(Tbot > T_cold + 100.0){
                //Tank at energy capacity
                Trec = T_cold;
                if(tstrt > 0.0){
                        //Turbine in startup
                        mrec = min(mrec, mcyc);
                }
```

```
                              else{
                                      mrec = min(mrec, mc0);
                              }
                              Rloss = Rloss + (Prec - mrec*cp_l*(T_hot - Trec)/1.0e6)*dt;
                              Prec = mrec*cp_l*(T_hot - Trec)/1.0e6;
                      }

                      //THERMOCLINE TANK DISPATCH CONTROL INDICATOR
                      if(mcyc > mrec){
                              //Tank discharge needed
                              Flag = 1;
                      }
                      else{
                              //Tank in charge or standby
                              Flag = 0;
                      }

                      if(tstrt > 0.0 && tstrt < 0.001 && hourt < 2.0){
                              //Turbine attempting to startup with less than 2 hours of stored
energy
                              if(PTWF[step+1]<Qdes || PTWF[step+2]<Qdes ||
PTWF[step+3]<Qdes || PTWF[step+4]<Qdes){
                                      //Future sunlight is not sufficient to start turbine
                                      mcyc = 0.0;
                                      tstrt = 0.0;
                              }
                      }

                      if(Tflag == 1 && Wgrs < 0.1){
                              //Return turbine to deactivated state
                              Tflag = 0;
                      }

                      //New code to modify turbine warmup time 27Dec12
                      if(Wgrs < 0.1 && tstrt < 0.0001){
                              //Turbine is off and not in warmup
                              //Calculate required startup and rampup times
                              t_off = t_off + dt/3600.0;
                              t_end = 40.0/60.0;
                              t_ramp = 25.0/60.0;
                              if(t_off > 12.0){
                                      t_end = 160.0/60.0;
                                      t_ramp = 100.0/60.0;
                                      if(t_off > 72.0){
                                              t_end = 270.0/60.0;
```

```
                             t_ramp = 160.0/60.0;
                    }
            }
    }
    else{
            //Turbine is active
            t_off = 0.0;
    }

    //Update cumulative receiver power and turbine output
    Sunq = Sunq + Prec*dt;          //MJ
    Elec = Elec + Wgrs*(1.0-0.103)*dt;  //MJ  net value

    //Calculate thermocline tank storage effectiveness
    Qmax = Qmax + Prec*dt/(3600.0);
    Qtnk = Qtnk + mcyc*cp_l*(Theel-T_cold)*dt/(1.0e6*3600.0);
    if(Theel > 599.8){
            Qhot = Qhot + mcyc*cp_l*(Theel-T_cold)*dt/(1.0e6*3600.0);
    }

    //Calculate mass flow rate at tank floor (+) discharge (-) charge
    mass_bot = mcyc - mrec;

    //Calculate mass flow and temperature entering bed
    if(mass_bot >= 0.0){
            //Discharge
            mass_in = mass_bot;
            Temp_in = T_cold;
            //Tbot = Temp_in;
    }
    else{
            //Charge (mass_bot < 0.0)
            rhob = 2090.0 - 0.636*Tbot;
            Ttop = Theel;
            rhot = 2090.0 - 0.636*Ttop;

            TMs = (1.0-pp)*rho_s*cp_s;
            TMtop = pp*rhot*cp_l + TMs;
            TMbot = pp*rhob*cp_l + TMs;
            mass_in = mass_bot*TMtop/TMbot;
            Temp_in = Theel;
    }

    //Calculate thermocline bed mass and energy
    Eold = 0.0; mold = 0.0;
```

```
fbed = fopen(bed_file, "r");
for(j = 0; j < n; j++){
        fscanf(fbed,"%f,", &fx[j]);
        fscanf(fbed,"%f,", &fT1[j]);
        fscanf(fbed,"%f,", &fT2[j]);
        fscanf(fbed,"%f\n", &fm[j]);

        //Need to calculate bed energy content
        volc = dx*area;
        rho1 = 2090.0 - 0.636*fT1[j];
        Eliq = pp*volc*rho1*cp_l*(fT1[j] - 300.0);
        Esol = (1.0-pp)*volc*rho_s*cp_s*(fT2[j] - 300.0);
        Eold = Eold + Eliq + Esol;
        mold = mold + pp*volc*rho1;
}
fclose(fbed);

//Calculate total standby time
if(mass_in == 0.0){
        standby = standby + dt;
}

//SOLVE THERMOCLINE MODEL TO UPDATE TANK BED
storage(mass_in, Temp_in);

//Calculate updated bed mass and energy
Enet = 0.0; mliq = 0.0; timet = 0.0;
fbed = fopen(bed_file, "r");
for(j = 0; j < n; j++){
        fscanf(fbed,"%f,", &fx[j]);
        fscanf(fbed,"%f,", &fT1[j]);
        fscanf(fbed,"%f,", &fT2[j]);
        fscanf(fbed,"%f\n", &fm[j]);

        //Need to calculate bed energy content
        volc = dx*area;
        rho1 = 2090.0 - 0.636*fT1[j];
        Eliq = pp*volc*rho1*cp_l*(fT1[j] - 300.0);
        Esol = (1.0-pp)*volc*rho_s*cp_s*(fT2[j] - 300.0);
        Enet = Enet + Eliq + Esol;
        mliq = mliq + pp*volc*rho1;

        if(fT1[j] > Tmin){
                //Approximation using only salt data
                theta = (fT1[j] - 300.0)/(300.0);
```

```
                        mass1 = volc*rho1;
                        //Updated for parasitics
                        rate = (-
0.59764*pow(theta,3.0)+0.39901*pow(theta,2.0)+1.4306*theta-0.23253)*mc0;
                        timet = timet + (mass1/rate)/60.0;
                    }
                }
                fclose(fbed);

                //Update liquid heel mass
                dm_dt = (mold - mliq)/dt;  /*Negative of mass change in bed*/
                M_kg = M_kg + dm_dt*dt;

                //Update liquid heel energy
                mass_bot = fm[0];
                mass_top = fm[n-1];
                Ttop = fT1[n-1];
                kheel = 0.443 + 1.9e-4*Theel;          /*Use old heel temperature to
calculate k at boundary*/
                diffusion = kheel*area*(Theel - Ttop)/(dx/2.0);  /*diffusion from heel to
bed*/

                if(mass_bot < 0.0){
                        //Charge
                        E_in = mrec*cp_l*(T_hot - T_cold);
                        E_out = mcyc*cp_l*(Theel - T_cold) - mass_top*cp_l*(Theel -
T_cold) + diffusion;
                }
                else{
                        //Discharge
                        E_in = mrec*cp_l*(T_hot - T_cold) + mass_top*cp_l*(Ttop -
T_cold);
                        E_out = mcyc*cp_l*(Theel - T_cold) + diffusion;
                }
                dE_dt = (E_in - E_out)/1.0e6;
                E_MJ = E_MJ + dE_dt*dt;

                //Update liquid heel temperature
                T_ave = T_cold + E_MJ*1.0e6/(M_kg*cp_l);
                Etank = (Enet/1.0e6 + E_MJ)/3600.0;

                //Check if heel temperature exceeds the hot limit which is not physical

                if(T_ave > T_hot){
                        //Artificially reduce heel energy to compensate for this
```

```
                //This exhibits less error than modifying the heel mass instead
                //In reality the total liquid mass should remain constant at all times

                T_ave = T_hot;
                E_MJ = M_kg*cp_l*(T_ave - T_cold)/1.0e6;
        }
        liquid = mliq + M_kg;

        //Estimate remaining turbine output duration provided by thermocline tank
        if(T_ave > Tmin){
                theta = (T_ave - 300.0)/300.0;
                rate = (-
0.59764*pow(theta,3.0)+0.39901*pow(theta,2.0)+1.4306*theta-0.23253)*mc0;
                timet = timet + (M_kg/rate)/60.0;
        }
        timet = 15.0*floor((timet/1.17)/15.0);  //1.17 is a fudge factor

        //Prevent reporting a turbine time increase due to standby diffusion
        if(mrec < 1.0){
                hourt = min(timet/60.0,hourt);
        }
        else{
                hourt = timet/60.0;
        }

        //Update heel file
        fheel = fopen(heel_file, "w");
        fprintf(fheel,"%f, %f, %f", M_kg, E_MJ, T_ave);
        fclose(fheel);

        //Correction for output file
        if(hour > 23.5){
                nday = nday - 1.0;
        }

        //15 minute summary
        if(t_step % 300 == 0){
                output = fopen(min_file,"a+");

        fprintf(output,"%.0f,%.2f,%.2f,%.1f,%.2f,%.2f,%.2f,%.2f,%.1f,%.1f,%.1f,%.4f,%
.4f,%.2f,%d,%.2f,%d,%.4f\n",nday,hour,Prec,Trec,mrec,mcyc,mass_bot,mass_top,Tbot,
Ttop,T_ave,Enet/(1.0e6*3600.0),E_MJ/3600.0,Wgrs,Flag,hourt,Tflag,liquid/1000.0);
                fclose(output);
        }
```

```
        //Daily summary performed at 5:45am (time when turbine always off)
        if(hour == 5.75 && nday > 1){
                eff = Qtnk/Qmax;
                CF = Elec/(time*Wnet);  //MJ/MJ
                //Prat = Elec/Sunq;

                //Record (1) day, (2) Qmax, (3) Qtnk, (4) Qhot,
                //(5) CF, (6) net work, (7) thermal discard
                CSPout = fopen(day_file,"a+");
                fprintf(CSPout,"%.0f,%.2f,%.2f,%.2f,%.5f,%.4f,%.2f\n",nday-
1,Qmax,Qtnk,Qhot,CF,Elec/(1000.0*3600.0),Rloss/3600.0);
                fclose(CSPout);

                if(Rloss > Loss_old){
                        sat = sat + 1;
                        Loss_old = Rloss;
                }
        }
}

//Annual capacity factor
CF = Elec/(time*Wnet);

//Output annual performance
printf("\nReceiver absorbed energy is %0.5f GWh\n", Sunq/(3600.0*1000.0));
printf("Net turbine output is %0.5f GWh\n", Elec/(3600.0*1000.0));
printf("Annual net capacity factor is %0.5f\n", CF);
printf("Number of saturation events is %d\n", sat);
printf("Thermal energy discard is %0.5f GWh\n", Rloss/(3600.0*1000.0));
printf("Annual tank effectiveness is %0.5f\n", Qtnk/Qmax);
printf("Theoretical max CF is %0.5f\n\n", (Sunq+Rloss)*n_cyc*(1.0-
0.103)/(Wnet*24.0*365.0*3600.0));

printf("Number of hot starts:  %d\n", hot);
printf("Number of warm starts: %d\n", warm);
printf("Number of cold starts: %d\n", cold);
printf("Standby time: %0.5f days\n", standby/(3600.0*24.0));

//Output total calculation time
proc = clock() - proc;
printf("Calculation time was %0.2f minutes\n\n",
((float)proc)/(CLOCKS_PER_SEC*60.0));

//Write annual plant results to day summary file
CSPout = fopen(day_file,"a+");
```

```
        fprintf(CSPout,"%.0f,%.5f,%.5f,%.4f,%.2f\n",nday,eff,CF,Elec/(1000.0*3600.0),
Rloss/3600.0);
        fprintf(CSPout,"\nStorage time is %.1f h (0.5 hour overdesign)\n", hour_tank);
        fprintf(CSPout,"Maximum storage capacity is %.2f MWh\n", Emax);
        fprintf(CSPout,"Thermocline tank area is %0.2f m2\n", area);
        fprintf(CSPout,"\nReceiver absorbed energy is %0.5f GWh\n",
Sunq/(3600.0*1000.0));
        fprintf(CSPout,"Net turbine output is %0.5f GWh\n", Elec/(3600.0*1000.0));
        fprintf(CSPout,"Annual net capacity factor is %0.5f\n", CF);
        fprintf(CSPout,"Number of saturation events is %d\n", sat);
        fprintf(CSPout,"Thermal energy discard is %0.5f GWh\n",
Rloss/(3600.0*1000.0));
        fprintf(CSPout,"Annual tank effectiveness is %0.5f\n", Qtnk/Qmax);
        fprintf(CSPout,"Theoretical max CF is %0.5f\n", (Sunq+Rloss)*n_cyc*(1.0-
0.103)/(Wnet*24.0*365.0*3600.0));
        fprintf(CSPout,"Number of hot starts:  %d\n", hot);
        fprintf(CSPout,"Number of warm starts: %d\n", warm);
        fprintf(CSPout,"Number of cold starts: %d\n", cold);
        fprintf(CSPout,"Standby time: %0.5f days\n", standby/(3600.0*24.0));
        fprintf(CSPout,"Calculation time was %0.2f minutes\n",
((float)proc)/(CLOCKS_PER_SEC*60.0));
        fclose(CSPout);


        return 0;
}
double storage(double mass_in, double Temp_in){

        //THERMOCLINE TANK MODEL
        //Update temperature profile inside tank
        int i, j, k;
        double dx, TMs, Hs, as0, T_in, rho_in, vel_in, TM_in, xp[n], Salt[n];
        double Rock[n], T1[n], T2[n], Tp0, Ts0, rho0, H0, ap0[n], it1[n], it2[n];
        double rhop, H1, up, Fp, mflow[n], temp, mu, kl, Re, Pr, Nu, hv[n], Sp, Sc;
        double Tw, rhow, uw, aw[n], ae[n], b1[n], ap1[n], Fw, dp_e, dp_w, Fe;
        double a_x[n], b_x[n], c_x[n], d_x[n], phi_x[n], bs1, as1, mtemp[n], west, east;
        double phi_b, ks, beta, phi, numk, denk, keff, gamma, ab, Theel, speed_in;
        double r_e, r_w, psi_e, psi_w, numsum1, densum1, numsum2, densum2, res1,
res2, sumres;
        double ite, ke, gamheel, gam_east, gam_e, gam_w, tempe;
        float fx[n], fT1[n], fT2[n], fm[n], M_kg, E_MJ, T_ave;
        FILE *fbed, *fheel;

        dx = height/n;
        TMs = (1.0-pp)*rho_s*cp_s;
        Hs = TMs;
```

```
as0 = Hs/dt;

T_in = (Temp_in - T_cold)/(T_hot - T_cold);
rho_in = density(T_in);
vel_in = mass_in/(rho_in*area);
speed_in = fabs(vel_in);
TM_in = pp*rho_in*cp_l + TMs;

//Read in bed temps
fbed = fopen(bed_file, "r");
for(j = 0; j < n; j++){
        fscanf(fbed,"%f,", &fx[j]);
        fscanf(fbed,"%f,", &fT1[j]);
        fscanf(fbed,"%f,", &fT2[j]);
        fscanf(fbed,"%f\n", &fm[j]);

        xp[j] = fx[j];
        Salt[j] = fT1[j];
        Rock[j] = fT2[j];
}
fclose(fbed);

//Artificial inversion of temp field for hot inflow (charge)
for(j = 0; j < n; j++){
        if(vel_in >= 0.0){
                //Discharge
                k = j;
        }
        else{
                //Charge
                k = n - 1 - j;
        }
        T1[k] = (Salt[j] - T_cold)/(T_hot - T_cold);
        T2[k] = (Rock[j] - T_cold)/(T_hot - T_cold);
}

//Read in heel temp to get phi_b for diffusion
fheel = fopen(heel_file, "r");
fscanf(fheel,"%f, %f, %f", &M_kg, &E_MJ, &T_ave);
Theel = T_ave;
fclose(fheel);
phi_b = (Theel - T_cold)/(T_hot - T_cold);

//Implicit method with TDMA solver
//Iteration necessary for non-linearity and equation coupling
```

```
sumres = 1.0; i = 0;
while(sumres > 1e-6 && i < 10){

        //Loop through discrete bed locations
        numsum1 = 0.0; densum1 = 0.0;
        for(j = 0; j < n; j++){
                Tp0 = T1[j];
                Ts0 = T2[j];
                rho0 = density(Tp0);
                H0 = pp*rho0;
                ap0[j] = H0*dx/dt;

                if(i == 0){
                        it1[j] = T1[j];
                        it2[j] = T2[j];
                        if(j < n-1){
                                ite = T1[j+1];
                        }
                }
                else{
                        if(j < n-1){
                                ite = it1[j+1];
                        }
                }

                //H, F, Sp, and Sc calculation
                rhop = density(it1[j]);
                H1 = pp*rhop;
                up = (pp*rhop*cp_l + TMs) * (rho_in*speed_in/rhop)/TM_in;
                Fp = rhop * up;
                mflow[j] = rhop*up*area;
                if(vel_in < 0.0){
                        mflow[j] = -mflow[j];
                }

                temp = it1[j]*(T_hot - T_cold) + T_cold;
                mu = (22.714-0.12*temp+2.281e-4*pow(temp,2.0)-1.474e-
7*pow(temp,3.0))/1000.0;
                kl = 0.443 + 1.9e-4*temp;
                Re = rhop*up*d_s/mu;
                Pr = mu*cp_l/kl;
                Nu = 6.0*(1.0-pp)*(2.0 + 1.1*pow(Re,0.6)*pow(Pr,0.333));
                hv[j] = Nu*kl/pow(d_s,2.0);
                Sp = -hv[j]/cp_l;
                Sc = (hv[j]/cp_l)*it2[j];
```

```
//Calculation of effective thermal conductivity
ks = 5.0;
beta = (ks - kl)/(ks + 2.0*kl);
phi = 1.0 - pp;
numk = 1.0+2*beta*phi+(2*pow(beta,3.0)-
0.1*beta)*pow(phi,2.0)+pow(phi,3.0)*0.05*exp(4.5*beta);
denk = 1.0 - beta*phi;
keff = kl*numk/denk;
gamma = keff/cp_l;

//Calculation of east cell thermal conductivity
if(j < n-1){
        tempe = ite*(T_hot - T_cold) + T_cold;
        ke = 0.443 + 1.9e-4*tempe;
        beta = (ks - ke)/(ks + 2.0*ke);
        numk = 1.0+2*beta*phi+(2*pow(beta,3.0)-
0.1*beta)*pow(phi,2.0)+pow(phi,3.0)*0.05*exp(4.5*beta);
        denk = 1.0 - beta*phi;
        gam_east = (ke*numk/denk)/cp_l;
}
gamheel = (0.443 + 1.9e-4*Theel)/cp_l;

if(j == 0){
        //Upwind scheme and adiabatic diffusion boundary
        Tw = T_in;
        rhow = density(Tw);
        uw = speed_in;

        if(vel_in >= 0.0){
                //Discharge or idle (Adiabatic boundary)
                ab = 0.0;
                gam_e = 1.0/(0.5/gamma + 0.5/gam_east);

                aw[j] = 0.0;
                ae[j] = gam_e/dx;
                b1[j] = Sc*dx + rhow*uw*Tw;
                ap1[j] = H1*dx/dt + Fp - Sp*dx + gam_e/dx;
        }
        else{
                //Charge (Fixed temperature of heel)
                ab = gamma*2.0/dx;
                gam_w = gamheel;
                gam_e = 1.0/(0.5/gamma + 0.5/gam_east);
```

```
                                        aw[j] = 0.0;
                                        ae[j] = gam_e/dx;
                                        b1[j] = Sc*dx + rhow*uw*Tw +
gamheel*(2.0/dx)*phi_b;

                                        ap1[j] = H1*dx/dt + Fp - Sp*dx + (gam_e +
2.0*gamheel)/dx;

                                }

                                west = 0.0;
                                east = ae[j]*it1[j+1];
                        }
                        if(j == 1){
                                //Upwind scheme
                                Tw = it1[j-1];
                                rhow = density(Tw);
                                uw = (pp*rhow*cp_l + TMs) *
(rho_in*speed_in/rhow)/TM_in;
                                Fw = rhow*uw;

                                gam_w = gam_e;
                                gam_e = 1.0/(0.5/gamma + 0.5/gam_east);

                                aw[j] = gam_w/dx + Fw;
                                ae[j] = gam_e/dx;
                                b1[j] = Sc*dx;
                                ap1[j] = H1*dx/dt + Fp - Sp*dx + (gam_w + gam_e)/dx;

                                west = aw[j]*it1[j-1];
                                east = ae[j]*it1[j+1];
                        }
                        if(j > 1 && j < n-1){
                                Tw = it1[j-1];
                                rhow = density(Tw);
                                uw = (pp*rhow*cp_l + TMs) *
(rho_in*speed_in/rhow)/TM_in;
                                Fw = rhow*uw;

                                //Quadratic limiter scheme
                                r_e = (it1[j+1] - it1[j])/(it1[j] - it1[j-1]);
                                r_w = (it1[j] - it1[j-1])/(it1[j-1]-it1[j-2]);
                                psi_e = 0.0;
                                psi_w = 0.0;
                                if(r_e > 0.0 && r_e < 2.0){
                                        psi_e = (2.0*r_e + pow(r_e,2.0))/(2.0 + r_e +
pow(r_e,2.0));
```

```
                                    }
                                    if(r_w > 0.0 && r_w < 2.0){
                                            psi_w = (2.0*r_w + pow(r_w,2.0))/(2.0 + r_w +
pow(r_w,2.0));
                                    }
                                    if(r_e > 2.0){
                                            psi_e = 1.0;
                                    }
                                    if(r_w > 2.0){
                                            psi_w = 1.0;
                                    }
                                    dp_e = psi_e * 0.5 * (it1[j] - it1[j-1]);
                                    dp_w = psi_w * 0.5 * (it1[j-1] - it1[j-2]);
                                    Fe = Fp;

                                    gam_w = gam_e;
                                    gam_e = 1.0/(0.5/gamma + 0.5/gam_east);

                                    aw[j] = gam_w/dx + Fw;
                                    ae[j] = gam_e/dx;
                                    b1[j] = Sc*dx + Fw*dp_w - Fe*dp_e;
                                    ap1[j] = H1*dx/dt + Fp - Sp*dx + (gam_w + gam_e)/dx;

                                    west = aw[j]*it1[j-1];
                                    east = ae[j]*it1[j+1];
                            }
                            if(j == n-1){
                                    //Upwind Scheme and constant temp diffusion BC (if idle)
                                    Tw = it1[j-1];
                                    rhow = density(Tw);
                                    uw = (pp*rhow*cp_l + TMs) *
(rho_in*speed_in/rhow)/TM_in;
                                    Fw = rhow*uw;

                                    if(vel_in >= 0.0){
                                            //Discharge or standby (Fixed temperature of heel)
                                            ab = gamma*2.0/dx;
                                            gam_w = gam_e;
                                            gam_e = gamheel;

                                            aw[j] = gam_w/dx + Fw;
                                            ae[j] = 0.0;
                                            b1[j] = Sc*dx + gamheel*(2.0/dx)*phi_b;
                                            ap1[j] = H1*dx/dt + Fp - Sp*dx + (gam_w +
2.0*gamheel)/dx;
```

```
                }
                else{
                        //Charge (Adiabatic)
                        ab = 0.0;
                        gam_w = gam_e;

                        aw[j] = gam_w/dx + Fw;
                        ae[j] = 0.0;
                        b1[j] = Sc*dx;
                        ap1[j] = H1*dx/dt + Fp - Sp*dx + gam_w/dx;
                }

                west = aw[j]*it1[j-1];
                east = 0.0;
        }

        a_x[j] = ap1[j];
        b_x[j] = ae[j];
        c_x[j] = aw[j];
        d_x[j] = b1[j] + ap0[j]*Tp0;

        //Residual calculation
        numsum1 = numsum1 + fabs(east + west + d_x[j] - a_x[j]*it1[j]);
        densum1 = densum1 + a_x[j]*it1[j];
}

//Update liquid temps with TDMA
TDMA(a_x, b_x, c_x, d_x, phi_x);
for(j = 0; j < n; j++){
        it1[j] = phi_x[j];
}

//Update solid temps (using old hv)
numsum2 = 0.0; densum2 = 0.0;
for(j = 0; j < n; j++){
        bs1 = hv[j]*it1[j];
        as1 = as0 + hv[j];

        //Residual calculation
        numsum2 = numsum2 + fabs(bs1 + as0*T2[j] - as1*it2[j]);
        densum2 = densum2 + as1*it2[j];

        it2[j] = (as0*T2[j] + bs1)/as1;
}
```

```
            res1 = numsum1/densum1;
            res2 = numsum2/densum2;
            sumres = res1+res2;
            i = i + 1;
        }

        //Output failure to converge within tolerance
        if(sumres > 1e-6){
            printf("Res > 1e-6\n");
        }

        //Reinvert temperature profile if hot inflow
        for(j = 0; j < n; j++){
            T1[j] = it1[j];
            T2[j] = it2[j];

            if(vel_in >= 0.0){
                k = j;
            }
            else{
                k = n - 1 - j;
            }
            Salt[k] = T1[j]*(T_hot - T_cold) + T_cold;
            Rock[k] = T2[j]*(T_hot - T_cold) + T_cold;
            mtemp[k] = mflow[j];
        }

        //Record updated bed temperatures
        fbed = fopen(bed_file, "w");
        for(j = 0; j < n; j++){
            fx[j] = xp[j];
            fT1[j] = Salt[j];
            fT2[j] = Rock[j];
            fm[j] = mtemp[j];

            fprintf(fbed,"%f,",fx[j]);
            fprintf(fbed,"%f,",fT1[j]);
            fprintf(fbed,"%f,",fT2[j]);
            fprintf(fbed,"%f\n",fm[j]);
        }
        fclose(fbed);
        return 0;
}
double density(double T_norm){
```

```
        //Calculate and return molten salt density
        double temp, rho;
        temp = T_norm*(T_hot - T_cold) + T_cold;
        rho = 2090.0 - 0.636*temp;
        return rho;
}
double TDMA(double a_x[n],double b_x[n],double c_x[n],double d_x[n],double
phi_x[n]){

        //Tri-diagonal matrix algorithm (direct solver)
        int i;
        double P[n], Q[n];
        for(i = 0; i < n; i++){
                if(i == 0){
                        P[i] = b_x[i]/a_x[i];
                        Q[i] = d_x[i]/a_x[i];
                }
                if(i > 0 && i < n-1){
                        P[i] = b_x[i]/(a_x[i] - c_x[i]*P[i-1]);
                        Q[i] = (d_x[i] + c_x[i]*Q[i-1])/(a_x[i] - c_x[i]*P[i-1]);
                }
                if(i == n-1){
                        P[i] = 0;
                        Q[i] = (d_x[i] + c_x[i]*Q[i-1])/(a_x[i] - c_x[i]*P[i-1]);
                        phi_x[i] = Q[i];
                }
        }
        for(i = n-2; i > -1; i--){
                phi_x[i] = P[i]*phi_x[i+1] + Q[i];
        }
        return 0;
}
```

Appendix I.   C Script for System-level Simulation of a CSP Plant with Latent Heat
Thermocline Energy Storage


```c
#include <stdio.h>
#include <stdlib.h>
#include <math.h>
#include <time.h>
#define max(a,b) a > b ? a : b
#define min(a,b) a < b ? a : b

//Scott Flueckiger
//April 11, 2013

#define n 1000              //number of thermocline bed cells
#define data 35040          //number of solar receiver data points
double TDMA(double a_x[n],double b_x[n],double c_x[n],double d_x[n],double
phi_x[n]);
double storage(double mass_bot, double temp_in);
double density(double temp);
double annual(double hour_tank);
double T_hot = 600.0;       //Hot temperature limit
double T_cold = 300.0;      //Cold temperature limit
double pp = 0.22;           //Thermocline porosity
double dt = 3.0;            //Time step
double height = 11.0;       //Thermocline bed height
double cp_l = 1520.0;       //Molten salt specific heat
double cp_s = 830.0;        //Rock specific heat
double rho_s = 2500.0;      //Rock density
double d_s = 0.01;          //Rock diameter
double URF = 0.95;          //Under relaxation factor for sol/liq energy transport
double area;                //Tank area
double tcount;

double Stefan = 0.5;
double epsilon = 1.0;
double latent;
double thmelt[n];
double Tmelt[n];
double Tsol[n];
double Tliq[n];
char min_file[255], day_file[255], bed_file[255], heel_file[255], sat_file[255];

double Tmin = 473.0;        //Minimum salt temperature for steam gen
double Pmin = 95.04;        //Minimum receiver power for steam gen
```

```c
double n_cyc = 0.4116;          //Rated cycle efficiency
double Wnet = 100.0;            //Net electrical output (MW)
double SM = 2.3;               //Solar multiple (defines dynamic folder names)

int main(void) {

        int i;
        double hour_tank;

        //Batch mode for different tank size
        /*for(i = 0; i < 7; i++){
                hour_tank = 6.0 + 2.0*i;        //tank size h
                annual(hour_tank);
        }*/

        latent = cp_s*Stefan*(T_hot - T_cold);
        hour_tank = 8.0;
        annual(hour_tank);
        return 0;
}

double annual(double hour_tank){

        int i, j, count_max, t_step, step, Flag, Tflag;
        int sat, hot, warm, cold, sol[n], tanksat, satflag;
        double Eheel, del_E, tstrt, Loss_old, Qdes, Emax, mc0, E_A, rho_h, t_off;
        double t_end, standby, mass_in, Temp_in, dx, t_max, xp[n], Salt[n], Rock[n];
        double Theel, Tbot, rhob, Ttop, diam, rhot, dm_dt, dE_dt, Tadd, mass_top;
        double mass_bot, mflow[n], time, Tdiff, hour, Prec, mrec, mcyc, Qout, nday;
        double TMs, B, mbot, theta, Trec, Peff, Wgrs, volc, rho1, Eliq, hourt, Esol;
        double Enet, Etank, Eold, mold, mliq, flow, timet, mass1, mass2, rate, Elec;
        double Sunq, Qtnk, Qmax, eff, CF, Prat, Rloss, liquid, t_ramp, frac, e_liq;
        double e_sol, e_heel, Snet, Sgen, ks, beta, kl, phi, numk, denk, keff, dTdx;
        double Esen, Elat, trated, tderated, kheel, E_in, E_out, diffusion;
        float fx[n], fT1[n], fT2[n], fm[n], fsol[n];
        float M_kg, E_MJ, T_ave, DAY[data], PTWF[data];
        clock_t proc;
        FILE *fbed, *fheel, *fp1, *output, *fp2, *CSPout, *fsat;
        proc = clock();

        //Create dynamic filenames
        sprintf(min_file, "%.0fh_SM=%.1f_15m_Ste=%.2f_Cascade.txt", hour_tank, SM,
Stefan);
        sprintf(day_file, "%.0fh_SM=%.1f_day_Ste=%.2f_Cascade.txt", hour_tank, SM,
Stefan);
```

```
        sprintf(bed_file, "%.0fh_SM=%.1f_bed_Ste=%.2f_Cascade.txt", hour_tank, SM,
Stefan);
        sprintf(heel_file,"%.0fh_SM=%.1f_liq_Ste=%.2f_Cascade.txt", hour_tank, SM,
Stefan);
        sprintf(sat_file, "%.0fh_SM=%.1f_sat_Ste=%.2f_Cascade.txt", hour_tank, SM,
Stefan);


        //Size thermocline tank
        Qdes = Wnet/((1.0-0.103)*n_cyc);           //0.103 parasitic term from DELSOL
        Emax = (hour_tank + 0.5)*Qdes*1.0;         //Half hour overdesign
        mc0 = Qdes*1.0e6/(cp_l*(T_hot - T_cold));
        rho_h = 2090.0 - 0.636*T_hot;
        e_liq = pp*rho_h*cp_l*(T_hot-T_cold);          //J/m3
        e_sol = (1.0-pp)*(rho_s*cp_s*(T_hot-T_cold));  //J/m3 (Sensible only)
        e_heel = rho_h*cp_l*(T_hot-T_cold);            //J/m3
        E_A = (height*(e_liq + e_sol) + 0.9*e_heel)/(1.0e6*3600.0);
        area = Emax/E_A;
        diam = pow(area*4.0/3.14159,0.5)*100.0/(2.54*12.0); //tank diameter in feet

        //Area constraint
        if(diam > 160.0){
                //Single thermocline is too large
                //Operate two thermocline tanks (in parallel!)
                //Model is based on area, not diameter, so nothing changes

                diam = pow(0.5*area*4.0/3.14159,0.5)*100.0/(2.54*12.0);
                printf("Two tanks are required\n");
        }

        printf("\nStorage time is %.1f h (half hour overdesign)\n", hour_tank);
        printf("Maximum storage capacity is %.2f MWh\n", Emax);
        printf("Thermocline tank area is %0.2f m2\n", area);
        printf("Thermocline tank diameter is %0.2f feet\n", diam);
        printf("Stefan number is %.2f\n", Stefan);

        dx = height/n;
        count_max = 365*24*1200;   //1 year

        //Initial thermocline bed temperatures and mass flow
        for(j = 0; j < n; j++){
                xp[j]= j*dx + dx/2.0;
                Salt[j] = T_cold;
                Rock[j] = T_cold;
                mflow[j] = 0.0;
```

```
            //Define PCM regions
            if(xp[j] >= height/1.5){
                    //Top third
                    thmelt[j] = 0.95;
            }
            if(xp[j] >= height/3.0 && xp[j] < height/1.5){
                    //Middle third
                    thmelt[j] = 0.75;
            }
            if(xp[j] < height/3.0){
                    //Bottom third
                    thmelt[j] = 0.25;
            }
            Tmelt[j] = T_cold + thmelt[j]*(T_hot - T_cold);
            Tliq[j] = Tmelt[j] + epsilon;
            Tsol[j] = Tmelt[j] - epsilon;

            //Calculate solid PCM Fraction
            if(Rock[j] <= Tsol[j]){
                    sol[j] = 1.0;
            }
            else if(Rock[j] > Tliq[j]){
                    sol[j] = 0.0;
            }
            else{
                    sol[j] = (Tliq[j] - Rock[j])/(Tliq[j] - Tsol[j]);
            }
    }
    Tbot = T_cold;
    mass_bot = mflow[0];
    mcyc = 0.0;

    //Generate thermocline bed text file
    fbed = fopen(bed_file, "w+");
    for(j = 0; j < n; j++){
            fx[j] = xp[j];
            fT1[j] = Salt[j];
            fT2[j] = Rock[j];
            fm[j] = mflow[j];
            fsol[j] = sol[j];

            fprintf(fbed,"%f,",fx[j]);
            fprintf(fbed,"%f,",fT1[j]);
            fprintf(fbed,"%f,",fT2[j]);
            fprintf(fbed,"%f,",fm[j]);
```

```c
                fprintf(fbed,"%f\n",fsol[j]);
        }
        fclose(fbed);

        //Generate liquid heel text file
        fheel = fopen(heel_file, "w+");

        /*Fix initial (cold) heel height to 0.57 m*/
        /*Heel will expand to max 0.9m at hot temp*/
        M_kg = 0.57*area*(2090.0 - 0.636*T_cold);
        E_MJ = 0.0; T_ave = T_cold;
        fprintf(fheel,"%f, %f, %f", M_kg, E_MJ, T_ave);
        fclose(fheel);

        //Generate 15 min model summary data file
        output = fopen(min_file,"w+");
        fprintf(output,"day,hour,Prec,Trec,mrec,mcyc,mbot,mtop,Tbot,Ttop,Theel,Esen,E
lat,Wgrs,Flag,timet,Tflag\n");
        fclose(output);

        //Generate daily model summary data file
        CSPout = fopen(day_file,"w+");
        fprintf(CSPout,"Day,Qmax,Qtnk,CF,Work,Discard\n");
        fclose(CSPout);

        //Read in Day and PTWF (SOLERGY) data
        fp1 = fopen("PTWF_100MW_15Jan13.txt", "r");
        for(i = 0; i < data; i++){
                fscanf(fp1,"%f", &DAY[i]);
                fscanf(fp1,"%f", &PTWF[i]);
        }
        fclose(fp1);

        Elec = 0.0; Sunq = 0.0; Qtnk = 0.0; Qmax = 0.0; Rloss = 0.0; tstrt = 0.0;
        standby = 0.0; Tflag = 0; Loss_old = 0.0; sat = 0; t_end = 40.0/60.0;
        t_off = 0.0; hot = 0; warm = 0; cold = 0; tanksat = 0; Snet = 0.0; satflag = 0;
        trated = 0.0; tderated = 0.0;
        //TRANSIENT CSP PLANT ANALYSIS
        for(t_step = 0; t_step < count_max; t_step++){

                tcount = t_step;
                time = (t_step)*dt;
                hour = time/3600.0;
                while(hour > 24.0){
                        hour = hour - 24.0;
```

```
        }

        //Read in bed (to get floor temps)
        fbed = fopen(bed_file, "r");
        for(j = 0; j < n; j++){
                fscanf(fbed,"%f,", &fx[j]);
                fscanf(fbed,"%f,", &fT1[j]);
                fscanf(fbed,"%f,", &fT2[j]);
                fscanf(fbed,"%f,", &fm[j]);
                fscanf(fbed,"%f\n", &fsol[j]);
        }
        Tbot = fT1[0];
        Ttop = fT1[n-1];
        fclose(fbed);

        //Call day of the year and current receiver power
        step = floor(time/900.0);
        nday = DAY[step];
        Prec = PTWF[step];

        //Read in heel (to get Theel)
        fheel = fopen(heel_file, "r");
        fscanf(fheel,"%f, %f, %f", &M_kg, &E_MJ, &T_ave);
        Theel = T_ave;
        fclose(fheel);
        theta = (Theel - T_cold)/(T_hot - T_cold);
        Eheel = M_kg*cp_l*(Theel - 300.0)/(1.0e6*3600.0);

        //Calculate receiver inlet temp (Trec)
        Trec = T_cold;
        mbot = max(-mass_bot, 0.0); //Only non-zero during charge
        if(mcyc + mbot > 0.0){
                Trec = (mcyc*T_cold + mbot*Tbot)/(mcyc + mbot);
        }

        //SOLVE POWER BLOCK MASS FLOW RATE 25Sep12
        if(Theel > Tmin){
                if(Theel > 599.8){
                        //Rated turbine output
                        mcyc = mc0;
                        Wgrs = Wnet/(1.0-0.103);
                }
                else{
                        //Derated turbine output
```

```
                              mcyc = (-0.59764*pow(theta,3.0)+0.39901*pow(theta,2.0)
+1.4306*theta-0.23253)*mc0;
                              Wgrs = -190.20*pow(theta,3.0)+491.16*pow(theta,2.0)-
226.38*theta+36.865;
                      }
              }
              else{
                      //Thermocline too cold for steam generation
                      mcyc = 0.0;
                      Wgrs = 0.0;
              }

              //STARTUP CONTROL 3Dec12
              if(Tflag == 1 || tstrt > t_end){
                      //Turbine is fully activated
                      if(Tflag == 0){
                              //Count hot, warm, or cold start
                              if(t_end > 40.0/60.0){
                                      if(t_end > 160.0/60.0){
                                              cold = cold + 1;
                                      }
                                      else{
                                              warm = warm + 1;
                                      }
                              }
                              else{
                                      hot = hot + 1;
                              }
                      }
                      Tflag = 1;
                      tstrt = 0.0;
              }
              else{
                      if(hourt > 1.5 || tstrt > 0.0){
                              //Turbine startup (expect 2h of storage before rampup);
                              mcyc = Pmin*1.0e6/(cp_l*(Theel - T_cold));
                              Wgrs = 0.0;
                              tstrt = tstrt + dt/3600.0;

                              //Turbine rampup
                              if(tstrt > (t_end - t_ramp)){
                                      frac = 1.0 + 0.7*(tstrt - t_end)/t_ramp;
                                      mcyc = mc0*(-0.080227*pow(frac,2.0)
+1.0243*frac+0.055298);

                                      Wgrs = Wnet*frac/(1.0 - 0.103);
```

```
                }
        }
        else{
                //Turbine in shutdown
                mcyc = 0.0;
                Wgrs = 0.0;
        }
}

//Reset heliostat storage saturation flag
if(hour < 0.5 && satflag == 1){
        satflag = 0;
}

//SOLAR RECEIVER FLOW RATE (Tank overcharge control) 29Dec12
mrec = Prec*1.0e6/(cp_l*(T_hot - Trec));
if(Tbot > T_cold + 100.0 || satflag == 1){
        //Tank at energy capacity
        Trec = T_cold;
        satflag = 1;
        if(tstrt > 0.0){
                //Turbine in startup
                mrec = min(mrec, mcyc);
        }
        else{
                //Turbine at rated condition
                mrec = min(mrec, mc0);
        }
        //Thermal energy discard
        //Modified receiver power (heliostat defocus)
        Rloss = Rloss + (Prec - mrec*cp_l*(T_hot - Trec)/1.0e6)*dt;
        Prec = mrec*cp_l*(T_hot - Trec)/1.0e6;

        if(tanksat < 1){
                //Record saturation profile
                fsat = fopen(sat_file, "w+");
                for(j = 0; j < n; j++){
                        fprintf(fbed,"%.4f,",fx[j]);
                        fprintf(fbed,"%.2f,",fT1[j]);
                        fprintf(fbed,"%.2f,",fT2[j]);
                        fprintf(fbed,"%.2f,",fm[j]);
                        fprintf(fbed,"%.4f\n",fsol[j]);
                }
                fclose(fsat);
                tanksat = 1;
```

```
                }
        }

        //THERMOCLINE TANK DISPATCH CONTROL
        if(mcyc > mrec){
                //Tank discharge needed
                Flag = 1;
        }
        else{
                //Tank in charge or standby
                Flag = 0;
        }

        if(tstrt > 0.0 && tstrt < 0.001 && hourt < 2.0){
                //Turbine attempting to startup with < 2h of stored energy
                if(PTWF[step+1]<Qdes || PTWF[step+2]<Qdes ||
PTWF[step+3]<Qdes || PTWF[step+4]<Qdes){
                        //Future sunlight not sufficient to start turbine
                        mcyc = 0.0;
                        tstrt = 0.0;
                }
        }

        if(Tflag == 1 && Wgrs < 0.1){
                //Return turbine to deactivated state
                Tflag = 0;
        }

        //Turbie shutdown and warmup times (in hours)
        if(Wgrs < 0.1 && tstrt < 0.0001){
                //Turbine is off and not in warmup
                //Calculate required startup and rampup times
                t_off = t_off + dt/3600.0;
                t_end = 40.0/60.0;
                t_ramp = 25.0/60.0;
                if(t_off > 12.0){
                        t_end = 160.0/60.0;
                        t_ramp = 100.0/60.0;
                        if(t_off > 72.0){
                                t_end = 270.0/60.0;
                                t_ramp = 160.0/60.0;
                        }
                }
        }
        else{
```

```
                //Turbine is active
                t_off = 0.0;
        }


        //Monitor rated and derated turbine output time
        if(Wgrs > 0.0){
                if(Wgrs == Wnet/(1.0-0.103)){
                        trated = trated + dt/(3600.0);
                }
                else{
                        tderated = tderated + dt/(3600.0);
                }
        }


        //Update cumulative receiver power and turbine output
        Sunq = Sunq + Prec*dt;          //MJ
        Elec = Elec + Wgrs*(1.0-0.103)*dt; //MJ  net value


        //Calculate thermocline tank storage effectiveness
        Qmax = Qmax + Prec*dt/(3600.0);                              //MWh
        Qtnk = Qtnk + mcyc*cp_l*(Theel-T_cold)*dt/(1.0e6*3600.0);    //MWh


        //Calculate mass flow rate at tank floor (+) discharge (-) charge
        mass_bot = mcyc - mrec;


        //Calculate temperature entering bed (Continuity Analysis!)
        if(mass_bot >= 0.0){
                //Discharge
                Temp_in = T_cold;
        }
        else{
                Temp_in = Theel;
        }


        //Calculate bed mass and energy
        Eold = 0.0; mold = 0.0;
        fbed = fopen(bed_file, "r");
        for(j = 0; j < n; j++){
                fscanf(fbed,"%f,", &fx[j]);
                fscanf(fbed,"%f,", &fT1[j]);
                fscanf(fbed,"%f,", &fT2[j]);
                fscanf(fbed,"%f,", &fm[j]);
                fscanf(fbed,"%f\n", &fsol[j]);

                //Need to calculate bed energy content
```

```
                    volc = dx*area;
                    rho1 = 2090.0 - 0.636*fT1[j];
                    Eliq = pp*volc*rho1*cp_l*(fT1[j] - 300.0);
                    Esol = (1.0-pp)*volc*rho_s*(cp_s*(fT2[j]-300.0) + latent*(1.0-
fsol[j]));

                    Eold = Eold + Eliq + Esol;
                    mold = mold + pp*volc*rho1;
            }
            fclose(fbed);

            //Calculate total standby time
            if(mass_bot == 0.0){
                    standby = standby + dt;
            }

            //SOLVE THERMOCLINE MODEL TO UPDATE TANK BED
            storage(mass_bot, Temp_in);

            //Calculate updated bed mass and energy
            Enet = 0.0; mliq = 0.0; timet = 0.0; Sgen = 0.0; Esen = 0.0; Elat = 0.0;
            fbed = fopen(bed_file, "r");
            for(j = 0; j < n; j++){
                    fscanf(fbed,"%f,", &fx[j]);
                    fscanf(fbed,"%f,", &fT1[j]);
                    fscanf(fbed,"%f,", &fT2[j]);
                    fscanf(fbed,"%f,", &fm[j]);
                    fscanf(fbed,"%f\n", &fsol[j]);

                    //Need to calculate bed energy content
                    volc = dx*area;
                    rho1 = 2090.0 - 0.636*fT1[j];
                    Eliq = pp*volc*rho1*cp_l*(fT1[j] - 300.0);
                    Esol = (1.0-pp)*volc*rho_s*(cp_s*(fT2[j]-300.0) + latent*(1.0-
fsol[j]));

                    Enet = Enet + Eliq + Esol;

                    Esen = Esen + Eliq + (1.0-pp)*volc*rho_s*cp_s*(fT2[j]-300.0);
                    Elat = Elat + (1.0-pp)*volc*rho_s*latent*(1.0-fsol[j]);
                    mliq = mliq + pp*volc*rho1;

                    if(fT1[j] > Tmin){
                            //Approximation using only salt data
                            theta = (fT1[j] - 300.0)/(300.0);
                            mass1 = volc*rho1;
```

```
                          rate = (-0.59764*pow(theta,3.0)+0.39901*pow(theta,2.0)
+1.4306*theta-0.23253)*mc0;
                          timet = timet + (mass1/rate)/60.0;
                    }
              }
              fclose(fbed);

              //Update liquid heel mass
              dm_dt = (mold - mliq)/dt;
              M_kg = M_kg + dm_dt*dt;

              //Update liquid heel energy
              mass_bot = fm[0];
              mass_top = fm[n-1];
              Ttop = fT1[n-1];
              kheel = 0.443 + 1.9e-4*Theel;          /*Use old heel temperature to
calculate k at boundary*/
              diffusion = kheel*area*(Theel - Ttop)/(dx/2.0);  /*diffusion from heel to
bed*/

              if(mass_bot < 0.0){
                    //Charge
                    E_in = mrec*cp_l*(T_hot - T_cold);
                    E_out = mcyc*cp_l*(Theel - T_cold) - mass_top*cp_l*(Theel -
T_cold) + diffusion;
                    }
              else{
                    //Discharge
                    E_in = mrec*cp_l*(T_hot - T_cold) + mass_top*cp_l*(Ttop -
T_cold);
                    E_out = mcyc*cp_l*(Theel - T_cold) + diffusion;
              }
              dE_dt = (E_in - E_out)/1.0e6;
              E_MJ = E_MJ + dE_dt*dt;

              //Update liquid heel temperature
              T_ave = T_cold + E_MJ*1.0e6/(M_kg*cp_l);
              Etank = (Enet/1.0e6 + E_MJ)/3600.0;

              //Check if heel temperature exceeds the hot limit which is not physical
              if(T_ave > T_hot){
                    //Artificially reduce heel energy to compensate for this
                    //This exhibits less error than modifying the heel mass instead
                    //In reality the total liquid mass remains constant
```

```
                        T_ave = T_hot;
                        E_MJ = M_kg*cp_l*(T_ave - T_cold)/1.0e6;
                }
                liquid = mliq + M_kg;

                //Estimate remaining turbine time provided by thermocline tank
                if(T_ave > Tmin){
                        theta = (T_ave - 300.0)/300.0;
                        rate = (-
0.59764*pow(theta,3.0)+0.39901*pow(theta,2.0)+1.4306*theta-0.23253)*mc0;
                        timet = timet + (M_kg/rate)/60.0;
                }

                //Calculate future turbine time
                //Includes a 1.17 fudge factor to improve accuracy
                timet = 15.0*floor((timet/1.17)/15.0);

                //Prevent reporting a turbine time increase due to standby diffusion
                if(mrec < 1.0){
                        hourt = min(timet/60.0,hourt);
                }
                else{
                        hourt = timet/60.0;
                }

                //Update heel file
                fheel = fopen(heel_file, "w");
                fprintf(fheel,"%f, %f, %f", M_kg, E_MJ, T_ave);
                fclose(fheel);

                //Correction for output file
                if(hour > 23.5){
                        nday = nday - 1.0;
                }

                //15 minute summary
                if(t_step % 300 == 0){
                        output = fopen(min_file,"a+");

        fprintf(output,"%.0f,%.2f,%.2f,%.1f,%.2f,%.2f,%.2f,%.2f,%.1f,%.1f,%.1f,%.4f,%
.4f,%.2f,%d,%.2f,%d,%.1f\n",nday,hour,Prec,Trec,mrec,mcyc,mass_bot,mass_top,Tbot,
Ttop,T_ave,Esen/(1.0e6*3600.0),Elat/(1.0e6*3600.0),Wgrs,Flag,hourt,Tflag,liquid/1000.
0);
                        fclose(output);
                }
```

```
                    //Daily summary performed at 6am (time when turbine always off)
                    if(hour == 5.75 && nday > 1){
                            eff = Qtnk/Qmax;
                            CF = Elec/(time*Wnet);  //MJ/MJ
                            //Prat = Elec/Sunq;

                            //Record (1) day, (2) Qmax, (3) Qtnk, (4) CF, (5) Net Work, (6)
Discard
                            CSPout = fopen(day_file,"a+");
                            fprintf(CSPout,"%.0f,%.2f,%.2f,%.5f,%.4f,%.2f\n",nday-1,Qmax,
Qtnk,CF,Elec/(1000.0*3600.0),Rloss/3600.0);
                            fclose(CSPout);

                            if(Rloss > Loss_old){
                                    sat = sat + 1;
                                    Loss_old = Rloss;
                            }
                    }
            }

        //Annual capacity factor
        CF = Elec/(time*Wnet);

        //Output annual performance
        printf("\nReceiver absorbed energy is %0.5f GWh\n", Sunq/(3600.0*1000.0));
        printf("Net turbine output is %0.5f GWh\n", Elec/(3600.0*1000.0));
        printf("Annual net capacity factor is %0.5f\n", CF);
        printf("Number of saturation events is %d\n", sat);
        printf("Thermal energy discard is %0.5f GWh\n", Rloss/(3600.0*1000.0));
        printf("Annual tank effectiveness is %0.5f\n", Qtnk/Qmax);
        printf("Theoretical max CF is %0.5f\n\n", (Sunq+Rloss)*n_cyc*(1.0-
0.103)/(Wnet*24.0*365.0*3600.0));

        printf("Number of hot starts:  %d\n", hot);
        printf("Number of warm starts: %d\n", warm);
        printf("Number of cold starts: %d\n", cold);
        printf("Standby time: %0.5f days\n", standby/(3600.0*24.0));
        printf("Rated output time: %0.5f hours\n", trated);
        printf("Derated output time: %0.5f hours\n", tderated);

        //Output total calculation time
        proc = clock() - proc;
        printf("Calculation time was %0.2f minutes\n\n",
((float)proc)/(CLOCKS_PER_SEC*60.0));
```

```
        //Write annual plant results to day summary file
        CSPout = fopen(day_file,"a+");
        fprintf(CSPout,"%.0f,%.2f,%.2f,%.5f,%.4f,%.2f\n",nday,Qmax,Qtnk,CF,Elec/(10
00.0*3600.0),Rloss/3600.0);
        fprintf(CSPout,"\nStorage time is %.1f h (0.5 hour overdesign)\n", hour_tank);
        fprintf(CSPout,"Maximum storage capacity is %.2f MWh\n", Emax);
        fprintf(CSPout,"Thermocline tank area is %0.2f m2\n", area);
        fprintf(CSPout,"\nReceiver absorbed energy is %0.5f GWh\n",
Sunq/(3600.0*1000.0));
        fprintf(CSPout,"Net turbine output is %0.5f GWh\n", Elec/(3600.0*1000.0));
        fprintf(CSPout,"Annual net capacity factor is %0.5f\n", CF);
        fprintf(CSPout,"Number of saturation events is %d\n", sat);
        fprintf(CSPout,"Thermal energy discard is %0.5f GWh\n",
Rloss/(3600.0*1000.0));
        fprintf(CSPout,"Annual tank effectiveness is %0.5f\n", Qtnk/Qmax);
        fprintf(CSPout,"Theoretical max CF is %0.5f\n", (Sunq+Rloss)*n_cyc*(1.0-
0.103)/(Wnet*24.0*365.0*3600.0));
        fprintf(CSPout,"Number of hot starts:  %d\n", hot);
        fprintf(CSPout,"Number of warm starts: %d\n", warm);
        fprintf(CSPout,"Number of cold starts: %d\n", cold);
        fprintf(CSPout,"Standby time: %0.5f days\n", standby/(3600.0*24.0));
        fprintf(CSPout,"Calculation time was %0.2f minutes\n",
((float)proc)/(CLOCKS_PER_SEC*60.0));
        fprintf(CSPout,"Rated output time: %0.5f hours\n", trated);
        fprintf(CSPout,"Derated output time: %0.5f hours\n", tderated);
        fclose(CSPout);


        return 0;
}
double storage(double mass_bot, double Temp_in){

        //THERMOCLINE TANK MODEL
        //Update temperature profile inside tank
        int i, j, k;
        double dx, TMs, Hs, as0, T_in, rho_in, vel_in, TM_in, xp[n], Salt[n], vp[n], xday;
        double Rock[n], T1[n], T2[n], Tp0, Ts0, rho0, H0, ap0[n], it1[n], it2[n], sol[n];
        double rhop, H1, up, Fp, mflow[n], temp, mu, kl, Re, Pr, Nu, hv[n], Sp, Sc;
        double Tw, rhow, uw, aw[n], ae[n], b1[n], ap1[n], Fw, dp_e, dp_w, Fe, temp2,
dFdT;
        double a_x[n], b_x[n], c_x[n], d_x[n], phi_x[n], bs1, as1, mtemp[n], west, east;
        double phi_b, ks, beta, phi, numk, denk, keff, gamma, ab, Theel, speed_in,
phi_wall;
        double r_e, r_w, psi_e, psi_w, numsum1, densum1, numsum2, densum2, res1,
res2;
```

```
double sumres, Ts1[n], Tl1[n], tempe, ke, gam_east, gam_e, gam_w, gam_heel,
double gam_floor;
float fx[n], fT1[n], fT2[n], fm[n], fsol[n], M_kg, E_MJ, T_ave;
FILE *fbed, *fheel;

dx = height/n;
T_in = (Temp_in - T_cold)/(T_hot - T_cold);
rho_in = density(T_in);

//Read in thermocline bed temps
fbed = fopen(bed_file, "r");
for(j = 0; j < n; j++){
        fscanf(fbed,"%f,", &fx[j]);
        fscanf(fbed,"%f,", &fT1[j]);
        fscanf(fbed,"%f,", &fT2[j]);
        fscanf(fbed,"%f,", &fm[j]);
        fscanf(fbed,"%f\n", &fsol[j]);

        xp[j] = fx[j];
        Salt[j] = fT1[j];
        Rock[j] = fT2[j];
}
fclose(fbed);

//Artificial inversion of temp field for hot inflow (charge)
for(j = 0; j < n; j++){
        if(mass_bot >= 0.0){
                //Discharge
                k = j;
        }
        else{
                //Charge
                k = n - 1 - j;
        }
        T1[k] = (Salt[j] - T_cold)/(T_hot - T_cold);
        T2[k] = (Rock[j] - T_cold)/(T_hot - T_cold);

        Ts1[k] = Tsol[j];        //Invert solidus and liquidus?
        Tl1[k] = Tliq[j];
}

//Read in heel temp to get phi_b for diffusion
fheel = fopen(heel_file, "r");
fscanf(fheel,"%f, %f, %f", &M_kg, &E_MJ, &T_ave);
Theel = T_ave;
```

```
fclose(fheel);
phi_b = (Theel - T_cold)/(T_hot - T_cold);

//Implicit method with TDMA solver
//Iteration necessary for non-linearity and equation coupling
sumres = 1.0; i = 0;
while(sumres > 1e-6 && i < 75){

        if(i == 0){
                /*Initialize iteration temperatures*/
                for(j = 0; j < n; j++){
                        it1[j] = T1[j];
                        it2[j] = T2[j];
                }
        }

        /*Continuity*/
        if(mass_bot >= 0.0){
                /*Discharge (solve from inflow to outflow)*/
                for(j = 0; j < n; j++){
                        if(j == 0){
                                /*Cold inflow*/
                                Tw = T_in;
                                uw = mass_bot/(density(T_in)*area);
                        }
                        else{
                                /*Interior cells and hot outflow*/
                                Tw = it1[j-1];
                                uw = vp[j-1];
                        }
                        rhow = density(Tw);             /*west density*/
                        rhop = density(it1[j]);         /*current density*/

                        rho0 = density(T1[j]);          /*old density*/

                        vp[j] = (rhow*uw*dt - pp*(rhop-rho0)*dx)/(rhop*dt);
                        vp[j] = max(vp[j],0.0);         /*prevent neg vel*/
                }
                vel_in = mass_bot/(density(T_in)*area);
        }
        else{
                /*Charge (solve from outflow to inflow)*/
                for(j = n-1; j > -1; j--){
                        if(j == n-1){
                                /*Cold outflow*/
```

```
                        Tw = it1[j-1];
                        vp[j] = -mass_bot/(density(it1[j])*area);
                }
                if(j > 0 && j < n-1){
                        /*Interior cells*/
                        Tw = it1[j-1];
                        vp[j] = uw;
                }
                if(j == 0){
                        /*Hot inflow*/
                        Tw = T_in;
                        vp[j] = uw;
                }
                rhow = density(Tw);             /*west density*/
                rhop = density(it1[j]);         /*current density*/

                rho0 = density(T1[j]);          /*old density*/
                uw = (rhop*vp[j]*dt + pp*(rhop-rho0)*dx)/(rhow*dt);
                uw = max(uw,0.0);               /*prevent neg vel*/
        }
        vel_in = -uw;
}
speed_in = fabs(vel_in);

/*Energy Transport*/
numsum1 = 0.0; densum1 = 0.0;
for(j = 0; j < n; j++){

        /*Previous time step*/
        Tp0 = T1[j];            /*old fluid temp*/
        Ts0 = T2[j];            /*old solid temp*/
        rho0 = density(Tp0);    /*old fluid density*/
        H0 = pp*rho0;           /*porosity X density*/
        ap0[j] = H0*dx/dt;

        /*Fluid Property Calculation*/
        rhop = density(it1[j]);
        H1 = pp*rhop;
        up = vp[j];
        Fp = rhop * up;
        mflow[j] = rhop*up*area;
        if(vel_in < 0.0){
                mflow[j] = -mflow[j];
        }
```

```
                temp = it1[j]*(T_hot - T_cold) + T_cold;
                mu = (22.714-0.12*temp+2.281e-4*pow(temp,2.0)-1.474e-
7*pow(temp,3.0))/1000.0;
                kl = 0.443 + 1.9e-4*temp;
                Re = rhop*up*d_s/mu;
                Pr = mu*cp_l/kl;
                Nu = 6.0*(1.0-pp)*(2.0 + 1.1*pow(Re,0.6)*pow(Pr,0.333));
                hv[j] = Nu*kl/pow(d_s,2.0);

                Sp = -hv[j]/cp_l;
                Sc = (hv[j]/cp_l)*it2[j];

                /*Calculation of current cell thermal conductivity*/
                ks = 5.0;        /*Solid conductivity*/
                beta = (ks - kl)/(ks + 2.0*kl);
                phi = 1.0 - pp;
                numk = 1.0+2*beta*phi+(2*pow(beta,3.0)-
0.1*beta)*pow(phi,2.0)+pow(phi,3.0)*0.05*exp(4.5*beta);
                denk = 1.0 - beta*phi;
                keff = kl*numk/denk;
                gamma = keff/cp_l;

                /*Calculation of east cell thermal conductivity*/
                if(j < n-1){
                        tempe = it1[j+1]*(T_hot - T_cold) + T_cold;
                        ke = 0.443 + 1.9e-4*tempe;
                        beta = (ks - ke)/(ks + 2.0*ke);
                        numk = 1.0+2*beta*phi+(2*pow(beta,3.0)-
0.1*beta)*pow(phi,2.0)+pow(phi,3.0)*0.05*exp(4.5*beta);
                        denk = 1.0 - beta*phi;
                        gam_east = ke*(numk/denk)/cp_l;
                }
                gam_heel = (0.443 + 1.9e-4*Theel)/cp_l;

                /*Cycle through cells*/
                if(j == 0){
                        /*Inflow cell (Upwind Conv Scheme)*/
                        Tw = T_in;
                        rhow = density(Tw);
                        uw = speed_in;

                        if(vel_in >= 0.0){
                                //Discharge or idle (Cold limit)
                                //ab = 0.0;
                                phi_wall = 0.0;
```

```
                                        gam_floor = gamma;
                                        gam_e = 1.0/(0.5/gamma + 0.5/gam_east);

                                        aw[j] = 0.0;
                                        ae[j] = gam_e/dx;
                                        b1[j] = Sc*dx + rhow*uw*Tw +
gam_floor*(2.0/dx)*phi_wall;
                                        ap1[j] = H1*dx/dt + Fp - Sp*dx + (gam_e +
2.0*gam_floor)/dx;
                                }
                                else{
                                        //Charge (Heel Temp)
                                        //ab = gamma*2.0/dx;
                                        phi_wall = phi_b;
                                        gam_w = gam_heel;
                                        gam_e = 1.0/(0.5/gamma + 0.5/gam_east);

                                        aw[j] = 0.0;
                                        ae[j] = gam_e/dx;
                                        b1[j] = Sc*dx + rhow*uw*Tw +
gam_heel*(2.0/dx)*phi_wall;
                                        ap1[j] = H1*dx/dt + Fp - Sp*dx + (gam_e +
2.0*gam_heel)/dx;
                                }

                                west = 0.0;
                                east = ae[j]*it1[j+1];
                        }
                        if(j == 1){
                                /*Second cell (Upwind Conv Scheme)*/
                                Tw = it1[j-1];
                                rhow = density(Tw);
                                uw = vp[j-1];
                                Fw = rhow*uw;

                                gam_w = gam_e;
                                gam_e = 1.0/(0.5/gamma + 0.5/gam_east);

                                aw[j] = gam_w/dx + Fw;
                                ae[j] = gam_e/dx;
                                b1[j] = Sc*dx;
                                ap1[j] = H1*dx/dt + Fp - Sp*dx + (gam_w + gam_e)/dx;

                                west = aw[j]*it1[j-1];
                                east = ae[j]*it1[j+1];
```

```
                  }
                  if(j > 1 && j < n-1){
                          /*Interior cells (Quadratic Flux Limiter)*/
                          Tw = it1[j-1];
                          rhow = density(Tw);
                          uw = vp[j-1];
                          Fw = rhow*uw;

                          //Quadratic limiter scheme
                          r_e = (it1[j+1] - it1[j])/(it1[j] - it1[j-1]);
                          r_w = (it1[j] - it1[j-1])/(it1[j-1]-it1[j-2]);
                          psi_e = 0.0;
                          psi_w = 0.0;
                          if(r_e > 0.0 && r_e <= 2.0){
                                  psi_e = (2.0*r_e + pow(r_e,2.0))/(2.0 + r_e +
pow(r_e,2.0));
                          }
                          if(r_w > 0.0 && r_w <= 2.0){
                                  psi_w = (2.0*r_w + pow(r_w,2.0))/(2.0 + r_w +
pow(r_w,2.0));
                          }
                          if(r_e > 2.0){
                                  psi_e = 1.0;
                          }
                          if(r_w > 2.0){
                                  psi_w = 1.0;
                          }
                          dp_e = psi_e * 0.5 * (it1[j] - it1[j-1]);
                          dp_w = psi_w * 0.5 * (it1[j-1] - it1[j-2]);
                          Fe = Fp;

                          gam_w = gam_e;
                          gam_e = 1.0/(0.5/gamma + 0.5/gam_east);

                          aw[j] = gam_w/dx + Fw;
                          ae[j] = gam_e/dx;
                          b1[j] = Sc*dx + Fw*dp_w - Fe*dp_e;
                          ap1[j] = H1*dx/dt + Fp - Sp*dx + (gam_w + gam_e)/dx;

                          west = aw[j]*it1[j-1];
                          east = ae[j]*it1[j+1];
                  }
                  if(j == n-1){
                          /*Outflow cell (Upwind Conv Scheme)*/
                          /*constant temp diffusion BC (if idle)*/
```

```
                          Tw = it1[j-1];
                          rhow = density(Tw);
                          uw = vp[j-1];
                          Fw = rhow*uw;

                          if(vel_in >= 0.0){
                                  //Discharge or standby (heel temp)
                                  //ab = gamma*2.0/dx;
                                  phi_wall = phi_b;
                                  gam_w = gam_e;
                                  gam_e = gam_heel;

                                  aw[j] = gam_w/dx + Fw;
                                  ae[j] = 0.0;
                                  b1[j] = Sc*dx + gam_heel*(2.0/dx)*phi_wall;
                                  ap1[j] = H1*dx/dt + Fp - Sp*dx + (gam_w +
2.0*gam_heel)/dx;
                          }
                          else{
                                  //Charge (Cold limit)
                                  //ab = 0.0;
                                  phi_wall = 0.0;
                                  gam_w = gam_e;
                                  gam_floor = gamma;

                                  aw[j] = gam_w/dx + Fw;
                                  ae[j] = 0.0;
                                  b1[j] = Sc*dx + gam_floor*(2.0/dx)*phi_wall;
                                  ap1[j] = H1*dx/dt + Fp - Sp*dx + (gam_w +
2.0*gam_floor)/dx;
                          }

                          west = aw[j]*it1[j-1];
                          east = 0.0;
                  }
                  a_x[j] = ap1[j];
                  b_x[j] = ae[j];
                  c_x[j] = aw[j];
                  d_x[j] = b1[j] + ap0[j]*Tp0;

                  //Residual calculation
                  numsum1 = numsum1 + fabs(east + west + d_x[j] - a_x[j]*it1[j]);
                  densum1 = densum1 + a_x[j]*it1[j];
          }
```

```
            //Update liquid temps with TDMA
            TDMA(a_x, b_x, c_x, d_x, phi_x);
            for(j = 0; j < n; j++){
                    it1[j] = it1[j] + URF*(phi_x[j] - it1[j]);
            }

            //Update solid temps (using old hv)
            numsum2 = 0.0; densum2 = 0.0;
            for(j = 0; j < n; j++){

                    temp2 = it2[j]*(T_hot - T_cold) + T_cold;
                    if(temp2 > Ts1[j] && temp2 < Tl1[j]){
                            dFdT = -0.5/epsilon;
                    }
                    else{
                            dFdT = 0.0;
                    }

                    TMs = (1.0-pp)*rho_s*(cp_s - latent*dFdT);
                    Hs = TMs;
                    as0 = Hs/dt;

                    bs1 = hv[j]*it1[j];
                    as1 = as0 + hv[j];

                    //Residual calculation
                    numsum2 = numsum2 + fabs(bs1 + as0*T2[j] - as1*it2[j]);
                    densum2 = densum2 + as1*it2[j];

                    it2[j] = it2[j] + URF*((as0*T2[j] + bs1)/as1 - it2[j]);
            }

            res1 = numsum1/densum1;
            res2 = numsum2/densum2;
            sumres = res1+res2;
            i = i + 1;
    }

    if(sumres > 1e-5){      //Only print out residuals above 1e-5
            xday = ceil(tcount*dt/(24.0*3600.0));
            printf("Res is %f on day %0.1f, hour %0.4f\n", sumres, xday,
(tcount*dt/3600.0)-24.0*(xday-1.0));
    }

    //Reinvert temperature profile if hot inflow (charge)
```

```
        for(j = 0; j < n; j++){
                T1[j] = it1[j];
                T2[j] = it2[j];

                if(mass_bot >= 0.0){
                        k = j;
                }
                else{
                        k = n - 1 - j;
                }
                Salt[k] = T1[j]*(T_hot - T_cold) + T_cold;
                Rock[k] = T2[j]*(T_hot - T_cold) + T_cold;
                mtemp[k] = mflow[j];

                if(Rock[k] <= Tsol[k]){
                        sol[k] = 1.0;
                }
                else if(Rock[k] > Tliq[k]){
                        sol[k] = 0.0;
                }
                else{
                        sol[k] = (Tliq[k] - Rock[k])/(Tliq[k] - Tsol[k]);
                }
        }

        //Record updated bed temperatures
        fbed = fopen(bed_file, "w");
        for(j = 0; j < n; j++){
                fx[j] = xp[j];
                fT1[j] = Salt[j];
                fT2[j] = Rock[j];
                fm[j] = mtemp[j];
                fsol[j] = sol[j];

                fprintf(fbed,"%f,",fx[j]);
                fprintf(fbed,"%f,",fT1[j]);
                fprintf(fbed,"%f,",fT2[j]);
                fprintf(fbed,"%f,",fm[j]);
                fprintf(fbed,"%f\n",fsol[j]);
        }
        fclose(fbed);
        return 0;
}
double density(double T_norm){
```

```
        //Calculate and return molten salt density
        double temp, rho;
        temp = T_norm*(T_hot - T_cold) + T_cold;
        rho = 2090.0 - 0.636*temp;
        return rho;
}
double TDMA(double a_x[n],double b_x[n],double c_x[n],double d_x[n],double
phi_x[n]){

        //Tri-diagonal matrix algorithm (direct solver)
        int i;
        double P[n], Q[n];
        for(i = 0; i < n; i++){
                if(i == 0){
                        P[i] = b_x[i]/a_x[i];
                        Q[i] = d_x[i]/a_x[i];
                }
                if(i > 0 && i < n-1){
                        P[i] = b_x[i]/(a_x[i] - c_x[i]*P[i-1]);
                        Q[i] = (d_x[i] + c_x[i]*Q[i-1])/(a_x[i] - c_x[i]*P[i-1]);
                }
                if(i == n-1){
                        P[i] = 0;
                        Q[i] = (d_x[i] + c_x[i]*Q[i-1])/(a_x[i] - c_x[i]*P[i-1]);
                        phi_x[i] = Q[i];
                }
        }
        for(i = n-2; i > -1; i--){
                phi_x[i] = P[i]*phi_x[i+1] + Q[i];
        }
        return 0;
}
```

VITA

VITA

Scott M. Flueckiger received a Bachelor of Science in Mechanical Engineering from Purdue University in 2007. He then received a Master of Science in Mechanical Engineering from Purdue in 2009 for his thesis on thermal property characterization of hydrogen storage materials under the advisement of Prof. Yuan Zheng and Prof. Timothy S. Fisher. Scott is currently pursuing a Ph.D. in Mechanical Engineering at Purdue under the advisement of Prof. Suresh V. Garimella. As part of this program, he interned at the Sandia National Laboratories Concentrating Solar Technologies Department in the summer of 2011. His current research interests include concentrating solar power and thermal energy storage. After graduation, Scott will join The Aerospace Corporation in El Segundo, California as a Member of Technical Staff.

PUBLICATIONS

PUBLICATIONS

S. M. Flueckiger, B. D. Iverson, S. V. Garimella, "Economic optimization of a concentrating solar power plant with molten-salt thermocline storage," ASME Journal of Solar Energy Engineering, *accepted for publication*.

S. M. Flueckiger, B. D. Iverson, S. V. Garimella, J. E. Pacheco, "System-level simulation of a solar power tower plant with thermocline thermal energy storage," Applied Energy, vol. 113, pp. 86-96, 2014.

S. M. Flueckiger, Z. Yang, S. V. Garimella, "Review of molten-salt thermocline tank modeling for solar thermal energy storage," Heat Transfer Engineering, vol. 34, pp. 787-800, 2013.

S. M. Flueckiger, Z. Yang, S. V. Garimella, "Thermomechanical simulation of the Solar One thermocline storage tank," ASME Journal of Solar Energy Engineering, vol. 134, pp. 041014, 2012.

S. M. Flueckiger, S. V. Garimella, "Second-law analysis of molten-salt thermal energy storage in thermoclines," Solar Energy, vol. 86, pp. 1621-1631, 2012.

S. M. Flueckiger, F. Volle, S.V. Garimella, R. K. Mongia, "Thermodynamic and kinetic investigation of a chemical reaction-based miniature heat pump," Energy Conversion and Management, vol. 64, pp. 222-231, 2012.

S. Flueckiger, Z. Yang, S. V. Garimella, "An integrated thermal and mechanical investigation of molten-salt thermocline energy storage," Applied Energy, vol. 88, pp. 2098-2105, 2011.

S. Flueckiger, T. Voskuilen, T. Pourpoint, T. S. Fisher, Y. Zheng, "In situ characterization of metal hydride thermal transport properties," International Journal of Hydrogen Energy, vol. 35, pp. 614-621, 2009.

S. M. Flueckiger, S. V. Garimella, "Latent heat augmentation of thermocline energy storage for concentrating solar power – a system-level assessment," *in review*.

B. D. Iverson, S. J. Bauer, S. M. Flueckiger, "Thermocline bed properties for deformation analysis," *in review*.

S. M. Flueckiger, B. D. Iverson, S. V. Garimella, "Simulation of a concentrating solar power plant with molten-salt thermocline storage for optimized annual performance," Proceedings of the ASME Energy Sustainability Conference, 2013, Minneapolis, MN.

S. M. Flueckiger, S. V. Garimella, E. A. Groll, "Numerical study of supercritical CO_2 convective heat transfer in advanced Brayton cycles for Concentrated Solar Power," Proceedings of the ASME Energy Sustainability Conference, 2012, San Diego, CA.

B. D. Iverson, S. M. Flueckiger, B. Ehrhart, "Trough heat collection element deformation and solar intercept impact," SolarPACES, 2011, Granada, Spain.

S. Flueckiger, Z. Yang, S. V. Garimella, "Thermocline energy storage in the Solar One power plant: an experimentally validated thermomechanical investigation," Proceedings of the ASME Energy Sustainability Conference, 2011, Washington D.C.

S. Flueckiger, T. Voskuilen, Y. Zheng, T. Pourpoint, "Advanced transient plane source method for the measurement of thermal properties of high pressure metal hydrides," Proceedings of the ASME Summer Heat Transfer Conference, 2009, San Francisco, CA.

S. Flueckiger, Y. Zheng, T. Pourpoint, "Transient plane source method for thermal property measurements of metal hydrides," Proceedings of the ASME Summer Heat Transfer Conference, 2008, Jacksonville, FL.